Melting modes in laser powder bed fusion additive manufacturing

by

Sagar Patel

A thesis
presented to the University of Waterloo
in fulfillment of the
thesis requirement for the degree of
Doctor of Philosophy
in
Mechanical and Mechatronics Engineering

Waterloo, Ontario, Canada, 2021

Examining Committee Membership

The following served on the Examining Committee for this thesis. The decision of the Examining Committee is by majority vote.

External Examiner: Milan Brandt, Distinguished Professor
Department of Advanced Manufacturing
RMIT University

Supervisor: Mihaela Vlasea, Assistant Professor
Dept. of Mechanical and Mechatronics Engineering
University of Waterloo

Internal Member: Fue-Sang Lien, Professor
Dept. of Mechanical and Mechatronics Engineering
University of Waterloo

Internal Member: Elliott Biro, Assistant Professor
Dept. of Mechanical and Mechatronics Engineering
University of Waterloo

Internal Member: Stewart McLachlin, Assistant Professor
Dept. of Mechanical and Mechatronics Engineering
University of Waterloo

Internal-External Member: Thomas Willett, Assistant Professor
Dept. of Systems Design Engineering
University of Waterloo

Author's Declaration

This thesis consists of materials all of which I authored or co-authored: see the section of Statement of Contributions. This is a true copy of the thesis, including any required final revisions, as accepted by my examiners. I understand that my thesis may be made electronically available to the public.

Statement of Contributions

Chapter 4 of this thesis consists of an article that was co-authored by myself, my supervisor, Professor Yu Zou, and Ms. Haoxiu Chen. I conducted the simulations, LPBF processing, X-ray computer tomography analysis, and wrote the article. Haoxiu Chen conducted the metallography of the samples. All authors guided the research, and helped with reviewing and editing of the article.

Chapter 5 of this thesis consists of an article that was co-authored by myself, my supervisor, and Dr. Allan Rogalsky. I conducted the simulations, LPBF processing, microscopy, and wrote the article. Dr. Allan Rogalsky created the contour plots for the results and discussion section of the paper, and provided guidance on statistical analysis of the design of experiments. All authors guided the research, and helped with reviewing and editing of the article.

Chapter 6 of this thesis consists of an article that was co-authored by myself, my supervisor, Dr. Mohsen Keshavarz, and Ms. Sharon Ann Varghese. I conducted the simulations, LPBF processing, X-ray computer tomography analysis, microscopy, and wrote the article. Ms. Sharon Ann Varghese conducted the residual stress analysis and helped with the write-up of the corresponding sections. Dr. Mohsen Keshavarz helped with the literature review and discussion for the origins of cracking. All authors guided the research, and helped with reviewing and editing of the article.

Abstract

Laser powder bed fusion (LPBF) is a metal AM technology that has one of the highest industrial uptake at the moment in the aerospace, automotive, and biomedical sectors. LPBF enjoys such popularity as it enables the manufacturing of near-net-shape geometrically complex metal parts. LPBF allows for optimised designs to be explored for manufacturing, such as topology optimised or loading field-driven designs for product lightweighting and customization, while also reducing environmental impact through energy reduction and low carbon dioxide emissions, helping the transition towards sustainable manufacturing. The manufacturing of products using LPBF is almost entirely digitally controlled, from a computer-aided design model to layer-by-layer customization of process parameters, to monitoring and controlling the process while parts are being manufactured. The digitization of metal AM opens up exciting new avenues in areas of design, process planning, process monitoring, and process control. This thesis focuses primarily on process planning for LPBF. Process planning involves developing a theoretical understanding of the effects of the numerous process parameters that could be digitally controlled in LPBF on the final product outcomes. Within LPBF process planning, it is highly challenging to understand and model the complex laser-material interaction phenomena in LPBF, often resulting in marginally stable process parameters or resulting in a high number of experiments in the development of process parameters required to meet part quality metrics.

This thesis focuses on process physics modelling and simulation at the mesoscale to develop a theoretical understanding of the impact of LPBF process parameters on outcomes such as porous defects, surface topography, and residual stresses. For this purpose, normalized processing diagrams have been developed to visualize the three melting modes (conduction, transition, and keyhole mode) observed in LPBF. The normalized processing diagrams obtained in this thesis, for the first time in LPBF, are shown to be independent of material, LPBF system, and processing parameters such as powder layer thickness within the datasets presented herein. Additionally, a temperature prediction model has been developed to predict the thresholds between the conduction, transition, and keyhole melting modes. The efficacy of these predicted thresholds has been evaluated experimentally for low reflectivity (titanium and ferrous) alloys and high reflectivity (aluminium) alloys. For low reflectivity alloys, a vaporisation depth greater than 0.5 and 0.8 times the beam spot radius corresponds to the thresholds between conduction to transition mode and transition to keyhole mode respectively. For high reflectivity alloys, surface vaporisation and a vaporisation depth greater than 0.5 times the beam spot radius used corresponds to the thresholds between conduction to transition mode and transition to keyhole mode respectively. Simulations using the normalized processing diagrams and the temperature

prediction model are then used to develop a fundamental understanding of porous defects, surface topography, and residual stresses during LPBF of an aluminium alloy (AlSi10Mg) and two titanium alloys (Ti-6Al-4V and Ti-6242Si).

For high reflectivity materials such as aluminium alloys, when considering density optimization, divergent beams with resulting focal diameters >100 µm help to obtain a conduction mode microstructure leading to parts with densities of over 99.98%. When working with a focused beam, stabilizing melt pool and spatter dynamics in the transition melting mode by using an appropriate laser power and velocity combination can help in minimizing defects and obtaining densities close to 99.98%, similar to conduction mode densities, albeit with a narrower process parameter window for success. Additionally, a melt pool aspect ratio (ratio of depth to width) of ≈0.4 is observed to be the threshold between conduction and transition/keyhole mode melt pools, which differs from the conventionally assumed melt pool aspect ratio of 0.5. This thesis thereby provides a novel method to obtain high-quality aluminium alloy parts with defocused and focused beams in LPBF. Such findings can be expanded to other high reflectivity alloys for LPBF.

For low reflectivity alloys, when considering density optimization during LPBF of Ti-6242Si, the use of processing diagrams alongside X-ray computer tomography and imaging show that Ti-6242Si has a broad process window with parts above 99.90% density observed in conduction, transition, and keyhole melting modes of LPBF. While the highest density parts (up to 99.98%) are observed in the transition melting mode for Ti-6242Si, transition and keyhole mode LPBF of Ti-6242Si could also lead to macroscopic cracking perpendicular to the build direction, which is attributed primarily to the higher residual stresses during solidification.

Furthermore, when considering surface topography, a combination of statistical approaches, simulations, and experiments show that LPBF processing parameters that lie in the keyhole melting mode with lower beam velocity settings and conservative laser powers lead to surface roughness, Sa, values of lesser than 10 µm, which is significantly lower the roughness values obtained for conduction and transition mode LPBF process parameters for Ti-6Al-4V and Ti-6242Si. This significant reduction in surface roughness is due to a negligible contribution from partially melted powder particles in the keyhole melting mode border.

Lastly, the fundamental understanding of LPBF developed in this thesis was leveraged towards biomedical, military, and defence applications. The North American industry has shown a cautious approach to the adoption of LPBF, due to high initial investment costs, the iterative R&D nature of part production, and emerging certification needs. Successful industry adoption of metal additive manufacturing relies on understanding the complex

interactions between design, materials, and process to ensure high product quality and reliability. This thesis would help lower the risk of LPBF technology adoption by virtue of offering a better understanding of the physics behind the laser-material interaction in the process and reducing the need for extensive empirical approaches toward part quality-driven process parameter development.

Acknowledgements

I would like to thank all the people who made this thesis possible, and who made the journey feel like a team-driven effort.

I would like to first thank my PhD supervisor, Prof. Mihaela Vlasea, for her exceptional guidance and mentorship. I had little to no idea about how my PhD journey would look like with Prof. Vlasea before I landed in Canada, and I am elated to have chosen this journey with a role model like her. I would also like to thank my Master's supervisor, Prof. Matthew Kuttolamadom, for his guidance and mentorship. I would not be at this moment without his mentorship as his initial guidance on academic research still plays a part in my decision making. I would also like to thank Prof. Yu Zou, Prof. Stewart McLachlin, and Prof. Farhang Honarvar for their guidance and support in multiple previous and ongoing collaborative projects.

I would like to extend a special thanks to the technical and research staff members that supported my work throughout this journey - Jerry Ratthapakdee, Grace Kurosad, Karl Rautenberg, James Farnsworth, Karl Janzen, Robert Cieniawski, Allan Rogalsky, Mark Kirby, Vlad Paserin, and Farzad Liravi.

I have been fortunate to forge numerous friendships at work through my time at the University of Waterloo. Thank you to Gitanjali Shanbhag, Sera Ertay, Martine McGregor, Lisa Brock, Paola Russo, Alex Martinez, Henry Ma, Pablo Enrique, Reza Esmaeilizadeh, Ali Keshavarzkermani, Brian Zhang, Yanli Zhu, Issa Rishmawi, Brian Jeong, Mehrnaz Salarian, Ramy Tannous, Dogan Sinar, Haoxiu Chen, Pranav Agarwal, Gijs Johannes Jozef van Houtum, Jigar Patel, Marc Wang, Shahriar Shahabad, Elham Davoodi, Yuze Huang, Mohsen Keshavarz, Tatevik Minasyan, Sai Sravanthi, Yahya Mahmoodkhani, Ramona Fayazfar, Roman Boychuk, Kevin Hugh Zhang, Esmat Arani, Hamed Asgari, Ken Nsiempba, Osezua Ibhadode, Katayoon Taherkhani, Mazyar Ansari, Nivas Ramachandiran, Elahe Jabari, Ehsan Marzbanrad, Esmaeil Sadeghi, Paria Karimi, Apratim Chakraborty, Ruijian He, Evan Wheat, Mike Andary, Jordan Savage, Caleb Shepherd Davis, Sharon Ann Varghese, Mariya Peskova, Justin Memar, and Ophelie Lesage Fongue.

Finally, I would like to thank my family and dearest friends for their unconditional love and support.

Dedication

To my cherished family

Table of Contents

List of Figures

xix

List of Tables

Chapter 1

Introduction

Sustainable manufacturing involves producing high-quality production throughput, while reducing the environmental impact of manufacturing through reductions in input energy, raw materials wastage, and carbon dioxide emissions [53]. Powder metallurgy (PM) technologies are the only manufacturing technologies that can utilize more than 90% of input raw materials, thereby aiding the transition towards a sustainable manufacturing industry [53]. PM includes a set of metal-forming processing technologies that use metal powders, tools, and equipment to produce semi-dense or fully dense components for multiple industries, including aerospace, defence, automotive, medical, industrial machinery, and agriculture equipment. Metal injection moulding and powder-based metal additive manufacturing (AM) are the two fastest growing segments in the global PM market at the moment [54]. Metal AM technologies in particular are expected to have a near-100% material utilization and a sustained growth rate over the coming years, due to capabilities in AM of producing high-quality products for numerous industries requiring complex geometries and tailored material properties [55].

Metal AM technologies have come a long way from being used for prototyping nearly 30 years ago, to extensive usage for making aerospace, defence, medical, and dental products, with other sectors such as automotive and energy bridging the gap in technology adoption as well [56]. Space agencies such as the National Aeronautics and Space Administration (NASA) and the European Space Agency (ESA) have even launched initiatives that could one day allow astronauts to print their own metal tools aboard the International Space Station; ESA's project titled "Additive Manufacturing Aiming towards Zero waste and Efficient production of high-tech metal products" (AMAZE) is one example of a large scale AM initiative for aerospace products [57].

There are numerous examples of industrial metal AM applications. General Electric Aviation (USA) has replaced 855 conventional components in a turboprop engine with a dozen metal AM components [58]. AVIC Laser (China) foresees a potential to reduce the cost of complex structural titanium components to 5% of the original cost with the use of metal AM technologies [59]. While the use of metal AM in the automotive industry appears to be in the nascent stage, there has been a transition towards adoption. In North America, a metal powder manufacturer (GKN Powder Metallurgy) and an AM machine manufacturer (EOS) have teamed up to accelerate business-to-business metal AM for the automotive industry [60]. In Europe, an automaker (Daimler AG), a public research institute (Fraunhofer Institute for Laser Technology ILT), and an AM machine manufacturer (Concept Laser) have initiated a collaboration to produce structural parts, engine components, as well as components to be used directly inside vehicles [61]. In Australia, a biotech company (Anatomics), a hospital (St Vincent's Hospital), and a public research institute (CSIRO) collaborated to create the first titanium heel bone implant for a cancer patient facing amputation below the knee [62]. It took two weeks from the initial phone call (by the surgeon) to surgery which was an accelerated timeline made by possible by metal AM that saved the patient's leg from immediate amputation. These examples strengthen the industry and academic interest in growing the potential, the robustness, and reliability of metal AM technologies across sectors.

Metal additive manufacturing (AM) is the "process of joining materials to make parts from 3D model data, usually layer upon layer, as opposed to subtractive manufacturing and formative manufacturing methodologies" [63]. Figure 1.1 shows the popular variants of metal AM - directed energy deposition (DED) and powder bed fusion (PBF) - which generally differ by the type of heat source, either electron beam, laser, gas metal arc, or plasma arc and the type of feedstock input (wire or powder) [1]. Laser powder bed fusion (LPBF) is a metal AM technology that has one of the highest industrial uptake at the moment in the aerospace, automotive, and biomedical sectors [64].

The proposed research focuses on LPBF. LPBF is a metal AM process in which thin layers of powder are spread onto a build plate, then a laser energy source selectively fuses regions of the powder bed, depending on the locations provided by an execution build file which references stacked layers of a computer-aided design (CAD) part model. When one layer is fused, a new layer of powder is applied, and the process is repeated until a three-dimensional (3D) part is obtained. An illustration of a typical LPBF system at the process scale is shown in the left side of Figure 1.1. LPBF enables the manufacturing of near net-shape geometrically complex parts. LPBF allows for optimized designs to be explored for manufacturing, such as topology optimized or loading field driven designs for product lightweighting and customization [65], while also reducing environmental impact
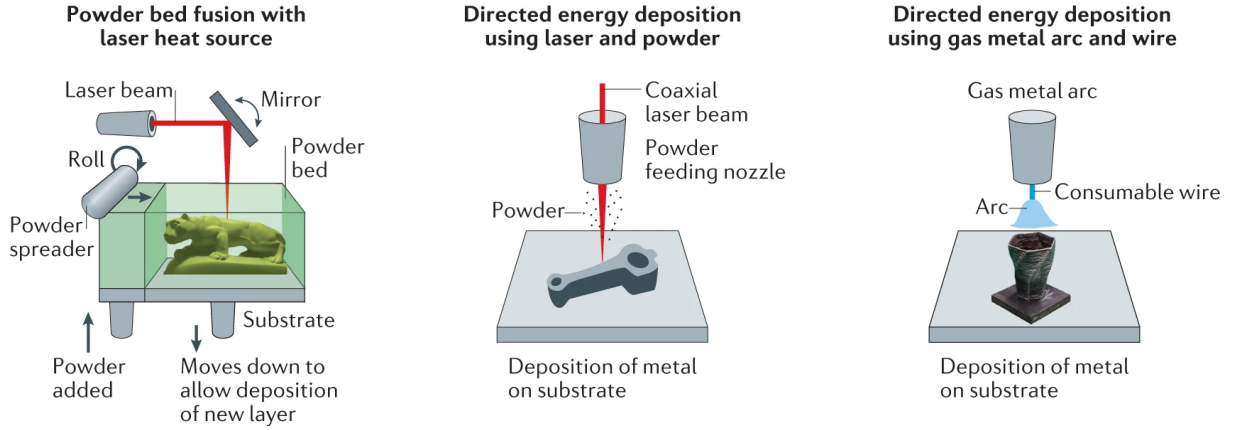
Figure 1.1: Process scale schematic of laser powder bed fusion (left), directed energy deposition using powder and laser (centre), and directed energy deposition using wire and gas metal arc (right). Reprinted with permission from [1].

through input energy reduction and carbon dioxide emissions [53].

1.1 Motivations

LPBF is particularly attractive for manufacturing high-quality complex geometries and for enabling assembly consolidation in numerous applications. The production of complex three-dimensional (3D) parts in metal AM technologies (including LPBF) is digitally controlled, from a computer-aided design model, to layer-by-layer customization of process parameters, to monitoring and controlling the process while parts are being manufactured. The digitization of metal AM opens up exciting avenues in areas of design, process planning, process monitoring, and process control. This thesis focuses primarily on process planning for LPBF. Process planning involves developing a theoretical understanding of the effects of the numerous process parameters in LPBF on the final product outcomes.

Emerging research efforts in LPBF process planning focus on correlating the process parameters, process signatures, and/or product quality through design of experiments [66, 67, 68, 69], surrogate modelling [70, 71, 72, 73], process physics modelling and simulation [74, 75, 76, 77], as well as advanced characterization-driven analytics [78, 79, 80, 3, 81, 82]. Each approach has a different computational cost and experimental footprint. Despite these efforts, it is highly challenging to understand and explain the complex laser-material interaction phenomena in LPBF, often resulting in marginally-

3

stable process parameters (also called process recipes) or a high number of experiments in the development of such process parameters to meet part quality metrics. This thesis focuses on process physics modelling and simulation at the mesoscale to develop a theoretical understanding of the impact of LPBF process parameters on outcomes such as
85 porous defects, surface topography, and residual stresses. This approach is of particular significance, as the common approach so far is to use rigorous experimentation to identify process parameters in order to produce high-quality products.

LPBF involves stitching of individual weld lines (melt pools) to form a layer and the stacking of multiple of layers on top of each other to obtain a three-dimensional (3D) part,
90 as demonstrated by the melt pool layout along the build (Z) direction in Figure 1.2. Melt pool shapes and their overlapping characteristics govern the final porosity characteristics in a given parts. The dominance of heat conduction or heat convection generally dictates the melt pool shapes and thereby porosity characteristics. For a given material, when the input energy density is lower than a certain threshold value, heat conduction is the dominant heat
95 transfer mechanism, leading to conduction mode melting in LPBF. The cross section of melt pools created in conduction mode is generally semicircular (i.e. the melt pool depth is about equal to its half-width), as shown in the left side of Figure 1.3. Conduction mode melting is generally associated with lack-of-fusion irregular-shaped defects as depicted in the left side of Figure 1.2. In contrast, keyhole mode melting is observed when the input energy
100 density exceeds a threshold value such that a deep vapour cavity forms within the molten metal due to intense localized heating and vaporisation of alloying elements. Additionally, lack-of-fusion irregular-shaped defects are also possible in the keyhole melting mode when there is an improper choice in process parameters leading to an inadequate stitching of melt pools. In keyhole mode of laser melting, the depth of the molten pool is controlled by the
105 recoil momentum pressure (also known as recoil pressure) generated by the vaporisation of the melt pool material. Convective heat transfer (particularly due to thermo-capillary convection, also known as Bénard-Marangoni convection) is the dominant mode of heat transfer within the molten pool [83, 84]. As shown in the right side of Figure 1.3, the keyhole mode melt pool is deep and narrow, with the shape influenced by the significant effects
110 of recoil pressure and Bénard-Marangoni convection. Figure 1.4 shows the molten pool formation during keyhole mode LPBF under the combined effects of Bénard-Marangoni convection and vapour recoil pressure. Following the creation of a vapour depression, temperature gradients in the melt pool lead to surface tension gradients. These gradients drive melt flow from the hot spot beneath the laser beam towards the cold rear, leading to
115 a centrifugal fluid flow in the melt pool [2, 85]. Additionally, the front wall angle that the vaporised depression forms to the incident laser beam then determines the extent of laser beam reflections inside the vapour depression leading to additional absorption of the input

4

laser energy density that add to the vapour recoil pressure and cause the formation of a deep and narrow melt pool shape [3]. Vaporisation instability related melt pool defects are common in the keyhole melting mode resulting in large rounded pores, as depicted in the right side of Figure 1.2. Additionally, there exists a regime between conduction and keyhole mode called the transition mode. Transition melting mode has been observed to have characteristics of both the conduction and keyhole melting modes, but its effect on the porosity characteristics of a final part is not fully understood. This thesis focuses on development of processing diagrams and a temperature prediction model to help predict the thresholds between the conduction, transition, and keyhole melting modes in LPBF. This theoretical understanding is imperative to assist with effective process planning for targeting desired micro- and mesoscale material quality outcomes.
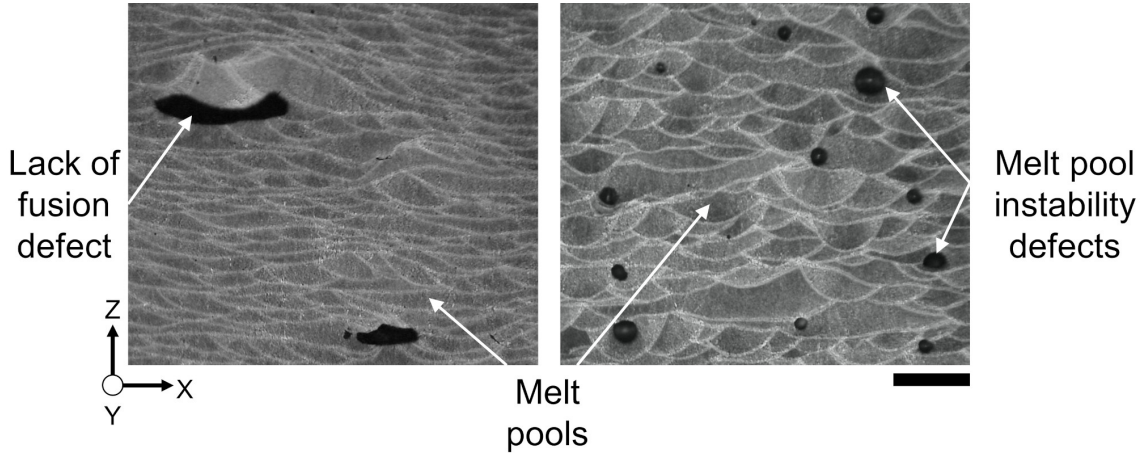
Figure 1.2: Common defect types observed in conduction mode LPBF (left) and keyhole mode LPBF (right). The black scale bar corresponds to 100 μm.

While there have been previous attempts at development of process diagrams and predicting melting mode thresholds [86, 87] in LPBF, the predictions have generally been material and machine dependent. To address these limitations, this thesis is the first attempt in LPBF to predict melting mode thresholds which are machine and material independent. Additionally, previous modelling attempts do not consider the differences between the laser absorptivity characteristics of high reflectivity (aluminium) alloys and low reflectivity (titanium, ferrous, and nickel) alloys, which is proposed for the first time in this thesis. The modelling tool developed in this thesis is of particular importance to increase LPBF technology adoption in numerous industries, as a machine-agnostic tool would help reduce the barrier for translating high-quality process parameters from one machine to another. Similarly, a material-agnostic modelling tool helps overcome the
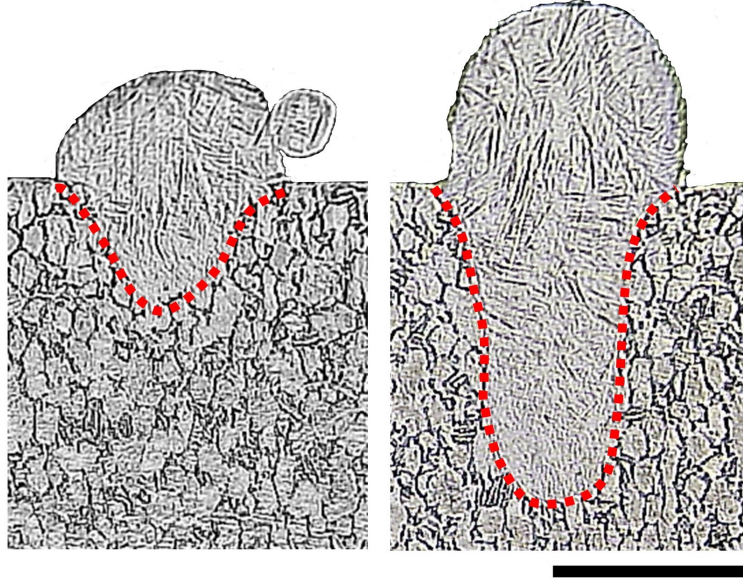
Figure 1.3: A conduction mode melt pool (left) and a keyhole mode melt pool (right) during LPBF of Ti-6Al-4V on a titanium build plate. The black scale bar corresponds to 100 µm.
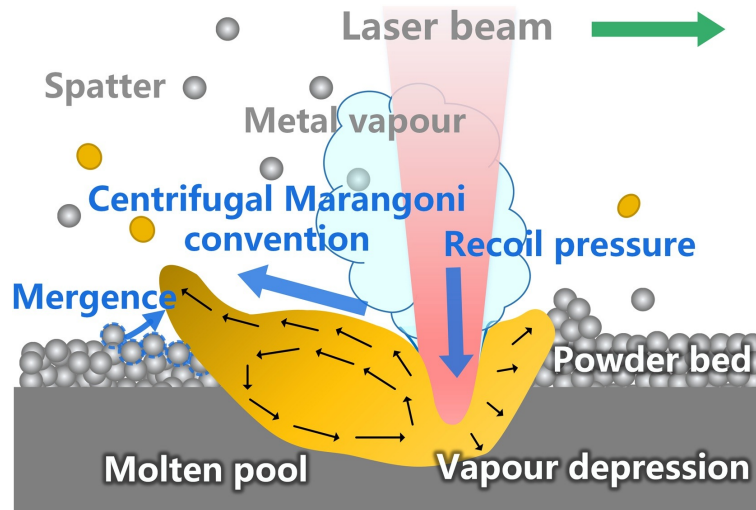
Figure 1.4: A illustration of the deep and narrow melt pool formation in keyhole mode LPBF due to the effects of vapour recoil pressure and Bénard-Marangoni convection. Reprinted with permission from [2].

challenges of cost and time typically associated while adopting a new material system for LPBF.

There is also a literature gap in showcasing machine-agnostic process performance maps and accelerated process parameter refinement methodologies for various material systems; this thesis looks to address this gap. The theoretical understanding of LPBF gained from the development of the modelling tools has been deployed in this thesis towards demonstrating the feasibility of accelerated process parameter developmental efforts for obtaining high-quality parts from AlSi10Mg, Ti-6Al-4V, and Ti-6242Si. Additionally, while numerical modelling attempts at the mesoscale offer additional insights into melting mode physics [88, 89], the computational times involved is generally multiple hours and often days [90]. When an accelerated process parameter development cycle is needed for new materials and machines, a rapid modelling tool reduce the scope the design of experiments is of importance. Analytical approaches such as the one developed in Chapter 3 have a computational cost in the order of seconds [90, 91]. This model can be deployed as web-based application with a graphical user interface (GUI) which is part of ongoing work to expand the reach of this thesis.

Lastly, the theoretical developments in this thesis have been deployed to meet and/or explore application-specific requirements:

Biomedical applications:

While the PBF of titanium (Ti) and Ti-6Al-4V lattices has been studied extensively for bone implants and augmentation devices, the optimal parameters for Ti and Ti-6Al-4V lattice designs corresponding to the natural micro- and meso-scale architecture of human trabecular and cortical bone are not well understood [92, 93]. Implanting a stiffer material like Ti or Ti-6Al-4V adjacent to bone is known to cause stress shielding of bone, leading to implant loosening and subsequent failure [94]. Therefore, it is imperative that designs of Ti and Ti-6Al-4V implants are tailored to more closely match the natural mechanical response of bone tissue. A review comparing the natural architecture in human bone to Ti and Ti-6Al-4V lattice structures manufactured by PBF technologies is provided as supplementary information to this thesis. Appendix A provides a comprehensive review to compare the natural lattice architecture properties in human bone to Ti and Ti-6Al-4V lattice structures manufactured by PBF technologies for bone repair and augmentation. Based on the findings of the literature review, recommendations for the design of Ti and Ti-6Al-4V lattice structures geared towards addressing recognized performance gaps due to manufacturability constraints of powder bed fusion technologies are provided. Some example of lattice structures manufacturable by LPBF are shown in Figure 1.5.
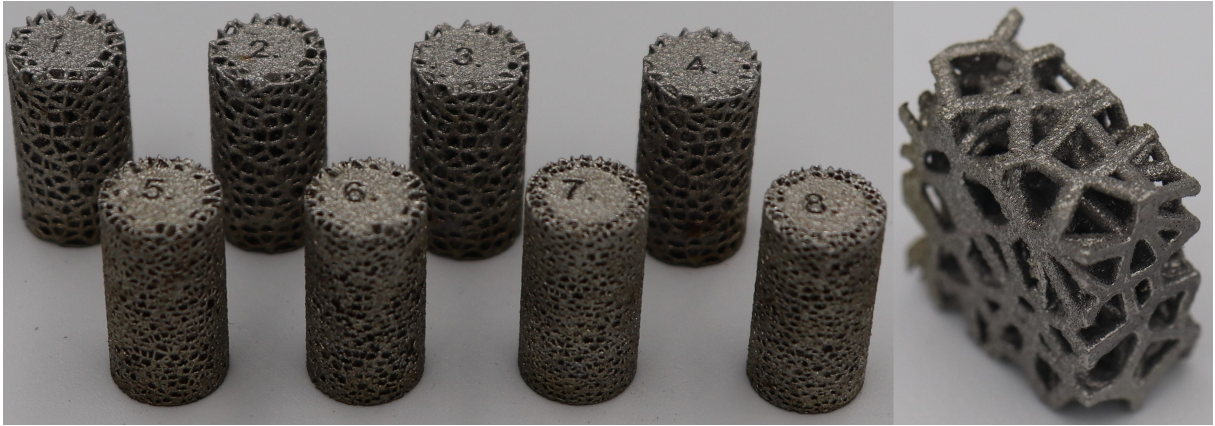
Figure 1.5: Demonstration of various strut-based lattice structures manufactured using LPBF.

Military applications:

While industrial uptake of LPBF in the civilian aerospace industry has been high, metal AM parts are still at a less advanced stage of development for military applications, since the currently available materials and technology do not meet military requirements [54]. One such example is the United States (US) Air Force which previously used additively manufactured Ti-6Al-4V to substitute for conventional high strength aluminium alloys. This is because conventional high strength aluminium alloys are susceptible to cracks during additive manufacturing [95]. The modelling attempts from this thesis were used to recommend Scalmalloy® as a high strength aluminium that can be successfully manufactured by LPBF as part of the "Materials Hurdles" challenge in the inaugural "Advanced Manufacturing Olympics" [96]. This application was supplementary to this thesis, and is summarized in Appendix B.
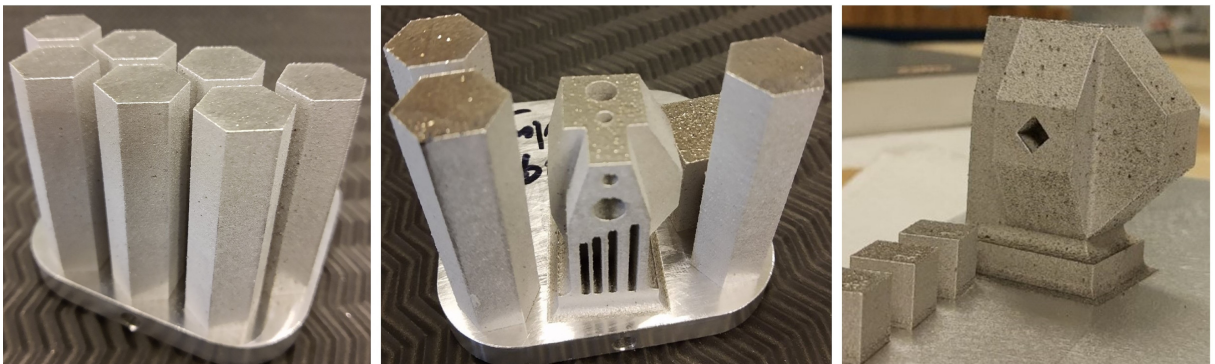
Figure 1.6: Tensile specimens, complex artifacts, cubes manufactured using Scalmalloy® for increasing technology adoption for military applications

8

Defence applications:

Light detection and ranging (LiDAR) technologies can benefit from the metal AM's ₁₉₀ capabilities to produce high-quality products with complex shapes or geometry as well. The global market for LiDAR technologies is currently worth $3.1 billion and is expected to grow to $8.7 billion by 2025 [97]. Modelling attempts from this thesis and design for additive manufacturing (DFAM) guidelines were used to conceptualise and manufacture a monolithic quantum sensing interferometer using LPBF in ₁₉₅ collaboration with the Quantum Photonics Laboratory at the Institute for Quantum Computing, University of Waterloo [98]. The material of choice was Invar36. The low coefficient of thermal expansion (CTE) of Invar36 compared to most known Invar alloys [99] made it suitable for this work requiring high dimensional stability. An image of the monolithic interferometer on top of a LPBF build plate is shown in ₂₀₀ Figure 1.7. The monolithic design, made possible by LPBF, is an important feature in creating a practical interferometer because it enables consistent engineering of a particular thermal expansion and stability. This application was supplementary to this thesis, and is summarized in Appendix C.
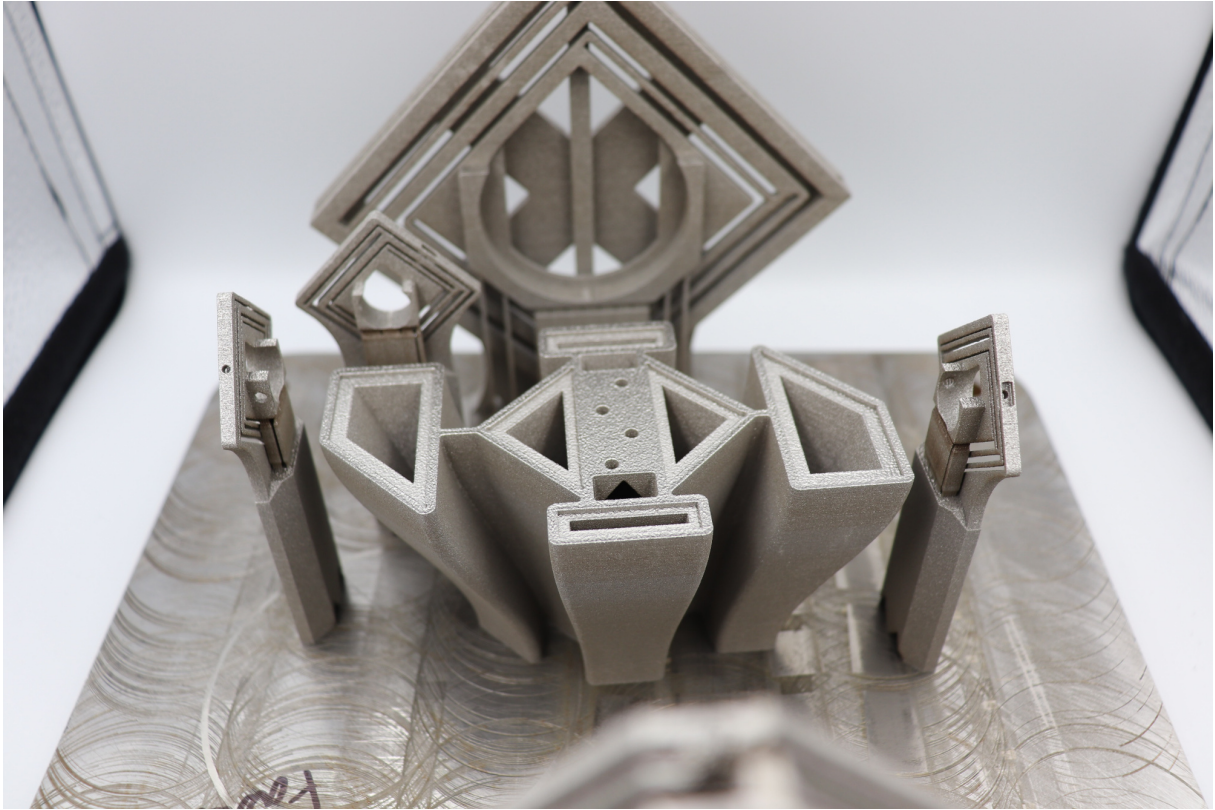
Figure 1.7: An image of the monolithic quantum sensing interferometer additively manufactured using Invar36 on a Renishaw AM 400 LPBF system.

1.2 Thesis objectives

This thesis is geared towards developing a better understanding of LPBF at the mesoscale and macroscale. The thesis has three objectives:

- Objective 1: To create a rapid modelling tool that can be deployed for mapping of process quality outcomes in LPBF to reduce the need for computationally-intensive numerical modelling efforts.

- Objective 2: To demonstrate the efficacy of the modelling tool in reducing the scope of design of experiments for accelerated process parameter development for two classes of materials, materials with high and low reflectivity.

- Objective 3: To apply the theoretical developments towards meeting and/or exploring application-specific quality requirements such as density, surface topography, and residual stresses with applications spanning various sectors.

The chapters corresponding to each objective are visualised in Figure 1.8, with the biomedical, military, and defence applications excluded from the main body of the thesis for brevity.
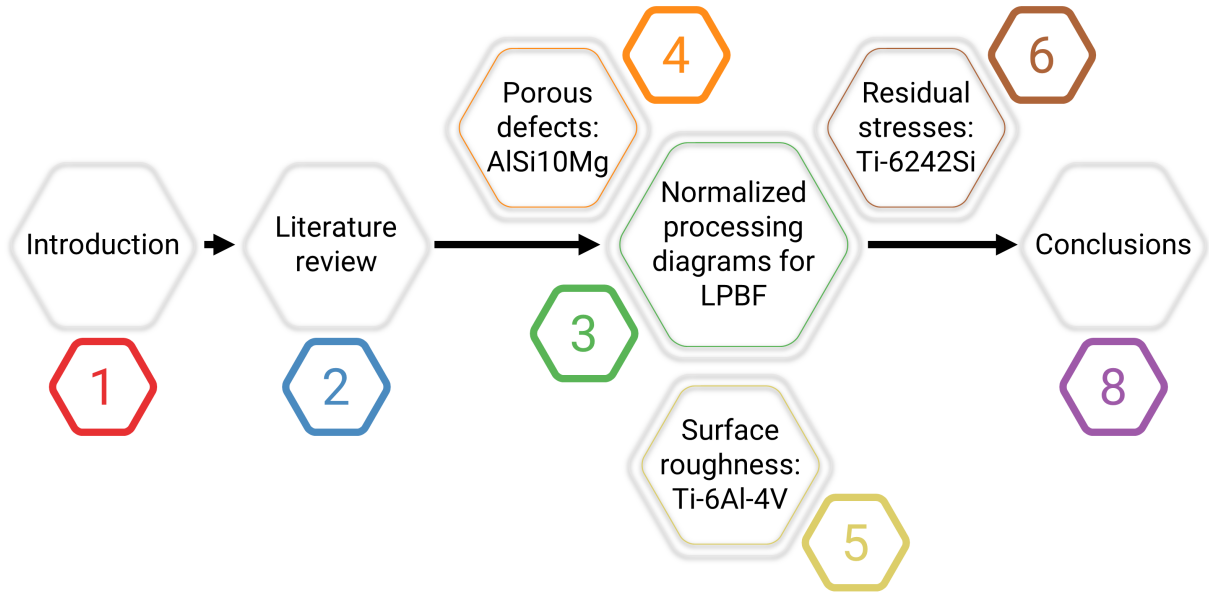
Figure 1.8: Graphical abstract of the thesis showing the connected chapters, with the chapter numbers as indicated

1.3 Thesis outline

This thesis includes seven chapters.

Chapter 2 begins with a literature review of the important LPBF process parameters to help gain familiarity with the multitude of inputs which can influence quality outcomes in this metal AM technology. A review of previous attempts at predicting melting mode thresholds in laser welding and LPBF is then provided to outline the need for addressing gaps in modelling theory. A review of the challenges with porous defects occurrence during LPBF of high reflectivity aluminium alloys in is then provided to provide context

11

to the work on AlSi10Mg in Chapter 4 of this thesis. This is followed by an introduction to the effects of LPBF process parameters on surface roughness and residual stresses to help understand the significance of the work on Ti-6Al-4V in Chapter 5 and Ti-6242Si in Chapter 6 respectively of this thesis.

Chapter 3 provides details about the development of normalized processing diagrams and a temperature prediction model to visualize and predict the conduction, transition, and keyhole melting modes in LPBF. The tool developed in this chapter is shown to be independent of material for specific classes of materials, of LPBF system, of laser modulation, and of powder layer thickness.

Fundamental studies using the processing diagrams from Chapter 3 to understand porosity, side-skin surface roughness, and residual stresses in LPBF are shown in Chapters 4, 5, and 6 respectively. Chapter 4 focuses on studying the effects of the three melting modes on the porous defects in AlSi10Mg using processing diagrams, metallography, and X-ray computed tomography. Chapter 5 uses design of experiments and LPBF processing diagrams to analyze and interpret effects of LPBF melting modes on side-skin surface characteristics in Ti-6Al-4V. LPBF processing diagrams are used to investigate the impact of melting modes on macroscale characteristics of the Ti-6242Si such as density, surface roughness, residual stresses, and cracking in Chapter 6.

In Chapter 7, conclusions and proposed future studies are presented.

Chapter 2

Literature review

2.1 Process parameters in laser powder bed fusion additive manufacturing[1]

The LPBF process is conceptually simple; however the physics governing process outcomes is complex and covers a broad range of time and length scales. Over 130 process parameters have an influence on LPBF outcomes [100], therefore identifying the parameters and interactions that have the largest impact on the process outcomes is critical for optimisation of part quality for a given application. Parameters such as the laser power (P), beam velocity (v), and beam diameter (σ), are known to control the length, width, and depth of the melt pool, as well as influence the complex phenomena such as molten material flow, material vaporisation, material ejection, condensate formation, and many more effects [74]. The ideal laser-material interaction in LPBF is tailored towards producing stable melt pool morphologies with minimum variability from layer-to-layer.

In terms of spatial and temporal scale in LPBF, beam diameters (σ) of generally 50 – 100 µm, laser powers (v) of 50 – 400 W, and laser beam velocities (v) of 200 – 2500 mm/s are generally used. The beam diameter (σ) generally corresponds to the D4σ, D86, or $1/e^2$ width measurements that would give the same value for an ideal single-mode Gaussian beam [101, 102, 103]. The laser-material interaction results in a localised melt pool, with the bulk of the material undergoing re-melting, cyclic heating, and cooling as a function of the beam path trajectory. As a result, prediction, tailoring, and control of the geometry of melt pool is important, as the melt pool width, depth, and length can affect part

---

[1]Section is adapted from a published article [10].

density via phenomena such as lack-of-fusion [104], material spattering [105, 106], unstable keyhole melting [85, 107] powder denudation effects [85, 108], and layer delamination or crack formation due to thermal stresses [109, 6].

It is also important to consider the importance of other variables, which although are not as significant as the ones mentioned above for the goals of this thesis, do hold importance in printing successful parts. Examples of such variables are powder recoating effects [110, 111], chromatic or spectral aberration caused by the use of f-theta lenses for the laser scanning systems [112, 113], consistency of powder flow depending on the powder feeding or powder dousing system of a given machine [114], build plate material type and thickness [115, 116], powder collection and re-circulation [117, 118, 114], laser properties such a wavelength, operating mode, beam shape and quality [119, 120], build chamber atmospheric conditions [121, 122, 123], powder properties [115, 114], and build file setup (location, orientation, recoater offset angle, etc.) [124, 125, 126]. More comprehensive lists of important variables can be found in literature [127, 128, 129]. In this present work, these parameters are considered to be secondary and their direct effects will not be in scope for process prediction nor for experimental analytics.

2.2 Melting mode thresholds

In LPBF, a term known as volumetric energy density (VED) is commonly used to study the effects of important process parameters on final controllable outcomes [130, 131, 132, 127] which is described in Equation 2.1.

$$VED = \frac{P}{vh_d l_t} \tag{2.1}$$

In Equation 2.1, P is the laser power [W], v is the laser beam velocity [m/s], h_d is the hatching distance [m], and l_t is the powder layer thickness [m]. The expression for volumetric energy density [J/m^3] is a measure of energy input and is machine dependent. The VED formulation does not include material properties (e.g. thermal conductivity, thermal diffusivity) and machine parameters (e.g. beam diameter, layer thickness), which have a direct impact on the heat input to a given material. VED also assumes that power is only absorbed by the powder layer, which is an incorrect since a significant amount of input energy density is absorbed by the previously printed layer (substrate) as well, as shown in the melt pool images from Figure 1.3. Additionally, VED is shown to have numerous limitations as a design parameter, particularly to predict melting mode thresholds in LPBF [133, 127].

14

Depending on the processing conditions, laser processes which involve melting have broadly two different operational regimes: conduction mode and keyhole mode. When the power density is lower than a certain threshold value, heat conduction is the dominant heat transfer mechanism, particularly for determining the depth of the molten pools created. This regime is called the conduction mode of laser melting. The cross section of melt pools created in conduction mode is generally semicircular (i.e. the melt pool depth is about equal to its half-width) as predicted by Eagar and Tsai's conduction mode model [134]. The vaporisation of metals in conduction mode melting is considered to be negligible, particularly for laser welding.

In contrast, keyhole mode melting is observed when the power density exceeds a threshold value such that a deep vapour cavity forms within the molten metal due to intense localised heating and vaporisation of alloying elements. In keyhole mode of laser melting, the depth of the molten pool is controlled by the recoil momentum pressure (also known as recoil pressure) generated by the vaporisation of the melt pool materials. Convective heat transfer (due to Marangoni flows) is the dominant mode of heat transfer within the molten pool, particularly for materials with low thermal conductivity such as Ti-6Al-4V, 304L SS, 316L SS, and vanadium [135]. High temperature gradients in keyhole mode melting lead to drastic surface tension gradients. These gradients drive melt flow from the hot spot beneath the laser beam towards the cold rear; such effects are known as Marangoni convection effects [85]. The melt pool depth in keyhole mode laser melting is typically greater than the half-width of the melt pool defined at the top of a given melt pool.

2.2.1 Melting mode thresholds in laser welding versus laser powder bed fusion

Laser welding researchers have shown that laser power, scan speed, and laser beam diameter are important process parameters for predicting the threshold between conduction mode and keyhole mode [136, 137]. Numerical modelling has helped in observing the importance of materials parameters as thermal diffusivity, laser absorptivity, melting point, and boiling point in predicting heat transfer and fluid flow during keyhole mode laser welding [135].

A commonly used model is proposed by Hann et al. [137], who use findings from numerical modelling efforts to derive a simple relation for normalized enthalpy $(\Delta H/h_s)$, which relates melt pool depth to material and laser welding process parameters.

$$\frac{\Delta H}{h_s} = \frac{AP}{h_s\sqrt{\pi\alpha v\sigma^3}} = f\left(\frac{d}{\sigma}\right) \tag{2.2}$$

15

In Equation 2.2, ΔH is the specific enthalpy [J/m³], h_s is the enthalpy at of the solid material at the solidus temperature [J/m³], A is the laser absorptivity of the solid material, α is the thermal diffusivity of the solid material at the solidus temperature [m²/s], σ is the laser beam diameter [m], and d is the melt pool depth [m]. The enthalpy at the solidus temperature is given by $h_s = \rho C_p T_m$, where C_p is the specific heat capacity [J/kg K], ρ is the density of the material [kg/m³], and T_m is the melting temperature of the material [K]. The normalized enthalpy model assumes that the thermal properties of the material are constant and ignores the effects of latent heat of fusion, thermal convection, and material vaporization. A normalized enthalpy threshold of $\Delta H/h_s = 10$ was shown to predict the threshold between conduction to keyhole mode for laser welding datasets from 304L stainless steel (SS), Ti-6Al-4V, tantalum (Ta), and vanadium (V) [137]. This value of 10 was shown to be approximately equal to the ratio of enthalpy of vaporisation to the enthalpy of melting for 304L SS, Ti-6Al-4V, Ta, and V [137].

There are complexities and differences in LPBF in contrast to laser welding, such as the presence of powder in LPBF, and the frequent turning points along the laser beam scanning path for a given layer in LPBF. Laser scanning mirrors generally slow down and accelerate at turning points of the hatch pattern during LPBF leading to the rapid formation and collapse of deep vaporised regions due to the laser beam velocity, thereby trapping the atmospheric gas in the solidified part [81]. This phenomenon would not be expected in laser welding due to the single-pass scanning path of the laser beam. Furthermore, there are significant effects of differences in spatial resolution, temporal resolution, material properties are summarized below:

2.2.1.1 Spatial resolution

The lower beam diameters commonly used in LPBF (compared to laser welding) are shown to cause high conduction losses and also lower vaporisation thresholds [138]. The lower diameters reduce the threshold for vaporisation in LPBF. This was observed through high-speed and high-resolution X-ray imaging by Cunningham et al. [3]. In their work, they have observed that vaporisation is present even in conduction mode melt pools of LPBF, whereas laser welding literature shows no vaporisation is expected in conduction mode melt pools [139].

2.2.1.2 Temporal resolution

The laser beam velocities used in LPBF are also typically higher than laser welding, which lead to liquid metal instability caused due to Marangoni convection (melt flow driven from

16

the hot laser spot to the cold rear of the melt pool). These instabilities lead to liquid metal spatter because of the low viscosity of the heated melt pool [85]. At high beam velocities during laser welding, molten metal ejection has also been observed to occur due to liquid metal instability, particularly, when the liquid-vapour interface moves normal to the laser beam [140]. The phenomenon of the liquid metal breaking up into small droplets is due to surface tension tendencies of minimizing surface energy due to a variant of Plateau-Rayleigh instability theory [141].

Additionally, adjacent weld lines controlled through hatching distance and hatch beam path trajectories, as well as stacking of layers through melting of subsequent powder layers also have the potential to cause defects through phenomena such as lack-of-fusion [104], or through excessive powder denudation effects [85, 108]. Cyclic thermal loading of heating, re-melting and re-solidification of previously parsed zones also has an overall effect on local and global part properties.

2.2.1.3   Presence of powder

The presence of powder in LPBF adds an additional complexity to modelling LPBF when compared to laser welding since modelling the interaction between the laser beam and powder bed dynamics is only possible through modelling approaches such as the smoothed-particle hydrodynamics (SPH) method (a Lagrangian mesh-free numerical method) [142, 143, 144, 145], the Lattice Boltzmann method (LBM) [146, 147, 148, 149, 150], and the arbitrary Lagrangian-Eulerian (ALE) method [77, 151, 152, 153]. These modelling efforts are critical in understanding the change in melt pool dynamics due to the presence of powder, as well to understand the effect of powder related phenomena such as powder spatter [154, 155, 156] and powder denudation [108, 157] which have been shown to have a significant impact on LPBF part properties. Additionally, the vapour plume created due to laser interactions with the powder bed exerts an additional pressure force that ejects liquid metal [157], which would cause additional melt pool spatter and add to the roughness of a given layer in LPBF.

The differences in spatial resolution, temporal resolution, and presence of powder add significant complexity to modelling of the melting mode thresholds since some of the assumptions used in the laser welding melting mode threshold efforts do not hold true for LPBF.

2.2.2 Melting mode thresholds in LPBF

King et al. [86] used Equation 2.2 to study the onset of keyhole mode in LPBF of 316L stainless steel (SS) at a powder layer thickness of 50 µm, and varying levels of laser power, beam velocity and beam diameter. They observed all of their conduction and keyhole mode melt pool datasets to fall above the normalized enthalpy threshold of $\Delta H/h_s = 10$ recommended by Hann et al. [137] for traditional laser welding processes. They instead found the threshold to lie at $\Delta H/h_s \approx 30\pm4$ for SS316L powders. This increased threshold is due to the presence of material vaporisation effects, even in conduction mode LPBF melt pools due to the significantly lower beam diameters used in LPBF when compared to laser welding. Evidence of vaporisation in conduction mode LPBF melt pools (Figure 2.1) was shown by using ultrahigh-speed X-ray imaging of the LPBF fusion process [3]. Figure 2.1 shows nearly all combinations of power and velocity commonly used during the LPBF of Ti-6Al-4V using a laser diameter of 95 µm, that exhibited a substantial vapour depression across possible melting modes. Hence, the model developed by Hann et al. [137] and the associated threshold applies consistently to most materials subjected to laser welding, where vaporisation is negligible in conduction mode melt pools, and does not apply as well to LPBF melt pool datasets, where vaporisation is significant even in conduction mode melt pools.

Chapter 3 of this thesis includes details about the development of an enhanced model that helps offset the limitations of Hann et al.'s normalized enthalpy model [137] in the context of LPBF, along with the associated in-depth literature pertinent to to theoretical development of processing diagrams and temperature prediction models. Since the threshold between conduction to keyhole mode melting in LPBF is temperature-driven, an enhanced heat conduction-based temperature prediction model and a methodology to predict the threshold between conduction to keyhole tailored for LPBF is proposed in this thesis, where vaporisation is significant in both conduction and keyhole processing conditions. This model proposed in Chapter 3 helps in developing a better understanding of porosity characteristics and would help better correlate the origin of a given pore to its cause based on LPBF process physics. The processing maps obtained from the model are further deployed in this thesis work for various classes of materials such as, but not limited to titanium alloys, ferrous alloys, and aluminium alloys.
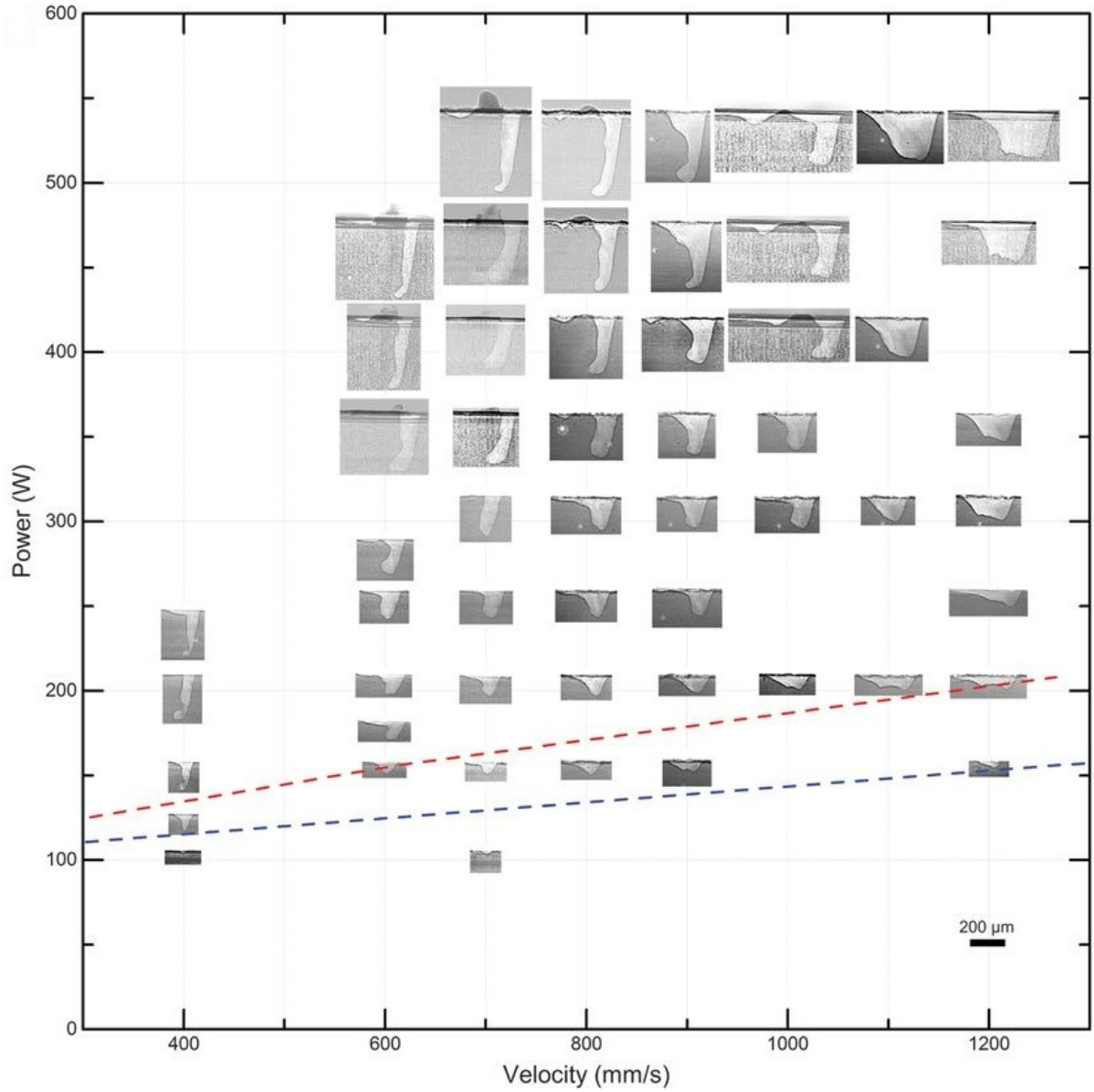
Figure 2.1: Vapour depressions inside melt pools across the P-V space of Ti-6Al-4V bare plate for a laser diameter of 95 μm. The vapour depression and melt pool morphology transitions are marked with blue and red dashed lines, respectively. Reprinted with permission from [3].

2.3 Effect of process parameters on porous defects in LPBF

Porous defects in LPBF are generally classified into lack-of-fusion defects or vaporisation instability-related defects, as described in the subsequent sections. However, entrapped gas in the feedstock powder particles can also cause porous defects in LPBF. These entrapped gases can be the cause of tiny near-spherical defects across melting modes in LPBF [10]. For aluminium alloys in particular, presence of moisture on the powder surfaces may also lead to tiny spherical hydrogen pores across melting modes as well [158, 130]. This is mainly associated to the reduction of hydrogen solubility in aluminium alloys during the resolidification of liquid aluminium [5].

2.3.1 Lack-of-fusion defects in LPBF

Lack-of-fusion defects are generally observed in the conduction mode of LPBF; however, it is possible to observe lack-of-fusion porosity in keyhole mode as well, particularly when the hatching distance and powder layer thickness is such that the heat input is not able to sufficiently melt enough material.

The in-layer distribution of weld lines controlled through hatching distance and laser scan trajectory, as well as subsequent stacking of layers through spreading powder layers with controlled thickness have the potential to cause porous defects through phenomena such as lack-of-fusion. Lack-of-fusion porosity is caused by an incomplete melting of material due to insufficient energy input. Assuming a dual half-elliptical melt-pool idealized cross-sectional shape, Tang et al. [104] use the following relation to predict full melting in three dimensional parts printed by LPBF:

$$O = \left(\frac{h_d}{w}\right)^2 + \left(\frac{l_t}{d}\right)^2 \leq 1 \tag{2.3}$$

In Equation 2.3, h_d is the hatching distance [m], l_t is the powder layer thickness [m], w is the melt pool width [m], and d is the melt pool depth [m]. O from Equation 2.3 can be termed as the overlap parameter, such that the criteria for full melting intra- and inter-layer i.e., the criteria for lack-of-fusion defects can be given by $O \leq 1$. This criteria applies well to the three dimensional parts printed by Dilip et al. [4] as shown in Figure 2.2. The melt pool width and melt pool depth were obtained by weld line data deposits produced on a Ti-6Al-4V alloy plate at a layer thickness of 30 µm [4].

20
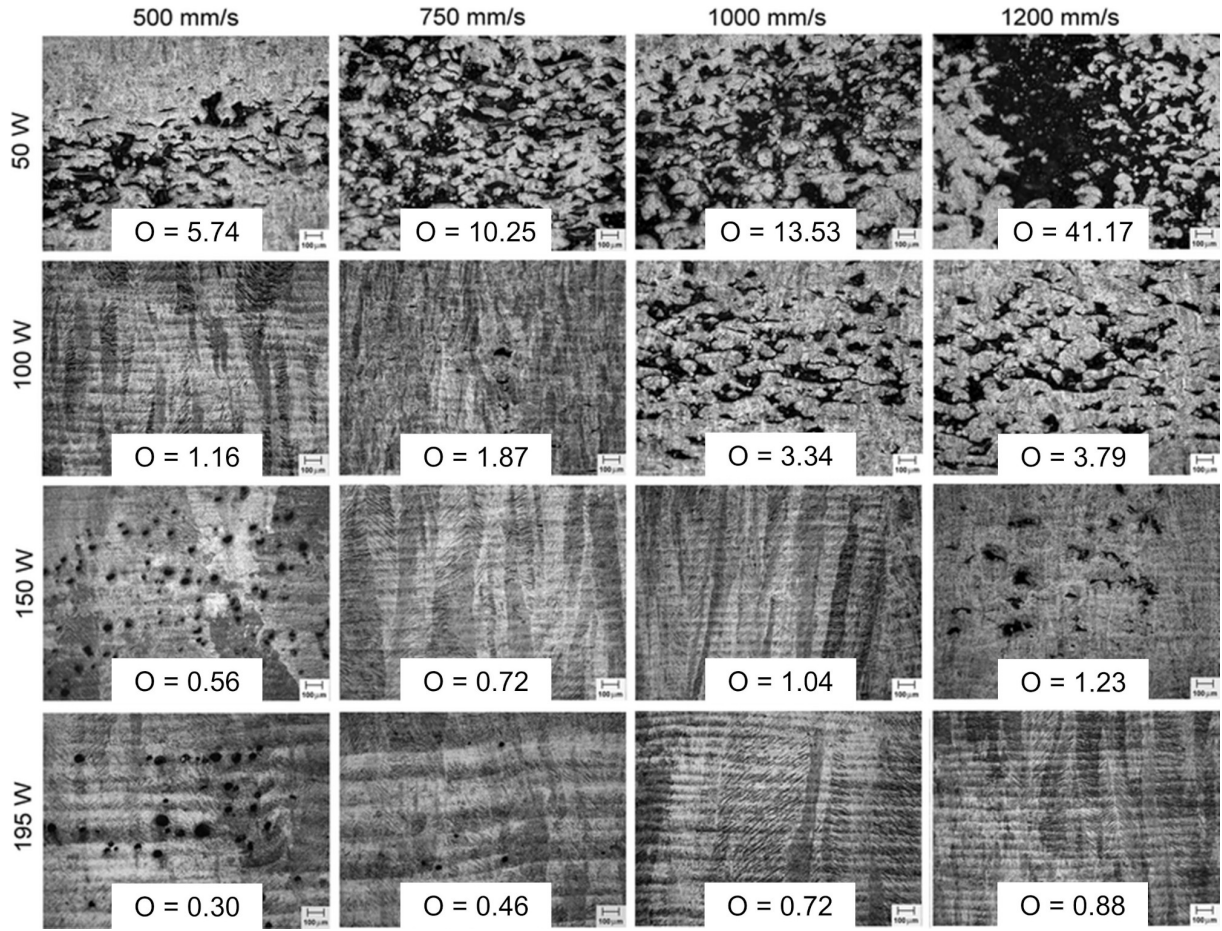
Figure 2.2: The overlap parameter was calculated and applied to Ti-6Al-4V melt pool datasets from literature [4] resulting in an illustration of lack-of-fusion in bulk samples printed on a EOS M270 with a hatching distance of 100 µm and layer thickness of 30 µm.

Across melting modes in LPBF, an inadequate selection of LPBF process parameters such as hatching distance and powder layer thickness could cause insufficient stitching or overlap of melt tracks, causing lack-of-fusion defects, as observed by Choo et al. [159]. Additionally, incomplete re-melting of material ejecta from previous layers or from neighbouring scan tracks and incomplete re-melting of irregular surface topographies from previous layers can lead to lack-of-fusion defects [156] . Further insights into lack-of-fusion defects and their causes are given in Chapters 3 and 4.

2.3.2   Vaporisation instability related defects

Vaporisation instability related defects are commonly observed in keyhole mode melting during laser welding and LPBF. Keyhole mode melting is the most common form of laser welding prevalent in literature [160, 161]. For laser welding, Duley [162] describes the equilibrium between a stationary laser produced keyhole and its surroundings in Equation 2.4.

$$p_v + p_l = p_\sigma + p_g + p_h \qquad (2.4)$$

The typical values for the pressures in laser welding obtained from Duley [162] are as follows. In Equation 2.4, p_v is vaporisation pressure ($\approx 10^4$ N/m^2), p_l is radiation pressure (≈ 50 N/m^2), p_σ is surface tension pressure ($\approx 10^4$ N/m^2), p_g is hydrostatic pressure (≈ 75 N/m^2), and p_h is hydrostatic pressure (≈ 0 N/m^2) - for low welding speeds). The terms p_v, p_l, and p_h act to keep the keyhole open. In laser welding literature, the terms p_l and p_g are considered small when compared to p_v and p_σ, and are hence neglected. Additionally, since p_h is the hydrodynamic term that is affected by the momentum in the melt pool, it is neglected in laser welding, as the melt pools observed are generally small [163]. Hence, the surface tension pressure (caused by thermo-capillary flow) and vapour pressure (caused by the recoil momentum created by the vaporising material) are the only terms of significance in laser welding. To achieve a stable keyhole mode, the sum of all pressures on the liquid surface must be zero; this means that if the surface tension pressure decreases the vapour pressure must also be decreased [164]. If thermo-capillary flow (also referred to as Marangoni flow) induced by surface temperature gradients (also known as Bénard–Marangoni flow) and recoil (vapour) pressure are not balanced out, melt pool instabilities occur. Such instabilities are also known to create porous defects during keyhole mode LPBF [165].

The different mechanisms for porosity formation in unstable keyhole mode melting are illustrated in Figure 2.3. One type of porosity that is often encountered, type D in

Figure 2.3, is a pore created by a collapse of part of the keyhole during solidification. Pores of spherical shape are formed by gas inclusion during the molten phase, where sufficient time leads to a melt equilibrium spherical shape before being trapped during solidification. This gas inclusion could be due to the inert gas used in the process chamber or due to other gases dissolved in the melted material; one typical mechanism is the formation of small hydrogen pores in aluminium, as the solubility of hydrogen is high in the liquid phase but drops significantly during solidification. Moreover, lack-of-fusion and cold laps often appears as non-spherical pores that can have a rather irregular or elongated shape (or even be hardly visible, but it lacks fusion, i.e. atomic bonding). The irregular shape indicates that the solidification speed was greater than surface tension driven contraction mechanisms.
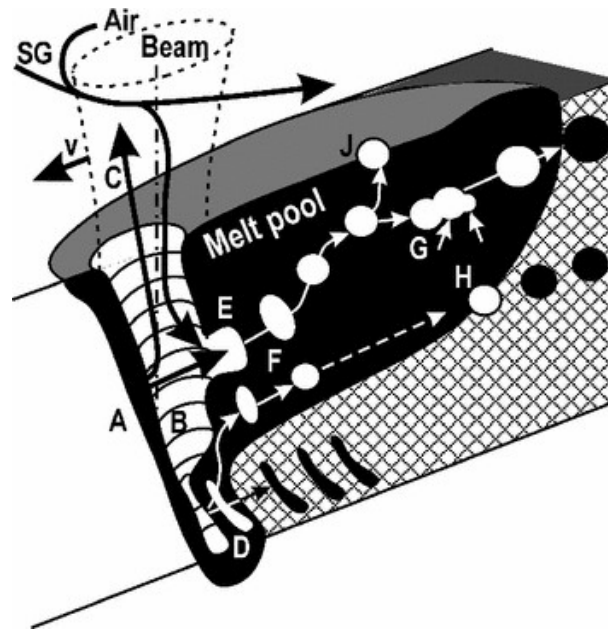
Figure 2.3: Illustration of a typical melt pool in keyhole mode melting. Mechanisms for porous defect formation: D - collapse and rapid solidification of the keyhole bottom section, E - metal vapour jet generates a bubble, F - irregular cavity contracting to a spherical pore, G - combining pores, H - hydrogen pore caused by solubility drop, J - pore emerging and relaxing at the surface (A - melting front, B - keyhole, C - vapour flow, v - speed, SG - shielding gas). Reprinted with permission from [5].

It is important to note that that laser welding generally involves scanning along a single path line and LPBF involves frequent turning points depending on a hatching pattern. It

has been recently noted that keyhole porosity in LPBF has been observed to form every time the laser scanning mirrors slow down and accelerate at turning points of the hatch pattern [81]. In modulated (pulsed) LPBF systems which involves scanning of 1 single point at a time, the stability of keyholes is impacted every time the laser scanning mirrors even slightly deviate from their intended straight line path since the melt pool continuity would be affected, which becomes a significant issue when the scan vector path is complex (e.g. circular). Precise control of the laser scanning mirrors could be critical for both modulated and continuous LPBF systems to reduce porous defects.

In summary, porosity in the keyhole melting mode is strongly related to the flow behaviour of melt pools in LPBF. The generally accepted explanation for melt pool dynamics in keyhole mode laser material processing is based on understanding the combined effects of thermo-capillary flow (Bénard-Marangoni flow induced by surface temperature gradients) and recoil pressure due to evaporation of the material [166, 167]. However, the use of powder in laser powder bed fusion adds complexity to the melt pool dynamics leading to effects such as vapour entrainment-driven denudation of metal powder particles and distribution of molten droplets [85, 168]. This added complexity leading to additional causes for potential vaporisation related defects [85, 169]. Further insights into vaporisation instability related defects and their causes are given in Chapters 3, 4, and 6.

2.4 Effect of process parameters on surface roughness in LPBF

An interplay between build file characteristics, machine characteristics, feedstock characteristics, and LPBF process parameters generally drives the final surface roughness of a given part. More precisely, build file characteristics such as feature geometry, feature orientation, feature location on the build plate, and beam path strategy, machine characteristics such laser beam quality, and atmospheric gas flow, and powder morphology and size distribution are some of the primary drivers for roughness of a given surface, alongside LPBF process parameters previously discussed. From the four influencing factors, LPBF process parameters such as laser power, velocity, and beam spot diameter are known to have the greatest effect on roughness.

Surfaces in LPBF are generally identified with their orientation with respect to the build (Z) direction used for manufacturing as shown by in Figure 2.4. The four types of surfaces include - up-facing horizontal surfaces that are parallel to the build plate (XY plane), up-skin surfaces which are typically on an incline, but facing upwards, side-skin

24

(or vertical) surfaces perpendicular to build plate (along Z axis), and down-skin surfaces. These surfaces are distinctly different contributors towards the final surface roughness in the printed final structure. Additional details and visuals of the different surfaces in LPBF are provided in Appendix A. Physics-based modelling of surface roughness as a function of LPBF process parameters hasn't been attempted in prior literature. This is likely due to the computation challenges associated with a model to keep track of powder dynamics (powder spatter, ejections, and balling phenomena) as well as melt pool splatter for large three-dimensional surfaces [170, 85]. In the subsequent section on understanding the effect of LPBF process parameters on surface roughness, the horizontal and up-skin surfaces are grouped into one category of upward-facing surfaces, alongside vertical and down-skin surfaces.
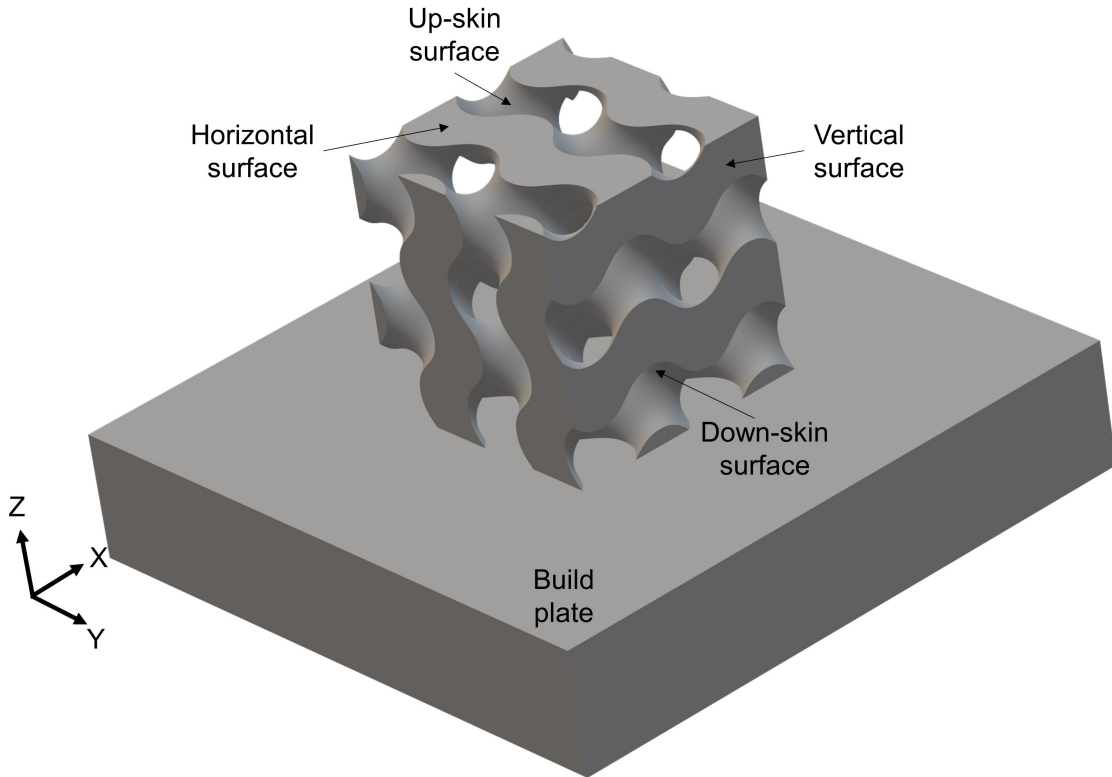
Figure 2.4: An illustration of a gyroid lattice structure on a LPBF build plate showcasing the different types of surfaces observed in a laser powder bed fusion with respect to the build orientation along the Z-axis

25

2.4.1 Upward facing surface topography characteristics

Up-facing and up-skin surface characteristics generally includes visibility of the melt pool tracks alongside partially fused adhered powder, particularly for the up-skin surfaces [171, 172]. Strano et al. [172] developed the only mathematical model to predict the up-skin surface roughness at different sloping angles, while also accounting for the presence of adhered powder particles common for most surfaces in LPBF. Their model, however, does not account for the effect of LPBF process parameters which drive melting modes in LPBF. There have been a few attempts at improving the roughness of upward facing surfaces in LPBF parts via empirical approaches as summarized below.

For altering the up-facing surface roughness of LPBF parts, Yasa et al. [173] observed that laser re-melting can greatly improve the surface roughness of SS 316L parts (roughness, Ra, reduction by about 90%). Similarly, Kruth et al. [174] observed that laser re-melting improved the surface quality of Ti-6Al-4V parts printed by a continuous laser based system. They remelted the last 20 layers of parts of with a XY cross-section 10*10 mm^2 with 2.1 mm build height. The re-melting of the 20 layers was performed with scan vectors perpendicular to the previous vectors for the same layer. Roughness, Ra, values up to $1/3^{rd}$ of a non-remelted surface were observed in the study by Kruth et al. [174]. Additionally, they also found a correlations between the peak surface temperature of the LPBF process parameters used for remelting and the obtained roughness, Ra, values. While upward facing surface roughness was outside the scope of this thesis, the temperature prediction model developed in Chapter 3 can be used to obtain peak surface temperatures and thereby further understand the effect of remelting LPBF processing in term of melting modes on the final up-facing surface roughness of LPBF parts.

Additionally, when the last layer of an additively manufactured three-dimensional (3D) part is remelted, it is a replication the laser polishing technology, albeit with a generally higher laser beam radius [175]. Modelling attempts from laser polishing [176] could hence be adapted in the context of LPBF to predict and thereby improve the top surface roughness of LPBF parts which have been subjected to a rescanning of the last layer.

2.4.2 Down-skin surface characteristics

Down-skin surfaces are generally affected by partially fused adhered powder. At higher input energy density, formation of dross is also documented [177]. Generally, the down-skin surface roughness strongly depends on the melt pool depth [178, 179]. A melt pool depth close to the powder layer thickness is generally considered to be useful for lowering down-skin surface roughness values [178]. This can obtained by conduction mode melt pools at

lower energy densities. Similarly, while upward facing surface roughness was outside the scope of this thesis, the temperature prediction model developed in Chapter 3 can be used to design conduction melting mode melt pools for this purpose. Preliminary investigation of remelting scans down-skin surfaces have also shown the potential to reduce the roughness values of these surfaces [179].

2.4.3 Side-skin surface characteristics

There have been only a few studies on understanding the effect of LPBF process parameters on side-skin surface roughness [180, 181, 182, 183]. Based on these studies, side-skin surfaces are known to be dominated by partially fused adhered powder in LPBF. Side-skin (vertical) surfaces are a type of surface wherein remelting would generally not help further improve surface roughness, when compared to a well-executed first side-skin scan [183]. But in μ-LPBF, it has been shown that the effects of partially fused adhered powder particles can be reduced by a higher energy input, leading to lower roughness values [184]. The temperature prediction model developed in Chapter 3 can be used to design transition and/or keyhole melting mode melt pools for this purpose. These findings have been the main motivation for Chapter 5 wherein a detailed literature review on previous work on side-skin surface is provided, followed by a study involving statistical and simulation-based approaches to understanding the impact of core and border LPBF process parameter on side-skin surface roughness in LPBF. Chapter 5 begins by providing a detailed investigation on the effect of core process parameters followed by a preliminary investigation on border process parameters on side-skin surface in LPBF of Ti-6Al-4V. This study is continued in Chapter 6, wherein the effect of border process parameters is further investigates across melting modes for LPBF of Ti-6242Si. The findings in Chapters 5 and 6 are supplemented with simulation from the model developed in Chapter 3, which help in develop a fundamental understanding of the origins of side-skin surface roughness across materials in LPBF.

2.5 Effect of process parameters on residual stresses in LPBF

Residual stress in LPBF is affected by the material selected and the process parameters in particular [6]. In terms of material properties, Bartlett and Li [6] observed a linear

relationship between a materials' thermal diffusivity and thermal conductivity on the resulting residual stresses during LPBF for 5 popular materials - Ti64, SS 316L, Inconel 718, commercially pure Ti (CP Ti), and 18Ni300 Maraging steel. A lower thermal conductivity and diffusivity value led to high residual stresses, on average.
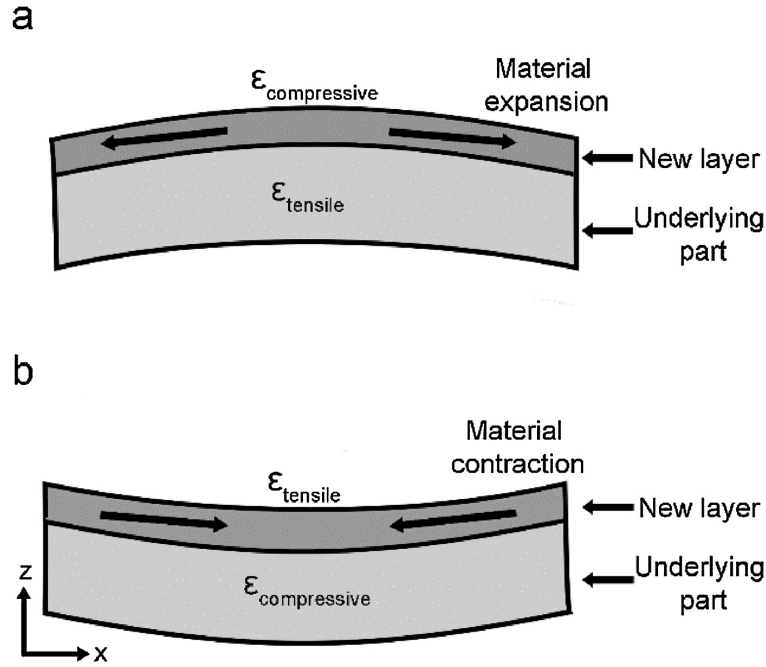
Figure 2.5: Mechanisms of residual stress and plastic deformation during LPBF: a) during heating and expansion of new layer and b) during cooling and contraction of a new layer. Reprinted with permission from [6].

In terms of LPBF processing, melting and vaporising metal powder particles onto a relatively cooler substrate by default creates steep temperature gradients thereby leading to residual stresses and thermal strain in as-printed parts [109]. The high cooling rates of 1–40 K/µs associated with LPBF [185] is one of the major contributors to residual stresses [6] in this process. During the heating phase of LPBF, when a new (top) layer is melted (and thereby heated to a temperature above the underlying part), it leads to a thermal expansion of the new layer. Since this expansion is restricted by the much cooler underlying part, it leads to compressive stresses in the new layer and tensile stresses in the underlying part, as shown in Figure 2.5 (a). During the cooling phase of LPBF, the new layer cools rapidly leading to contraction at a rate much higher than the underlying part can accommodate. This results in tensile stresses in the new layer and compressive

stresses in the underlying part, as shown in Figure 2.5 (b). However the simple mechanism shown in Figure 2.5 is more complex in reality, primarily since each layer is scanned using a so-called "laser scanning strategy" which leads to different sections of a new layer to heat and cool separately causing complex stress distributions. These mechanism also lead to higher in-plane (XY) residual stresses, when compared to stresses along the printing (Z) direction. Numerous researchers having confirmed through experiments and simulation that the top (last few layers) and bottom (attached to the build plate) portions of a part have tensile residual stresses and the middle region has compressive residual stresses [6]. The mechanism causing tensile residual stresses at the top and compressive residual stresses in the central portion of part is illustrated in Figure 2.5. The connection of a LPBF part to the build plate results in tensile residual stresses towards the bottom portion of a part. Tensile residual stresses in particular are known to affect the fatigue life and cracking tendency of LPBF components [186, 6]. Additionally, a layer-to-layer (interlayer) rotation of the scanning strategy leads to a homogeneous in-plane (XY) residual stress distribution [187, 188, 189, 6].

Residual stresses are commonly known to cause part distortion, cracking, and delamination of material layers [190, 191, 192, 193]. Residual stresses have also been reported to have an impact on the fatigue performance and fracture resistance of LPBF parts due to the presence of micro-cracks in parts with high residual stresses [109]. To reduce residual stresses, the commonly used methods involve preheating of the LPBF build plate, varying the heat input through modification of laser power and laser beam velocity, decreasing powder layer thickness, and changing the scanning strategy [170]. Although preheating the base plate and varying the heat input could mitigate the issues with residual stresses, such approaches would also influence the melt pool morphology and thereby the melting modes, which could lead to additional porosity thereby impacting final mechanical properties. It is hence important to first identify a set of process parameters that could help meet the target density for a given application, before proceeding to change the heat input strategies to reduce residual stresses. These findings motivated the study on residual stress during LPBF of Ti-6242Si in Chapter 6 wherein additional insights on residual stresses during LPBF of titanium alloys is provided, along with a pertinent literature context.

Chapter 3

Processing diagrams and temperature prediction model to visualize and predict melting modes in laser powder bed fusion

3.1 Preface

Depending on processing conditions, laser powder bed fusion (LPBF) is known to have two operational regimes – conduction mode and keyhole mode. Heat conduction is the dominant heat transfer mechanism for conduction mode melting, whereas heat convection is the dominant heat transfer mechanism for keyhole mode melting. In addition, there exists a transition mode, which lies between the conduction and keyhole mode, wherein the dominance of conduction or convection depends upon the processing conditions. In this work, normalized processing diagrams are obtained to visualize the three melting modes - conduction mode, transition mode, and keyhole mode. The normalized processing diagrams obtained from this work are shown to be independent of material for specific classes of materials, of LPBF system, of laser modulation, and of powder layer thickness. Additionally, an analytical model is proposed to robustly predict the threshold between the three melting modes for two different classes of materials, (i) materials with low reflectivity and low thermal conductivity such as titanium, ferrous, and nickel alloys, and (ii) materials with high reflectivity and high thermal conductivity such as aluminium alloys. The normalized processing diagrams, alongside the identified melting mode thresholds, can provide a useful

30

tool in diagnosing the origins of porous defects and enable accelerated process optimization efforts towards tailoring material properties in LPBF. This chapter is adapted from a published article [10]. Section 3.3.2 on absorptivity scaling laws includes majority of the changes, compared to the published article. Due to changes in Section 3.3.2, figures from Section 3.5.2 have changed, compared to the published article. These changes, however, do not impact the significant findings and conclusions of this chapter; the changes rather are enhancements since the article submission.

3.2 Introduction

Depending on the processing conditions, laser processes which involve melting have broadly two different operational regimes: conduction mode and keyhole mode [194, 86]. When the power density is lower than a certain threshold value, heat conduction is the dominant heat transfer mechanism, particularly for determining the depth of the molten pools created; this regime is called the conduction mode of laser melting. The cross section of melt pools created in conduction mode is generally semicircular (i.e. the melt pool depth is lesser than or equal to its half-width), as predicted by Eagar and Tsai's conduction mode model [134]. The vaporization of metals in conduction mode melting is considered to be negligible, particularly for laser welding [139].

In contrast, keyhole mode melting is observed when the energy density exceeds a threshold value such that a deep vapour cavity forms within the molten metal due to intense localized heating and vaporization of alloying elements. In keyhole mode of laser melting, the depth of the molten pool is controlled by the recoil momentum pressure (also known as recoil pressure) generated by the vaporization of the melt pool materials. Convective heat transfer (due to thermo-capillary convection, also known as Bénard–Marangoni convection) is the dominant mode of heat transfer within the molten pool [135]. Keyhole mode melt pools are generally deep and narrow, with the morphology influenced by the significant effects of recoil pressure and Bénard-Marangoni convection. The melt pool depth in keyhole mode laser melting is typically greater than the half-width of the melt pool defined at the top of a given melt pool.

In LPBF, a model proposed by Hann et al. [136, 137] for laser welding has been used to predict the threshold between conduction mode and keyhole mode [86]. In this model, laser power, beam velocity, and beam spot size have been deemed as important processing parameters for predicting the threshold between conduction mode and keyhole mode. The observed melting mode threshold for LPBF data of 316L stainless steel (SS) at a powder layer thickness of 50 µm was observed to be much higher than predicted, approximately

31

30 ± 4 compared to the predicted value of 6 [86]. This observation was associated to the crudeness of the model and the lack of incorporation of the effects of powder layer thickness as noted by King et al. [86]. The higher observed threshold could also be due to the presence of material vaporization effects, even in conduction mode LPBF melt pools, due to the significantly lower beam spot sizes used in LPBF when compared to laser welding [3]. Hence, the model developed by Hann et al. [137] and the associated threshold applies consistently to most materials subjected to laser welding, where vaporization is negligible in conduction mode melt pools, and does not apply as well to LPBF melt pool datasets, where vaporization is significant even in conduction mode.

This chapter focuses on the development of processing diagrams and an enhanced model that helps in adapting Hann et al.'s normalized enthalpy model [137] in the context of LPBF. In this work, the authors propose an enhanced heat conduction-based temperature prediction model and a methodology to predict the threshold between conduction and keyhole modes tailored for LPBF, where vaporization is significant in both conduction and keyhole processing conditions. This proposed model could help in developing a better understanding of LPBF parts based on process physics. The processing maps obtained from the model are tested for various classes of materials such as titanium, ferrous, and aluminium alloys. Emerging research has shown that the dominance of conductive heat transfer during conduction mode melting and the dominance of convective heat transfer during keyhole mode melting impart differences in microstructure and thereby mechanical properties in Ti-6Al-4V, SS 316L, and Al7050 [195, 196, 167, 197]. Processing maps from this work, along with beam path planning algorithms, could be used to tailor microstructure and thereby mechanical properties for industrial applications. Such findings are part of upcoming works and are beyond the scope of the present thesis.

3.3 Theoretical development of processing diagrams and temperature prediction model

3.3.1 Normalized processing diagrams for LPBF

Mapping the thresholds for melting modes in LPBF is an important step in predicting part quality outcomes. The dimensionless variables defined by Ion et. al. [139] are used to compare and map the process controllable input parameters against part quality outcomes

for laser materials processing and are given by the following equations:

$$q^* = \frac{AP}{r_b \lambda (T_m - T_0)} \tag{3.1}$$

$$v^* = \frac{v r_b}{\alpha} \tag{3.2}$$

In Equation 3.1, q^* is the dimensionless beam power, A is effective laser absorptivity, P is laser power [W], r_b is beam spot radius [m], λ is thermal conductivity [W/(m.K)], T_m is melting temperature [K], and T_0 is initial (or powder bed) temperature [K]. In Equation 3.2, v^* is dimensionless beam velocity, v is the laser beam velocity [m/s], and α is thermal diffusivity [m^2/s]. Thermal diffusivity, α, is given by:

$$\alpha = \frac{\lambda}{\rho C_p} \tag{3.3}$$

In Equation 3.3, ρ is density [kg/m^3] and C_p is specific heat capacity at constant pressure [J/(kg.K)]. To account for powder layer thickness effects, we define a dimensionless heat input term, E^*, where we normalize the dimensionless beam power, q^*, by a dimensionless layer thickness term, l^* such that:

$$E^* = \frac{q^*}{l^*} \tag{3.4}$$

With the assumption of a moving heat source of cross-sectional area $2r_b \cdot l_t$, where l_t is the powder layer thickness, the dimensionless layer thickness term, l^* has been defined by Thomas et al. [87] as shown below:

$$l^* = \frac{2l_t}{r_b} \tag{3.5}$$

In the following section, the methodology used for selecting A (laser absorptivity) is described which has been observed to depend upon multiple LPBF process parameters that govern melting modes [7, 198, 9].

3.3.2 Absorptivity scaling laws for LPBF

Absorptivity during LPBF is observed to strongly depend on processing parameters such as laser power, velocity, and beam spot radius, which directly influence the presence of conduction, transition, or keyhole melting modes. For processing conditions commonly used in LPBF, the powder layer and some amount of the underlying substrate always undergo melting. Under these processing conditions, the measured laser absorptivity, typically done through micro-calorimetry, has been observed to be independent of powder layer thickness [7, 198, 9]. This phenomena can be explained by low heat capacity and thermal conductivity of the point-contacted powder particles, which results in powder melting in front of the melt pool [74]. In addition to laser power and velocity, the low beam diameters typically deployed in LPBF systems, with diameters $\sigma \approx [50 \dots 100]$ µm, where $\sigma = 2 \cdot r_b$, have a larger impact in determining the laser absorptivity in conduction, transition, and keyhole modes, as observed by Ye et al. [7], and observed in Figure 3.1. This increase in absorptivity is inversely proportional to the beam spot diameter and can be associated with the lower threshold for vaporization associated with smaller beam spot sizes, even in conduction mode melt pools; this was observed by Cunningham et al. [3] and is illustrated in Figure 3.2 (a). These findings mean that in LPBF, unlike in conventional laser welding processes where the beam diameter is substantially larger, the process can observe a significant vaporization of material, thereby adding to the challenge of controlling and modelling the process.

The absorptivity measurements in Figure 3.1 were obtained by Ye et al. [7] on a micro-calorimetry setup demonstrated previously by Trapp et al. [9]. Figure 3.1 shows absorptivity measurements from different materials as a function of beam velocity (Figure 3.1 A) and laser beam spot diameters (Figure 3.1 B). The terms normalized enthalpy, β_{Am} and normalized thermal diffusion length, L_{th}^* were defined by Ye et al. [7] in equations 3.6 and 3.7 respectively.

$$\beta_{Am} = \frac{A_m P}{\pi \rho C_p (T_m - T_0)\sqrt{\alpha v r_b^3}} \tag{3.6}$$

$$L_{th}^* = \frac{\alpha}{v r_b} \tag{3.7}$$

A_m in Equation 3.6 is the minimum value of absorptivity on a flat melt surface of a given material; estimated values are summarized in Table 3.1 for Ti-6Al-4V (also known as Ti64), Inconel 625 (IN 625), and stainless steel 316L (SS 316L) [7]. By comparing the
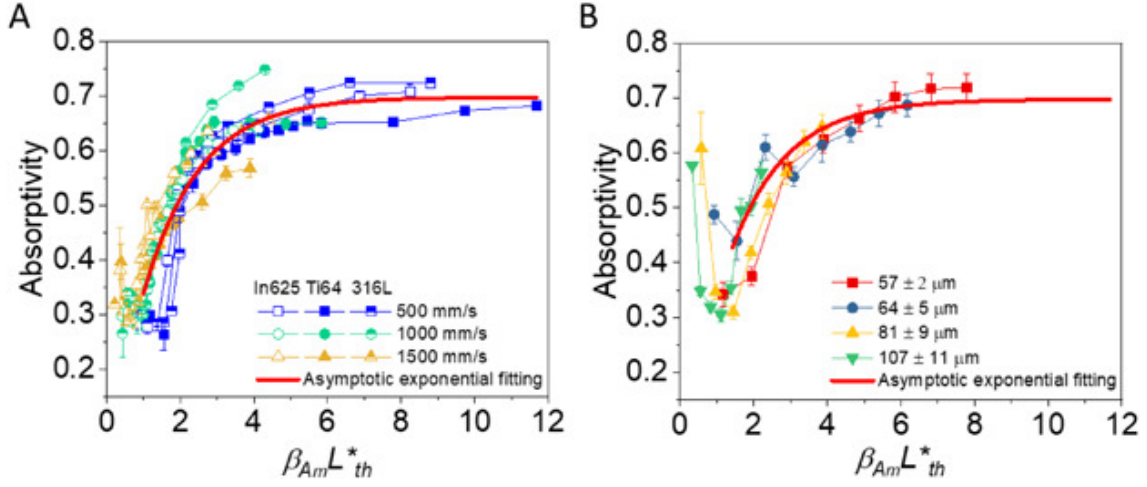
Figure 3.1: In situ measured absorptivity during LPBF as a function of $\beta_{Am}\ L_{th}^*$ of Ti64, IN625, and SS316L bare substrates at varied scan velocities and powers (A, 57 µm beam diameter) and beam diameters (B, Ti64, 500 mm/s scan velocity). The red solid lines are asymptotic exponential fitting of all data points above the thresholds of conduction to keyhole transition. Reprinted with permission from [7].

terms in Equations 3.1 and 3.2 to equations 3.6 and 3.7 respectively, the $\beta_{Am}{}^*L_{th}^*$ term can be represented as:

$$\beta_{Am}L_{th}^* = \frac{q_m^*}{\pi v^*} \tag{3.8}$$

In Equation 3.8, the term q_m^* is similar to the q^* term given in Equation 3.1, but the minimum melt absorptivity, A_m is used instead of effective laser absorptivity, A as shown by Equation 3.9.

$$q_m^* = \frac{A_m P}{r_b \lambda (T_m - T_0)} \tag{3.9}$$

In Figure 3.1, the high absorptivity measurements estimated at low heat input values values illustrated on the X-axis ($\beta_{Am}{}^*L_{th}^*$) between 0 and 1 are associated to the roughness of the powder layers which is expected to result in enhanced absorption before melting initiates in conduction mode LPBF [7]. As the heat input increases to values of 1-2 on the X-axis, the local laser material interaction area is heated above the melting point, which leads to surface smoothening by surface tension effects, leading to a decrease in

35
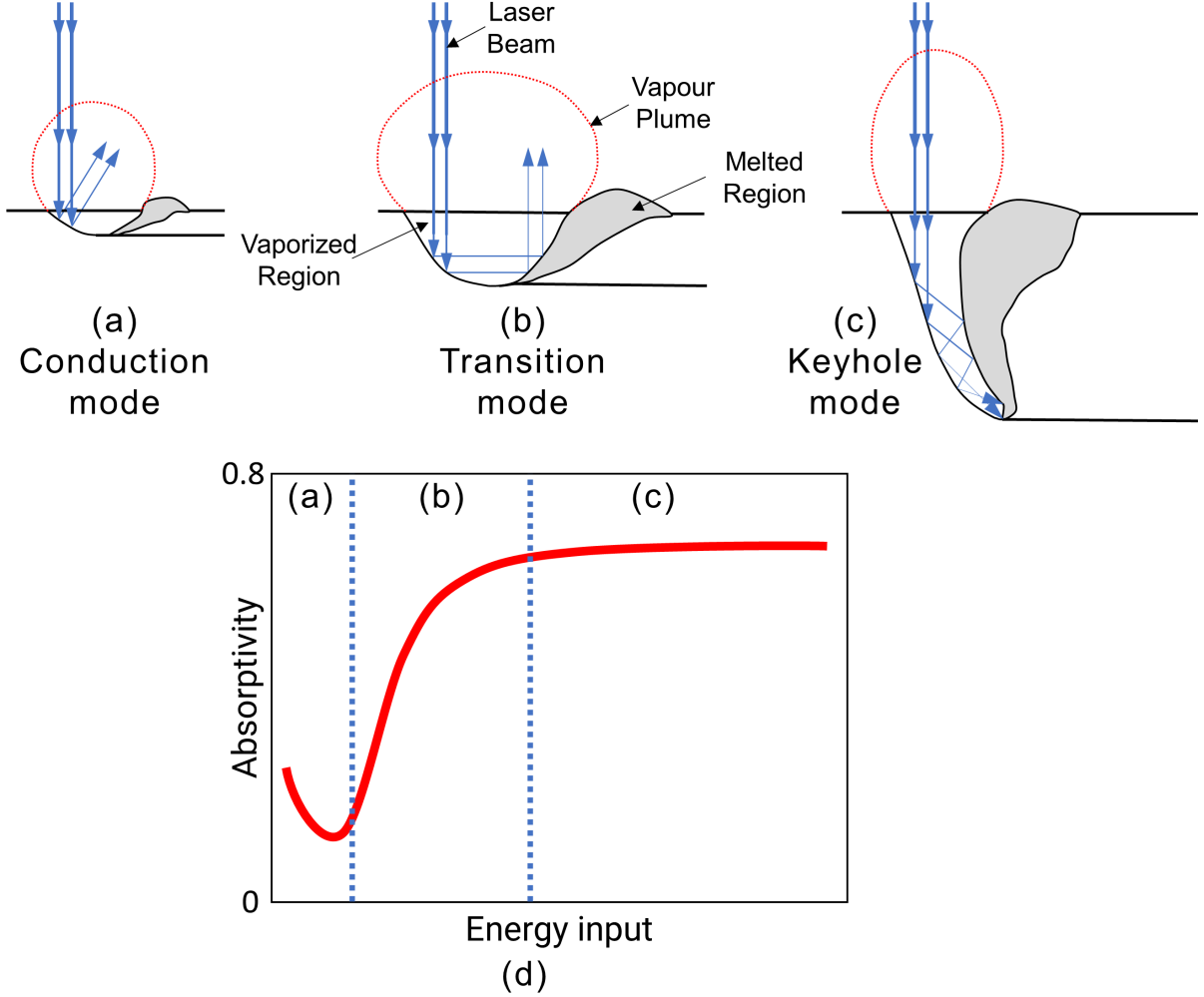
Figure 3.2: An illustration of conduction mode (a), transition mode (b), keyhole mode (c) melt pools in terms of the vaporized region shape, and a schematic of melting mode driven absorptivity in LPBF (d). The shape of the vaporized region (dependent on the front vaporization wall angle (θ) illustrated in Figure 3.3) determines the number of laser reflections inside the vaporized region of the melt pools. The white regions correspond to the vaporized region of the melt pools. The grey regions correspond to temperatures between the melting and boiling point in the melt pools of a given material. The arrows correspond to the laser beam reflections inside the vaporized region of the melt pools. Figures (a), (b), and (c) are adapted from Fabbro et al. [8]

.

Table 3.1: Minimum absorptivity of the flat melt surfaces of Ti-6Al-4V, IN 625, and SS 316L during laser powder bed fusion. Data obtained from Ye et al. [7].

Materials	Minimum melt absorptivity, A_m
Ti-6Al-4V	0.26
IN 625	0.28
SS 316L	0.28
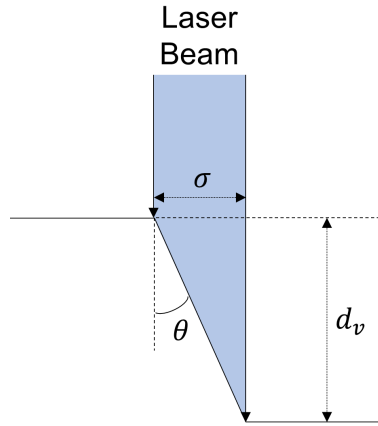
Figure 3.3: Schematic of vaporized region depth (d_v) and front vaporization wall angle (θ), where σ corresponds to the beam spot diameter of a given LPBF system. Figure adapted from Fabbro et al. [8]

.

absorptivity. This regime is the conduction mode regime in Figure 3.1 where the lowest absorptivity of ≈ 0.3 is the value used by Ion et al. [139] for creating conduction mode laser welding processing diagrams. The high absorptivity measurements at low heat input values and during melting also represented schematically in Figure 3.2 (d) for conduction mode LPBF. The trend in laser absorptivity after the onset of surface vaporization are captured by an asymptotic exponential function by Ye et al. [7] shown by the red solid line in Figure 3.1 and given by Equation 3.10.

$$A = 0.70(1 - \exp{-0.66\beta_{Am}L_{th}^*}) \tag{3.10}$$

Equation 3.10 can be represented by the dimensionless terms derived in Section 3.3.1

by Equation 3.11.

$$A = 0.70 \left(1 - \exp \frac{-0.66 q_m^*}{\pi v^*} \right) \tag{3.11}$$

The gradually increasing slope following surface vaporization in Figure 3.1 is an indication of the regime in-between conduction and keyhole mode called the transition mode, as illustrated in Figure 3.2 (d). Transition melting mode was first observed in laser welding and has been shown to have characteristics of both conduction and keyhole melting modes in observed melt pools [199, 200, 201]. In commonly used processing conditions for LPBF, vaporization of a material is expected in conduction, transition, and keyhole modes, as illustrated in 3.2 and observed experimentally [3]. The extent (depth) of vaporization is the driving factor for the thresholds between the three melting modes, as reported by high-speed x-ray imaging of the LPBF process by Cunningham et al. [3]. The vaporization depth (d_v) can be directly related to the beam spot diameter (σ) through the front vaporization wall angle (θ), by Fabbro et al's [8] analytical model, which is illustrated in 3.3. The relation between the three variables can hence be given by:

$$d_v = \frac{\sigma}{tan\theta} \tag{3.12}$$

Fabbro et al's model has been validated for LPBF through the use of high-speed X-ray imaging by Cunningham et al [3]. The transition melting mode occurs when the melt pool depths are dependent on fluctuating laser absorptivity, which depends on the number of reflections inside the vaporized portion of a melt pool, as observed at laser powers greater than ≈100 W by Ye et al. [7] for Ti-6Al-4V, Inconel 625, and SS 316L. The increase in laser absorptivity as a function of heat input in transition mode is observed due to the increasing number of reflections of the laser beam in the vaporization walls of the melt pool before the laser beam eventually gets reflected out of the keyhole as illustrated in Figure 3.2 (b). After a certain amount of increase in heat input, the laser absorptivity saturates at about 0.7 for most materials as shown in Figure 3.1, regardless of beam spot size, thus representing the fully developed keyhole mode, also illustrated in Figure 3.2 (d). This saturated value of absorptivity in keyhole mode is because the multiple reflections of the laser beam are now trapped inside the melt pool instead of being reflected outside the melt pool as illustrated in Figure 3.2 (c), in contrast to the conduction and transition mode melt pools illustrated in Figure 3.2 (a) and Figure 3.2 (b) respectively, where some of the reflections escape. Of importance, the laser absorptivity in the fully-developed keyhole mode always saturates well below 1 for keyhole mode, because part of the laser beam undergoes absorption and

reflection in the vapour plume and, due to the Gaussian distribution of laser intensity, only a part of the laser beam enters the keyhole zone [9]. The saturated value of 0.7 in LPBF keyhole mode is close to the value of 0.8 reported in keyhole mode laser welding literature [139]. The discrepancy between the keyhole mode absorptivity for LPBF and laser welding could be associated to greater laser scattering from the vapour plume in LPBF due to effects like powder entrainment [168] and powder spatter [169] in the path of the laser beam.

In summary, the conduction and keyhole melting modes result in melt pools with respective depths being a function of primarily the input energy density, as the laser is either mainly absorbed through multiple reflections inside the keyhole developed (keyhole mode) or the laser is reflected outside of the vaporized keyhole developed after a few reflections (conduction mode). For transition mode melting in LPBF, in addition to the heat input, melt pool dimensions are also dependent on the fluctuations in laser absorptivity, which depends on the number of reflections the laser beam undergoes before it exits the keyhole formed by the vaporized material.
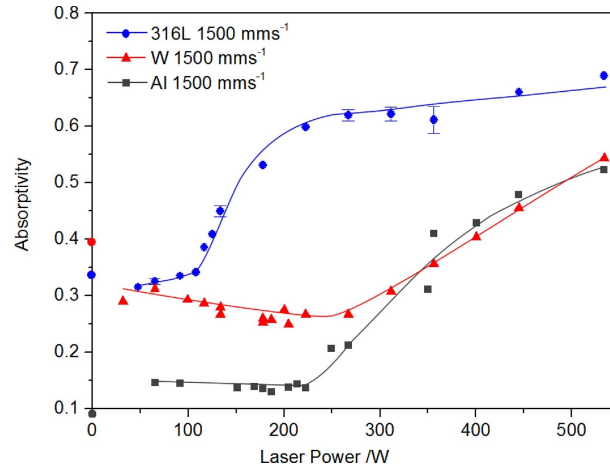
Figure 3.4: In situ absorptivity measurements of aluminum alloy 1100 (Al 1100), tungsten (W) and stainless steel 316L (SS 316L) discs as a function of laser power for a beam spot diameter of 60 ± 5 µm and scanning speed of 1500 mm/s. Reprinted with permission from [9]
.

Other reasons contributing to the fluctuations observed in laser absorptivity values in the three melting modes include and are not limited to the wavelength and polarization state of the laser beam, temperature of the material, surface roughness of the previous

Table 3.2: Laser absorptivity selected in the three melting modes for high reflectivity materials such as aluminium alloys [9]

Material	Conduction	Transition	Keyhole
Al alloys	0.15	0.425	0.7

layer, the surface morphology of powder particles [9, 202], the angle of incidence of the laser beam, the absorption or reflection of the laser in the vapour plume generated when the laser hits the metal surface [9], the absorption by vapour plume inside the keyhole which then re-radiates energy to the wall of the vaporized region [202], the bi-product of absorptivity of the laser beam in the powder layer alongside the molten track as a result of the Gaussian laser intensity distribution [9], the powder entrainment in the laser beam resulting in beam scattering by the powder particles [168], and the powder denudation due to an interplay among melt pool geometry, ambient gas pressure, and metal vapour flow [108].

The scaling law of laser absorptivity given by Equation 3.11), as adapted from Ye et al. [7], will be deployed in Section 3.3.3, where a methodology is developed to predict the thresholds between the three melting modes by predicting the vaporization depth through a temperature prediction model. For low reflectivity material such as titanium, ferrous, and nickel alloys, the scaling law developed by Ye et al. [7] will be shown to hold well for purposes of predicting melting mode thresholds. However, this scaling law does not apply to high reflectivity materials like aluminium alloys. For high reflectivity materials such as aluminium alloys, the laser absorptivity in conduction mode LPBF is observed to be ≈ 0.15 for a beam spot size of 60 ± 5 µm [9, 203], as shown in Figure 3.4. Since data for laser absorptivity of high reflectivity materials such as AlSi10Mg is not available for varying beam spot sizes, a constant value depending on the melting mode is assumed as shown in Table 3.2. In keyhole mode melt pools, laser absorptivity has previously been observed to be independent of material properties [204] and hence we choose a value of 0.7 for AlSi10Mg, similar to the value observed in Figure 3.1. For transition mode LPBF, it is proposed to pick an average value (0.425) between the conduction and keyhole as shown in Table 3.2. Further research is required to derive absorptivity scaling laws for high reflectivity aluminium and copper alloys, alongside high entropy alloys.

The predictions from the temperature prediction model developed in Section 3.3.3 are then used concomitantly with the normalized process diagram from Section 3.3.1 to predict the conduction, transition, and keyhole melting modes in LPBF. These prediction are then validated by the ground truth for the melting mode of a given melt pool obtained from a

40

unique set of LPBF process parameters from Section 3.4. The ground truth is determined by considering experimental measurements of the melt pool aspect ratios. Melt pool aspect ratios from individual melt pool datasets presented in Section 3.4 are used to experimentally identify melt pools in the three melting modes. The melt pool aspect ratio is defined herein as the ratio between the melt pool depth and width. For this work, we assume conduction mode regimes as resulting in melt pools where the aspect ratio of melt pools are lesser than 0.5 [86, 205, 206]. Assuncao et al. [207, 208] observe that the melt pool aspect ratios defining the threshold from transition to keyhole mode depend on beam interaction time. From Assuncao's work on S355 mild steel [207, 208], it is observed that the transition mode lies between melt pool aspect ratios of 0.5 to 0.8, and keyhole mode is observed for melt pool aspect ratios greater than 0.8, as also noted by Tenbrock et al. [120]. For high reflectivity aluminium alloys however, a melt pool aspect ratio of 0.4 has been observed to be the threshold between the conduction and transition melting modes, which is used for this work [209]. Furthermore, in this present work, it is intended to theoretically develop normalized processing diagrams to predict and visualize the thresholds in between these melting modes and compare the performance of the melting mode thresholds in comparison with experimental datasets. To achieve this, a temperature prediction model is proposed to predict the threshold between conduction, transition, and keyhole modes; the model is described in section 3.3.3.

3.3.3 Analytical model for predicting melting mode thresholds

The objective of this section is to develop an analytical temperature prediction model with the goal of predicting the thresholds between conduction, transition, and keyhole melting modes in LPBF. The temperature field $T(r,t)$ at a point laying at radial distance r from the centre of the beam, as a function of time t, caused by a point energy source can be given by the well-established Rosenthal's analytical equation [210]:

$$T = T_0 + \frac{AP}{2\pi\lambda vt} \exp \frac{-r^2}{4\alpha t} \tag{3.13}$$

In Equation 3.13, A is laser absorptivity, P is laser power [W], λ is thermal conductivity [W/(m.K)], v is the laser scanning velocity [m/s], and α is thermal diffusivity [m^2/s]. The main assumptions of Rosenthal's equation are that the convection and radiation heat losses are being neglected, the workpiece is semi-infinite, the thermal properties of the material are constant, and the scan speed and laser power are constant. Ashby et al. [211] used Equation 3.13 to predict the microstructure of laser welds and observed that the equation

provides a good description of most structural changes occurring in laser welds. However, Ashby et al. [212] and Ion et al. [213] observed that Equation 3.13 is less satisfactory when describing the physical shape of the melt pool or the neighbouring isotherms for welds on thick plates. This limitation is due to the infinitesimal point source energy input approximation along a straight-line path on the plate surface; this assumption is a relatively limited approximation for the physics happening in the laser-material interaction. This problem can be partially overcome if the point source is replaced by a circular disc source, of radius r_b, tracking with velocity v in the x direction across the surface of a plate, which is a step closer to an approximation of reality.

In the pursuit of more appropriate approximations of the laser energy input profile in relationship to the thermal output profile, Rykalin et al. [214] proposed an analytical solution for the two-dimensional temperature field $T(y, z, t)$ for a Gaussian heat source travelling in the x direction with velocity v as given by Equation 3.14. The assumptions in this solution include the velocity of the beam being high enough to be treated as a line source of finite width in the y-direction, but infinitesimally thin in the x-direction, and material properties being independent of temperature. The formulation for the temperature profile is:

$$T = T_0 + \frac{AP}{2\pi\lambda v\sqrt{t(t + t_0)}} \exp \frac{-1}{4\alpha} \left(\frac{z^2}{t} + \frac{y^2}{t + t_0} \right) \tag{3.14}$$

where

$$t_0 = \frac{r_b^2}{4\alpha} \tag{3.15}$$

In Equation 3.15, t is time [s] and t_0 is the characteristic time [s], which is defined as the time taken by the beam to diffuse over the beam spot radius, r_b. It is important to note that when $z^2 + y^2 >> r_b^2$ and $t >> t_0$, Equation 3.14 reduces to the Rosenthal's solution for a point heat source as given by Equation 3.13.

The challenge is that both Equation 3.13 and Equation 3.14 lead to infinite temperatures at the surface where the beam acts. This is due to the assumption of high velocity, meaning that a finite amount of energy is injected into the solid at $t = 0$. To approximate laser surface treatments, the width of the beam in both the x and y directions must be included. Ashby et al. [212] hence proposed replacing the real source in the plane $z = 0$ by an apparent source at $z = z_0$ above the surface, such that the temperature field Equation

$T(y, z, t)$ becomes:

$$T = T_0 + \frac{AP}{2\pi\lambda v\sqrt{t(t+t_0)}} \exp\frac{-1}{4\alpha}\left(\frac{(z+z_0)^2}{t} + \frac{y^2}{t+t_0}\right) \qquad (3.16)$$

Immediately below the centre o the beam $(y = 0)$, Equation 3.16 becomes:

$$T = T_0 + \frac{AP}{2\pi\lambda v\sqrt{t(t+t_0)}} \exp\frac{-1}{4\alpha}\left(\frac{(z+z_0)^2}{t}\right) \qquad (3.17)$$

The heating and cooling rates can be obtained by differentiating Equation 3.17 with respect to time:

$$\frac{dT}{dt} = \frac{T - T_0}{t}\left[\frac{(z+z_0)^2}{4\alpha t} - \frac{1}{2}\left(\frac{2t+t_0}{t+t_0}\right)\right] \qquad (3.18)$$

940   The peak temperature, T_p, is obtained when $dT/dt = 0$, leading to:

$$\frac{t_p(2t_p + t_0)}{t_p + t_0} = \frac{(z+z_0)^2}{2\alpha} \qquad (3.19)$$

In Equation 3.19, t_p is the time taken to reach peak temperature, T_p. To find peak temperature T_p, we should find the solution for t_p from Equation 3.19 and substitute it in Equation 3.17. However, Equation 3.19 does not have a closed-form analytical solution. Hence, to simplify Equation 3.19, Ashby et al. [212] propose an assumption of $t_p \ll t_0$

945   for laser processing methods which involve just heat treatment. Examples of such laser processing methods are laser hardening, laser annealing, and laser carburising [139]. Similarly, Ashby et al. [212] propose an assumption of $t_p \gg t_0$ for laser processing methods which involve melting and vaporization. Examples of such methods are laser cladding, laser melting, laser alloying, laser cutting, conduction mode laser welding, and keyhole

950   mode laser welding [139]. The beam interaction time, t_b, at any given point for a moving heat source can be given by:

$$t_b = \frac{2r_b}{v} \qquad (3.20)$$

If heat is constantly acting on a given point, $t_p \gg t_0$ it can be assumed that the time taken to reach peak temperature, t_p, at a given point is approximately equal to the beam

interaction time, t_b i.e. $t_p \approx t_b$. Hence, Ashby's assumptions of $t_p >> t_0$ for LPBF (which involves melting and vaporization) can be rewritten as $t_b >> t_0$. From Equation 3.15 and Equation 3.20, we obtain:

$$\frac{2r_b}{v} >> \frac{r_b^2}{4\alpha} \qquad (3.21)$$

Equation 3.21 can be rearranged to obtain

$$\frac{vr_b}{\alpha} << 8 \qquad (3.22)$$

From Equation 3.2 and Equation 3.22, we obtain:

$$v^* << 8 \qquad (3.23)$$

The assumption from Equation 3.23 holds well for data in the work by Ashby et al. [212]. However for some of the keyhole welding literature points studied by Ion et al. [139], we observe that $v^* \approx 8$ or $t_p \approx t_0$. Similarly, for the LPBF data listed in Table 3.3, the values for v^* range from about 1 to 8. Hence, we assume $t_p \approx t_0$ holds true for LPBF literature listed in this work. Equation 3.19 hence becomes:

$$t_p = \frac{(z + z_0)^2}{3\alpha} \qquad (3.24)$$

Similarly, the term $\sqrt{t_p(t_p + t_0)}$ from Equation 3.17 becomes:

$$\sqrt{t_p(t_p + t_0)} = \sqrt{2}t_p = \frac{\sqrt{2}(z + z_0)^2}{3\alpha} \qquad (3.25)$$

Substituting values for t_p and $\sqrt{t_p(t_p + t_0)}$ from Equation 3.24 and Equation 3.25 into Equation 3.17, we obtain the equation for peak temperature, T_p, as:

$$T_p = T_0 + \frac{3A\alpha}{2\sqrt{2}\pi\lambda e^{0.75}} \cdot \frac{P}{v} \cdot \frac{1}{(z + z_0)^2} \qquad (3.26)$$

44

In addition to the q^* and v^* terms in Equation 3.1 and 3.2 herein, Ion et al. [139] propose additional terms such as:

$$t^* = t/t_0$$

dimensionless time

(3.27)

$$z^* = z/r_b$$

dimensionless depth

(3.28)

$$T^* = \frac{T - T_0}{T_m - T_0}$$

dimensionless temperature

(3.29)

Equation 3.26 can hence be written in dimensionless form to obtain dimensionless peak temperature, T_p^*, as:

$$T_p^* = \frac{3}{2\sqrt{2}\pi e^{0.75}} \cdot \frac{q^*}{v^*} \cdot \frac{1}{(z^* + z_0^*)^2}$$

(3.30)

To account for powder layer thickness effects, we substitute q^* with E^* to obtain:

$$T_p^* = \frac{3}{2\sqrt{2}\pi e^{0.75}} \cdot \frac{E^*}{v^*} \cdot \frac{1}{(z^* + z_0^*)^2}$$

(3.31)

The parameter z_0^* is found by equating T_p^* from Equation 3.30 to a solution for the peak surface temperature produced by a stationary beam acting for a time equal to the beam interaction time $(t_b = 2 \cdot r_b/v)$ [69]. In dimensionless terms, the solution becomes:

$$T_p^* = \frac{q^*}{\pi^{1.5}} tan^{-1} \left(\sqrt{\frac{8}{v^*}} \right)$$

(3.32)

The procedure used to obtain Equation 3.32 is the same as the one adopted by Ion et al [139]. To account for powder layer thickness effects, we substitute q^* with E^* to obtain:

$$T_p^* = \frac{E^*}{\pi^{1.5}} tan^{-1} \left(\sqrt{\frac{8}{v^*}} \right)$$

(3.33)

45

Equation 3.31 is then set equal to Equation 3.33 with $z^* = 0$ to obtain z_0^* as:

$$z_0^* = \sqrt{\frac{3\sqrt{\pi}}{2\sqrt{2}e^{0.75}} \cdot \frac{1}{v^* tan^{-1}(\sqrt{8/v^*})}} \tag{3.34}$$

z_0^* obtained from Equation 3.34 is then substituted into Equation 3.31 to obtain the normalized peak temperature at given values of dimensionless energy input (E^*), dimensionless beam velocity (v^*), and dimensionless depth (z^*). Conditions required to attain a surface peak temperature which is less than the melting temperature $(T_p^* \leq 1)$ can be found from Equation 3.31 with the value of z_0^* obtained from Equation 3.34. These equations could be useful for in situ heat treatments during LPBF processing of materials. The predictions from the temperature prediction model developed in this section are used in conjunction with the normalized process diagram methodology from Section 3.3.1 to predict the conduction, transition, and keyhole melting modes in LPBF. These predictions are then validated by the ground truth for the melting mode of a given melt pool obtained from a unique set of LPBF process parameters from Section 3.4.

3.4   Materials and Methods

3.4.1   Methods for obtaining and assessing LPBF melt pool datasets

The efforts presented in this work will first focus on leveraging existing literature in the development of normalized processing diagrams. From existing literature, the laser processing parameters (laser power, beam spot radius, and effective laser beam velocity) values are summarized in Table 3.3. Unless otherwise specified, the powder bed temperature (T_0) for all reported values in Table 3.3 was assumed to be room temperature, which is assumed to be 293 K. Values for material constants are taken at the solidus temperature for a given material from [215, 216], and are given in Table 3.4. In this present work, the method for plotting the normalized processing diagrams to visualize and predict melting modes was deployed for the first time to LPBF and inspired from previous laser processing literature [139].

3.4.1.1   Datasets from literature

All reported melt pool depth data in works listed in Table 3.3, except for the authors' work on AlSi10Mg, were obtained from coating one layer of powder with a layer thickness

46

Table 3.3: Summary of the LPBF machine and processing parameters reviewed in this study

Source	Material	LPBF system	Beam spot radii, r_b [µm]	Power, P [W]	Velocity, v [mm/s]	Layer thickness, l_t [µm]
Dilip et al. [4]	Ti-6Al-4V	EOS M270	50	50-195	500-1200	30
Wang et al. [217]	Ti-6Al-4V	Concept Laser M2	27	100-400	200-1600	50
Present work	Ti-6Al-4V	Renishaw AM 400	35	150-300	733-1363	30
Kamath et al. [66]	SS 316L	Concept Laser M2	27	150-400	500-1800	30
Present work	AlSi10Mg	Renishaw AM 400	35-102	150-400	500-786	30, 50

given in Table 3.3, on a given machine's build plate, and then scanning weld lines at a given combination of laser beam power and laser beam velocity. The data for AlSi10Mg was obtained experimentally from melt pool depths measured at the last layer of three-dimensional parts. The experimental methods focused on obtaining melt depth from our work on Ti-6Al-4V and AlSi10Mg is summarized in detail in section 3.4.1.2 and section 3.4.1.3 respectively.

In a modulated LPBF system (in the context of this study, a Renishaw AM 400), the beam velocity variable (v) is derived from the point distance (p_d) and exposure time (t_e), as illustrated in Figure 3.5 (A). This modulation of the laser beam provides an additional degree of control which is not possible in continuous LPBF systems. For modulated laser systems, p_d is the distance between adjacent exposure points (point distance) [m], t_e is the time when the laser is acting on the material (exposure time) [s], and t_d is the time when the laser is off and repositioning to the next exposure point (drill delay time) [s]. The drill delay time, t_d, is assumed to be 10 µs for Renishaw AM 400, as recommended by the manufacturer. For modulated laser beam inputs, an effective laser power (P_{eff}) term given by Equation 3.35 is used for the laser beam power values instead of P in

Table 3.4: Thermo-physical properties of Ti-6Al-4V, SS 316L, and AlSi10Mg taken at the solidus temperature.

Properties	Ti-6Al-4V	SS 316L	AlSi10Mg
Density, ρ [kg/m^3]	4430	7800	2670
Thermal Conductivity, λ [W/(mK)]	28.09	29.77	113
Specific heat capacity, C_p [J/(kgK)]	524.61	592.55	565.29
Solidus temperature, T_s [K]	1878	1693	831
Liquidus (melting) temperature, T_m [K]	1928	1733	867
Vaporisation (boiling) temperature, T_v [K]	3315	3086	2740

Equation 3.1 (q^*) and future references in this document, as illustrated in Figure 3.5 (A). Equation 3.36 is used to obtain the values for beam velocity in modulated systems in this work. The equations given below have also been reported in prior LPBF literature for process development using normalized process maps [218].

$$P_{eff} = \frac{P \cdot t_e}{t_e + t_d} \tag{3.35}$$

$$v = \frac{p_d}{t_e + t_d} \tag{3.36}$$

3.4.1.2 Ti-6Al-4V experimental datasets

Pre-alloyed plasma atomized Ti-6Al-4V powder of Grade 23 with a particle size distribution of 15 – 45 µm (D10 of 20 µm), D50 of 34 µm, and D90 of 44 µm) was used in a Renishaw AM 400 LPBF machine. The machine uses a modulated laser with nominal maximum power 400 W. For the Renishaw AM 400 system, the beam spot radius at the focal point is given by $r_0 = 35$ µm, and the wavelength of the laser beam used is $\lambda = 1070$ nm. The weld lines were printed on the reduced build plate of the Renishaw AM 400. A powder bed layer thickness of 30 µm was used for the experiments. The weld lines were printed using multiple combinations of laser power, point distance, and exposure time as shown in Table 3.5. The depth, width, and height of the weld lines were analyzed using a laser
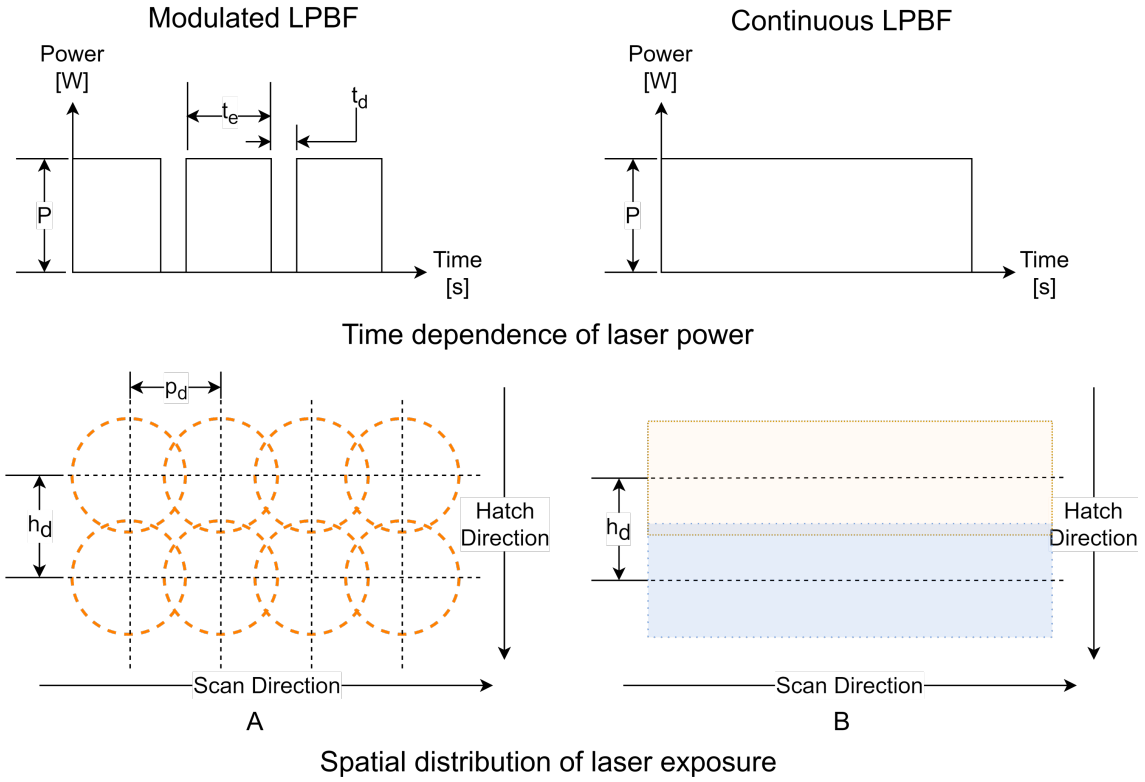
Figure 3.5: Schematic illustration of the temporal and spatial dependence differences between a modulated beam LPBF system (A) and a continuous beam LPBF system (B). P is the laser power, t_e is the exposure time, t_d is the drill delay time, p_d is the point distance, and h_d is the hatching distance.

Table 3.5: Factors used for the experimental design for Ti-6Al-4V weld lines on a build plate

Factor	Levels
Laser powder [W]	150, 200, 250, 300
Point distance [µm]	55, 65, 75
Exposure time [µs]	45, 55, 65

confocal microscope (Keyence VK-X250). Further methods and results from the weld lines printed on the substrate artifacts and the base plate are summarized in Appendix D.

3.4.1.3 AlSi10Mg experimental datasets

Pre-alloyed AlSi10Mg powder with a particle size distribution of $25 - 67$ µm (D10 of 19 µm), D50 of 28 µm, and D90 of 63 µm) was used in a Renishaw AM 400 LPBF machine. The weld lines were printed on top of substrate artifacts which were build on an aluminium build plate of Renishaw AM 400. The substrate artifacts were built using a set of previously identified parameters; optimization of the substrate recipe was not in the scope of the present work. A visualization of the layout of the weld lines on substrate artifacts are provided in Appendix D. A powder bed layer thickness of 30 µm was used for the experiments. The weld lines were printed using multiple combinations of laser power, point distance, exposure time, and beam spot diameter as shown in Table 3.6. For the Renishaw AM 400 system, the beam spot radius at the focal point is given by $r_0 = 35$ µm, and the wavelength of the laser beam used is $\lambda = 1070$ nm. The higher beam spot diameters for Renishaw AM 400 were obtained by defocusing the focal point of the laser beam to a point above the build plate of the system ($z > 0$), to obtain divergent beams. The beam spot diameters ($\sigma = 2r_b$) in Table 3.6 were obtained from the equation for a Gaussian distribution of a laser beam [219]:

$$r_b = r_0 \sqrt{1 + \left(\frac{z\lambda}{\pi r_0^2} \right)^2} \tag{3.37}$$

The depth and width of the weld lines were analyzed using a laser confocal microscope (Keyence VK-X250). The results from the weld lines printed on the substrate artifacts are summarized in Appendix D.

Table 3.6: Factors used for the experimental design for AlSi10Mg weld lines on substrate artifacts

Factor	Levels
Laser powder [W]	150 - 400
Point distance [µm]	45, 55, 60, 75
Exposure time [µs]	24 - 230
Beam spot diameter [µm]	70, 108, 128, 146, 167, 183, 203

3.5 Results and discussion

3.5.1 Normalized processing diagrams for LPBF

Plotting the dimensionless heat input term, E^*, versus dimensionless beam velocity, $v*$, for all the experiments results in a distinct transition between the overlapping regions of the three melting modes as shown in Figure 3.6. Notably, for the data captured in this present work, the transition is observed to not be sensitive to material type (Figure 3.6b), nor to powder bed layer thickness (Figure 3.6c). These findings are hence the first attempt at predicting melting mode thresholds for LPBF with an independence of material, LPBF system, and processing parameters such as powder layer thickness.

The dimensionless processing diagrams for LPBF obtained in this work illustrate that the observed experimental melt pool morphology datasets can be used to identify the distinct conduction, transition, and keyhole melting mode clusters, irrespective of material and layer thickness. This important finding is indicative that the melting mode can be predicted through modeling efforts. In the following section, we intend to predict the theoretical thresholds between conduction, transition, and keyhole melting modes using a temperature prediction model.

3.5.2 Melting mode thresholds for LPBF

The low beam spot diameters typically deployed in LPBF (50 – 100 µm) lead to onset of vaporization in virtually all levels of commonly used laser power (100 – 550 W) and velocity (400 – 1200 mm/s) as shown by Cunningham et al [3]. Due to the onset of vapor-ization, in almost all laser power and velocity levels, accurate modelling the LPBF process

51
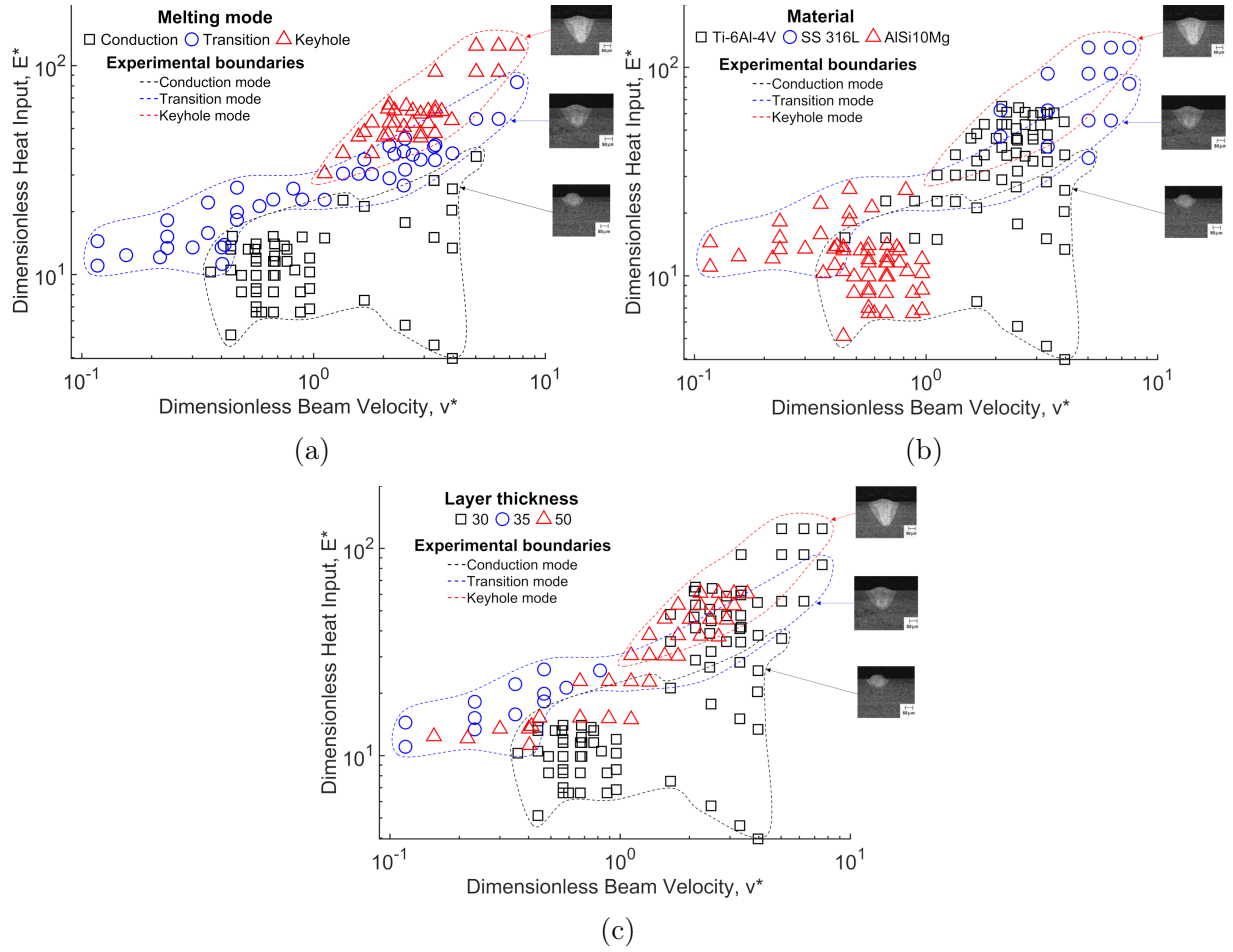
Figure 3.6: Processing diagram for experimental LPBF data listed in Table 3.3, plotted using dimensionless heat input (E^*) and dimensionless beam velocity (v^*), and identified by melting modes (a), material (b), and powder layer thickness (c)

through analytical modelling efforts becomes highly challenging, since it is not possible to accurately model the effects of recoil momentum pressure generated by vaporization of a given material and convective heat transfer generated by Marangoni convection due to surface temperature gradients, also known as thermo-capillary flow [220, 221]. In particular, the depth of the molten pools would be dictated by the effects of recoil momentum pressure. Models which include such complex effects are computationally expensive and would be difficult to implement for process mapping or in high speed automatic process control of LPBF. An analytical model like the one proposed in Section 3.3.3 can be used for rapidly obtaining processing charts for any given material, as long the values for bulk density, thermal conductivity, specific heat capacity, and melting temperature are known. In the following sections, the focus is to demonstrate a methodology to predict the melting mode transition for low reflectivity materials (Ti-6Al-4V and SS 316L) and high reflectivity materials (AlSi10Mg).

3.5.2.1 Melting mode thresholds for low reflectivity and low thermal conductivity materials

Materials such as Ti-6Al-4V, SS 316L, and Inconel 625 can be termed as low reflectivity materials since their laser absorptivity coefficients in conduction mode melting are significantly higher than materials such as AlSi10Mg [9, 203], which has a high reflectivity coefficient, as discussed in section 3.3.2. For these low reflectivity materials, we observe from experimental datasets of melt pools that the threshold between conduction to transition mode lies at a temperature contour of $T_p^* = 1.75$ at $z^* = 0.5$ as shown in Figure 3.7. $T_p^* = 1.75$ corresponds to the approximate vaporization temperature (boiling point) as described in Equation 3.29 for low reflectivity materials such as Ti-6Al-4V, SS 316L, and Inconel 625 [222]. $z^* = 0.5$ corresponds to a vaporization depth, $d_v = 0.5r_b$ i.e. a vaporization depth equal to half the beam spot radius. From Equation 3.38, we observe that the front vaporization wall angle (θ) can be determined by the relation

$$\theta = tan^{-1}\left(\frac{2r_b}{d_v}\right) \tag{3.38}$$

Hence, the threshold between conduction and transition mode would be at an approximate front vaporization wall angle, $\theta = tan^{-1}\left(\frac{2r_b}{0.5r_b}\right) = 75.96°$. Similarly, we observe the threshold between transition to keyhole mode to lie at a temperature contour of $T_p^* = 1.75$ at $z^* = 0.8$ as shown in Figure 3.7. In this instance, $z^* = 0.8$ corresponds to a vaporization depth, $d_v = 0.8r_B$ i.e. a vaporization depth equal to 0.8 times the beam spot radius. Hence,

the threshold between transition and keyhole mode would be at a front vaporization wall angle, $\theta = tan^{-1}\left(\frac{2r_b}{0.8r_b}\right) = 68.2°$. Additionally, we plot the $T_p^* = 1.75$ at $z^* = 0$ contour in Figure 3.7 to show the trend seen experimentally by Cunningham et al. [3], where a certain amount of vaporization is expected at commonly used LPBF processing parameters even in conduction mode LPBF. $T_p^* = 1.75$ at $z^* = 0$ corresponds to vaporization at the surface, which approximates fairly well the melting mode transition in laser welding [77] due to the higher beam spot radiuses, but it does not appear to be suitable for melting mode threshold predictions in LPBF.
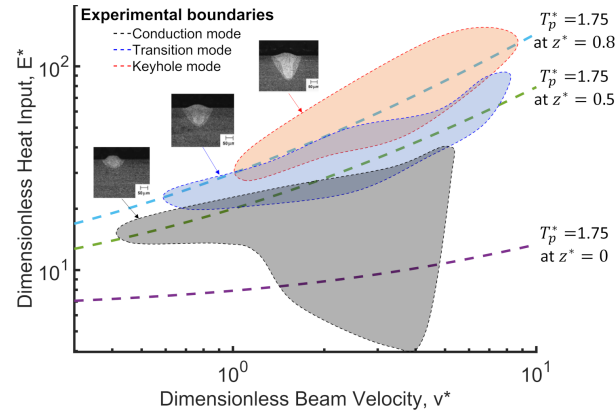
Figure 3.7: LPBF processing diagram, showing the practical operating regions for conduction, transition, and keyhole modes (shaded regions with dashed contours) based on experimental datasets for Ti-6Al-4V and SS 316L, and model predictions of the onset of transition mode and keyhole mode (dashed curves).

The normalized processing diagram from Figure 3.7 can be used to understand the physical origin of defects in three-dimensional LPBF parts as shown in Figure 3.8. In conduction mode parts, lack-of-fusion defects would be expected, particularly at low power and high velocity regions in the process diagram. The lower energy input in conduction mode melt pools could lead to melt pool dimensions lower than the powder layer thickness causing incomplete melting of powder particles. If these powder particles are not melted in subsequent layers, such occurrences would lead to irregularly-shaped lack-of-fusion defects as shown in Figure 3.8 A and observed by Cunningham et al [223]. Additionally, inadequate selection of LPBF processing parameters such as hatching distance and powder layer thickness could cause insufficient stitching or overlap of melt tracks, causing lack-of-fusion defects. Even in transition and keyhole modes where the melt pools obtained would be deeper than in conduction mode, selection of sufficient melt track overlap depth is important, since an inadequate ratio of the hatch spacing to melt pool width could cause

54

lack-of-fusion defects, as observed by Choo et al. [159]. Another common cause of defects in LPBF parts comes from entrapped gas in the feedstock powder particles. Such

1130 entrapped gas can be caused by the powder synthesis process, and can be the cause tiny near-spherical defects in all three melting modes as shown in Figure 3.8 B [223]. Additionally, for aluminium alloys, presence of moisture on the powder surfaces leads to spherical hydrogen pores in all three melting modes [158, 130]. This is due to the reduction of hydrogen solubility in aluminium alloys during the resolidification of liquid aluminium [5].
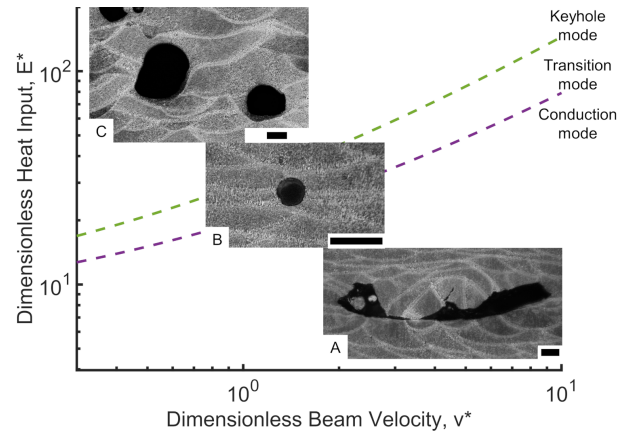
Figure 3.8: LPBF processing diagram, showing the operating regions for conduction, transition, and keyhole modes, along with the common types of defects observed in the three melting modes. (A) Lack-of-fusion defects commonly observed in conduction mode, (B) entrapped gas defects from powder which could be observed in all three melting modes, (C) excessive vaporization related defects commonly observed in transition and keyhole melting modes. The black scale bars correspond to 50 µm.

1135   The excessive vaporization of metal, particularly in keyhole mode, is another source of defects due to the interplay between the thermo-capillary force introduced by the temperature gradient, drag force induced by the melt flow, and recoil pressure due to material vaporization as shown in Figure 3.8 C [85, 224]. As such, the defects which occur in transition and keyhole modes have various morphologies: collapse and rapid solidification of

1140 the bottom section of the vaporized region resulting in irregularly-shaped defects, the cavities from the bottom section of the vaporized region which contract to a spherical bubble and solidify as a pore resulting in spherical defects, pores created by the vapour jet of the vaporized metal resulting in spherical defects, and pore coalescence resulting in irregularly-shaped defects [223, 5]. Additionally, during transition and keyhole mode processing at

1145 high laser beam velocities, elongated molten pool regions near the side and rear walls of the

55

vaporized region could rise from the top of the melt pool thereby breaking into droplets of molten metal called melt pool spatter [225]. Melt pool spatter, along with powder ejecta [156] and powder denudation [108] are expected to cause surface irregularities on the layer being printed, leading to deterioration of the wetting behaviour of next layer and possible causing defects in either of the three melting modes [85]. The presence of irregularly shaped defects and near-spherical defects is hence possible in all three melting modes, but the origins of the defects depend upon the melting mode. The processing diagrams, along with the melting mode threshold prediction model from this work can hence help identify the origin of defects in LPBF depending on where the processing conditions for a given part lie.

The threshold predictions from the model developed in section 3.3.3 hence depend on both T_p^* and z^*, and thereby both material properties (density, thermal conductivity, specific heat capacity, melting temperature, and vaporization temperature) and LPBF system properties (beam spot radius). In Figure 3.9 and Figure 3.10, the authors showcase the model's applicability to different LPBF systems and different low reflectivity materials (Ti-6Al-4V and SS 316L respectively). In Figure 3.9, the thresholds are calculated at $T_p^* = 1.72$, where 1.72 is the ratio of the boiling point of Ti-6Al-4V and its melting point. Similarly, for SS 316L in Figure 3.10, we plot the thresholds at $T_p^* = 1.78$, where 1.78 is the ratio of the boiling point of SS 316L to its melting point.

For low reflectivity (and hence high absorptivity) materials such as Ti-6Al-4V, SS 316L, and Inconel 625, it is expected that surface vaporization leads to the formation of a vaporized region with a front vaporization wall angle, $\theta > 75.96°$, which leads to a vaporized region shape as shown in Figure 3.2 (a). Such high angles of the vaporization front wall lead to the laser beam reflecting outside of the keyhole after just one reflection. Hence, Cunningham et al. [3] observe conduction mode melt pools in LPBF when the peak surface temperature is above the boiling point of Ti-6Al-4V. If the heat input is increased to an extent such that the front vaporization wall angle, $68.2° < \theta < 75.96°$, the keyhole shape resembles that of Figure 3.2 (b). This leads to the transition mode in LPBF, where the laser beam undergoes multiple reflections before eventually escaping the keyhole, where the number of reflections and hence the laser absorptivity depend on the beam spot size and heat input. In conduction and transition mode melt pools, the laser absorptivity is strongly dependent on the material properties and laser beam spot radius as discussed in section 3.3.2. If the heat input is further increased such that $\theta < 68.2°$, the vaporized region shape resembles that of Figure 3.2 (c). This leads to the onset of keyhole mode the laser absorptivity saturates at about 0.7 for most materials regardless of beam spot size [7].

The model developed for predicting melting mode thresholds assumes a 2D Gaussian

56
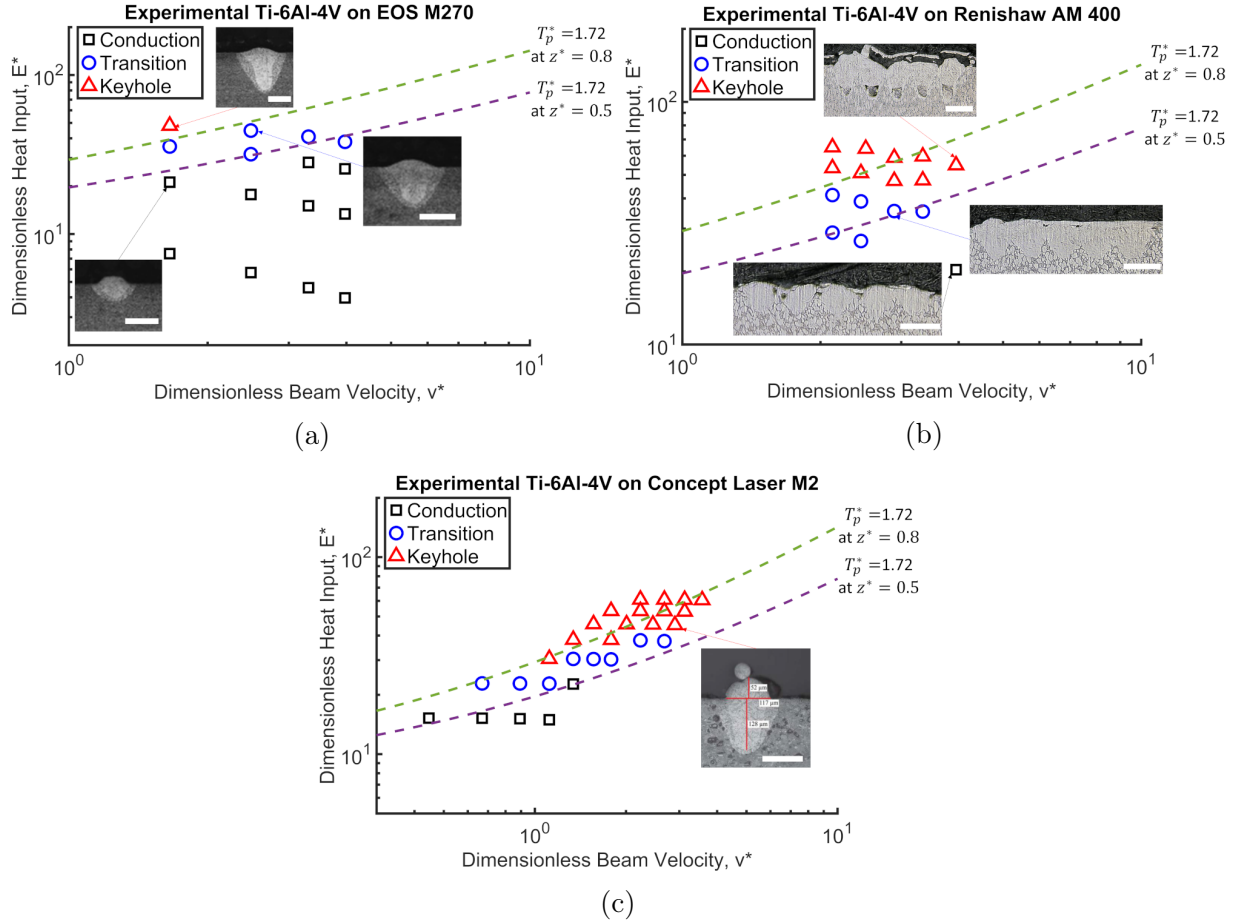
Figure 3.9: LPBF processing diagram, showing the conduction, transition, and keyhole mode regions in Ti-6Al-4V processed on EOS M270 (a), Renishaw AM 400 (b), and Concept Laser M2 (c) as per sources listed in Table 3.3; and model predictions of the onset of transition mode and keyhole mode (dashed curves). The white scale bars correspond to 100 µm.
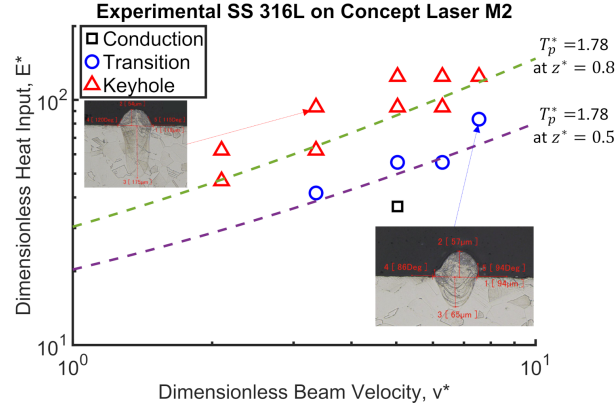
Figure 3.10: LPBF processing diagram, showing the conduction, transition, and keyhole mode regions in stainless steel 316L (SS 316L) processed on Concept Laser M2 as per sources listed in Table 3.3; and model predictions of the onset of transition mode and keyhole mode (dashed curves).

heat source, which has limitations in temperature predictions when compared to volumetric heat sources, particularly for deeper melt pools observed in keyhole mode, as noted by laser welding and LPBF researchers [226, 227]. Since the melting mode threshold model is expected to break down in the later regimes of transition mode, the threshold recommended by the model between transition and keyhole modes would be expected to have greater uncertainty. A possible oversimplification of the layer thickness effects, the assumption of temperature independent physical properties, the assumption of angle of incidence being perpendicular to the substrate, ignoring heat loss by refraction in the vapour plume, and various other LPBF machine related properties also contribute to the uncertainty margins in the identified melting mode thresholds.

3.5.2.2 Melting mode thresholds for high reflectivity and high thermal conductivity materials

Aluminium alloys are known to have a higher reflectivity (and hence, lower absorptivity) and higher thermal conductivity when compared to materials such as Ti-6Al-4V, SS 316L, and Inconel 625, as reported in LPBF literature [215, 9, 203, 228, 229]. At the solidus temperature, the thermal conductivity of AlSi10Mg is 113 W/(m.K) compared to 28.09 W/(m.K) for Ti-6Al-4V, 29.77 W/(m.K) for SS 316L, and 28.57 W/(m.K) for Inconel 625 [215]. Therefore, for AlSi10Mg, most of the incident beam is reflected and melting does not progress as easily as it would in the low reflectivity materials. Therefore, once the

58

front face of the material reaches the melting point and begins to melt, melting progresses rapidly. Thus, the transition range between conduction mode welding and keyhole mode welding for aluminium is narrow, and the melt pool morphology is very sensitive to the heat input [205].
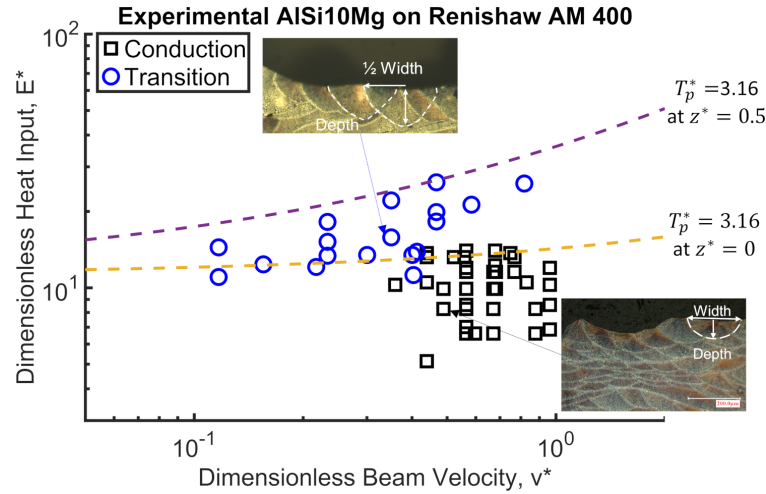
Figure 3.11: Proposed LPBF processing diagram for AlSi10Mg, showing the conduction, transition, and keyhole mode regions in AlSi10Mg processed on Renishaw AM 400; and model predictions of the onset of transition mode and keyhole mode (dashed curves).

Additionally, aluminium alloys like AlSi10Mg having a high concentration of volatile alloying elements such as magnesium, are more easily vaporized by the laser beam. These volatile elements, due to their high vapour pressures, help in the development of a keyhole by reducing the threshold heat input required to achieve keyhole mode, when compared to other aluminium alloys with lower concentration of such elements [204]. Taking into account the very low surface tension of aluminum at the boiling point (about 0.28 N/m [216]), the additional pressure to overcome surface tension is minimal for most aluminium alloys as soon as vaporization initiates [9]. These reasons point towards the discrepancies in melting mode thresholds observed in this work.

In this present work, based on our observations, it is hypothesized that the onset of surface vaporization as predicted at $z^* = 0$ in AlSi10Mg leads to the formation of a keyhole cavity with front vaporization wall angle, $\theta < 75.96°$. The shape of the keyhole would thereby resemble the one shown in Figure 3.2 (b). We hence propose the use of the temperature contour $T_p^* = 3.16$ at $z^* = 0$ for the threshold between conduction and transition mode and the temperature contour $T_p^* = 3.16$ at $z^* = 0.5$ as the threshold

59

between transition and keyhole mode as shown in Figure 3.11. The value 3.16 is the ratio of the boiling point of aluminum and its melting point.

With the 52 combinations of processing parameters used in this work for AlSi10Mg, the aspect ratio of the deepest melt pool was 0.71 which is assumed to lie in transition mode. Since there are no keyhole mode melt pools (aspect ratio > 0.8) reported in this work, the threshold between transition mode and keyhole mode for AlSi10Mg requires further experimental validation studies. Additionally, the conduction mode melt pools were obtained by defocusing the focal point of the laser beam to a point above the build plate of the system, thereby yielding higher beam spot radiuses. Use of varying beam spot radiuses might also have effects on absorptivity values of melt pools, thus affecting their position on the processing diagram. These issues, along with the limitations of the analytical melting mode threshold model discussed in section 3.5.2.1, contribute to the uncertainty margins in the identified melting mode thresholds for this class of materials.

Overall, the processing diagrams proposed in this work could be useful for narrowing down the initial selection of LPBF processing parameters for new alloys to reduce the need for highly iterative experiments. Additionally, this work could be used to understand the physical origin of defects based on LPBF processing parameters such as laser power, velocity, and powder layer thickness. Lack-of-fusion defects would be anticipated for conduction mode melting, whereas shielding gas porosity due excessive vaporization would be expected for transition and keyhole mode melting. This work could also be used to understand the effects of the thermal history of conduction, transition, and keyhole mode melt pools and could thereby be used to tailor microstructure and mechanical properties in combination with beam path planning algorithms for industrial applications.

3.6 Conclusions

The key findings from this chapter are summarized below:

1. Ion et al.'s [139] and Thomas et al.'s [87] approach for constructing normalized processing diagrams has been extended to visualize the three melting modes (conduction mode, transition mode, and keyhole mode) observed in LPBF. The normalized processing diagrams obtained in this present work, for the first time in LPBF, are shown to be independent of material, LPBF system, and processing parameters such as powder layer thickness within the datasets presented herein.

2. Ashby et al.'s [212] model has been extended to account for the temporal resolution difference between LPBF and other laser processing methods to generate a model that

can predict the thresholds between the conduction, transition, and keyhole melting modes. The efficacy of these predicted thresholds has been evaluated experimentally for low reflectivity alloys and high reflectivity alloys.

3. For low reflectivity and low thermal conductivity materials such as titanium, ferrous, and nickel alloys, a vaporization depth greater than 0.5 and 0.8 times the beam spot radius used corresponds to the thresholds between conduction to transition mode and transition to keyhole mode respectively. For high reflectivity and high thermal conductivity materials such as aluminium alloys, surface vaporization and a vaporization depth greater than 0.5 times the beam spot radius used corresponds to the thresholds between conduction to transition mode and transition to keyhole mode respectively.

4. The methodology proposed in this work has potential for streamlining the optimization of LPBF processing parameters for new alloys, for analyzing the effects of variations in individual processing parameters, and for understanding the source of porous defects.

The methodologies developed in this chapter are to developed a fundamental understanding of porous defects, side-skin surface roughness, and residual stresses in LPBF as shown in Chapters 4, 5, and 6.

Chapter 4

Melting mode driven understanding of porous defects in a high reflectivity aluminium alloy - AlSi10Mg

4.1 Preface

The laser powder bed fusion (LPBF) of aluminium alloys is associated with numerous challenges when compared to other commonly used alloys (e.g., steels and titanium alloys) due to their higher reflectivity. This leads to a higher defect density in the final parts, commonly related to melt pool instabilities in the transition and keyhole melting modes. In this work, a theoretical modelling approach is deployed to construct processing diagrams geared towards virtual process parameter optimization for laser powder bed fusion (LPBF) of high reflectivity aluminium alloys. Simulations and experiments drive recommendations of using divergent beams for LPBF systems with resulting focal diameters >100 µm to obtain a conduction mode microstructure with ≈99.99% density. Analytical thresholds for stabilizing spatter dynamics help narrow into transition mode process parameters with ≈99.98% density, for focused beams with diameters <100 µm. The threshold between conduction and transition/keyhole mode melt pools for aluminium alloys is at a melt pool aspect ratio (ratio of melt pool depth to width) of ≈0.4, different from the conventionally assumed 0.5. Laser absorptivity differences of up to 50% are reported in conduction versus transition/keyhole melting mode in aluminium alloys. This work provides a machine and alloying element agnostic method to obtain near fully dense aluminium parts [209].

4.2 Introduction

The potential of powder bed fusion (PBF) technologies to produce high-quality complex
geometries and the ability to pursue assembly consolidation have been shown to increase
technology adoption in the aviation [230, 231, 232, 233, 234, 235, 56] and automotive
industries [236, 237, 238, 239, 240] in particular. Laser powder bed fusion (LPBF) is a PBF
technology with a high industrial uptake, owing to the minimum feature size, resolution,
and surface finish possible with the reduced beam spot sizes commonly used in LPBF,
when compared to the electron beam powder bed fusion (EB-PBF) technology [241]. The
use of lower achievable beam spot sizes, combined with the advances in design for additive
manufacturing (DfAM) competencies, help the industry in realizing the true potential of
LPBF for light weighting and design optimization of critical components.

With respect to materials, aluminium alloys are commonly used in aerospace and au-
tomotive applications which require a combination of high strength performance and low
weight. AlSi10Mg has been adopted widely in the LPBF community for these applications
[242, 243, 244]. The lower beam spot sizes used in LPBF, however, lead to the lowering
of the vaporization threshold of aluminium [3], which can be a disadvantage due to the
ease of porosity formation in the keyhole mode melting of aluminium alloys [245]. It has
hence been previously assumed in literature that keyhole mode melting is the dominant
melting mechanism in LPBF of aluminium alloys such as AlSi10Mg, while working with
a beam spot radius of 10 µm [246]. Similarly, for another experimentally intensive effort
on processing AlSi10Mg with a beam spot radius of 35 µm, keyhole mode porosity defects
were observed in three-dimensional coupons at laser power settings ranging from 88 to 390
W, and scan speeds ranging from 250 mm/s to 2500 mm/s [247]. Based on the litera-
ture, there are challenges in identifying stable process parameter windows for obtaining
defect-free components for aluminium alloys due to the rapid onset of transition/keyhole
melting mode driven by the interaction of a highly focused energy source acting on a high
reflectivity and high thermal conductivity material system [248, 249, 10]. The significant
differences in absorptivity characteristics for aluminium alloys in the conduction and tran-
sition/keyhole melting modes when compared to titanium, ferrous, and nickel alloys [9] also
contributes towards the difficulties in obtaining defect-free parts as the rapidly increasing
vapour cavity in the melt pool would make it difficult for a pore to escape during solidifi-
cation. One path towards exploring such defect-free process windows is by exploring the
effects of beam defocusing on achieving stable conduction-mode process windows [250, 167],
as proposed in the present work. Additionally, physics-driven analytical thresholds to help
stabilize melt pool and spatter dynamics are used to drive an appropriate selection of
LPBF process parameters for a focused beam in the transition melting mode. This is the

first attempt in literature using modelling-approaches to recommend a methodology for
₁₃₃₀ identifying defect-free process windows for the conduction and transition melting modes
during LPBF of aluminium alloys, with AlSi10Mg as the demonstrated material.

The motivation behind exploring defect-free stable melting across melting modes during LPBF of aluminium alloys is reinforced by the body of literature studying the effect of conduction, transition, and keyhole modes on microstructures, porosity and resulting
₁₃₃₅ mechanical properties of multiple other alloys [167, 196, 195, 197, 251, 120]. Qi et al. [167] observe a lower crack density in the keyhole melting mode for Al7050 but a higher and more uniform nano-hardness across the melt pool in conduction melting mode. Higher vaporization of Zn and Mg was observed in the keyhole melting mode for Al7050. Aggarwal et al. [196] observe a higher hardness, higher elongation, and finer cellular grains in stable
₁₃₄₀ keyhole mode coupons of 316L stainless steel, when compared to conduction mode coupons. Yang et al. [195] report a wider processing window for Ti-6Al-4V in the conduction melting mode and similar tensile properties for conduction and keyhole melting modes, but report a higher elongation for keyhole melting mode coupons. Using micro-scale simulations, Wang and Zou [197] report a more uniform thermal distribution during multi-track
₁₃₄₅ LPBF in the conduction mode when compared to keyhole melting mode, leading to a more uniform microstructure in Ti-6Al-4V. Patel et al. [251] reported reduced effects of adhered partially fused powder particles leading to low side-skin surface roughness for LPBF of Ti-6Al-4V using keyhole melting mode parameters when compared to conduction melting mode parameters. For a top-hat shaped laser beam profile, Tenbrock et al. [120] reported
₁₃₅₀ >99.95% density components in both the conduction and keyhole melting modes for 316L stainless steel with a gradual transition between the melting modes. A comparably uniform thermal distribution during multi-track printing leading to a uniform microstructure is hence a common characteristic observed in the stable conduction melting mode; with the potential for a finer microstructure, improved side-skin surface finish, and improved
₁₃₅₅ tensile properties for the stable keyhole melting mode.

In this work, for the first time, it is shown that a beam defocusing strategy can help in achieving stable conduction mode melting in LPBF of aluminium alloys, particularly for LPBF systems with nominally lower beam focal diameters (<100 µm). Additionally, an appropriate selection of laser power and velocity settings for a focused beam help in
₁₃₆₀ stabilizing melt pool and spatter dynamics in the transition melting mode thereby enabling a potential to obtain density values close to conduction mode densities. This approach helps ease the process parameter optimization efforts for material systems with high reflectivity and high thermal conductivity, especially for the goals of reducing porosity. Additionally, deploying a process parameter strategy resulting in defect-free LPBF of aluminium alloys
₁₃₆₅ leads to a drastic reduction in pore defects, specifically in the subsurface regions, which

are known to be the most important defects affecting fatigue life, as porous defects are the most likely site for crack initiation [252, 253, 254, 255, 256]; an example of a subsurface pore (diameter of ≈0.2 mm) leading to the fatigue crack in AlSi10Mg is shown by Plessis et al. [257]. Lastly, the opportunity to obtain defect-free parts across melting modes during LPBF of aluminium alloys opens up new avenues in terms of tailoring microstructure for application-specific requirements due to significant differences in microstructure reported in literature across melting modes.

4.3   Materials and Methods

A widely studied aluminium alloy, AlSi10Mg, was selected for demonstrating the theoretical concepts in this work. AlSi10Mg cubes of side-length 10 mm (for microstructure evaluation) and cylinders of diameter 5 mm and height 9 mm were printed on the reduced build volume (RBV) of a modulated LPBF system (AM 400, Renishaw, UK). Six sets of processing parameters, shown in Table 4.1, were investigated in this work, which were planned based on melting mode predictions from previous work [10]. For the AM 400 system, the beam spot radius at the focal point is given by 35 µm, and the wavelength of the laser beam used is $\lambda = 1070$ nm. A focused beam with the beam spot focused on the powder layer was used for samples C, D, E, and F. For samples A and B, the laser beam was defocused to a distance, z = 4.2 mm, above the build plate, to obtain a divergent beam. This leads to a beam spot radius (r) of 54 µm, obtained from the equation for a Gaussian distribution of a laser beam given by Equation 3.37.

Since the Renishaw AM 400 has a beam spot radius of 35 µm at the focal plane, a transition or keyhole melting mode is hence expected, unless the beam is defocused. The defocusing of the beam was kept to a position above the build plate to create a divergent beam (to an effective beam spot radius of 54 µm) at the laser-material interaction plane, instead of convergent beams obtained by defocusing to positions below the build plate.

The processing parameters listed in Table 4.1 were selected such that sample A and sample B would be expected to lie in the conduction melting mode from previous work on studying melt pools [10], while samples C, D, E, and F would be expected to lie in the transition melting mode. The powders used were plasma atomized AlSi10Mg with a size distribution of 15-63 µm and a D50 of 28 µm, which was used to determine the powder layer thickness value of 30 µm, as the steady state powder layer thickness obtained is effectively larger than the amount by which the build plate drops during each layer [217]. The hatching distance was kept constant at 100 µm for all the samples. The scan order was set such that the hatch volume (core) was scanned first, followed by the border;

the border scans having the same set of processing parameters as the core. Border scans are commonly used in LPBF to improve the dimensional accuracy and surface roughness of LPBF coupons [258]; surface topography optimization was beyond the scope of this present work. The meander scan strategy was used with a 67° rotation between each layer, to reduce residual stresses, anisotropy, surface roughness, and promote lower rates of defect propagation [259, 260]. These benefits a 67° inter-layer rotation could be attributed to the occurrence of an orientation that differs from an already used orientation by less than 10° only after 18 layers [261].

Table 4.1: Processing parameters for AlSi10Mg LPBF part production. The terms effective power and effective velocity are calculated from Equations 3.35 and 3.36 respectively.

Sample code	Power [W]	Point distance [μm]	Exposure time [μm]	Effective power [W]	Effective velocity [mm/s]	Beam radius [μm]	Expected melting mode
A	300	55	60	257	786	54	Conduction
B	350	55	80	311	611	54	Conduction
C	150	55	60	129	786	35	Transition
D	180	55	70	158	688	35	Transition
E	200	55	90	180	550	35	Transition
F	240	55	100	218	500	35	Transition

The AlSi10Mg cylinders were analyzed for porosity characteristics by a 3D X-ray computed tomography (XCT) scanner (ZEISS Xradia 520 Versa) using a 6 μm voxel size. To visualize the defect distribution within each sample, the CT scanned files were analyzed using an image processing software (Dragonfly 3.0, Object Research Systems Inc., Montreal, QC). The AlSi10Mg cubes were sectioned, polished, and etched with diluted phosphoric acid (9 g phosphoric acid and 100 ml H_2O) for studying their microstructure. Micrographs were taken at various locations including the top edge and core of the cubes. Five different melt pools were analyzed for each cube to obtain the melt pool depth and half width measurements as shown in Figure 4.1.

4.4 Results and discussion

In this work, laser beam defocusing was studied primarily with the intention of achieving stable conduction mode LPBF process parameters for AlSi10Mg. Based on literature
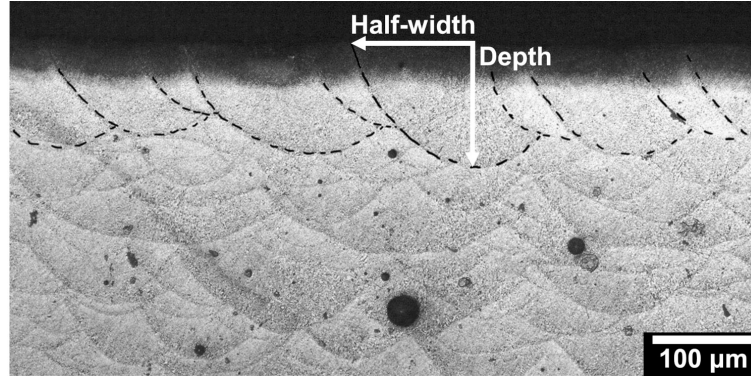
Figure 4.1: Measurement of the melt pool depth and half-width for one of the melt pools from sample E.

discussed in section 4.4.1, it is observed that during the LPBF of AlSi10Mg, conduction mode melting is not reported for beam spot radiuses below 50 µm. Since the Renishaw AM 400 has a beam spot radius of 35 µm at the focal plane, a transition or keyhole melting mode is hence expected, unless the beam is defocused. The defocusing of the beam was kept to a position above the build plate to create a divergent beam (to an effective beam spot radius of 54 µm) at the laser-material interaction plane, instead of convergent beams obtained by defocusing to positions below the build plate.

4.4.1 Defect space outcomes across melting modes based on micrographs

The effect of the divergent beam defocusing strategy is illustrated in Figure 4.2, wherein numerous keyhole type defects are observed for the samples built with the focused beam with a beam spot radius of 35 µm, whereas a conduction mode type microstructure with a few tiny defects are observed for the samples built with the divergent beam, attributed to hydrogen induced defects in aluminium alloys as reported by Weingarten et al. [158].

The defocusing strategy is particularly effective for systems with lower beam spot radiuses (<50 µm) [246, 247], wherein melt pool aspect ratios (melt pool depth/width) of greater than 0.5 have been reported for all ranges of powers of 100 – 400 W for aluminium alloys, which is considered to be the primary process variable driving the threshold between conduction and transition/keyhole melting modes. For AlSi10Mg melt pool datasets reported with systems such as EOS M290 with a higher beam spot radius of 50 µm at the focal point, most melt pools had an aspect ratio lesser than 0.5, except for power settings
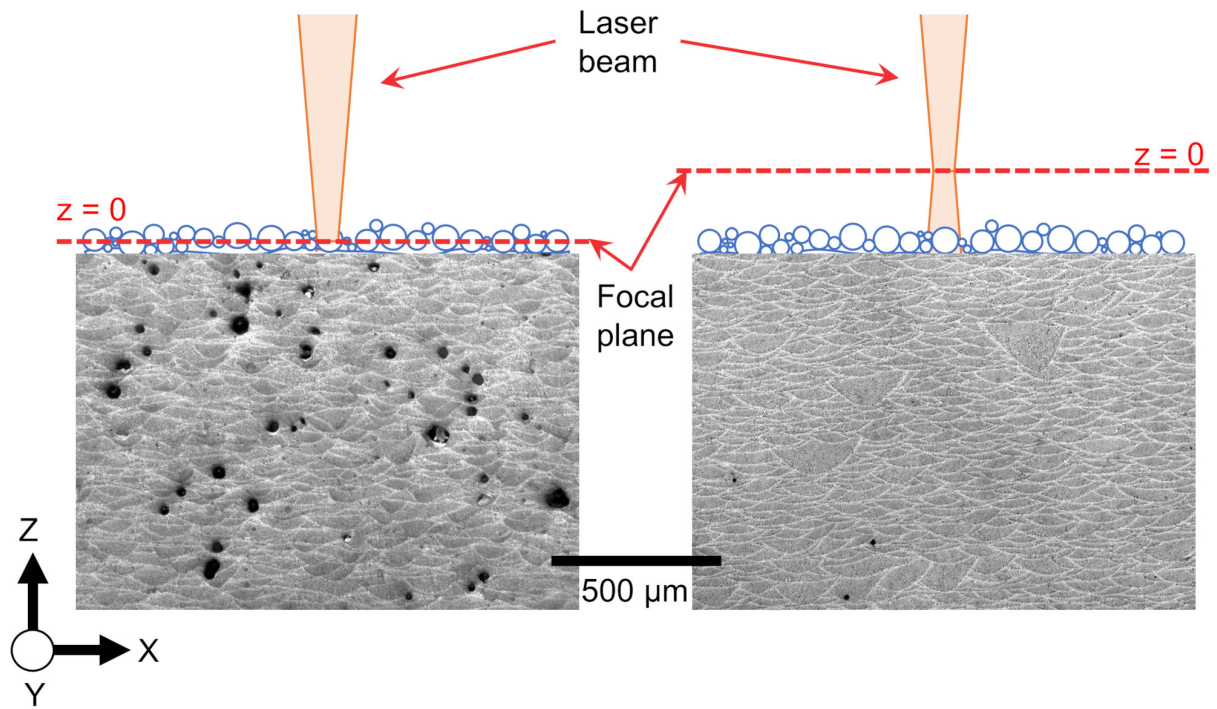
Figure 4.2: Typical microstructure of AlSi10Mg obtained with the focused beam (left, sample E) and with the defocused beam (right, sample B). The focused laser beam microstructure consists of numerous defects related to excessive vaporization in the transition/keyhole modes, while a few hydrogen solubility related defects are observed by using a diverging defocused beam.

above 275 W [262, 263]. Divergent beams help in reducing keyhole pores by reducing the effective beam power density as the melt pool formation progresses and have been used successfully in the laser welding of aluminium alloys [245] and LPBF of 316L stainless steel [250]. The cause of this could be associated to a deviance of the beam profile from a Gaussian distribution to resemble more closely a top-hat distribution during the divergence of the beam as shown by Nie et al. [264]. Assuming this deviance of the beam profile, the threshold power required for surface vaporization (commonly assumed to be the threshold between the conduction and transition modes) would be higher for divergent beams when compared to focused beams, when the other variables are kept constant. This assumption is based on the temperature prediction models proposed by Graf et al. [229] for predicting the threshold of surface vaporization for Gaussian and top-hat beam profiles for materials with high thermal conductivity and low surface tension such as aluminium and copper alloys. Graf et al. [229] show that in a Gaussian beam, when all other variables are held constant, lesser power is needed for initiating surface vaporization due to the higher peak intensity in Gaussian beam profiles, when compared to the top-hat distribution. To better understand the effect of the melt pool morphologies on porosity, measurements of the melt depth, widths, and the melt pool aspect ratios from the six samples are given in Table 4.2.

Table 4.2: Melt pool depths, widths, aspect ratios and inferred absorptivity values obtained for the LPBF process parameter combinations in Table 4.1. Avg: Average, Std Dev: standard deviation.

Sample code	Depth (µm)		Width (µm)		Melt pool aspect ratio	Inferred absorptivity	
	Avg	Std Dev	Avg	Std Dev	Avg depth/width	Avg	Variation
A	47.04	7.99	157.56	21.25	0.30	0.20	0.03
B	53.25	6.89	165.78	17.27	0.32	0.17	0.02
C	56.62	14.36	143.01	12.77	0.4	0.59	0.14
D	53.63	10.58	136.05	17.05	0.39	0.43	0.08
E	80.44	20.71	187.49	58.54	0.43	0.51	0.14
F	81.67	3.95	170.00	35.14	0.48	0.41	0.03

As observed in Table 4.2, samples A and B have a melt pool aspect ratios of ≈0.3 whereas samples C, D, E, and F have melt pool aspect ratios of ≈0.4 and higher. By these melt pool aspect ratios, based on existing literature, it would mean that all the six sample types would be expected to lie in the conduction melting mode; however, the optical
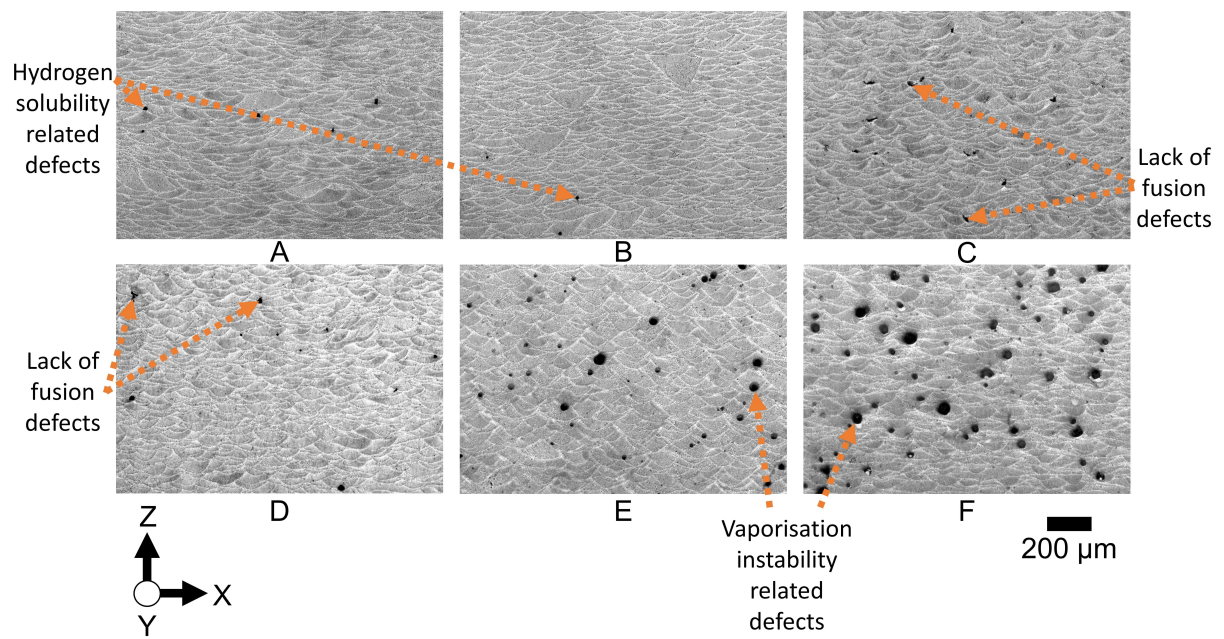
Figure 4.3: Optical micrographs of the samples A to F along the build direction. The different types of defects observed are pointed out by orange arrows.

micrographs of the six samples along the build direction (Z-axis) shows otherwise. As shown in Figure 4.3, the optical micrographs of samples E and F, in particular, reveal numerous rounded defects representative of keyhole instabilities implying that these sets of processing parameters likely lie in the transition/keyhole melting mode. Hence, a melt pool aspect ratio of 0.4 might be likely more representative of the threshold between the conduction and transition/keyhole melting modes for aluminium alloys. Samples C and D seem to have a similar porosity level to samples A and B in the microstructural images shown in Figure 4.3, but there are qualitative differences between the melt pool morphologies. The qualitative differences between the melt pool morphologies of samples C and D with respect to samples A and B are apparent by virtue of more variability in the melt pool layer-by-layer organization. The quantitative differences between the melt pool morphologies of samples A and B when compared to the rest are better represented in Table 4.2 by the lower standard deviations of their melt pool depths when compared to samples C, D, and E. Additionally, samples C and D seem to have melt pool depths comparable to samples A and B even when the laser power settings used for them were close to half, which would imply much lower input energy densities. This is due to the onset of vaporization in these samples due to the focused beam, as predicted in the normalized processing diagram in Figure 4.4. E^* and v^* in Figure 4.4 are given by Equations 3.4 and 3.2 respectively.

In Equation 3.4, E^* is the dimensionless heat input, A is laser absorptivity, P_eff is the effective laser power [W], l_t is the powder layer thickness [m], λ is the thermal conductivity [W/(mK)], T_m is the melting temperature [K], and T_0 is the initial (or powder bed) temperature [K], taken as 293 K. In Equation (3), v^* is the dimensionless beam velocity, v is the laser beam velocity [m/s], r_b is the beam radius used [m], and α is the thermal diffusivity [m^2/s]. The material properties used for Equations 3.4 and 3.2 are taken at the solidus temperature from [215] and are given in Table 4.3. For a modulated LPBF system used in the present study, the effective laser power, P_{eff}, and the effective beam velocity, v, are obtained from [10] and are given by Equations 3.35 and 3.36 respectively.

In Equation 3.35, P is the actual laser power used in the modulated LPBF system, t_e is the time when the laser is acting on the material (exposure time) [s] and t_e is the time when the laser is turned off and is repositioning to the next exposure point (drill delay time) [s], taken as 10 μs for the Renishaw AM 400 system. In Equation 3.36, p_d is the distance between two consecutive laser exposure points (point distance) [m].

The threshold between the conduction, transition, and keyhole melting modes during LPBF of AlSi10Mg in Figure 4.4 are given by contours of the dimensionless peak temperature, T_p^*, based on previous work [10]. The dimension peak temperature term, T_p^*, is given by Equation 3.31.
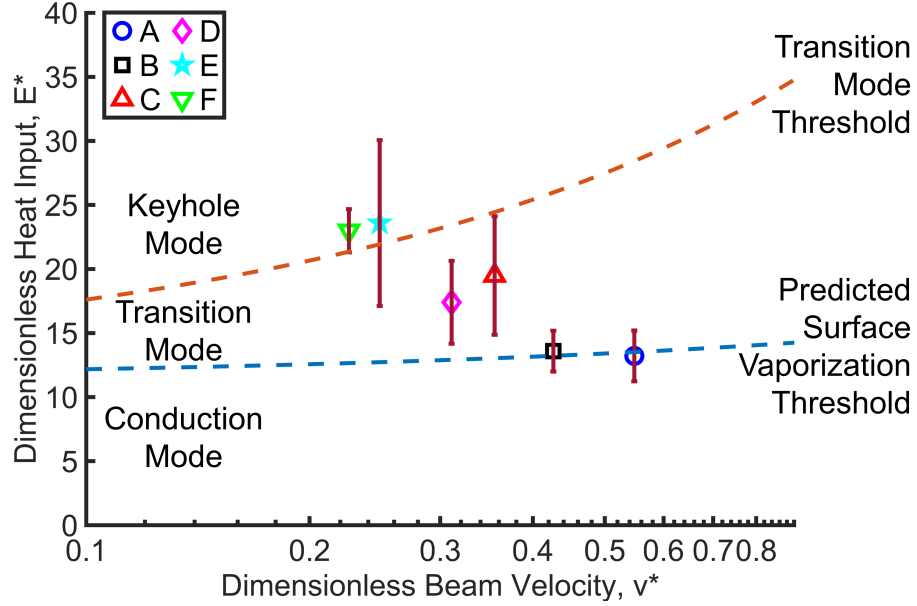
Figure 4.4: Normalized processing diagram for the six AlSi10Mg sample types used in this study.

Table 4.3: Thermo-physical properties of AlSi10Mg taken at the solidus temperature.

Properties	Material(AlSi10Mg)
Density, ρ [kg/m^3]	2670
Thermal conductivity, λ [W/(mK)]	113
Specific heat capacity, C_p [J/(kgK)]	565.29
Solidus temperature, T_s [K]	831
Liquidus temperature, T_m [K]	867
Vaporization temperature, T_v [K]	2740
Total latent heat (fusion and vaporization), H [J/kg]	10943000

In Equation 3.31, T_p is the peak temperature under consideration which is considered as the vaporization temperature (boiling point) of a given material. The terms z^* is dimensionless depth given the ratio of the dimension along the depth of a melt pool, z, and the beam spot radius, r_b, in Equation 3.28, which was first defined by Ion et al. [139]. The term z_0^* is the dimensionless distance of the apparent heat source above the surface of the melt pool, which is a function of v^* as given by Equation 3.34. The detailed derivation for T_p^* and associated terms is provided in previous work [10].

The threshold between the conduction and transition melting modes for AlSi10Mg in given by the temperature contour for $T_p^* = 3.16$ at $z^* = 0$ [10]. The value 3.16 is the ratio of the boiling point of aluminum and its melting point. The term $z^* = 0$ corresponds to surface vaporization and the contour in Figure 4.4 is thereby named as predicted surface vaporization threshold for LPBF of AlSi10Mg (or the threshold between the conduction and transition melting modes). Similarly, the threshold between the transition and keyhole melting modes for AlSi10Mg in given by the temperature contour for $T_p^* = 3.16$ at $z^* = 0.5$ [10]. The term $z^* = 0.5$ corresponds corresponds to a vaporization depth, $d_v = 0.5r_b$, i.e. a vaporization depth equal to half the beam radius used. The temperature contour for for $T_p^* = 3.16$ at $z^* = 0.5$ corresponds to the transition mode threshold given in Figure 4.4 [10]. The absorptivity values used for Equation 3.4 and given by the inferred absorptivity columns in Table 4.2 were obtained inversely by comparing the predicted melt pool depths with experimental measurements. The average measured melt pool depth was used to inversely calculate the average inferred absorptivity, while the highest value within the confidence interval of the melt pool depth was used to calculate the variation in inferred absorptivity. The values for the error bars for E^* in Figure 4.4 are calculated by substituting the variation in inferred absorptivity into the A term in Equation 3.4.

Recent attempts by Gan et al. [82] to develop universal scaling laws for keyhole porosity in LPBF make use of an exponential absorptivity scaling laws for titanium, ferrous, and aluminium alloys. The absorptivty law used by Gan et al. [82] was derived by Ye et al. [7] using in-situ micro-calorimetry measurements of absorptivity during LPBF of low reflectivity titanium, ferrous, and nickel alloys. While Gan et al. [82] use simulations to recommend the same scaling law for high reflectivity aluminium alloys as well, the recommendations by Gan et al. [82] do not hold true for aluminium alloys when applied to the melt pool datasets in this work as well as previous work [10, 247]. The inferred absorptivity calculations from melt pool data, as proposed in this work follow the experimentally measured values of absorptivity by Trapp et al. [9] much more closely. Further work in need on deriving absorptivity scaling laws for high reflectivity aluminium and copper alloys, as the first attempt at absorptivity measurements for copper also suggest a significant difference when compared to low reflectivity materials [265].

The temperature prediction model has some limitations such as assumptions of a 2D heat source, temperature independent material properties, oversimplification of powder layer thickness effects, and ignorance of heat loss by refraction in the vapour plume [10], which would contribute to the uncertainty margins in the identified surface vaporization threshold. Additionally, the latent heat of fusion, thermo-capillary phenomena (Marangoni effect) and varying laser power absorptivity due to the its angle of incidence (Brewster effect) are not incorporated into this modelling approach which could add to uncertainties [266, 267]. The use of standard deviation bars for E^* as inferred inversely via the melt pool datasets are also a reflection of some of the limitations in experimentally validating the precise location of each experimental point in the process map.

The onset of surface vaporization brings about a more pronounced change in laser absorption and thereby in melt pool behaviour for high reflectivity materials such as aluminium alloys. This is because the onset of surface vaporization adds to additional absorptivity (A) of the laser beam in the material that is equal to $1 - R^N$, where R is the reflectivity a material, and N is the number of reflections occurring in the vaporized cavity of the melt pool [229]. Materials such as aluminium alloys with higher reflectivity values compared to titanium, ferrous, and nickel alloys would thereby be expected to have differences in melt pool behaviour (melt pool dynamics and thereby solidified melt pool geometry) after the onset of surface of vaporization is crossed. This points towards the differences in absorptivity values that were obtained for samples A to F from the effective absorptivity obtained through the depths reported in Table 4.2, and the temperature prediction model proposed in [10]. The absorptivities values obtained for samples A and B are between 0.15 and 0.2, whereas samples C, D, E, and F have absorptivity values ranging from 0.4 to 0.7, which corresponds to the conduction and transition mode absorptivities for aluminium, based on in situ measurements of laser absorptivity during LPBF [9, 203].

In terms of porous defects, samples A and B have a small population of defects as shown in Figure 4.3, with the smallest defects being rounded and commonly attributed to hydrogen-induced defects observed in conduction LPBF of AlSi10Mg; this is also observed by Weingarten et al. [158]. The presence of moisture on the powder surfaces, is one of the main causes attributed to the reduction of hydrogen solubility in aluminium alloys during the resolidification of liquid aluminium [5]. For samples E and F, additional larger defects were observed as seen in Figure 4.3, particularly at the bottom of melt pool, close to the melt pool boundaries. The major source of these defects is expected due to the excessive vaporization of metal expected in transition and keyhole mode melt pools [10]. In conduction mode LPBF of aluminium, where vaporization is not expected, the measured absorptivity values for LPBF were ≈0.15 for a beam spot diameter of 60 ± 5 µm [9, 203]. However, the high reflectivity in such materials would be expected to aid

the overall absorptance significantly once vaporization initiates due to increased number of reflections of the laser beam inside the vaporized region, as observed for aluminium discs in transition mode [9]. High-speed and high-resolution X-ray imaging of two aluminium alloys (AlSi10Mg and Al6061) during LPBF has shown that fluctuations in their vaporized areas of melt pools lead to instabilities and thereby to the formation of porous defects, even with a shallow depth of the vaporization regions in transition/keyhole mode melting due to an increased number of laser beam reflections in the melt pool [268]. A few of the excessive vaporization-related defects are also observed in sample D, as pointed by the arrows in Figure 4.3.

4.4.2   Defect space outcomes across melting modes based on XCT

To further understand the effects of transition and conduction mode on defect formation in LPBF of AlSi10Mg, a visualization of the three-dimensional porous defect space (obtained by XCT) for all six samples are shown in Figure 4.5. Segmented defects with sizes below 5 interconnected voxels (voxel edge dimension is 6 µm) have been truncated out from the defect visualization and defect aspect ratio assessments since it is not possible to accurately separate features below this size due to instrument noise. The defect aspect ratio parameter is the ratio between the minimum and the maximum Feret diameter, where the minimum Feret diameter is the shortest length of a given feature, while the maximum Feret diameter is the longest span of a given feature, as described in [269, 270]. Defects with aspect ratios above 0.7 were considered as rounded defects in Figures 4.5 and 4.6. For calculating the density values shown in Figure 4.5, all the defects (defects with a voxel size of 1 or more) was considered. The density values are approximations of the true density and a relative assessment of part quality due to the voxel size detection limit. To visualize the locations of the defects, an orthographic projection along the build plate (XY) plane of all the porous defect space for each sample is shown in Figure 4.6.

In Figures 4.5 and 4.6, it can be observed that sample A has few irregular defects; these are lack-of-fusion defects, which are attributed to the slightly lower melt pool depths as noted in Table 2 [217]. There are numerous causes for lack-of-fusion defects in conduction mode LPBF such as, but not limited to incomplete melting of powder particles within one-layer, incomplete re-melting of material ejecta from previous layers or from neighbouring scan tracks, or incomplete re-melting of irregular surface topographies from previous layers. Such defects can propagate across subsequent layers, resulting in irregularly shaped lack-of-fusion defects [86] that can be observed in Figures 4.5 and 4.6.

The defect population in Samples C and D spans both irregularly shaped and rounded (near spherical) defects as seen in Figures 4.5 and 4.6, with a dominance of irregularly
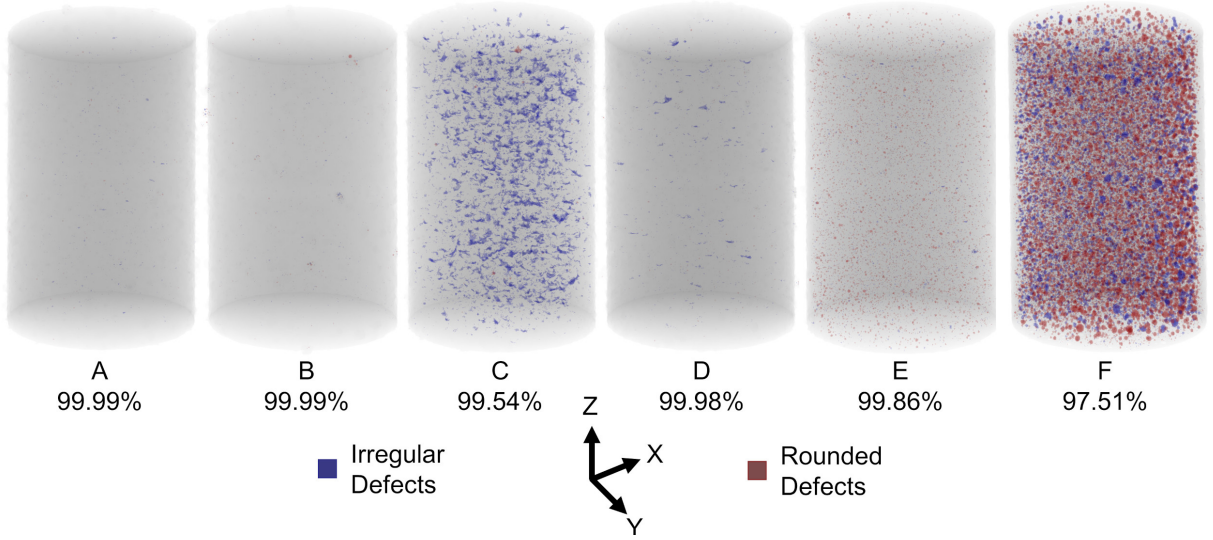
Figure 4.5: A three-dimensional visualization of the porous defect (above 4 voxels) space along the build direction (Z) from the XCT data of the six sample types, along with the density values obtained based on the XCT data.

shaped defects. While both samples C and D have similar melt pool dimensions as observed in Table 4.2, there is a significant difference in the density and frequency of irregularly shaped defects as visible in Figures 4.5. The main cause for the lower density of sample C when compared to sample D could likely be associated to the inefficient laser expulsion of metal spatter as predicted by the analytical relationship derived by Khairallah et al. [169] in Equation 4.1 and visualised for LPBF of AlSi10Mg at a beam diameter of 70 µm for the Renishaw AM 400 system in Figure 4.7. Khairallah et al. [169] used a combination of high-fidelity simulations and high-speed X-ray imaging of LPBF to derive a criteria for stabilizing melt pool dynamics and minimizing defects. They derived an analytical relationship to help identify combinations of laser power and velocity that can help in preventing large metal spatter from blocking the centre of a Gaussian laser beam. In Equation 4.1, H is the addition of the latent heat of fusion and vaporization, given by total latent heat in Table 4.3 and A_m the laser absorptivity of the melted surface of a given material which is assumed 0.185 (average of the conduction mode absorptivities in Table 4.2). The term r_s in Equation 4.1 is the radius of a spatter particle under consideration.

$$P_{threshold} = \frac{\pi \rho r_s^3 (C_p(T_v - T_0) + H)}{3 A_m r_b} v \tag{4.1}$$

76
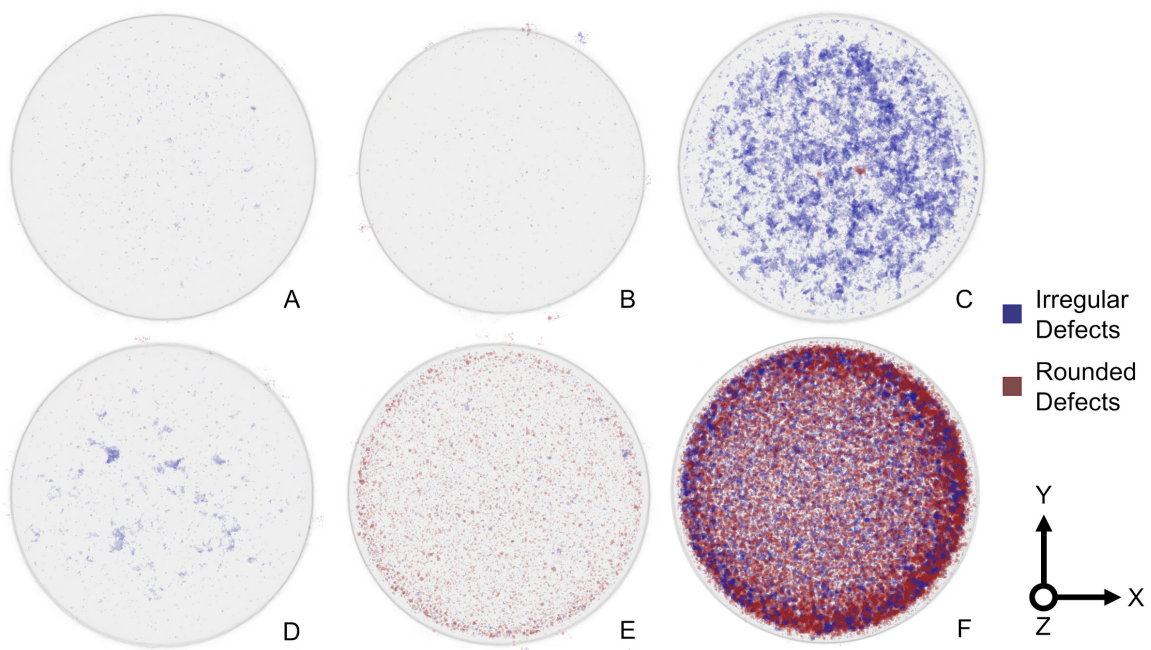
Figure 4.6: An orthographic projection of the porous defect (above 4 voxels) space along the build plate (XY) plane from the XCT data of the six sample types.

$$P_{threshold} = 227 * v \tag{4.2}$$

Khairallah et al. [169] observe that a spatter particle that is as large as the laser beam is capable of blocking the central high intensity region of a Gaussian laser beam, leading to sudden drop in melt pool depth. The rapid cooling caused by the sudden drop in melt pool depth thereby leads to defects as also observed by Martin et al. [81]. The radius of the spatter particle (r_s) used to derive the spatter expulsion threshold through Equation 4.1 for Figure 4.7 is hence assumed to be the same as the beam radius (35 µm) used for the samples C, D, E, and F. The exact relationship used for Figure 4.7 is given by Equation 4.2. Metal vaporization during LPBF was observed to be the largest driver of spatter issues by Khairallah et al. [169] and hence samples A and B were not plotted in Figure 4.4 as they would not be affected by spatter related challenges, as predicted by Figure 4.4. Additionally, powder ejecta [156] and melt pool splatter caused by the breaking up of elongated molten pool regions near the side and real walls of the vaporized region in transition and keyhole melting modes also contribute towards defect formation in samples C, D, E, and F by adding to the roughness of a given layer [85]. Additionally, powder denudation [108, 157] also contribute towards the surface roughness of a given layer, thereby deteriorating the wetting behaviour of the following layers causing melt pool instabilities and increasing the possibility of irregularly shaped defects as observed in the defect space visualization for samples C, D, E, and F [271].

There are additional reasons for the defects observed in the transition mode samples C and D. Although the average melt pool depth obtained for samples C and D is slightly higher than sample A, the higher standard deviation in melt pool depths observed for samples C and D (Table 4.2) can lead to random regions where under-melting may occur if the melt pool is too shallow leading to irregularly shaped lack-of-fusion defects, or random regions where the process transitions into the keyhole melting mode leading to keyhole defects (sample D in Figure 4.3). The average melt pool widths of samples C and D are also lower when compared to samples A and B, leading the possibility of lack-of-fusion defects caused by insufficient stitching of melt pools between hatches (hatch distance 100 µm) in a given layer. Additionally, as per Figure 4.4, it is predicted that surface vaporization has taken place in samples C, D, E, and F leading to the possibility of defects related to the melt pool instabilities during transition melting mode in LPBF caused by the interplay between the drag force induced by the melt flow, the thermo-capillary force cause by the surface temperature gradients, and the recoil pressure introduced by the onset of material vaporization [85, 224, 81]. The defects obtained due to melt pool instabilities are known to have both rounded and irregularly-shaped morphologies [10, 272]. In a comparative study between the laser welding of an aluminium alloy and a ferrous alloy, the higher
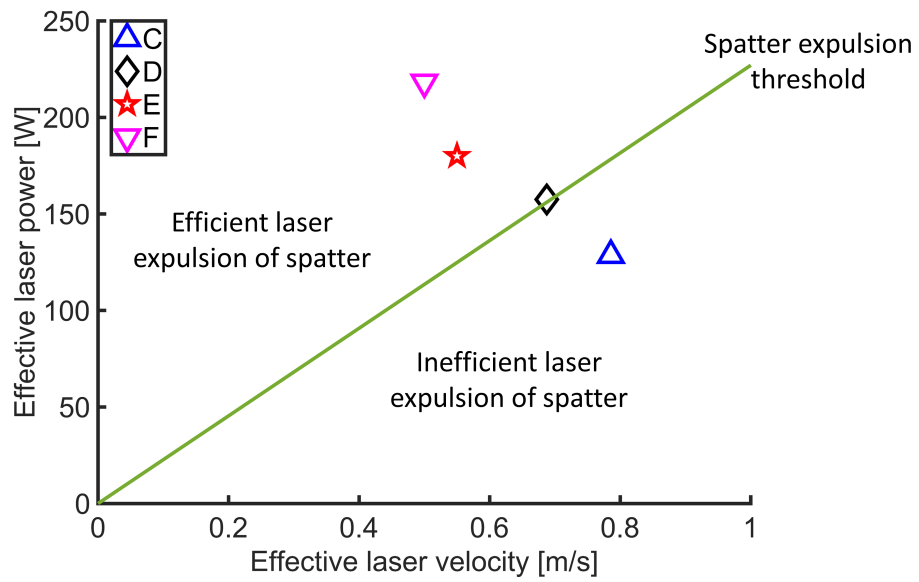
Figure 4.7: Spatter expulsion window based on effective laser power and velocity for LPBF of AlSi10Mg using a focused beam (beam radius = 35 µm) on the Renishaw AM 400 system. The expulsion threshold defines a power/velocity threshold that divides the plot into 2 regions depending on whether spatter of the same size as the beam radius can be expelled efficiently or not.

frequency of vaporized region collapse for aluminium alloys has been associated to the lower surface tension and viscosity of molten aluminium along with the presence of volatile magnesium which vaporizes a temperature much lower than that of aluminium [273]. These observations are in line with the hypothesis proposed by Tenbrock et al. [120], wherein the importance of keyholes as a quasi-black body might be more pronounced for materials with higher reflectivity (e.g. aluminium and copper alloys) when compared to titanium, ferrous, and nickel alloys.

Samples E and F are predicted to lie in the keyhole melting mode by the processing diagram shown in Figure 4.4. In the keyhole melting mode, vaporization related instabilities inside the melt pool would be expected to play a dominant role in the formation of rounded porous defects, as observed in Figures 4.5 and 4.6. To confirm this prediction, Figure 4.8 shows plots of defect aspect ratios of the defects versus frequency of defects and percentage of defect volume. The term frequency herein means the number of defects within a given sample identified by XCT. The aspect ratio data of the defects in Figure 4.8 and the volume data in Figure 4.9 is stored in 50 equally sized bins using MATLAB's built-in 'histcounts' function. A moving average of the frequency data with 5 nearest neighbours is then calculated using MATLAB's built-in 'movmean' which alongside the mid-point of each bin is used to interpolate the curves in Figure 4.8a and 4.9 by using MATLAB's built-in 'plot' function. Figure 4.8b was similarly obtained by creating a moving average of the volume data with respect to aspect ratio of the defects obtained from the XCT data.

The defect aspect ratio versus frequency plot in Figure 4.8a shows some indication to the preference of rounded defects in samples E and F, but the aspect ratio versus percentage of defect volume plot provides a better understanding of such behaviour. Since the curves for samples E and F lean towards a higher aspect ratio in the plot against percentage of defect volume in Figure 4.8b, it implies that most of the defects in samples E and F have a rounded morphology especially when compared to the other four samples. The rare occurrence of irregularly shaped defects can be associated to the higher average melt pool depths reported in Table 4.2, which are above two times the powder layer thickness used (30 µm). Typically, a melt pool depth of about 2 times (or more) the layer thickness is targeted in LPBF to avoid the possibility of lack-of-fusion defects [217].

Figure 4.6 shows a higher concentration of rounded porous defects near the side walls of the cylinders for samples E and F that can be related to the rapid formation and collapse of deep vaporized regions due to the laser beam velocity at the turn points which occurs at the edges of a given layer in LPBF, thereby trapping the atmospheric gas in the solidified part [81]. A plot of defect volume versus frequency in Figure 4.9 reveals that most of the defects in samples E and F still belong to the lower volume regions of below 0.0001 mm^3. However, defects closer to the side wall of the cylinders would still be expected to impact
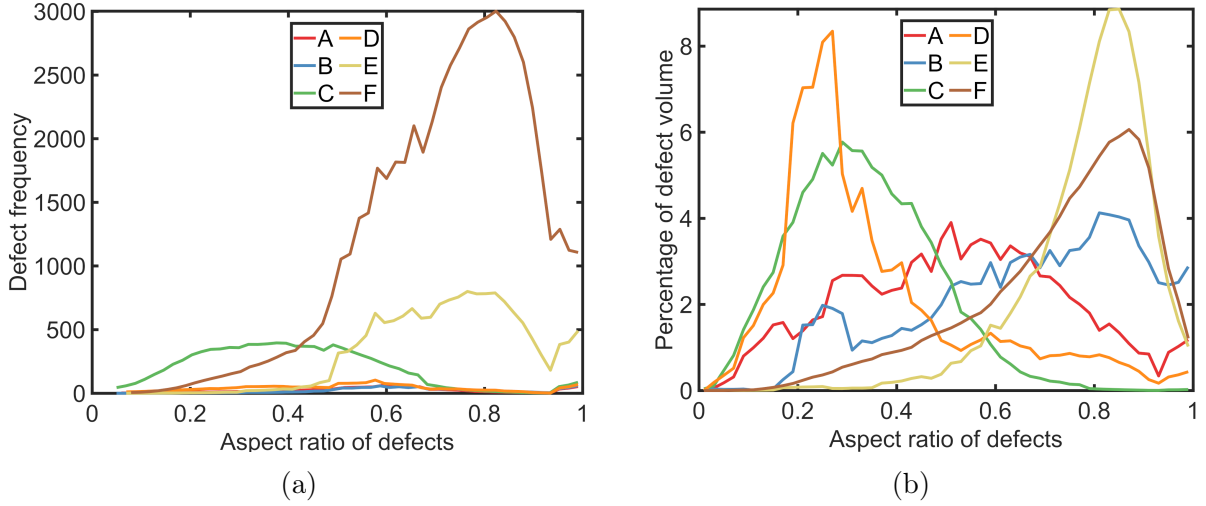
Figure 4.8: Aspect ratio of defects versus frequency of defects (a), and aspect ratio of defects versus percentage of defect volume (b) from the XCT data for the six samples.

its fatigue life, since the larger subsurface defects are the biggest factor impacting a parts fatigue life. The largest defect in sample F has a volume of 0.0053 mm^3. If this largest defect is assumed to be spherical, we would get a defect diameter of 0.22 mm which is close to the defects diameter of $\approx$0.2 mm that led to the fatigue crack initiation in AlSi10Mg as shown by Plessis et al. [257].

Samples A and B which are predicted to lie below the surface vaporization threshold seem to have almost no subsurface defects with the sporadic occurrence of small defects typical to LPBF caused by random process factors or systematic machine biases [10]. Since no particular pattern is observed in the defect space for samples A and B from Figrue 4.3, Figure 4.5, Figure 4.6, Figure 4.8, and Figure 4.9, the process parameter combinations involving the use of a divergent beam for samples A and B might be best suited for LPBF aluminium components for fatigue applications, particularly for systems with a lower beam spot radius at the focal point.

Sample D is another example of a process parameter combination during transition mode LPBF of aluminium alloys that leads to near fully dense parts with a few sporadic defects. The use of simulations in this work shows that the combination of process parameters chosen for sample D allows for an efficient expulsion of laser spatter thereby leading to stabilized molten pool dynamics when compared to samples C, E, and F. The process parameter combination used for sample D might be best suited for the potential to obtained

81
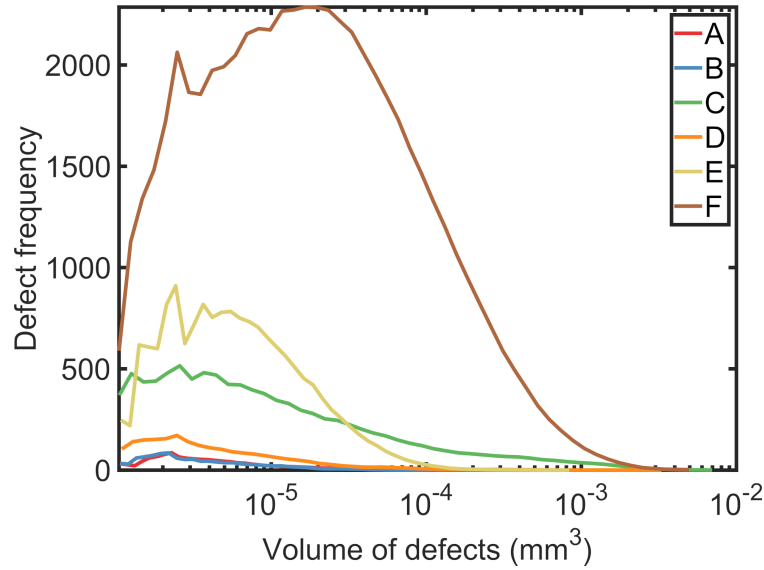
Figure 4.9: Volume of defects versus frequency of defects from the XCT data for the six samples.

a finer microstructure, improved side-skin surface finish, and improved tensile properties as has been shown in LPBF literature [167, 196, 195, 197, 251].

Overall, when observing the melt pool morphology and porous defect characteristics across the melting modes in conduction (samples A and B), transition (samples C and D) and keyhole (samples E and F), the benefit of deploying divergent beams in materials with a high reflectivity and high thermal conductivity becomes apparent. For these material systems, the use of a divergent beam as an energy source results in a more stable melt pool morphology, lower occurrence of porous defects in the core and sub-surface regions, and overall lower porous defect volumes. Furthermore, for such approaches, the hatch spacing, and power levels can be further optimized to minimize lack-of fusion random defects. For this class of material systems, while the use of a focused beam increases the challenging of finding stable melting process parameter combinations, the use of processing diagrams as proposed in this work alongside models for predicting the efficient expulsion of laser spatter can help identify stable melt pool morphologies, similar to the ones with divergent laser beams.

82

4.5 Conclusions

Normalized processing diagrams are constructed in this work for the goals of accelerated ₁₇₃₀ process parameter optimization for high reflectivity aluminium alloys. The key findings from simulations and experiments are summarized below:

1. For LPBF systems with nominal focal diameters <100 µm, divergent beams help in avoiding keyhole defects by reducing the effective beam power density as the melt pool formation progresses, thereby leading to parts with densities of over 99.98%, with ₁₇₃₅ close to no porous defects in the subsurface regions, by conduction mode melting.

2. Stabilising melt pool and spatter dynamics in the transition melting mode by using an appropriate laser power and velocity combination can help in minimizing defects and obtaining densities close to 99.98%, similar to conduction mode densities.

3. A melt pool aspect ratio (ratio of depth to width) of ≈0.4 is observed to be the ₁₇₄₀ threshold between conduction and transition/keyhole mode melt pools in aluminium alloys, which differs from the conventionally assumed melt pool aspect ratio of 0.5.

4. The inferred absorptivity values for conduction mode melt pools are between 0.15-2 while absorptivities of 0.4-0.7 are inferred for transition and keyhole mode melt pools, pointing to the significant differences in laser absorptivity (up to 50%) following the ₁₇₄₅ onset of surface vaporization in aluminium alloys, when compared to titanium, nickel, and ferrous alloys, due to its higher reflectivity. Further work is needed on in-situ measurements of laser absorptivity for aluminium and copper alloys to derive scaling laws specific to this challenging class of high reflectivity materials.

5. In general, a higher standard deviation was observed in the melt pool depths for the ₁₇₅₀ transition mode (10-15 µm) and keyhole mode (4-21 µm) melt pools, when compared to the conduction mode (6-8 µm) melt pools. The predicted absence of vaporization in conduction mode melt pools could be the cause for the relatively stable melting behaviour, when compared to transition and keyhole mode melt pools.

The application of the methods proposed in this work can help to quickly identify stable ₁₇₅₅ LPBF processing parameters for high-reflectivity aluminium alloys. The presence of close to no defects even near the boundaries of LPBF components helps increase the confidence of the process for load bearing and mission critical applications in particular. The fundamental understanding of porous defects during LPBF developed in this chapter is used to understanding porous defects during LPBF of Ti-6242Si in Chapter 6 and to make ₁₇₆₀ recommendations for complex Ti and Ti-6Al-4V lattice structures in Appendix A.

Chapter 5

Melting mode driven understanding of side-skin surface characteristics in a workhorse titanium alloy - Ti-6Al-4V

5.1 Preface

Additively manufactured parts produced via LPBF have limitations in their applications due to post-processing requirements caused by high surface roughness. The characteristics of side-skin surfaces are generally assumed to be dominated by adhered powder particles. This chapter aims to analyze and interpret effects of LPBF processing parameters on side-skin surfaces. As such, this work has two sections to investigate the effect of (i) core and (ii) border LPBF parameters on side-skin surface roughness for Ti-6Al-4V. The findings show that there is a robust correlation between both core and border LPBF parameters on side-skin surface morphologies. In terms of core LPBF parameters, an interaction between laser power and beam velocity is shown to influence side-skin surface roughness, resulting in Sa values in the range of 11-26 µm. Additionally, a preliminary investigation into the effect of melting mode phenomena at the border leads to a possibility of obtaining Sa values of <10 µm, with reduced effects of adhered and partially fused powder. This chapter is adapted from a published article [251]. Since the Chapter 3 had changes in the modelling technique leading to a methodology adjustment for obtaining the processing diagrams, figures from Section 5.4 have minor changes, when compared the the published article. These changes, however, do not make an impact on the significant findings and conclusions of this chapter, rather present refinements to the work, which progressed since the publication.

84

5.2 Introduction

Surface topography in LPBF parts can be a limiting factor in the manufacturing of highly complex parts, as it has been shown to influence optical properties, mechanical properties, frictional behaviour, fluid dynamics, and heat transfer [183]. Additionally, the high surface roughness values generally obtained in LPBF parts necessitate the use of post-processing operations such as machining or polishing thereby adding to the processing time and cost [274, 275].

The understanding of process-structure-property relationships is particularly important for titanium alloys such as Ti-6Al-4V. This material is a biocompatible alloy commonly used in load-bearing orthopaedic and dental applications, as it provides the necessary long-term mechanical and chemical attributes required for these applications, when compared to polymeric and ceramic materials [276]. Tuomi et al. [277] classify the application of AM in the medical sector into five major classes – (i) medical aids, orthoses, splints, and prostheses, (ii) tools, instruments, and parts for medical devices, (iii) inert implants, (iv) medical models for pre- and postoperative planning, education, and training, and (v) bio-manufacturing. Of the five classes, the first three classes are where metal AM has the potential to revolutionise the medical sector. However, multiple review papers [276, 277, 278, 279, 280] note the issues resulting from the lack of understanding of the processing-structure-property relationships, particularly for metals, which could inhibit the potential for growth of metal AM in the medical sector. Bose et al. [276] note that surface customization of metallic, ceramic, and polymeric biomaterials using multiple AM technologies, including LPBF, can prevent corrosion, enhance biocompatibility, and improve osseointegration without compromising the bulk material properties. Metal implant surfaces designed with pores and/or with a tailored surface topography have been shown to promote cell growth and thereby enhance the tissue integration and implant fixation, without sacrificing the near net-shape manufacturing ability of the medical implants [276, 281, 282].

Surfaces of LPBF parts can be identified by considering the orientation of the surfaces to the build plate. Chen et al. [258] classify the surfaces into horizontal surfaces (parallel to the LPBF build plate) [283, 284], vertical surfaces (perpendicular to the build plate and known as side-skin) [184], upward facing (up-skin) [178], and downward facing surfaces (down-skin) [178]. The effect of LPBF processing parameters on the up-skin and down-skin surfaces has been investigated in detail for Ti-6Al-4V, Hastelloy X, and AlSi10Mg [258, 283, 178, 181, 285]. However, understanding of the influence of LPBF processing parameters on side-skin surfaces has been limited [183, 184, 182]. Calignano [183] notes that for side-skin (vertical) surfaces in AlSi10Mg produced by LPBF, adherence of a large amount of partially-fused powder particles to the side-skin dictates the surface roughness values

obtained. Li et al. [182] provide an excellent study into the effects of LPBF processing parameters such as laser beam velocity, scanning strategies, and sample orientation on the side-skin surface roughness of LPBF AlSi10Mg samples, but they do not use border (also known as contour) scans in their study, which are commonly used to improve the dimensional accuracy and surface finish of LPBF parts [183, 258, 283, 178, 286]. Abele and Kniepkamp [184] provide a detailed study into the optimization of border LPBF processing parameters to improve the side-skin surface roughness of micro-LPBF (µ-LPBF). They show that increasing line energy density (laser powder/scan speed) actually leads to lower side-skin surface roughness values, as opposed to the recommendation by Chen et al. [258].

In this chapter, the focus is to analyze the effects of both core and border LPBF processing parameters of a commercial LPBF system on side-skin surface roughness, which is the first attempt of its kind in related literature. To this effect, the first step is to perform a design of experiment study using the central composite design and a Box-Behnken design to understand the effects of core LPBF processing parameters on side-skin surface roughness, when the border parameters are kept constant. The second step is to use the findings from the first step to guide the development of a preliminary study to understand the effects of border LPBF processing parameters on side-skin surface roughness when the core parameters are kept constant. In this work, it is observed that there is a robust correlation between the effects of both core and border LPBF processing parameters on side-skin surface roughness and the physics-based approach to parameter optimization of both is essential to achieve low side-skin surface roughness values in LPBF.

5.3   Materials and Methods

5.3.1   General LPBF processing details

A modulated LPBF system (AM 400, Renishaw, UK) was used for manufacturing cylindrical Ti-6Al-4V three-dimensional coupons with a diameter of 5 mm and a height of 8 mm. These cylinders were built on top of supporting structures on a reduced build volume of the system. The supporting structures had a height of 5 mm. For the AM 400 system, the beam spot radius at the focal point is given by 35 µm, which was kept constant for this study. The Ti-6Al-4V powders were of Grade 23, plasma atomized, with a particle size range of 15–45 µm (D10 of 20 µm, D50 of 34 µm, and D90 of 44 µm). A constant powder layer thickness of 30 µm was used for all experiments.

The goal of this work was to study the effects of core (experiment 1) and border (experiment 2) LPBF processing parameters on the side-skin surface topography of the
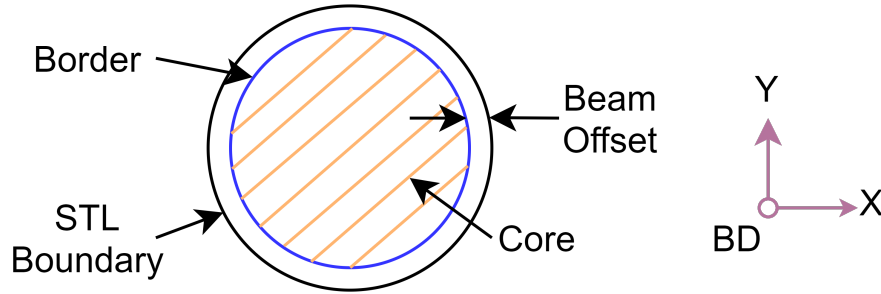
Figure 5.1: Illustration of the meander scanning strategy in the core along with the border scan for improving surface quality at the edges of each layer. The border is located at the edges of each core scanning vector. Beam offset is the distance between the boundary of the STL file and the border scanning vector. The build direction (BD) is perpendicular to the plan of the image.

manufactured coupons. Border scans (as illustrated in Figure 5.1), are used to improve the dimensional accuracy and surface roughness of LPBF coupons [258]. The scan path follows this order: scanning of the core using the meander scanning strategy, followed by a border scan that involves melting of the edge of each layer of a coupon. This scanning strategy of the core scan followed by a border scan is also recommended by Abele and Kniepkamp [184] for improving side-skin surface roughness values in µLPBF. The direction of core meander scanning was rotated by 67° between successive layers. The hatching distance, h_d, in the core used for all the samples was 100 µm, and the border scan was conducted at the edges of the core scan vectors as illustrated in Figure 5.1. To compensate for the dimensional error due to the beam spot diameter, Calignano et al. [283] recommend offsetting the scanning border to the inside of the STL file given by the beam offset parameter illustrated in Figure 5.1. The beam offset parameter was kept constant at 100 µm for all samples.

5.3.2 Normalized processing diagrams and melting mode predictions

For experiment 1 which involves the study of core LPBF processing parameters (parameters detailed in section 5.3.3), normalized processing diagrams are obtained through the methodology described in [10]. The terms E^* and v^* in Figure 5.2 are given by equation 3.4 and 3.2 respectively.
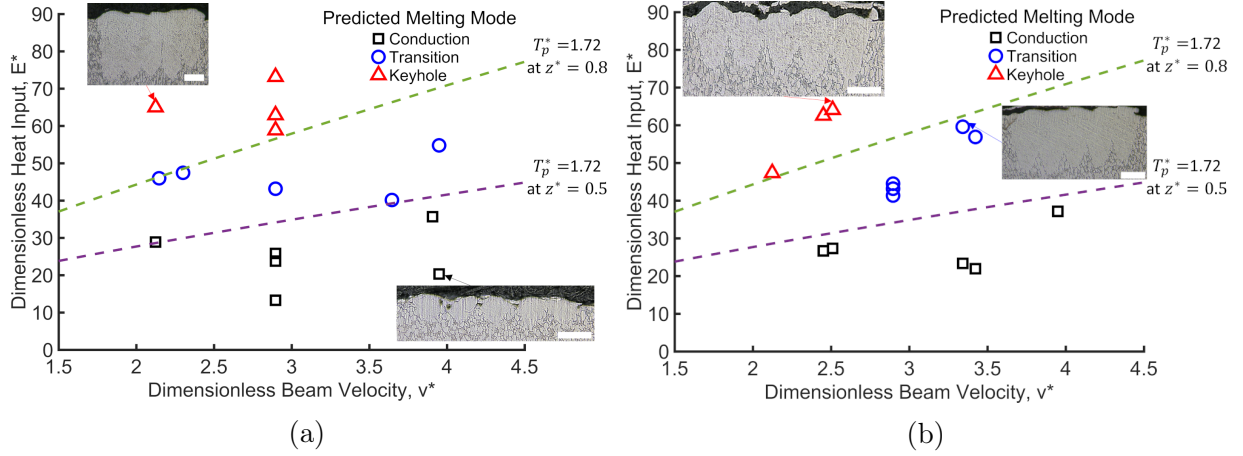
Figure 5.2: Visualization of the normalized processing diagrams and melt pool morphology validation data [10] for the 20 central composite design (CCD) points (a), and for the 15 Box-Behnken design points (b).

Values for the Ti-6Al-4V material constants used for equations 3.4 and 3.2 are taken at the solidus temperature and are given in Table 3.4. For a modulated LPBF system, such as the Renishaw AM 400 used in the present study, the effective laser power, P_{eff}, and the effective beam velocity, v, are given by equations 3.35 and 3.36 respectively. The dimensionless peak temperature, T_p^*, in the melt pool used for predicting the melting mode thresholds in Figure 5.2 is obtained by an analytical temperature prediction model derived in section 3.3.3 and a published paper [10].

The predicted threshold between conduction, transition, and keyhole modes have uncertainties associated with it, particularly due to changes in absorptivity with increasing heat input due to increasing number of reflections in the melt pool, as well as changes in the angle of incidence of the laser beam due to surface irregularities in the melt pool [9, 7, 185]. Additionally, temperature-dependent physical properties, particularly thermal conductivity as discussed by Johnson et al. [287], would have an added effect on the threshold uncertainty, which would be quantified through enhanced models as part of future work. However, since the goal of this work is to study the effects of increasing extent of vaporization, as showcased by the melt pool morphology differences of the melt pool images in Figure 5.2, the processing diagrams provide a useful approximation of the dominating melting mode. This should hold true in particular for the experimental points lying at the extremes of conduction and keyhole modes, which are used for discussing the differences in surface morphologies obtained in this work.

88

5.3.3 Design of experiments

To evaluate the effects of core LPBF processing parameters on side-skin surface roughness (experiment 1), core experimental design levels were selected to span the conduction, transition, and keyhole melting mode regimes as described in [10] and visualized in Figure 5.2. To cover a representative range of conditions with a reduced number of experiments, a rotatable central composite design (CCD) involving three processing variables (power, point distance, and exposure time) was used. The design levels used for the processing parameters are given in Table 5.1. Using 6 center point replicates per design replicate CCD results in a total of 20 parts per design replicate. Two design replicates were printed to obtain a total of 40 cylindrical Ti-6Al-4V parts. The second replicate for the CCD design was printed on a separate build to plate with the locations of the parts randomized to offset the effects of build plate location, build chamber conditions, and powder quality. Additionally, another experiment was designed using the Box-Behnken design with 3 centre points for the same design levels of the three processing variables (laser power, point distance, exposure time) as given in Table 5.1. The Box-Behnken design gives a total of 15 parts, and 1 replicate of each sample was printed on a separate build plate. For experiment 1, the border processing parameters were kept constant, as listed in Table 5.1, which are predicted to lie in conduction mode. Normalized processing diagrams for the CCD design points and Box-Behnken design points are obtained as described in section 5.3.3 and are given in Figure 5.2a and 5.2b respectively.

Table 5.1: Experimental design levels for the central composite design (CCD) and Box-Behnken (BB) design for core process parameters used in experiment 1 and the border parameters which were kept constant for experiment 1. Star points only apply to the central composite design.

Factors	Levels					Border parameters
	Star (-1.68)	Low (-1)	Center (0)	High (+1)	Star (+1.68)	
Laser power (W)	98.8	150	225	300	351	100
Point distance (µm)	48.2	55	65	75	81.8	45
Exposure time (µs)	38.3	45	55	65	71.8	40

For the study involving the effects of the core LPBF processing parameters on side-skin surface roughness (experiment 1), the border processing parameters were kept constant,

as listed in Table 5.1. For the study involving the effects of border LPBF processing parameters on side-skin surface roughness (experiment 2), a constant set of core processing parameters with a laser power of 225 W, a point distance of 65 µm, and an exposure time of 55 µs were used, which lie in the transition mode. This set of core processing parameters is the centre point in the design for both the CCD and Box-Behnken designs which were kept constant for experiment 2. Experiment 2 was designed as a preliminary study for evaluating the effects of conduction and transition mode border parameters on side-skin surface roughness. For experiment 2, two sets of parameters were studied, which are listed in Table 5.2. These parameters were selected based on the findings from experiment 1 to help guide the confirmed hypothesis from experiment 1. The type A set of parameters used for the border are the same as that used in experiment 1 which are predicted to lie in conduction mode. The type B set of parameters used for the border are predicted to lie in transition mode. The type B parameters were chosen to have a higher power setting for observing the effects of transition mode border parameters, and the low beam velocity (500 mm/s) was chosen to reduce the effects of balling, as observed by Abele and Kniepkamp [184] in µLPBF of stainless steel 316L (SS 316L). Three replicates of each type of border parameters were printed, with every replicate manufactured on a separate build plate with the locations of the parts randomised to offset the effects of build plate location, build chamber conditions, and powder quality. In the following section, the microscopy and imaging methods used to analyze the surface roughness features of the LPBF samples as discussed.

Table 5.2: Experimental design levels for the two sets of border processing parameters used in in experiment 2.

Factors	Border parameters	
	Type A	Type B
Laser power (W)	100	150
Point distance (µm)	45	30
Exposure time (µs)	40	50

5.3.4 Microscopy and imaging methods

The side-skin surface topography of the cylindrical parts is characterised via laser confocal microscopy (Keyence VK-X250). The image processing and roughness measurements are

completed using the microscopes processing software (Keyence VK-H1XME). A scanning area of approximately 1400x1000 µm² was scanned for every part, using a vertical z-axis resolution of 1 µm. The surface roughness metrics used in this study are Sa and Sz. Sa is the arithmetical mean height of a surface area which is defined as the absolute value of the height from the average surface. Sz is the sum of the largest peak height value and the largest pit depth value within a scanned area of a given surface. Surface correction for curvature is employed for all scans, since the side surface is curved. The roughness is measured near the middle of the sample height i.e. approximately halfway through the height of the sample. The measurements are taken from approximately the same surface location on all samples. This procedure is similar to the one adopted by Rogalsky et al. [288]. For experiment 2, the surface roughness for each sample was measured at 3 different locations by rotating the sample by 120° to offset any effects of the surface orientation with respect to the powder recoating or gas flow directions.

5.4   Results and discussion

For experiment 1, which involved studying the effect of core LPBF processing parameters on side-skin surface roughness, Sa, the central composite design (CCD) and Box-Behnken (BB) statistical designs were analyzed for model adequacy using analysis of variance (ANOVA) by the Minitab software. We refrain from the use of dichotomous p-values in our work due to the objections by multiple researchers around the same [289, 290, 291]. The ANOVA analysis of the CCD design (as shown in Table 5.3) reveals that the linear effects of the three variables laser power, point distance, and exposure time on the side-skin surface roughness values may not be significant when compared to the interaction terms – (laser power*exposure time) and (point distance*exposure time), which are judged by comparing the p-values of the listed terms. Amongst the linear effects, point distance has the lowest p-value out of the three variables. Since the square terms of the three variables in consideration also have high p-values in the CCD design, the Box-Behnken design was analyzed by considering only the linear and interaction terms of the three variables, as given in Table 5.4. From Table 5.4, we observe that the interaction terms again have a more significant effect when compared to the linear effects of the three variables. However, we note from both Table 5.3 and Table 5.4 that the interaction effects of (laser power*exposure time) have consistently lowest p-values across both designs. Additionally, the linear effect of point distance becomes significant. To better understand the physical origin of these effects, contour plots are created for the experimental design points design in Figure 5.3, with laser power and point distance as the two axes at fixed levels of exposure time.

Table 5.3: Analysis of Variance (ANOVA) table for the central composite design from experiment 1.

Source of variation	DF^a	Adjusted SS^b	Adjusted MS^c	F-value	P-value
Mode	9	121.067	13.4519	2.19	0.052
Linear	3	13.284	4.4281	0.72	0.548
Laser power	1	4.510	4.5099	0.73	0.399
Point distance	1	7.759	7.7591	1.26	0.270
Exposure time	1	1.015	1.0152	0.17	0.687
Square	3	11.487	3.8288	0.62	0.606
Laser power^2	1	8.105	8.1054	1.32	0.260
Point distance^2	1	1.287	1.2866	0.21	0.651
Exposure time^2	1	3.891	3.8905	0.63	0.433
Two-way interaction	3	96.296	32.0987	5.22	0.005
Laser power*Point distance	1	0.824	0.8240	0.13	0.717
Laser power*Exposure time	1	59.148	59.1481	9.62	0.004
Point distance*Exposure time	1	36.324	36.3240	5.91	0.021
Error	30	184.525	6.1508		
Lack-of-fit	5	50.047	10.0093	1.86	0.137
Pure error	25	134.479	5.3791		
Total	39	305.592			

^{a}: Degrees of freedom, ^{b}: sum of squares, ^{c}: mean squares

Table 5.4: Analysis of Variance (ANOVA) table for the Box-Behnken design from experiment 1.

Source of variation	DF[a]	Adjusted SS[b]	Adjusted MS[c]	F-value	P-value
Model	6	72.7719	12.1286	4.04	0.037
Linear	3	18.9536	6.3179	2.10	0.178
Laser power	1	3.6794	3.6794	1.22	0.301
Point distance	1	14.2992	14.2992	4.76	0.061
Exposure time	1	0.9751	0.9751	0.32	0.585
Two-way interaction	3	53.8182	17.9394	5.97	0.019
Laser power*Point distance	1	14.3864	14.3864	4.79	0.060
Laser power*Exposure time	1	37.7641	37.7641	12.56	0.008
Point distance*Exposure time	1	1.6677	1.6677	0.55	0.478
Error	8	24.0451	3.0056		
Lack-of-fit	6	14.6226	2.4371	0.52	0.775
Pure error	2	9.4225	4.7113		
Total	14	96.8170			

[a]: Degrees of freedom, [b]: sum of squares, [c]: mean squares
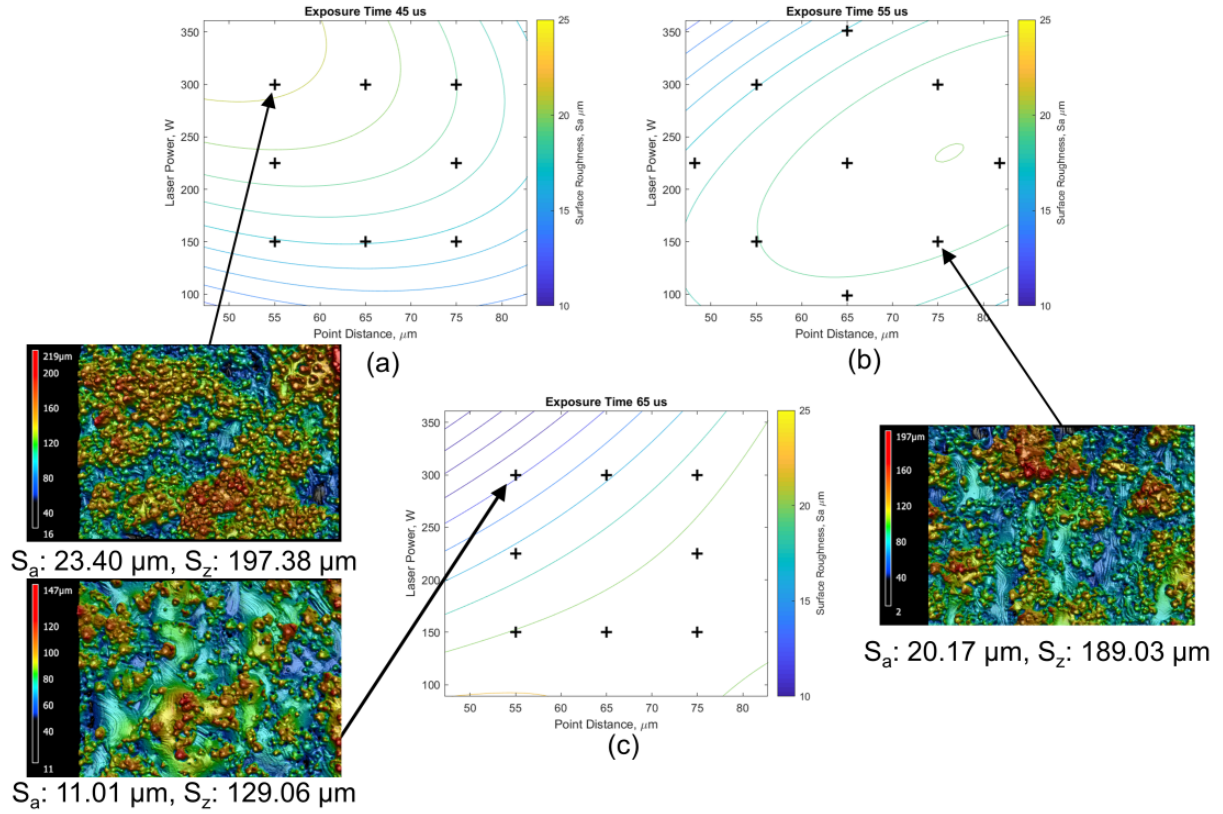
Figure 5.3: Contour plots showcasing the interaction effects of laser power and point distance at an exposure time of 45 µm (a), 55 µm (a), and 65 µm (c). The "+" symbols correspond to the actual experimental design points from which the contours were created. Height maps of representative samples to help understand the causes of the varying side-skin surface roughness values.

¹⁹⁷⁰ The lower values of side-skin surface roughness are consistently observed in the core LPBF parameters settings with high power and low beam velocity, as shown in the height map associated with Figure 5.3 (c). From the height maps, it is observed that the regions showing adhered powder are less prevalent in the high power and low beam velocity regimes. The lower side-skin surface roughness values in the high power and low velocity regimes of ¹⁹⁷⁵ experiment 1 could be attributed to the effects increased powder denudation [108], lower molten metal spatters [77], and reduced balling effects [292]. At high power regimes in the transition and keyhole modes, the denuded zone next to the edges of a given scan vector would be expected to have far greater dimensions when compared to lower power regimes in the conduction mode, as reported by Matthews et al. [108]. This could lead to ¹⁹⁸⁰ situations where transition and keyhole mode core LPBF processing parameters create a denudation zone large enough that the effects created by adherence of a large amount of partially-fused powder particles to the side-skin would be reduced, even with a following border scan that lies in conduction mode. Additionally, the sequence of printing, where the core scan is followed by the border scan, creates a situation where the lack of powder ¹⁹⁸⁵ at the border due to denudation may push the conduction mode border recipe to actually be in transition mode. In addition, the initial temperature of the substrate (core) may influence the border recipe outcomes. This results in re-melting deeper than anticipated at the border, but this is a hypothesis that will require further work. The reason why the same effects are not observed in samples with high power and high beam velocity could be ¹⁹⁹⁰ the additional effects of balling and molten pool spatters which would be expected at higher beam velocity settings. However, we do observe that there is still a considerable amount of adhered powder effects in the height maps of all samples shown in Figure 5.3. This could be associated to the conduction mode border processing parameter used in experiment 1. It is hence of value to probe the effects of border LPBF processing parameters as well as ¹⁹⁹⁵ we do for experiment 2.

Table 5.5: Side-skin surface roughness values for the samples from experiment 2

Border type	Sa [µm]		Sz [µm]	
	Average	Standard deviation	Average	Standard deviation
Type A	17.5	1.59	222.57	51.62
Type B	9.05	0.37	116.52	10.32

The findings from experiment 1 guide the process parameter selection for experiment 2. The type A border parameters are the same as the ones kept constant in experiment 1. A

higher power and lower beam velocity were selected for the type B border parameters as a result of the findings from experiment 1. Although a laser power of 300 W, point distance of 55 µm and exposure time of 65 µs in the core was found to give the lowest side-skin surface roughness values in experiment 1, there is the issue of elevated edges at the border when using high power and low velocity regimes for the border LPBF processing parameters as reported by Yasa et al. [293]. The effect of elevated edges due to the core LPBF processing parameters is compensated by the 67° hatch rotation between successive layers, however the scanning direction for the border remains the same which is strongly associated with elevated edges as well [293]. Elevated edges lead to the powder recoater hitting the edges of a given sample thereby disturbing the flow of powder on the LPBF build plate, and can also lead to recoater blade damage. Since we hypothesise that powder denudation due to transition and keyhole mode parameters at high power and low velocity regimes are associated with the reduced side-skin surface roughness, we perform a preliminary experiment of picking the type B LPBF processing parameters which lie between the transition and keyhole mode thresholds, while being conservative on selection of the laser power settings to avoid keyhole mode porosity in particular.

Table 5.5, showcases the difference in surface roughness (Sa and Sz) values between the type A and type B samples. As observed from Table 5.5, the type B samples which had the transition mode border LPBF processing parameters have Sa and Sz values which are much lower than the type A samples which had conduction mode border LPBF processing parameters. Additionally, the Sa value of 9.05 µm is much lower than the D10 value of 20 µm for the given particle sizes used in the study. The height maps and SEM images of one replicate of the type A and type B samples are given in Figure 5.4. From Figure 5.4b, it can be observed that the type B sample with the transition mode border LPBF processing parameters has much lesser partially fused powder particle effects on the side-skin surface.

The lower side surface roughness seen in the transition melting mode border parameters used in type B of experiment 2 could be associated to an interplay between increased powder denudation [108], lower molten pool spatters [77, 225], and reduced balling effects [294, 141]. In the domain of high laser powers and low laser beam velocity (as used for type B in experiment 2), since the border melt pools are in transition mode, the powder denudation area is expected to be large in a given layer as observed by Matthews et al. [108]. This means that, in the succeeding layer, the powder spread by the recoater would be impacted, next to the edges of the sample due the denuded area of the previous layer; as such, the current layer would likely have a lower powder packing density around the edges of the sample before melting has even begun. This phenomenon possibly extends throughout the manufacturing of a three-dimensional sample, leading to lesser powder particles being available next to edges of the sample during every layer when transition mode

96

S_a: 17.05 μm, S_z: 222.57 μm

(a)

S_a: 9.05 μm, S_z: 116.52 μm

(b)
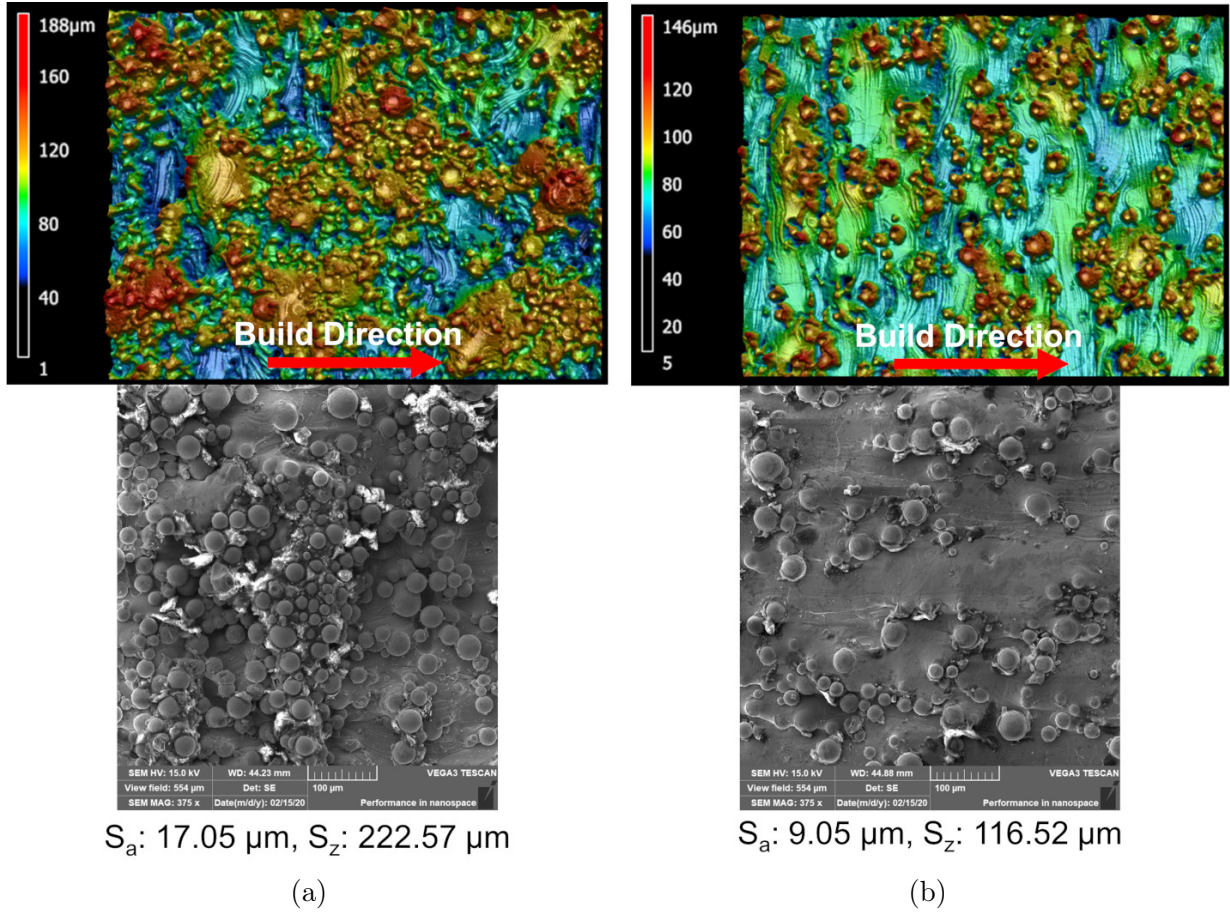
Figure 5.4: Height maps and SEM images of the side-skin surface of a type A sample - conduction mode border (a), and type B sample - transition mode border (b) from experiment 2.

border parameters are used. Since lesser powder particles are available at every given layer of such parts, the probability of partially fused powder particles governing the side-skin surface characteristics would be lower as we see in Figure 5.4b when compared to conduction mode borders which would have much lower powder denudation zones and thereby powder dependent surface characteristics as observed in Figure 5.4a. It is recommended that, as future work, these interactions be observed using in-process imaging techniques to capture these complex phenomena. The effective beam velocity used for the type B samples from experiment 2 is 500 mm/s also lies on the lower end of the spectrum for velocities commonly used in LPBF. Lower velocity settings help in reducing the effects of molten metal spatter and balling, which impart additional surface roughness to the side of a given part. The difference in the side-skin surface roughness values obtained by the conduction and transition mode border LPBF processing parameters could thereby be used to tailor surface morphologies in combination with beam path planning algorithms for industrial applications.

5.5 Conclusions

In this work, the effects of core and border LPBF processing parameters on the side-skin surface morphology of parts was studied. The results can be summarized as follows:

1. When using a constant set of border processing parameters that lie in conduction mode, the high power and lower beam velocity regimes (in transition and keyhole modes) used for core LPBF processing parameters could help in reducing the effects of adhered partially-fused powder particles, balling, and molten pool spatter for the side-skin.

2. The surface morphology for the side-skin can be greatly improved by adjusting the laser power and beam velocity of the border scan tracks. Border processing parameters that lie in transition and keyhole melting modes with lower beam velocity settings, and conservative laser powers (to avoid elevated edges) have surface roughness, Sa, values of lesser than 10 µm when compared to conduction mode border processing parameters which lead to Sa values greater than 17 µm. The transition mode surfaces at low velocity regimes open a possibility of obtaining surfaces with a negligible contribution from partially melted powder particles, which could be useful when working with irregularly shaped powder particles, and powders with a higher particle size range.

Additional work is needed to investigate the effects of a broader range of border LPBF processing parameters and border scanning strategies such as multiple borders on side-skin surface morphologies. The fundamental understanding of side-skin surface roughness during LPBF developed in this chapter is used to understand and tailor side-skin surface of Ti-6242Si in Chapter 6 and to make recommendations for complex Ti and Ti-6Al-4V lattice structures in Appendix A.

Chapter 6

Melting mode driven understanding of porosity, roughness, and cracking in a near-alpha titanium alloy - Ti-6242Si

6.1 Preface

Ti-6Al-2Sn-4Zr-2Mo-Si (Ti-6242Si) is a near-α phase titanium alloy that has a greater strength up to 565 °C compared to the workhorse Ti-6Al-4V alloy with a typical service temperature up to 400 °C. While there is a wealth of literature to help understand the laser powder bed fusion (LPBF) of Ti-6Al-4V, only a few research articles about LPBF of Ti-6242Si are available in the open literature. In this work, LPBF processing diagrams and temperature prediction models were used to investigate the impact of process parameters such as laser power, scan speed, and beam spot radius on macroscale characteristics of the builds such as density, surface roughness, residual stresses, and cracking. The use of processing diagrams allowed for exploration of density ranges between 99.55-99.98%, and surface roughness, Sa, ranges between 8-16 μm in Ti-6242Si processed by LPBF. Cracking in Ti-6242Si manufactured by LPBF is reported for the first time. Cracking during LPBF of Ti-6242Si was observed to strongly depend upon the predicted melting mode (conduction, transition, and keyhole) for a given set of LPBF process parameters. Residual stress evaluation of Ti-6242Si shows that higher residual stresses in the transition and keyhole melting modes are the primary cause for cracking in this near-α phase alloy that forms a non-equilibrium α' martensitic microstructure during LPBF.

100

6.2 Introduction

Laser powder bed fusion (LPBF) enables the manufacturing of near net-shape geometrically complex parts. LPBF allows for optimized designs to be explored for manufacturing, such as topology optimized or loading field driven designs for product lightweighting and customization [65], while also reducing environmental impact through input energy reduction and carbon dioxide emissions [53]. The potential of LPBF to build lightweight components has been shown to improve fuel consumption for aerospace and automotive applications, wherein titanium alloys are commonly used [295, 296].

While additively manufactured titanium alloys are already used for industrial applications in the aerospace [297, 298, 299] and biomedical sectors [300, 301, 302, 303], the low number of titanium alloys tailored and adopted for LPBF reduce the potential range of applications which can be explored[296]. From the available titanium alloys, the $\alpha+\beta$ alloy Ti-6Al-4V (Ti64) is known as the "workhorse" titanium alloy and it represents almost half of the total industrial usage of titanium alloys [297]. When compared to Ti64, the near-α Ti-6Al-2Sn-4Zr-2Mo-Si (Ti-6242Si) is known to have improved mechanical properties, particularly creep behaviour [296], which is useful for applications such as high-pressure compressor parts in aviation engines [304]. The nominal chemical composition of Ti-6242Si is obtained from the ASM Handbook [49] and is given in Table 6.1. Alpha (α) and near-α Ti alloys are commonly used in applications where higher strength and toughness, excellent creep resistance, and stress stability is desired at higher working temperatures up to 600 °C when compared to Ti64 that cannot be used beyond a service temperate of 400 °C [305]. From the available near-α Ti alloys, Ti-6242Si has been recommended for long-term applications requiring a combination of high strength-to-weight ratio, tensile strength, toughness, creep strength, adequate corrosion/oxidation resistance at room and elevated temperatures, and stability up to a temperature as high as 565 °C [50]. Ti-6242Si has been successfully utilised for aerospace applications at a service temperature of up to 538 °C [306]. Ti-6242Si has also been proposed to be better suited for certain superconductivity applications when compared to the common titanium alloy, Ti64 [307].

Table 6.1: Nominal composition of Ti-6242Si [49]

Designation	Nominal composition, wt %					Impurity limits, wt % (max)				
	Al	Sn	Zr	Mo	Si	N	C	H	Fe	O
Ti-6242Si	6	2	4	2	0.08	0.05	0.05	0.0125	0.25	0.15

A survey of open literature shows that LPBF of Ti-6242Si has been investigated by

two research groups to date. Fan and Yang [308] reported a successful use of LPBF to manufacture Ti-6242Si cubic and tensile samples for the first time. Density values of 95.7%-99.5%, hardness of 410 HV, ultimate tensile strength (UTS) of 1437 MPa, and ductility of 5% were reported for the as-built Ti-6242Si samples. A hardness of 450 HV, UTS of 1510 MPa, and ductility of 1.4% were reported for the Ti-6242Si samples aged at 595 °C for 8 hours. Rieger et al. [296] reported improved mechanical properties of LPBF Ti-6242Si at both room and elevated temperatures (500 °C) when compared to LPBF Ti64 and conventionally cast Ti-6242Si. A non-equilibrium hexagonal α' martensitic microstructure was reported for both Ti-6242Si and Ti64 in the as-built condition, as it is generally observed due to the high cooling rates (1–40 K/µs) associated with LPBF [185]. While using the same LPBF process parameters, Rieger et al. [296] reported smaller acicular α' grains in Ti-6242Si compared to Ti64, which were attributed to the smaller prior β grain structure in Ti-6242Si. Additionally, there have also been attempts at processing Ti-6242Si by electron beam powder bed fusion (also known as electron beam melting, EBM) [309] and boron modified Ti-6242Si [310, 311], alongside directed energy deposition (DED) of Ti-6242Si [84, 312]. Nonetheless, cracking during metal AM of Ti-6242Si was not reported in either of these articles. Specifically for LPBF of Ti-6242Si, Fan and Yang [308] manufactured cuboids of 10x10x8 mm^3 on a LPBF system with a laser power of 95 W, and were immediately subjected to an aging heat treatment afterwards at 595 °C for 8 hours in an Ar atmosphere. Laser scan speed was the only parameter varied in a range of 600-1200 mm/s. The low power of 95 W means that the process parameter range likely did not span all the melting modes in LPBF, as is observed by the micrographs in their work by a presence of lack-of-fusion defects and low density ranges of 95.5-99.5%. The immediate heat treatment would be another mechanism through which cracking could have been avoided in the work by Fan and Yang [308]. Reiger et al. [296] neither varied nor reported the LPBF process parameters used for manufacturing cuboid of 22x22x25 mm^3 and cylinders of diameter 12 mm and height 70 mm. The only information provided was the use of a volume energy density of 60 J/mm^3 without context of what equation was used to obtain this value. Additionally, while some of their cuboids were investigated in the as-build condition, all of their cylinders were subjected to an annealing heat treatment at 800 °C-850 °C for 1-3 hours in vacuum followed by air cooling. It is hence not possible to identify the causes as to why there was no reported cracking in the work by Reiger et al. [296].

This work is the first attempt at spanning all three melting modes during LPBF of Ti-6242Si, thereby testing the limits of processing this near-α alloy by LPBF. The work focuses on using normalized processing diagrams developed in Chapter 3 to investigate the influence of LPBF process parameter on density, side-skin surface roughness, and residual

stresses during LPBF of Ti-6242Si. Laser power, scan speed, and beam spot radius are the principal LPBF process parameters considered for this work.

6.3 Methods

6.3.1 General LPBF processing details

Two separate manufacturing build cycles of Ti-6242Si were evaluated in this work, as illustrated in Figure 6.1. Both build cycles, or prints, were conducted on the reduced build volume (RBV) of a modulated LPBF system (AM 400, Renishaw, UK). The Ti-6242Si powders (AP&C, Montreal, Canada) were plasma atomized, with a particle size range of 15–45 µm (D10 of 20 µm, D50 of 34 µm, and D90 of 44 µm). A constant powder layer thickness of 30 µm was used for both prints. The two prints defined as "Print 1" and "Print 2" herein are described in Section 6.3.1.1 and 6.3.1.2 respectively.

LPBF process parameters such as laser power, scan speed (by means of exposure time), and beam spot radius are known to be the variables that have the highest impact on driving the presence of conduction, transition, or keyhole melting modes [10]. This motivated the LPBF process parameter selection for the Print 1 and Print 2. A hatch distance equal to the beam diameter was chosen for a given sample to minimize the potential for lack-of-fusion defects.

In the modulated LPBF system used for this work (Renishaw AM 400), the beam velocity variable (v) is calculated by Equation 3.36 from Chapter 3 which has three variables - p_d, t_e, and t_d. p_d is the distance between adjacent exposure points (point distance) [m], t_e is the time when the laser is acting on the material (exposure time) [s], and t_d is the time when the laser is off and repositioning to the next exposure point (drill delay time) [s]. The drill delay time, t_d, is assumed to be 10 µs for Renishaw AM 400, as recommended by the manufacturer.

6.3.1.1 Print 1 - Process parameter selection and manufacturing

Print 1 was planned in a way to span the conduction, transition, and keyhole melting modes for evaluation of density and side-skin surface roughness. Two sets of samples were manufactured in the same build: cylindrical and cuboid samples. 12 cylindrical Ti6242 samples with a diameter of 10 mm and a height of 30 mm, and 9 cuboids of 5x5x10 mm^3 were manufactured on the reduced build volume (RBV) of a modulated LPBF system (AM

103

400, Renishaw, UK). The cylinders were used to explore the part quality outcomes across multiple melting mode domains as a first step towards optimising the process parameters of the core of the samples targeting high density, and cuboids were manufactured with the purposes of optimising process parameters to obtain low side-skin surface roughness. The diameter of the cylinders were selected to resemble ASTM rounded tensile samples [313]. The build plate layout of the parts with respect to the gas flow and powder flow is shown in the left side of Figure 6.1. All the manufactured samples from Print 1 were removed off the build plate by electrical discharge machining (EDM).
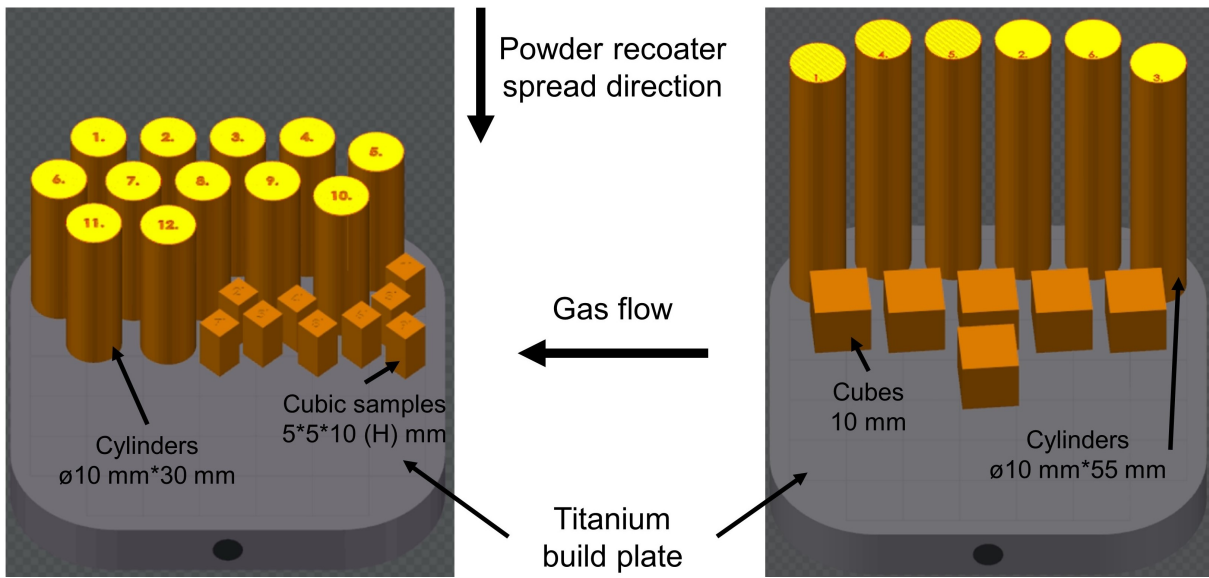
Figure 6.1: Illustration of the build plate layout on the reduced build volume of the modulated beam LPBF for the manufactured Ti-6242Si samples for Print 1 (left) and Print 2 (right).

The LPBF process parameters that were varied for the cylinders (for density evaluation) are shown in Table 6.2. The point distance was kept constant at 55 µm for all cylinders. The beam spot radius variations were obtained by defocusing the beam to positions above the build as illustrated in Figure 4.2 [209]. The modulated LPBF system provides a laser beam wavelength of $\lambda = 1070$ nm, and the beam spot radius at the focal point is nominally 35 µm. The laser beam was defocused to two distances (z) of 3.67 and 5.63 mm above the build plate, to obtain divergent beams of radiuses 50 and 65 µm respectively, as shown in Table 6.2. These values were calculated for a Gaussian distribution by Equation 3.37 from Chapter 3. For both cylinders and cuboids, the scanning strategy included scanning of the hatch volume (core) using the meander scanning strategy, followed

by a border scan that involves melting of the edge of each layer of a sample. The direction of core meander scanning orientation was rotated by 67° between successive layers. For the cylinders, the border parameters were kept constant with power 100 W, point distance 45 µm, and exposure time 40 µs, which are predicted to lie in the conduction melting mode, as per predictions from the processing diagrams developed using methodologies described in Chapter 3.

Table 6.2: LPBF process parameters used in the core of the Ti-6242Si cylinders for Print 1. Sample codes which have an asterisk sign (*) next to their labels are process parameters that are reevaluated in Print 2. Border parameters were kept constant for all cylinders.

Sample code	Power [W]	Exposure time [µm]	Beam radius [µm]	Hatch distance [µm]
1*	225	30	50	100
2*	150	30	35	70
3	300	30	65	130
4	375	30	65	130
5*	150	50	35	70
6*	300	50	50	100
7	375	50	65	130
8*	225	50	35	70
9	300	50	65	130
10*	225	50	50	100
11	300	30	50	100
12	225	30	35	70

In the cuboids, the core was kept constant at the process parameters used for cylindrical sample 10 from Table 6.2, with a laser power 225 W, point distance 55 µm, exposure time 50 µs, beam radius 50 µm, and hatch distance 100 µm. The parameters for the border scan were varied as shown in Table 6.3. In these samples, the point distance was kept constant at 55 µm, and the beam spot radius was 35 µm (focused beam) for the border.

6.3.1.2 Print 2 - Process parameter selection and manufacturing

Print 2 had a two fold purpose in the context of this study. The first purpose was to evaluate reproducibility of the findings from the six selected process parameters with varied build

Table 6.3: LPBF process parameters used in the border of the Ti-6242Si cuboids for Print 1 – side-skin surface roughness evaluation. The point distance was kept constant at 55 µm, and the beam spot radius was 35 µm (focused beam). Core parameters were kept constant for all cuboids.

Sample code	Power [W]	Exposure time [µm]
A	100	25
B	250	45
C	100	45
D	100	65
E	175	45
F	175	25
G	250	25
H	250	45
I	250	65

plate locations from Print 1. The second purpose was to evaluate the effect of sample dimensions of the outcome of cracking in particular. The core process parameters used for cylinders 1, 2, 5, 10, 6, and 8 in Table 6.2 were reevaluated for Print 2 and labelled as samples K, L, M, N, O, and P respectively in Table 6.4. For Print 2, the samples codes from Table 6.4 were used for manufacturing cylinders (diameter of 10 mm and a height of 55 mm) and cubes (edge length of 10 mm) as illustrated in the right side of Figure 6.1. Print 2 was monitored using a action camera (GoPro) while being printed to observe any unexpected occurrences during manufacturing. After the Print 2 was completed, the six cylinders shown in the right side of Figure 6.1 were evaluated using a X-ray residual stress analyzer, while all the samples were on the build plate. Additionally, photographs of the the samples, while on the build plate, were also taken to observe the presence of cracking. Following residual stress measurements, all the manufactured samples from Print 2 were removed off the build plate by electrical discharge machining (EDM) for imaging and metallography.

6.3.2   X-ray computed tomography (XCT) methods

All of the twelve cylinders from Print 1 and cylinder N from Print 2 were analyzed for porosity characteristics using a 3D X-ray computed tomography (CT) scanner (ZEISS

Table 6.4: LPBF process parameters for the core in the Ti-6242Si cylinders and cubes for Print 2. Border parameters were kept constant for all cylinders and cubes.

Sample code	Power [W]	Exposure time [µm]	Beam radius [µm]	Hatch distance [µm]
K	225	30	50	100
L	150	30	35	70
M	150	50	35	70
N	225	50	50	100
O	300	50	50	100
P	225	50	35	70

Xradia 520 Versa) using a 11 µm voxel size. The X-ray CT scanning parameters used are shown in Table 6.5. To visualize the pore distribution within each sample, the CT scans were analyzed using an image processing software (Dragonfly 3.0, Object Research Systems Inc.). For each cylinder from Print 1, the entire diameter of 10 mm and approximately 8.5 mm of height along the build (Z) direction, along the mid-height of the cylinders was analyzed. Cylinders 6 and 8 from Print 1, with process parameters as shown in Table 6.2 cracked on the build plate before EDM cutting. As a deviation from methodologies, due to the multiple horizontal cracks, it was not possible to evaluate the entire 8.5 mm height for density. A diameter of 10 mm and approximately 7.2 mm of height for cylinders 6 and 8 was hence evaluated. For cylinder N from Print 2, the entire sample was scanned after EDM cutting leading to a diameter of 10 mm and approximately 54 mm in height for the XCT data.

6.3.3 Microscopy and imaging methods

The surface topography of the side-skin surfaces of the cuboids from Print 1 with process parameters as shown in Table 6.3 was characterised using the Keyence VK-X250, a laser confocal microscope. The image processing and roughness measurements were completed using the microscope processing software (Keyence MultiFileAnalyzer). A scanning area of approximately 700x500 μm^2 was scanned on the 4 side-skin surfaces (surface along the build (Z) direction) of each cuboid, using a vertical z-axis resolution of 0.5 µm. Sa and Sz are the surface roughness metrics used in this work. Sa is the arithmetical mean height of a surface area which is defined as the absolute value of the height from the average surface. Sz is the sum of the largest peak height value and the largest pit depth value within a

Table 6.5: X-ray computed tomography parameters used for scanning the Ti-6242Si cylinders. .

Parameter	Unit	Value
Voxel size	[µm]	11
Source power	[W]	10
X-ray energy	[kV]	140
Filter	-	HE2
X-ray optic	-	0.4x lens
Source position	[mm]	23.1391
Detector position	[mm]	120.787
Exposure time	[s]	2.0
Number of projections	-	1001
Binning level	-	2

scanned area of a given surface. Surface correction for plane tilt was employed for all scans, to accommodate for the tilt cause by the roughness of the resting surface. The roughness was measured near the middle of the sample height i.e., approximately halfway through the build height of the sample for all 4 surfaces of each sample. Measurements of Sa and Sz from the 4 surfaces of every cuboid were used to calculate the average and standard deviation values of Sa and Sz. This procedure is similar to the one adopted by Patel et al. [251] and Rogalsky et al. [288].

6.3.4 Residual stress analysis

Approximately 43 hours after the Print 2 was completed, the six cylinders shown in the Print 2 configuration illustrated in Figure 6.1 were evaluated for residual stresses while all the samples were on the build plate; i.e. residual stress evaluation was performed before the EDM cutting operation. The cos α X-ray diffraction (XRD) technique was used in this study to measure residual stresses on the top surface of the samples. Compared to the traditional $\sin^2 \psi$ technique, the cos $alpha$ technique uses X-rays that are 360°-omnidirectionally diffracted from the sample surface, which are then detected by a 2-dimensional detector. This information is used to plot the Debye-Scherrer ring. The cos α technique is more advantageous than the $\sin^2 \psi$ technique as the incident X-ray angle can stay constant. A schematic illustration of the cos α X-ray diffraction (XRD) residual

stress measurement technique is shown in Figure 6.2.
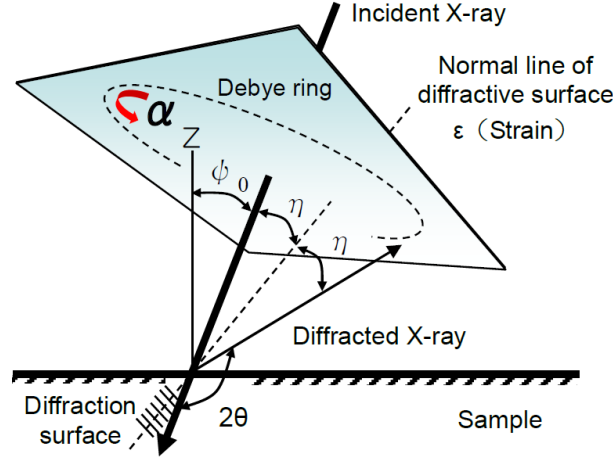
Figure 6.2: Schematic illustration of the X-ray residual stress measurement method used in this work via the cos α X-ray diffraction (XRD) technique [11].

As such, a portable X-Ray residual stress analyser (u-X360s, Pulstec, Hamamatsu, Japan), a machine that uses the cos α XRD technique, was used to conduct the measurements. The instrument (tube current 1.2 mA, tube voltage 30 kV) was equipped with V-Kα radiation source (wavelength 2.51 Å) and used a constant diffraction angle (2θ) and incidence angle (ψ_0) of 140.175° and 25° respectively. (hkl) values of (103) were used for analysis.

The residual stress measurements were taken at 49 points (7*7 grid) in intervals of 1 mm in X and Y, and the locations of the 49 measured points from the top surface of each cylinder are shown in Figure 6.3. The residual stresses were measured along the X-axis from right to left as shown by the orange arrows in Figure 6.3. The measurements obtained from the residual stress system thereby corresponds to the in-plane normal stresses, σ_{xx}. The average of all measured points calculated to provide a representative σ_{xx} value. It must be noted the certain points were excluded from σ_{xx} calculations as the XRD machine denoted that the values measured for these points were unreliable. These points were generally the start and end points in the first and second rows of the grid.
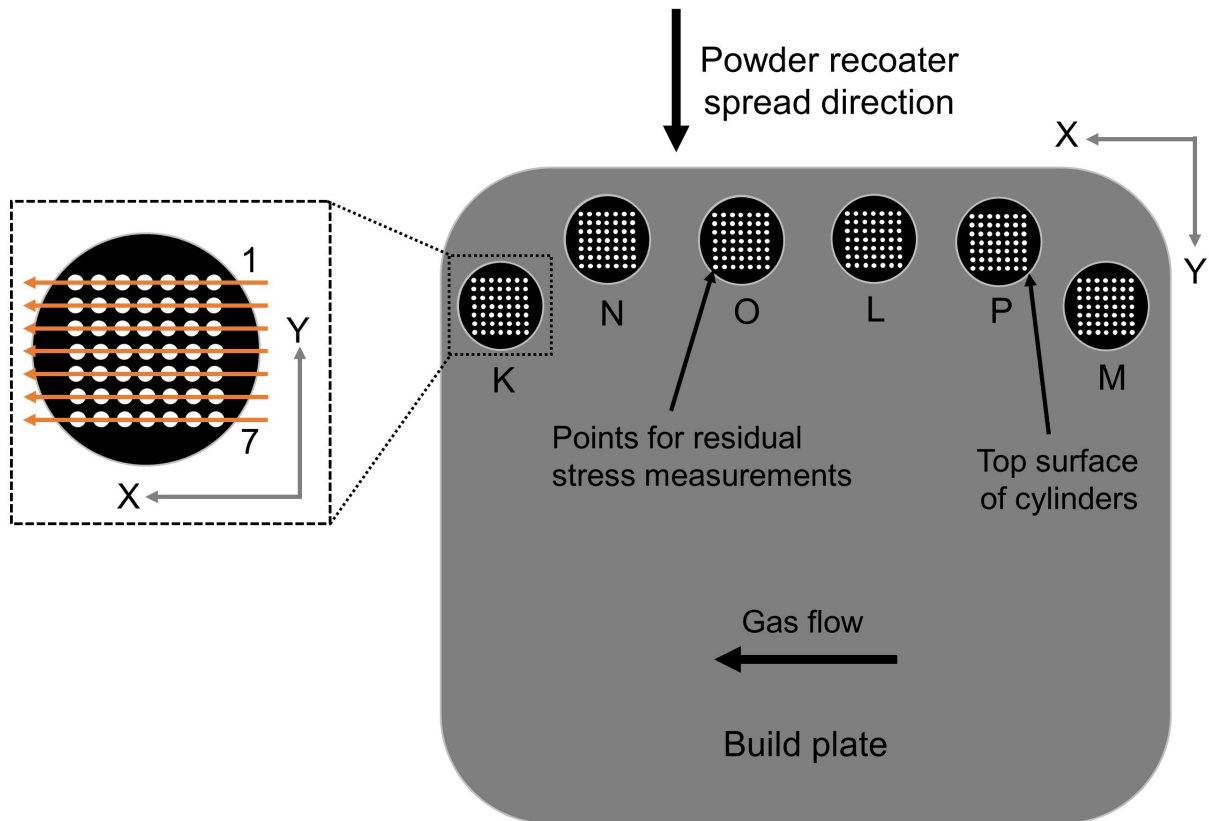
Figure 6.3: Location of residual stress measurements on the top surface of the 6 cylinders from Print 2. The orange arrows show the direction of residual stress measurement. The orange arrow numbered 1 corresponds to the first row of points measured and the orange arrow numbered 7 corresponds to the last row of point measured.

6.4 Results and discussion

6.4.1 Normalized processing diagrams to identify melting modes

The underlying normalized processing diagrams for Ti-6242Si shown in Figure 6.4 and Figure 6.5 are obtained through the methodology described in Chapter 3. Figure 6.4a corresponds to the processing diagram for the 12 cylinders from Print 1 alongside density values from XCT data. The 6 cylinders and 6 cubes from Print 2 had the same sample codes and are given in the processing diagram shown by Figure 6.4b. The samples that cracked for Print 1 and Print 2 are highlighted by an asterisk sign next to their label in Figure 6.4a and Figure 6.4b respectively. Figure 6.5 corresponds to the processing diagram for the 9 cuboids from Print 1; surface roughness metrics Sa and Sz are overlaid on the processing diagrams in Figures 6.5a and 6.5b respectively.

Table 6.6: Thermophysical properties of Ti-6242Si taken at room temperature [50, 51]

Properties	Material(Ti6242)
Density, ρ [kg/m^3]	4540
Thermal conductivity, λ [W/(mK)]	7
Specific heat capacity, C_p [J/(kgK)]	460
Solidus temperature, T_s [K]	1907
Liquidus temperature, T_m [K]	1941
Vaporization temperature, T_v [K]	3315

The terms E^* and v^* in Figure 6.4 and Figure 6.5 are given by Equation 3.4 and 3.2 respectively. The minimum melt absorptivity, A_m, value for Ti64 reported as 0.26 in Table 3.1 is used fir Ti-6242Si in this work. Values for the Ti-6242Si material constants are taken at the room temperature from Welsch et al. [50] and are summarized in Table 6.6. The solidus and liquidus temperature in Table 6.6 are obtained from Kawakami, 2002 [51]. The conduction mode threshold for Ti-6242Si is given by $T_p^* = 1.68$ at $z^* = 0.5$, where 1.68 is the ratio of the boiling point (vaporization temperature) of Ti-6242Si and its melting point. Similarly, $T_p^* = 1.68$ at $z^* = 0.8$ is the transition mode threshold for Ti-6242Si as shown in Figure 6.4 and Figure 6.5. All of the samples for Print 1 and 2 from Figure 6.4 were predicted to lie above the surface vaporization threshold $T_p^* = 1.68$ at $z^* = 0.5$ for

111
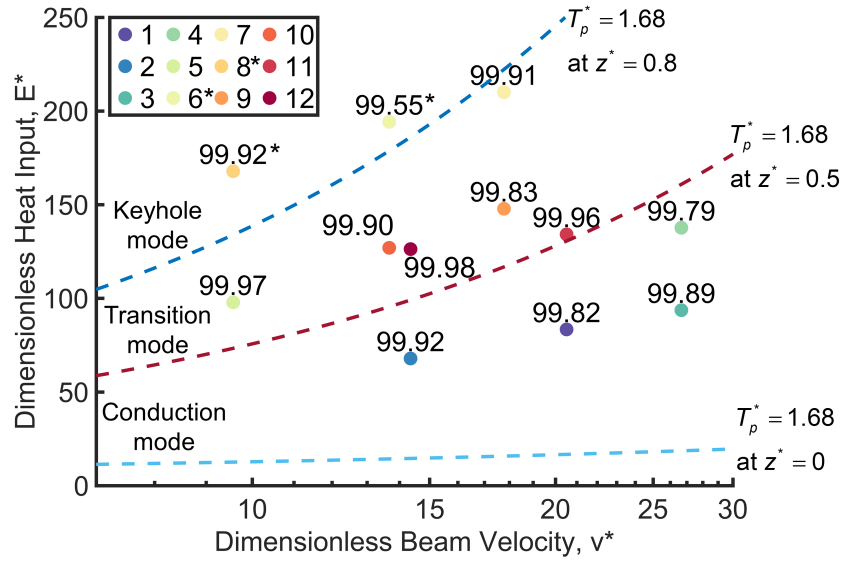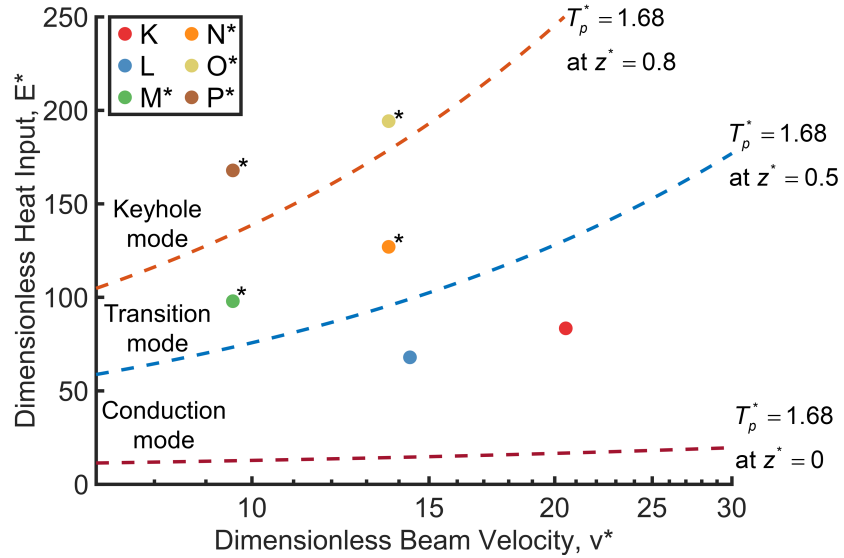
Figure 6.4: Normalized processing diagrams for the twelve Ti-6242Si cylinders from Print 1 (a) and the six cylinders and cubes from Print 2 (b). The density values obtained from XCT data in percentage (%) are provided next to the Print 1 points on the diagram. The cracked samples from Print 1 and Print 2 are shown by an asterisk sign (*) next to their labels and density values.

112

Ti-6242Si; this was motivated by previous work melt pool studies wherein melt pool depths greater than 1.5 times the powder layer thickness selected (30 µm) were observe to lie well above the surface vaporization threshold for Ti64 and SS 316L [10]; both materials being classified as having high absorptivity and low thermal conductivity.

6.4.2   Porosity analysis

The normalized processing diagrams for the density study in Print 1 are shown in Figure 6.4a, which help to predict the melting mode for a given set of LPBF process parameters, thereby enabling an understanding of the physical origin of porous defects in the three-dimensional cylinders. Density values for each cylinder were obtained from the XCT data and are shown next to each marker in Figure 6.4a. It is important to note that the density values obtained from XCT are approximations of the true density owing to the voxel size (11 µm) CT detection limit for the data acquisition setup. Nonetheless, Ti-6242Si seems to have a wide-processing window for near fully dense parts as cylinders with over 99.90% density are observed in the conduction mode (cylinder 2), transition mode (cylinders 5, 7, 10, 11, and 12), and keyhole mode (cylinder 8).

An orthographic projection along with build (XY) plane of the porous defect space for 6 representative cylinders from Print 1 is shown in Figure 6.6. Additionally, a three-dimensional visualization of the porous defect distribution in highest density sample (cylinder 5) from Figure 6.6 is shown in Figure 6.7 which confirms the presence of very few defects both in the core and along the sidewalls of the cylinder. In Figure 6.6 and Figure 6.7, defects with aspect ratios above 0.7 were considered as rounded defects and defects below this aspect ratio were considered as irregularly shaped defects, similar to our prior work [209]; as such, each class was colourised for contrasting the pore characteristics. All 6 samples in Figure 6.6 show a higher concentration of porous defects near the sidewalls of the cylinders. These porous defects are caused by rapid formation and collapse of deep vaporized regions due to the lower laser beam velocity at the turn points of a given layer, which is common across most LPBF systems [81]. The collapse of the vaporized regions of the melt pools leads to trapping of process chamber atmospheric gases (argon) in the solidified parts. Additionally, collapse of the vaporized regions can also lead to the trapping of metal vapour in the solidified parts [127]. The processing diagram for the cylinders in Figure 6.4a shows that all the samples (including the conduction mode samples) lie above the predicted surface vaporization threshold which is given by $T_p^* = 1.68$ at $z^* = 0$ for Ti-6242Si. Hence the presence of vaporization-related defects near the sidewalls of all cylinders thereby falls in line with the predictions from the processing diagrams. Additionally, most of the defects near the sidewalls of the cylinders seem to have an irregular morphology, as shown by the

113

(a)

(b)
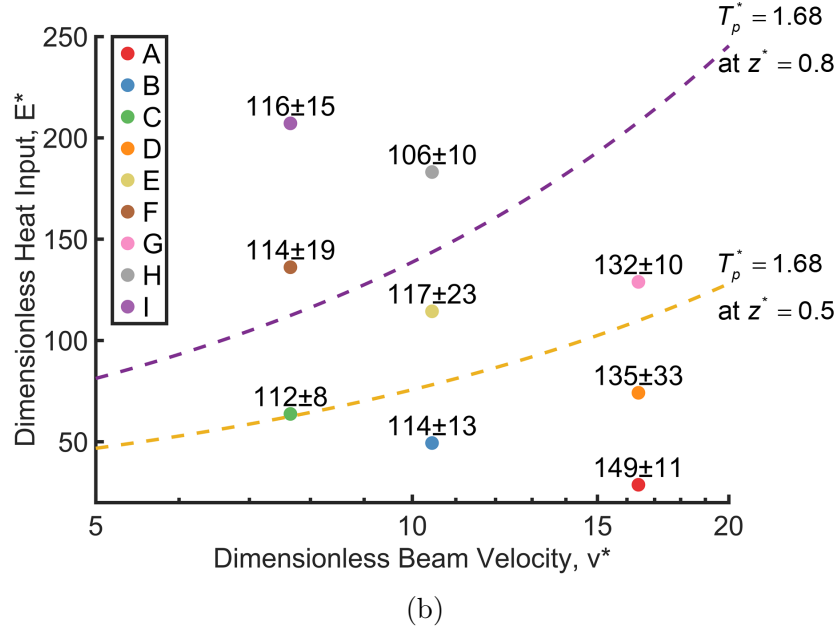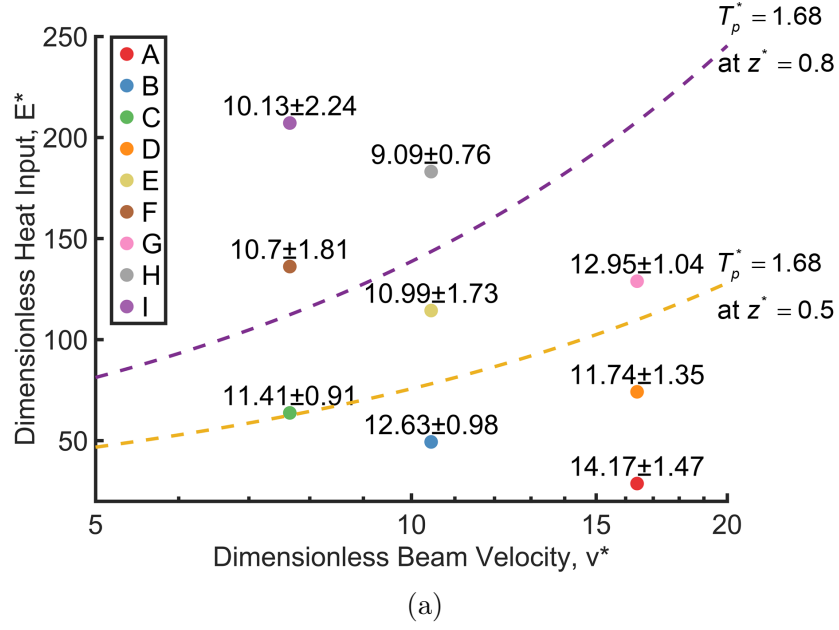
Figure 6.5: Normalized processing diagrams for the nine Ti-6242Si cuboids used for side-skin surface roughness from Print 1 evaluation with the Sa values in μm (a) and Sz values in μm (b).
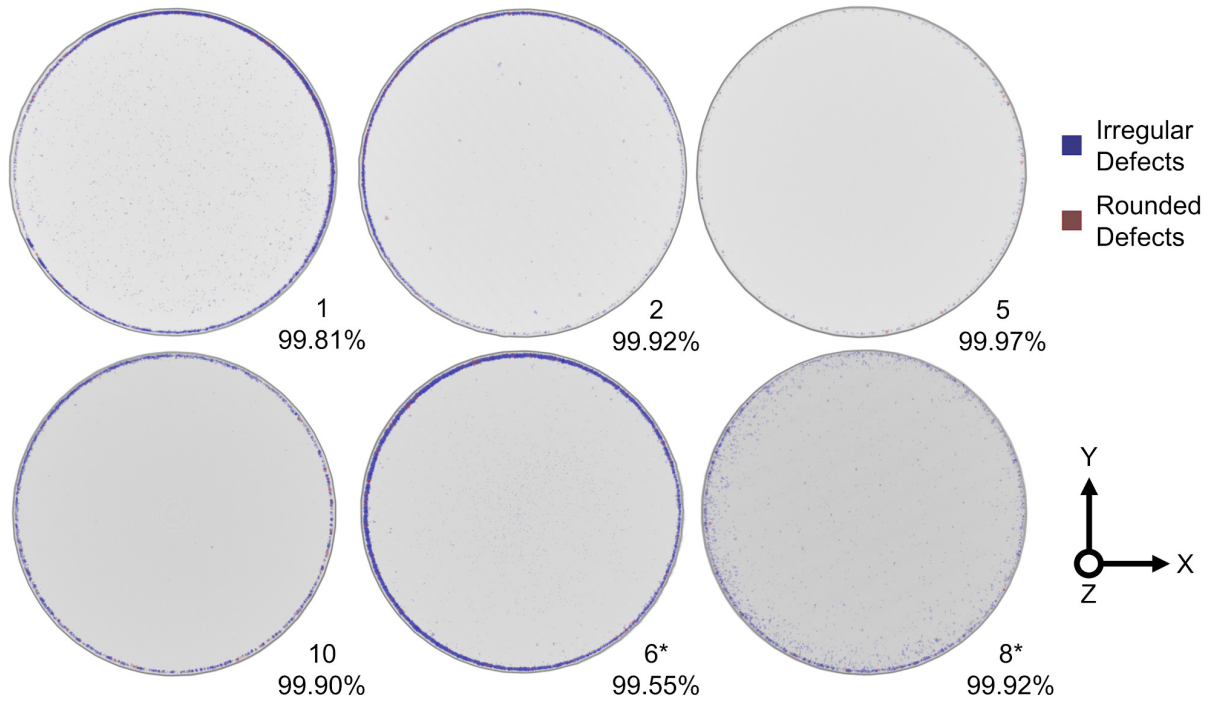
Figure 6.6: An orthographic projection of the porous defect space (above 4 voxels) in the build plate (XY) plane from the XCT data of conduction mode cylinders (1, 2), transition mode cylinders (5, 10), and keyhole mode cylinders (6, 8) from Print 1. The percentage values provided next to the cylinder labels are the density values also represented in Figure 6.4a.
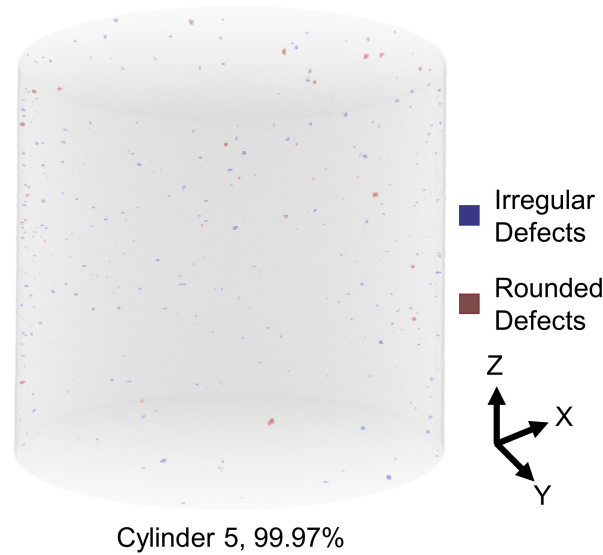
Cylinder 5, 99.97%

Figure 6.7: A three-dimensional (3D) visualization of the porous defect space (above 4 voxels) along the build direction (Z) from the XCT data of cylinder 5 (highest density) from Print 1, along with the density value obtained from the XCT data.

predominantly blue colourisation in Figure 6.6. It is known that defects which form due to material vaporization related instabilities may have both rounded and irregularly-shaped morphologies; defects due to collapse of the vaporized region in particular are known to have irregularly-shaped morphologies [10, 272].

The absence of large irregular lack-of-fusion defects in Figure 6.6 and Figure 6.7 indicates that the melt pool stitching resulting from the interplay of the selection of hatch distance and powder layer thickness was appropriate for the given sets of process parameters. The processing window for near-fully dense Ti-6242Si parts by LPBF on the modulated laser beam system in this study seems to be particularly focused in the transition melting mode, as observed by cylinders 5, 7, 10, 11, and 12 with densities over 99.90% as illustrated in Figure 6.4a. Amongst the 6 cylinders from Print 1 visualised in Figure 6.6, cylinder 5 seems to have the highest density of 99.97%. The absence of a large quantity of rounded vaporization instability-related defects in the two keyhole mode cylinders 6 and 8 in Figure 6.6 means that the LPBF process parameters selected for the samples were only marginally aggressive enough to cause such defects.

To evaluate the reproducibility of the density-related findings from Print 1 summarized in Figures 6.4a, Figure 6.6 and Figure 6.7, the entire 54 mm length of cylinder N from Print 2, which had replicated process parameters from cylinder 5 in Print 1, was evaluated

116

using XCT and the results are shown in Figure 6.8. Similar to cylinder 5 in Figures 6.6 and Figure 6.7, cylinder N is nearly fully dense across the entire sample length of 54 mm (Figure 6.8 (b)), and only has a few irregular and rounded defects along the sidewalls due to vaporization instability, as shown in Figure 6.8 (a). The high density of 99.99% for cylinder N from Print 2 is very close to its replicate cylinder 5 from Print 1 that has a density of 99.97%, which verifies the reproducibility of the density findings for a taller build and a different build plate location.

Similar to Ti64, Ti-6242Si is expected to form a primarily martensitic microstructure in LPBF [296, 308]. Literature suggests a broad range of LPBF processing parameters across the 3 melting modes to obtain near-fully dense parts for such titanium alloys [314, 217, 315, 316, 4], which is the outcome that is observed through this evaluation of melting modes on density of LPBF Ti-6242Si. Additionally, since it is not possible to observe melt pools in three-dimensional components made out of martensitic titanium alloys such as Ti64 [317], the use of normalized processing diagrams alongside non-destructive characterization equipment such as X-ray computer tomography is an effective method to rapidly develop process parameters for similarly-martensitic materials such as Ti-6242Si.

6.4.3 Surface roughness analysis

An evaluation of the effects of LPBF border process parameters (such as laser power and scan speed by virtue of point distance and exposure time) for the border scan showcases a trend towards reduced surface roughness (Sa and Sz) in the keyhole melting mode as mapped in Figure 6.5. These findings are similar to results in Chapter 5 (previously published in [251]) during LPBF of Ti64, where a preliminary investigation into the effects of border LPBF process parameters lead to Sa values of 9.05 ± 0.37 µm with transition/keyhole mode process parameters compared to 17.05 ± 1.59 µm for conduction mode process parameters. Figure 6.9 showcases a significantly reduced impact of balling and adhered partially fused powder particles on the side-skin surface of Ti-6242Si cuboids in the transition and keyhole mode LPBF border process parameters, when compared to the conduction mode border process parameters. The lowest surface roughness (Sa and Sz) values in Figure 6.5 were observed in the samples manufactured with a keyhole mode border process parameter combination, which could be associated to the effects of powder denudation caused by the increasing extent of vaporization shown by Matthews et al. [108], leading to lower side-skin surface roughness during LPBF, confirmed by Figure 6.9. It must be noted that studying the effect of core LPBF process parameters or studying the interaction of core and border process parameters on side-skin surface roughness of Ti-6242Si was outside the scope of this work. Care must be taken to understand the extent to which the border

(a)

Cylinder N, 99.99%

(b)
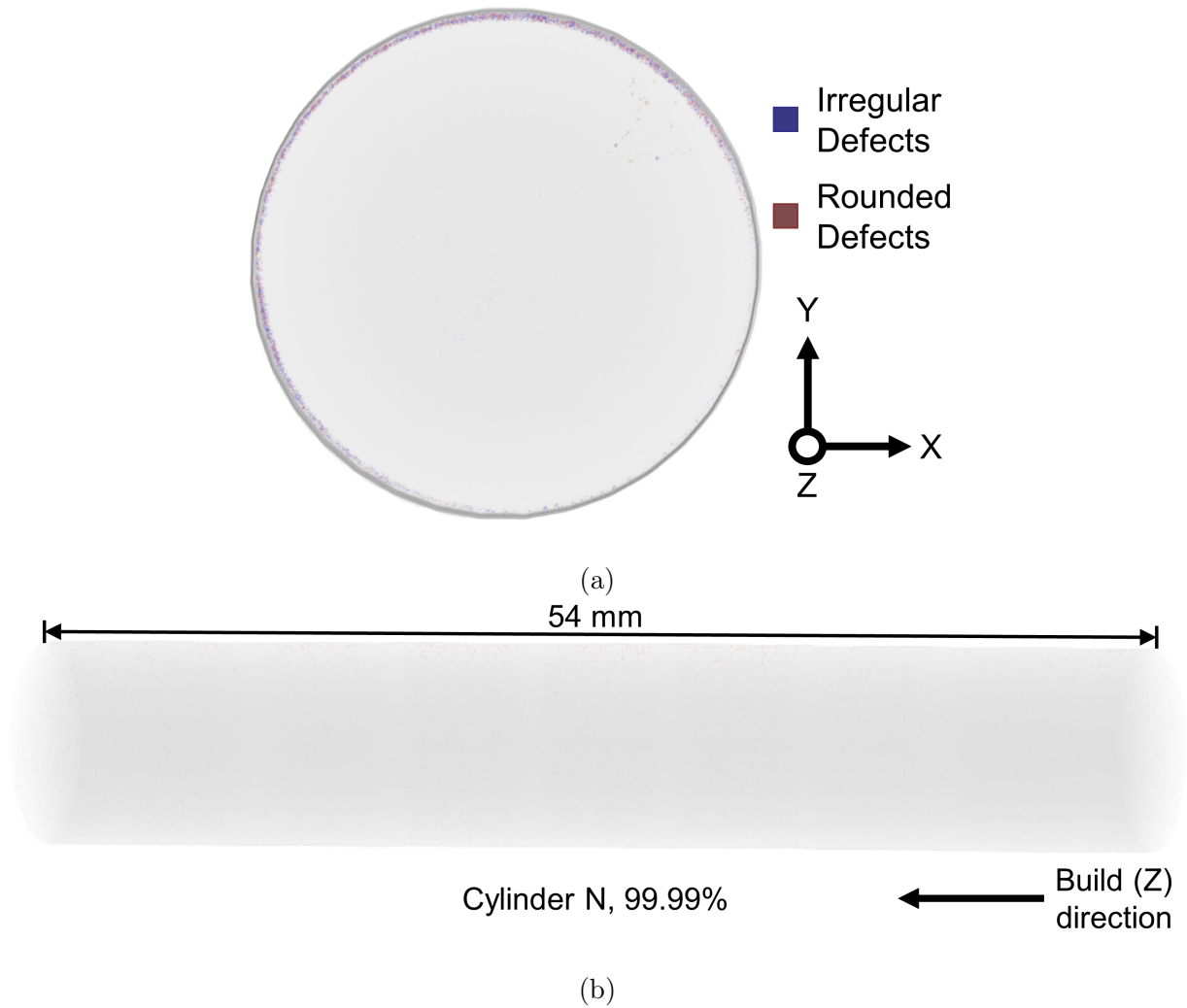
Figure 6.8: An orthographic projection of the porous defect space (above 4 voxels) in the build plate (XY) plane (a), and a 3D visualization of the porous defect space along the build direction (Z) (b) of cylinder N from Print 2, along with the density value obtained from the XCT data. Cylinder N from Print 2 has the same process parameters as cylinder 5 from Print 1 shown in Figures 6.6 and 6.7

parameters in keyhole melting mode may detrimentally contribute to sub-surface porosity
and elevated edges. Subsurface porosity will lead to a reduction in the fatigue life of a
given part [209], while elevated edges can lead to the powder recoater hitting the edges of
a given sample thereby disturbing the flow of powder on the LPBF build plate, and can
also lead to recoater blade damage [10].
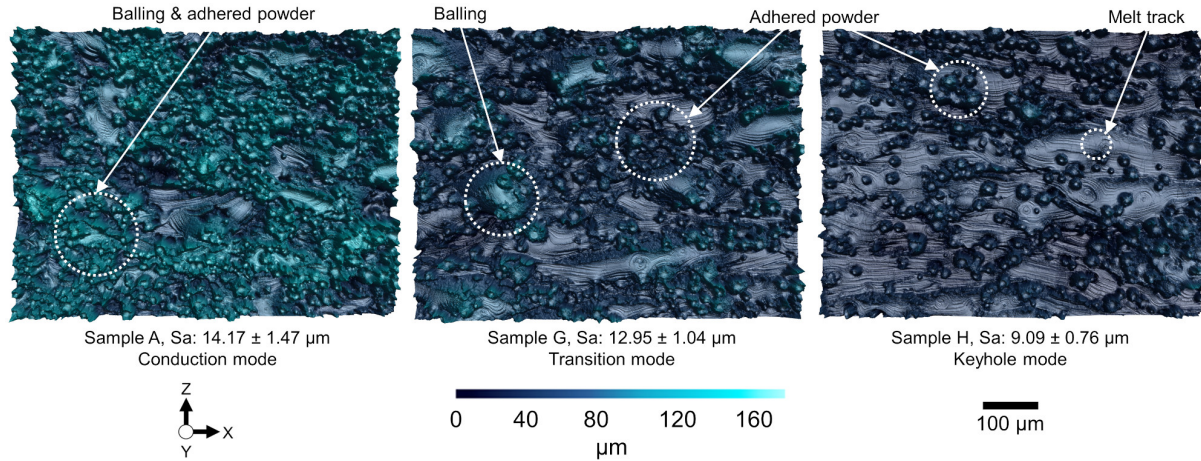
Figure 6.9: A three-dimensional height map representation of side-skin surface
characteristics along with Sa values for sample A (conduction mode), sample G
(transition mode), sample H (keyhole mode).

6.4.4   Origins of cracking in Ti-6242Si

While cylinders 6 and 8 from Print 1 had a high density in the XCT results shown in
Figure 6.6, macroscopic cracks were observed in both samples at 2 separate locations
perpendicular to the build direction as shown in Figure 6.10. An optical micrograph of
cylinder 8 along the XY plane and build (Z) direction in Figure 6.11 confirms the presence of
cracking perpendicular to the build direction alongside a near fully dense cylinder otherwise
as observed in XCT results of Figure 6.6. Cylinder 5 from Print 1 which had a density
of 99.97% is also visualised through optical micrographs along the XY plane and the Z
direction in Figure 6.11, thereby confirming the presence of close to no porous defects
in the core and subsurface regions as shown by XCT results in Figure 6.6 and Figure 6.7.
from Cracking during LPBF of Ti-6242Si has not been reported in the previous two studies
targeting LPBF of Ti-6242Si [296, 308].

119

As per laser and electron beam welding literature, titanium alloys, particularly α and near-α titanium alloys, are known to resist weld-metal liquation or heat affected zone (HAZ) cracking. Additionally, solidification cracking is generally observed in highly alloyed Ti-alloys, such as Ti-15V-3Al-3Cr-3Sn, which have a greater difference between the solidus and liquidus temperatures, thereby leading to a wider solidification temperature range [318]. The wider solidification temperature range issue is also a common limitation during the processing of traditional high-strength aluminium alloys (e.g. Al 6061 and Al 7075 with solidification ranges of over 100 K and 150 K respectively) by additive manufacturing [95]. Ti-6242Si has a solidification range ($T_m - T_s$ from Table 6.6) of 34 K and Ti-6A1-4V (Ti64) has a solidification range of 50 K ($T_m - T_s$ from Table 3.4, and these Ti alloys are hence not expected to present any solidification cracking occurrence; however, the martensitic α' microstructure observed during welding is known to create additional residual stresses [318].

LPBF involves the joining of sequential neighbouring micro-weld lines in a given layer (in 2D) and stacking of numerous layers containing a high number of weld lines (in 3D); as such, residual stresses are known to pose significant issues in LPBF [6]. Observed cracking during LPBF of Ti-6242Si could be potentially related to excessive shrinkage and higher residual stress in keyhole mode as reported by Song et al. for LPBF of Ti64 [319]. This was the primary hypothesis for understanding the origins of cracking during LPBF of Ti-6242Si that was investigated via Print 2.

Print 2 was monitored using a action camera (GoPro) while being printed, and nothing of significance was visible during the print capture. Immediately after printing, when Print 2 was being depowdered and taken out of the build chamber, cracking sounds were heard and cracks were observed in cylinder P and cube O, as shown in Figure 6.12. Cylinders P and cube O have the same parameters as cylinders 6 and 8 from Print 1 (keyhole mode) which had also cracked similarly as shown in Figure 6.10. Cracks appeared in cube P as well as shown by the left side of Figure 6.13. Two more cracks close to the build plate were also observed in cylinder P as shown in the right side of Figure 6.13. Following this imaging of the cracked samples, residual stress analysis was conducted on the top surface of the 6 cylinders as shown in Figure 6.3.

After all the parts were cut-off from the build by EDM, macroscopic cracks were observed in cylinders M and O (Figure 6.14) and cubes M and N (Figure 6.15). Hence, cracking was observed in 3 cylinders (M, O, and P) and 4 cubes (M, N, O, and P) which were predicted to lie in the transition (samples codes M and N) and keyhole (sample codes O and P) melting modes as per Figure 6.4b. No cracking was observed for any of the conduction mode cylinders and cubes from Print 2.
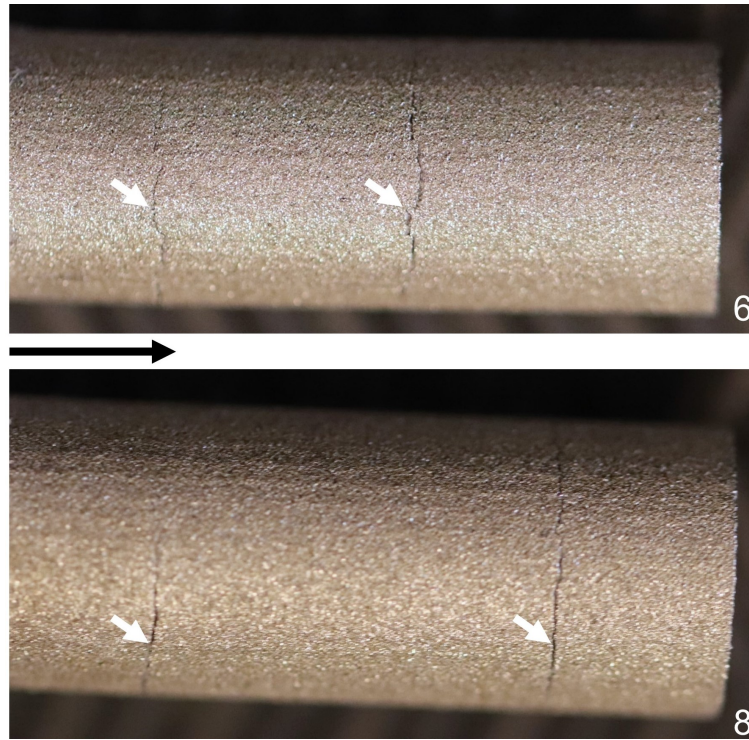
Figure 6.10: Macroscopic cracking (white arrows) observed in cylinders 6 and 8 from Print 1, which are predicted to have keyhole mode core process parameters as per Figure 6.4a. Build (Z) direction is given by the black arrow.
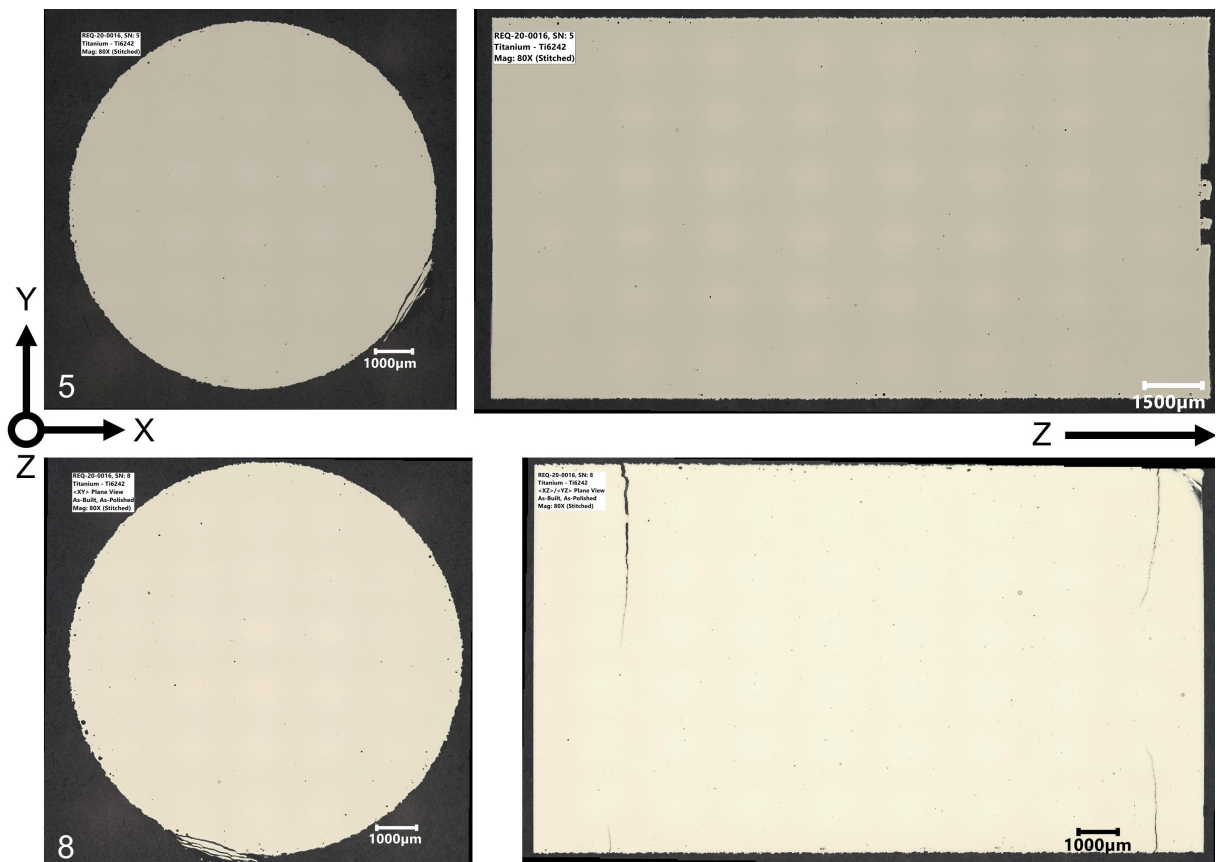
Figure 6.11: Optical micrographs of cylinder 5 (transition mode) and cylinder 8 (keyhole mode) from Print 1 along the XY plane and the build (Z) direction.
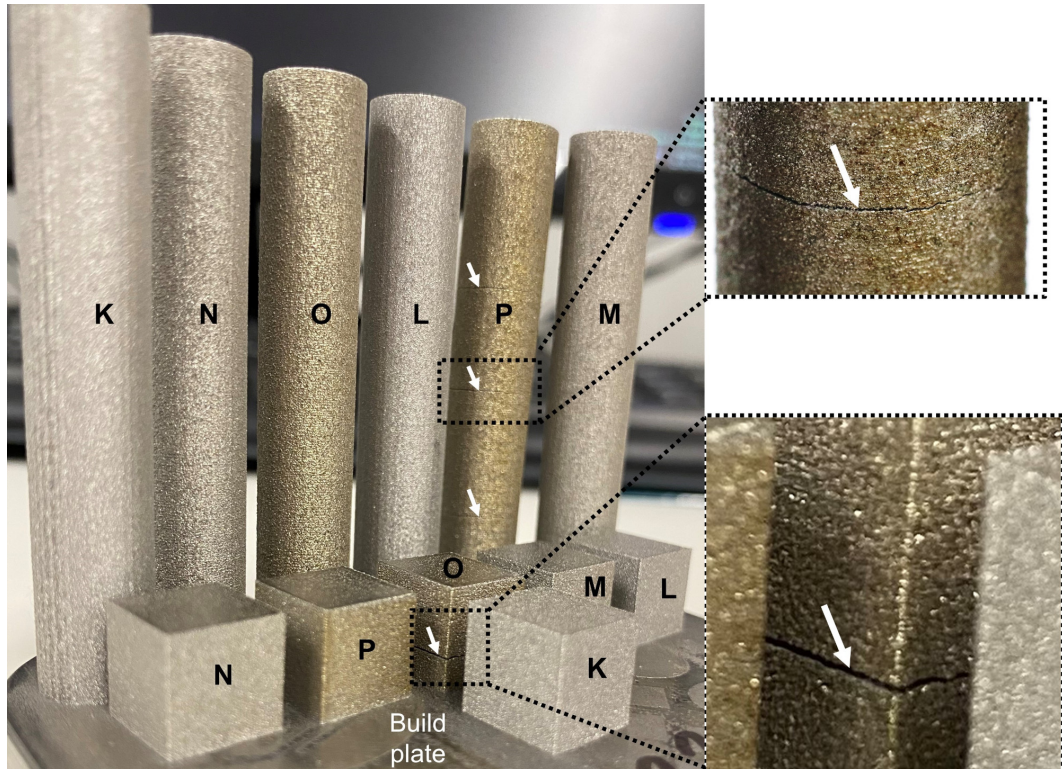
Figure 6.12: Macroscopic cracking (white arrows) observed in cylinder P and cube O from Print 2.
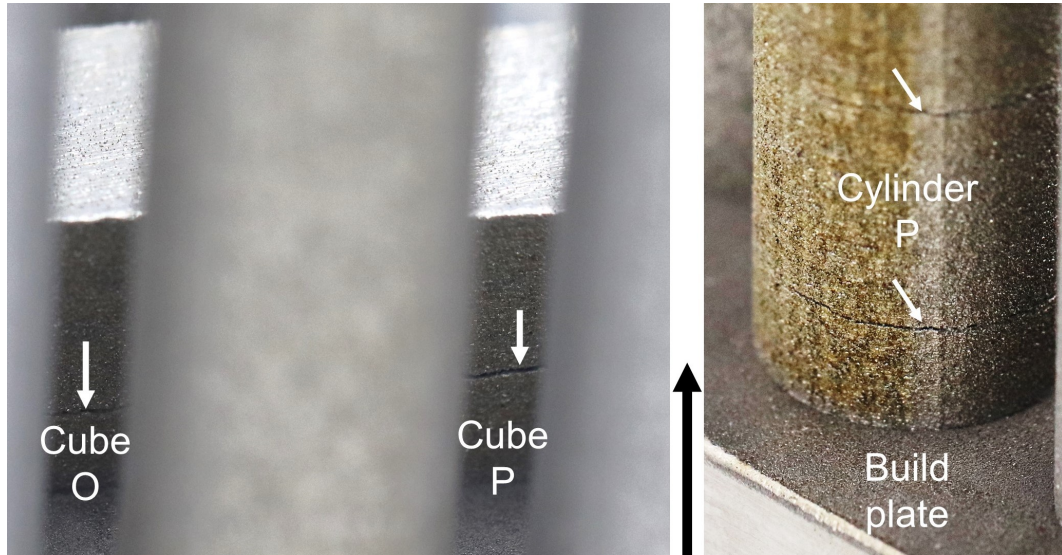
Figure 6.13: Macroscopic cracking (white arrows) in cubes O and P (left). Two additional cracks (white arrows) observed in cylinder P close to the LPBF build plate (right). Build (Z) direction is given by the black arrow.

The results obtained from the residual stress testing equipment from Print 2 are summarized in Table 6.7. Since cylinder P had cracked prior to the residual stress measurements, it has the lowest σ_{xx} of 466 MPa as the cracking mechanism relieved the residual stresses within this cylinder. Cylinder O did not have observable cracks before the residual stress measurement, but was observed to crack instantly after EDM cutting as shown in Figure 6.14. Although cylinder O from print 2 did not crack, cube O had macroscopic cracking right after Print 2 was completed as shown in Figure 6.12. This could mean that there may have been microscopic cracks within cylinder O which grew after the stresses of EDM cutting to lead to the numerous macroscopic crack eventually observed.

In LPBF parts, higher in-plane (XY) residual stresses are reported across literature when compared to stresses along the printing (Z) direction. LPBF simulations and experiments have shown that the top (last few layers) and bottom (attached to the build plate) portions of a part have tensile residual stresses and the middle region has compressive residual stresses. [6]. Tensile residual stresses are also known to affect cracking tendency of LPBF components [6, 186]. These findings guide the reasoning behind measuring residual stresses at the top surfaces of the Ti-6242Si coupons in this work. Additionally, cylinders M and O (Figure 6.15) and cubes M and N (Figure 6.14) developed cracks only after being cut-off from the LPBF build plate. This cracking phenomena that is observed only after

124

Cylinder O
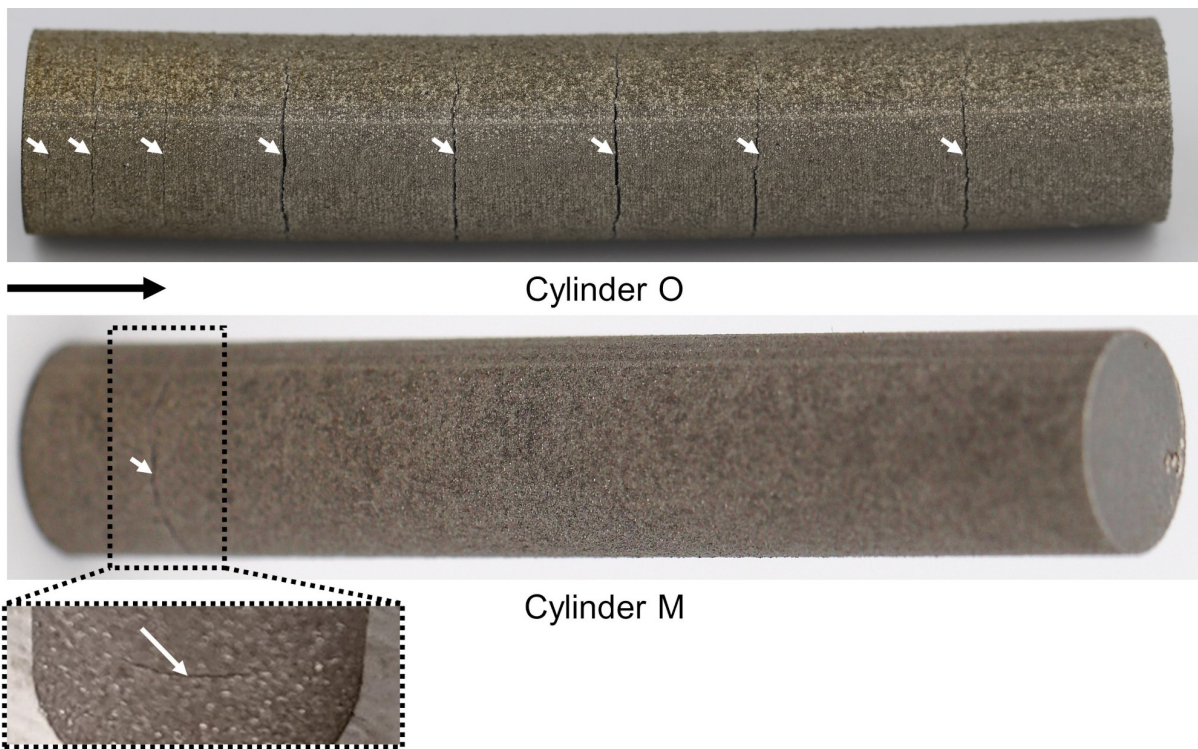
Cylinder M

Figure 6.14: Macroscopic cracking (white arrows) observed in cylinders O and cube M from Print 2 after EDM cutting from the build plate. Build (Z) direction is given by the black arrow.
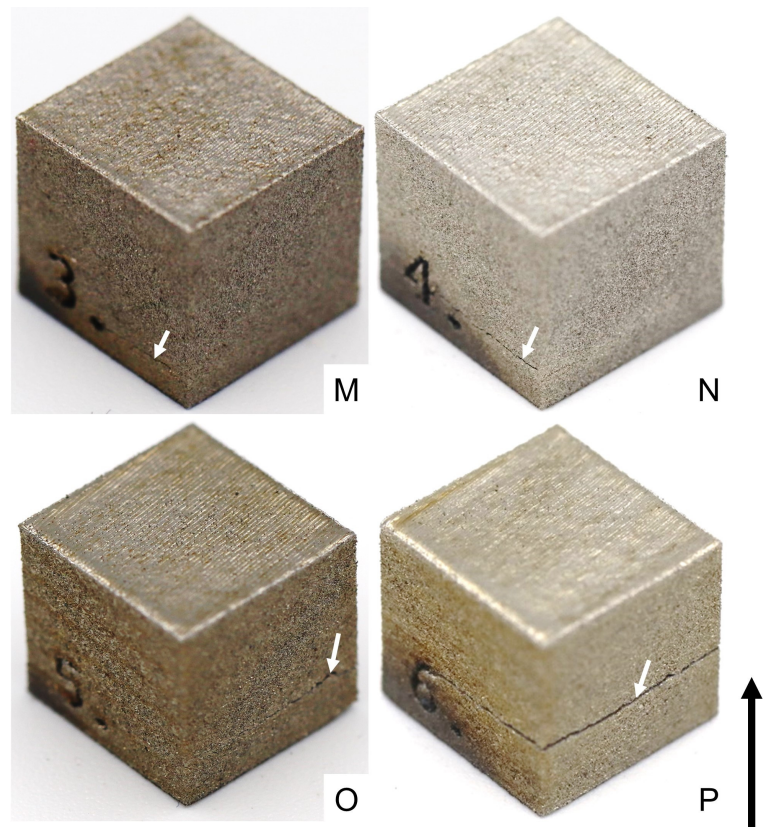
Figure 6.15: Macroscopic cracking (white arrows) observed in cubes M, N, O, and P from Print 2 after EDM cutting from the build plate. Build (Z) direction is given by the black arrow.

cutting is a common mechanism for the relaxation of residual stresses in LPBF [320, 321], which points towards residual stresses having a significant effect on the crack formation during LPBF of Ti-6242Si in this work. Another contributor towards cracking during LPBF of Ti-6242Si could be the interaction between residual stress-fields during part production and irregularly-shaped porous defects that are present in all samples studied in this work [6].

Additionally, the direction of core meander scanning orientation was rotated by 67° between successive layers for all coupons in the work. An inter-layer rotation of the scanning strategy, particularly by 67°, has been shown to lead to a homogeneous in-plane (XY) residual stress distribution in LPBF [188, 189, 6]. Hence, although σ_{yy} was not measured for this work, it would be expected to have a value approximately equal to σ_{xx} due to the inter-layer rotation of the scanning strategy by 67°.

The normal residual stress, σ_{xx}, from Table 6.7 was visualised versus two different dimensionless parameters in Figure 6.16. Figure 6.16a shows σ_{xx} versus a commonly used to term to visualize energy input for LPBF, normalized enthalpy, $\Delta H/h_s$ [86]. $\Delta H/h_s$, normalized enthalpy can be defined in terms of q^* (Equation 3.1) and v^* (Equation 3.2) by Equation 6.1. Figure 6.16b shows σ_{xx} versus $E^* \tan^{-1}(\sqrt{8/v^*})$ which is directly proportional to the equation for a stationary laser beam as defined in Equation 3.33 from previous work [10].

In Equation 6.1, ΔH is the specific enthalpy [J/m³], h_s is the enthalpy of the solid material at melting [J/m³], A is the laser absorptivity of the solid material, α is the thermal diffusivity of the solid material at the melting point [m²/s], and σ is the laser beam diameter [m]. The enthalpy at melting is given by $h_s = \rho C_p T_m$, where C_p is the specific heat capacity [J/kg K], ρ is the density of the material [kg/m³], and T_m is the melting temperature of the material [K].

The normal residual stress, σ_{xx}, scales better with $E^* \tan^{-1}(\sqrt{8/v^*})$ when compared to normalized enthalpy as is noted by the higher R^2 of 0.99 compared to 0.48. Another observation from Table 6.7 is the σ_{xx} values for the transition mode cylinders M (563 MPa) and N (631 MPa). These values of the residual stresses for the transition mode cylinders are quite close to the yield strength of heat-treated Ti-6242Si at 500 °C which is 740 ± 18 MPa [296]. This could potentially point to why cubes M and N cracked after EDM cutting as shown in Figure 6.15.

$$\frac{\Delta H}{h_s} = \frac{AP}{h_s \sqrt{\pi \alpha v \sigma^3}} = \frac{q^*}{\sqrt{8 \pi v^*}} \tag{6.1}$$
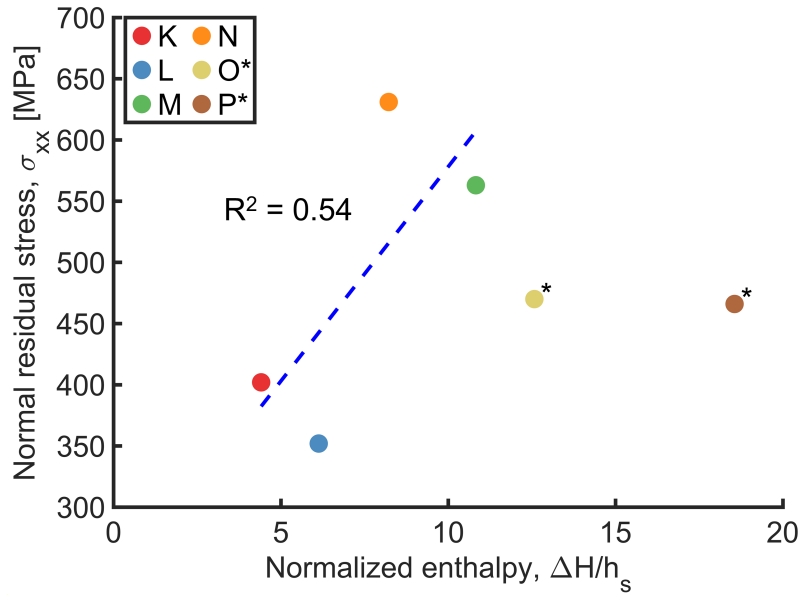
(a)
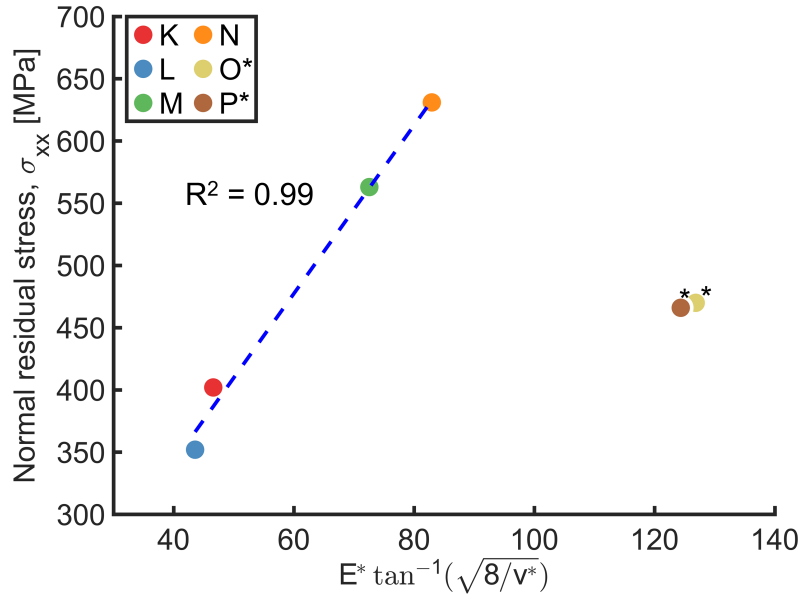
(b)

Figure 6.16: Scaling relationship for the normal residual stress, σ_{xx}, from Print 2 in MPa with respect to two dimensionless parameters. (a) σ_{xx} vs Normalized enthalpy, $\Delta H/h_s$. (b) σ_{xx} vs $E^* \tan^{-1}(\sqrt{8/v^*})$. The cracked cylinders are shown by an asterisk sign (*)

Table 6.7: Normal (σ_{xx}) residual stresses measured from the top surface of the six cylinders from Print 2. Avg: Average, Std. Dev.: standard deviation, RS: residual stress testing, EDM: EDM cutting from the build plate.

Cylinder code	σ_{xx} [MPa]		Cracking period	
	Avg	Std Dev	Before RS	After EDM
K	402	38		
L	352	36		
M	563	59		✓
N	631	60		
O	470	80		✓
P	466	88	✓	✓

Residual stresses in additive manufacturing (AM) components are affected by the technology selected, the material selected, and the process parameters used. Amongst the two classes of powder bed fusion technologies with a high industrial uptake [64], LPBF generally has a build chamber temperature close to room temperature, while EBM generally has a build chamber temperature of 500 °C-800 °C [6]. This results in a lower temperature gradient during EBM when compared to LPBF, thereby leading to a higher cooling rate during LPBF when compared to EBM [322, 323, 324]. The higher cooling rates lead to significant difference in resulting residual stresses in the final printed components, with a difference of up to 400 MPa reported in a comparative study of LPBF and EBM in Inconel 718 [325]. Bartlett and Li [6] reviewed the effect of material properties on residual stresses during LPBF for 5 popular materials - Ti64, SS 316L, Inconel 718, commercially pure Ti (CP Ti), and 18Ni300 Maraging steel. A linear relationship with an R^2 value of 0.95 was observed for the influence of thermal diffusivity on residual stresses. Similarly, residual stresses also scaled linearly with thermal conductivity with an R^2 value of 0.85. A lower thermal conductivity and diffusivity value led to high residual stresses, on average. In Table 6.8, a comparison between the thermal conductivity and diffusivity values of the 5 materials surveyed by Bartlett and Li [6], alongside AlSi10Mg and Ti-6242Si at room temperature is provided. Since the thermal conductivity and diffusivity values of Ti-6242Si are quite close to that of Ti64, higher residual stresses would be expected at similar sets of processing materials for these 2 alloys when compared to the other alloys from Table 6.8.

Besides material properties, LPBF process parameters and laser scanning strategy are known to have the greatest influence on residual stresses [52], particularly the beam energy input to the material [186, 6]. There is a fairly consistent trend of residual stresses increas-

Table 6.8: Thermal conductivity and thermal diffusivity of LPBF materials taken at room temperature [52]

Material	Thermal conductivity [W/(mK)]	Thermal diffusivity $10^{-6}[\text{m}^2/\text{s}]$
Ti-6242Si	7	3.35
Ti64	6.7	2.70
Inconcel 718	11.4	3.19
SS 316L	21.5	5.41
AlSi10Mg	113	43.95
CP Ti	16	6.82
18Ni300 Maraging Steel	15	4.12

ing with higher laser power and lower scanning speed for SS 316L [326, 327, 186] and Ti64 [328, 186]. Similarly, Bartlett and Li [6] note in their literature review that the penetration depth of the melt pool plays the largest role in determining the residual stresses in LPBF. The higher expected melt pool depths for the transition and keyhole mode samples from Print 2 could hence be the primary reason for the observed cracking in sample code M, N, O, and P, when compared to the conduction mode samples M and N which showed no cracking. Figure 6.16b shows a linear scaling relationship between the principal residual stress, σ_{xx}, and $E^* \tan^{-1}(\sqrt{8/v^*})$, and supports this melting mode-driven hypothesis, since the dimensionless term selected for Figure 6.16b is similar to the temperature prediction model used for predicting and visualizing the melting mode and thereby melt pool morphology thresholds in Chapter 3 [10].

There is also a possibility of hydrogen-induced embrittlement causing cracks in the martensitic microstructure, as observed by Silverstein and Eliezer during LPBF of Ti64 [329]. Additionally, subsolidus cracking during the arc welding of Ti-6211, an alpha-beta $(\alpha + \beta)$ Ti alloy, was observed to be caused by poor hot ductility of the martensitic alpha-prime (α') microstructure by Damkroger et al. [330]. Bowden and Starke [331] had previously found that Ti6211 structures with a larger prior beta (β) grain size were more susceptible to a high-temperature ductility loss than were samples with a smaller prior beta grain size, but Damkroger et al. [330] found the opposite to be true. Lastly, Figure 6.12 points to a discolouration of the keyhole mode coupons with codes O and P. This discolouration could point towards the role of a potential oxygen or nitrogen contamination during high energy density keyhole mode processing of Ti-6242Si using LPBF, as well

as material vaporisation phenomena, which could impact cracking by the formation of deleterious oxides and/or nitrides. These additional hypotheses for cracking origins during LPBF of Ti-6242Si pose interesting scientific queries for future research into crack formation for this material system.

6.5   Conclusions

This work involved the use of process diagrams and a temperature prediction model for investigating the effect of LPBF process parameters including laser power, scan speed, and beam spot radius, on the density and side-skin surface roughness of Ti-6242Si, a near-alpha titanium alloy. Additionally, cracking part quality outcomes were studied by virtue of imaging and residual stress measurements. The key findings are summarized below:

1. Normalized processing diagrams and X-ray computed tomography show that Ti-6242Si has a broad process window with parts above 99.90% density observed in conduction, transition, and keyhole melting modes of LPBF. The overall density range obtained was 99.55-99.98%. The highest density parts (up to 99.98%) are observed in the transition melting mode for Ti-6242Si, with reduced number of defects in both the core and subsurface regions.

2. Subsurface porous defects are the main contributor towards porosity across all melting modes for LPBF of Ti-6242Si. These defects are caused by rapid formation and collapse of deep vaporized regions due to the lower laser beam velocity at the turn points of a given layer, which is common across most LPBF systems. Simulations in this work predicted vaporization for all of the LPBF process parameters used, leading to the prevalence of subsurface defects in all samples.

3. Keyhole mode LPBF process parameters for border scans of Ti-6242Si leads to a side-skin surface roughness, Sa, values of less than 10 μm, which is the lowest roughness value when compared to transition and conduction mode LPBF process parameters. This reduction is associated with reduced effects of adhered partially fused powder particles and balling on the side-skin surfaces of Ti-6242Si.

4. Transition and keyhole mode LPBF of Ti-6242Si leads to macroscopic cracking perpendicular to the build direction, which is primarily attributed to the higher residual stresses during solidification which are close to the yield strength of Ti-6242Si at 500 °C.

The application of the methods proposed in this work can help quickly identify LPBF process parameters for successful production of near fully dense and crack-free Ti-6242Si with low surface roughness. This could increase the adoption of LPBF Ti-6242Si for additional high-temperature load bearing aerospace applications. The fundamental understanding of challenges during LPBF of titanium alloys developed in this chapter are used to make recommendations for the manufacturability of complex Ti and Ti-6Al-4V lattice structures in Appendix A.

Chapter 7

Conclusions and future work

The focus of this thesis was to develop a better understanding of LPBF at the mesoscale and macroscale by the creation of a tool to predict and visualize the conduction, transition, and keyhole melting modes in LPBF. The melting mode tool is used to develop an understanding of differences between low reflectivity (titanium, ferrous, and nickel) alloys and high reflectivity (aluminium) alloys through simulations and experiments for improving macroscale performance indicators including density, surface roughness, residual stresses, mechanical properties, and printability of complex structures for defence, aerospace, automotive, and biomedical applications.

Development of the modelling tool to visualize and predict the conduction, transition, and keyhole melting modes in LPBF is described in Chapter 3. This modelling tool is independent of material for specific classes of materials, of LPBF system, of laser modulation, and of powder layer thickness. Chapters 4, 5, and 6 use the modelling tool developed in Chapter 3 to understand porous defect characteristics in AlSi10Mg, side-skin surface characteristics in Ti-6Al-4V, and porous defects, side-skin surface characteristics, residual stresses, and cracking in Ti-6242Si respectively. While each chapter provides a conclusion specific to the chapter content, this chapter aims to summarize the main conclusions and proposed future work for continuation of this thesis.

7.1 Conclusions

The main conclusions from this thesis are summarized below:

133

- Normalized processing diagrams have been developed to visualize the three melting modes (conduction mode, transition mode, and keyhole mode) observed in LPBF. The normalized processing diagrams obtained in this thesis, for the first time in LPBF, are shown to be independent of material, LPBF system, and processing parameters such as powder layer thickness within the datasets presented herein.

- A temperature prediction model has been developed to predict the thresholds between the conduction, transition, and keyhole melting modes. The efficacy of these predicted thresholds has been evaluated experimentally for low reflectivity (titanium and ferrous) alloys and high reflectivity (aluminium) alloys.

- For low reflectivity alloys, a vaporization depth greater than 0.5 and 0.8 times the beam spot radius used corresponds to the thresholds between conduction to transition mode and transition to keyhole mode respectively. For high reflectivity alloys, surface vaporization and a vaporization depth greater than 0.5 times the beam spot radius used corresponds to the thresholds between conduction to transition mode and transition to keyhole mode respectively.

- For high reflectivity materials such as aluminium alloys, divergent beams with resulting focal diameters >100 µm help to obtain a conduction mode microstructure leading to parts with densities of over 99.98%, with close to no porous defects in the subsurface regions. When working with a focused beam, stabilizing melt pool and spatter dynamics in the transition melting mode by using an appropriate laser power and velocity combination can help in minimizing defects and obtaining densities close to 99.98%, similar to conduction mode densities. For aluminium alloys, a melt pool aspect ratio (ratio of depth to width) of ≈0.4 is observed to be the threshold between conduction and transition/keyhole mode melt pools in aluminium alloys, which differs from the conventionally assumed melt pool aspect ratio of 0.5.

- When low beam velocity regimes in the transition and keyhole melting modes are used for core LPBF processing parameters, a significant reduction in adhered partially-fused powder particles, balling, and molten pool spatter is achieved for side-skin surfaces, at the risk of increased core porosity. Similarly, border processing parameters that lie in the keyhole melting mode with lower beam velocity settings, and conservative laser powers (to avoid elevated edges) lead to surface roughness, Sa, values of lesser than 10 µm, which is significantly lower than the roughness values obtained for conduction and transition mode borders in Ti64 and Ti-6242Si. This significant reduction in surface roughness is due to a negligible contribution from partially melted powder particles in the keyhole melting mode border.

134

- Simulation and experimental efforts show that Ti-6242Si has a broad process window with parts above 99.90% density observed in conduction, transition, and keyhole melting modes of LPBF. While the highest density parts (up to 99.98%) are observed in the transition melting mode for Ti-6242Si, transition and keyhole mode LPBF of Ti-6242Si could also lead to macroscopic cracking perpendicular to the build direction, which is attributed primarily to the higher residual stresses during solidification which are close to the yield strength of Ti-6242Si at 500 °C.

7.2 Recommendations and future work

Absorptivity differences between high reflectivity and low reflectivity metallic materials

As LPBF is increasingly adopted for end-use products, the library of materials manufactured by this technology is bound to grow at a rapid rate. While the LPBF of low reflectivity materials such as titanium, ferrous, and nickel-based alloys have been extensively studied and is well understood [7], there is a vacancy in the understanding of high reflectivity materials such as aluminium and copper alloys. The absorptivity scaling laws developed by Ye et al. [7] for low reflectivity materials have applied well to the work in this thesis; however, it was also observed that the same scaling laws do not apply to the aluminium alloy studies in this thesis. In situ measurements of absorptivity during LPBF by Trapp et al. [9] for aluminium alloys and Gargalis et al. [265] for copper alloys have shown significant differences in the absorptivity characteristics when compared to low reflectivity materials. Additionally, the absorptivity scaling law proposed by Ye et al. [7] is also used in a keyhole stability prediction tool developed by Gan et al. [82]. In situ laser absorptivity measurements for low reflectivity and high reflectivity materials is hence of importance as it will help in making the normalized processing diagrams developed in this work independent of any material used by development of scaling laws to account for such differences, and it could be used in conjunction with other modelling efforts to predict keyhole stability.

Tailoring microstructure in LPBF

The production of complex parts in LPBF is digitally-controlled all the way from a computer-aided design model, to monitoring and controlling the process while parts are being manufactured. An important component in this digitization of LPBF is the attainment of

135

an almost complete control of the numerous process parameters involved and thereby the resulting material's microstructure [332]. There have been numerous attempts at tailoring a material's microstructure through digital control of process parameters [333, 334, 335, 336, 337]. In addition to the experimental attempts at controlling microstructure through control of LPBF process parameters, there have also been theoretical modelling attempts in order to develop of better understanding of microstructure development in LPBF [338, 339, 197, 340, 341]. In the aforementioned multi-level modelling attempts, a common thread is the development of a heat transfer modelling (either analytically or numerically) to first predict the morphology of melt pools. This thesis currently helps in predicting LPBF process parameters for near fully dense parts across the three melting modes in LPBF. Future work would involve modelling of melt pool morphologies across melting modes in LPBF which could feed into microstructure prediction models to predict differences in microstructure in LPBF. Simulations from this modelling attempt could then be used for predict microstructure at the part scale in LPBF. Following this, laser scan path strategies would be developed to tailor microstructure for application-specific requirements due to significant differences in microstructure reported in literature across melting modes.

References

[1] T. DebRoy, T. Mukherjee, H. Wei, J. Elmer, J. Milewski, Metallurgy, mechanistic models and machine learning in metal printing, Nature Reviews Materials 6 (2021) 48–68. doi:10.1038/s41578-020-00236-1.

[2] J. Yin, D. Wang, L. Yang, H. Wei, P. Dong, L. Ke, G. Wang, H. Zhu, X. Zeng, Correlation between forming quality and spatter dynamics in laser powder bed fusion, Additive Manufacturing 31 (2020) 100958.

[3] R. Cunningham, C. Zhao, N. Parab, C. Kantzos, J. Pauza, K. Fezzaa, T. Sun, A. D. Rollett, Keyhole threshold and morphology in laser melting revealed by ultrahigh-speed x-ray imaging, Science 363 (6429) (2019) 849–852, pMID: 30792298. doi:10.1126/science.aav4687.

[4] J. Dilip, S. Zhang, C. Teng, K. Zeng, C. Robinson, D. Pal, B. Stucker, Influence of processing parameters on the evolution of melt pool, porosity, and microstructures in ti-6al-4v alloy parts fabricated by selective laser melting, Progress in Additive Manufacturing 2 (3) (2017) 157–167.

[5] A. Kaplan, Metallurgy and imperfections of welding and hardening, in: The Theory of Laser Materials Processing, Springer, 2017, pp. 241–261. doi:10.1007/978-3-319-56711-2_8.

[6] J. L. Bartlett, X. Li, An overview of residual stresses in metal powder bed fusion, Additive Manufacturing 27 (2019) 131–149.

[7] J. Ye, S. A. Khairallah, A. M. Rubenchik, M. F. Crumb, G. Guss, J. Belak, M. J. Matthews, Energy coupling mechanisms and scaling behavior associated with laser powder bed fusion additive manufacturing, Advanced Engineering Materials 21 (7) (2019) 1900185.

[8] R. Fabbro, K. Chouf, Keyhole modeling during laser welding, Journal of Applied Physics 87 (9) (2000) 4075–4083. doi:10.1063/1.373033.

[9] J. Trapp, A. M. Rubenchik, G. Guss, M. J. Matthews, In situ absorptivity measurements of metallic powders during laser powder-bed fusion additive manufacturing, Applied Materials Today 9 (2017) 341–349. doi:10.1016/j.apmt.2017.08.006.

[10] S. Patel, M. Vlasea, Melting modes in laser powder bed fusion, Materialia 9 (2020) 100591. doi:10.1016/j.mtla.2020.100591.

[11] Pulstec, Residual stress analyzer μ-x360s operating manual, Tech. rep., Pulstec Industrial Co., Ltd., Japan (8 2016).

[12] X. S. Liu, X. H. Zhang, C. S. Rajapakse, M. J. Wald, J. Magland, K. K. Sekhon, M. F. Adam, P. Sajda, F. W. Wehrli, X. E. Guo, Accuracy of high-resolution in vivo micro magnetic resonance imaging for measurements of microstructural and mechanical properties of human distal tibial bone, Journal of Bone and Mineral Research 25 (9) (2010) 2039–2050.

[13] R. Gauthier, H. Follet, C. Olivier, D. Mitton, F. Peyrin, 3d analysis of the osteonal and interstitial tissue in human radii cortical bone, Bone 127 (2019) 526–536.

[14] T. Hildebrand, A. Laib, R. Müller, J. Dequeker, P. Rüegsegger, Direct three-dimensional morphometric analysis of human cancellous bone: microstructural data from spine, femur, iliac crest, and calcaneus, Journal of bone and mineral research 14 (7) (1999) 1167–1174.

[15] J. S. Thomsen, A. Laib, B. Koller, S. Prohaska, L. Mosekilde, W. Gowin, Stereological measures of trabecular bone structure: comparison of 3d micro computed tomography with 2d histological sections in human proximal tibial bone biopsies, Journal of Microscopy 218 (2) (2005) 171–179.

[16] D. L. Bartel, D. T. Davy, Orthopaedic biomechanics: mechanics and design in musculoskeletal systems, Prentice Hall, 2006.

[17] J. Park, R. S. Lakes, Biomaterials: an introduction, Springer Science & Business Media, 2007.

[18] A. H. Burstein, D. T. Reilly, M. Martens, Aging of bone tissue: mechanical properties., The Journal of bone and joint surgery. American volume 58 (1) (1976) 82–86.

[19] N. Taniguchi, S. Fujibayashi, M. Takemoto, K. Sasaki, B. Otsuki, T. Nakamura, T. Matsushita, T. Kokubo, S. Matsuda, Effect of pore size on bone ingrowth into porous titanium implants fabricated by additive manufacturing: An in vivo experiment, Materials Science and Engineering: C 59 (2016) 690–701.

[20] M. de Wild, R. Schumacher, K. Mayer, E. Schkommodau, D. Thoma, M. Bredell, A. Kruse Gujer, K. W. Grätz, F. E. Weber, Bone regeneration by the osteoconductivity of porous titanium implants manufactured by selective laser melting: a histological and micro computed tomography study in the rabbit, Tissue Engineering Part A 19 (23-24) (2013) 2645–2654.

[21] S.-H. Wu, Y. Li, Y.-Q. Zhang, X.-K. Li, C.-F. Yuan, Y.-L. Hao, Z.-Y. Zhang, Z. Guo, Porous titanium-6 aluminum-4 vanadium cage has better osseointegration and less micromotion than a poly-ether-ether-ketone cage in sheep vertebral fusion, Artificial organs 37 (12) (2013) E191–E201.

[22] W. Xue, B. V. Krishna, A. Bandyopadhyay, S. Bose, Processing and biocompatibility evaluation of laser processed porous titanium, Acta biomaterialia 3 (6) (2007) 1007–1018.

[23] J. Van der Stok, O. P. Van der Jagt, S. Amin Yavari, M. F. De Haas, J. H. Waarsing, H. Jahr, E. M. Van Lieshout, P. Patka, J. A. Verhaar, A. A. Zadpoor, et al., Selective laser melting-produced porous titanium scaffolds regenerate bone in critical size cortical bone defects, Journal of Orthopaedic Research 31 (5) (2013) 792–799.

[24] P. K. Srivas, K. Kapat, P. Dadhich, P. Pal, J. Dutta, P. Datta, S. Dhara, Osseointegration assessment of extrusion printed ti6al4v scaffold towards accelerated skeletal defect healing via tissue in-growth, Bioprinting 6 (2017) 8–17.

[25] J. Wieding, T. Lindner, P. Bergschmidt, R. Bader, Biomechanical stability of novel mechanically adapted open-porous titanium scaffolds in metatarsal bone defects of sheep, Biomaterials 46 (2015) 35–47.

[26] S. Ghouse, N. Reznikov, O. R. Boughton, S. Babu, K. G. Ng, G. Blunn, J. P. Cobb, M. M. Stevens, J. R. Jeffers, The design and in vivo testing of a locally stiffness-matched porous scaffold, Applied materials today 15 (2019) 377–388.

[27] D. Zhao, Y. Huang, Y. Ao, C. Han, Q. Wang, Y. Li, J. Liu, Q. Wei, Z. Zhang, Effect of pore geometry on the fatigue properties and cell affinity of porous titanium scaffolds fabricated by selective laser melting, Journal of the mechanical behavior of biomedical materials 88 (2018) 478–487.

[28] M. Fousová, D. Vojtěch, J. Kubásek, E. Jablonská, J. Fojt, Promising characteristics of gradient porosity ti-6al-4v alloy prepared by slm process, Journal of the mechanical behavior of biomedical materials 69 (2017) 368–376.

[29] S. Arabnejad, R. B. Johnston, J. A. Pura, B. Singh, M. Tanzer, D. Pasini, High-strength porous biomaterials for bone replacement: A strategy to assess the interplay between cell morphology, mechanical properties, bone ingrowth and manufacturing constraints, Acta biomaterialia 30 (2016) 345–356.

[30] K. Moiduddin, S. Darwish, A. Al-Ahmari, S. ElWatidy, A. Mohammad, W. Ameen, Structural and mechanical characterization of custom design cranial implant created using additive manufacturing, Electronic Journal of Biotechnology 29 (2017) 22–31.

[31] M. Taheri Andani, C. Haberland, J. M. Walker, M. Karamooz, A. Sadi Turabi, S. Saedi, R. Rahmanian, H. Karaca, D. Dean, M. Kadkhodaei, et al., Achieving biocompatible stiffness in niti through additive manufacturing, Journal of Intelligent Material Systems and Structures 27 (19) (2016) 2661–2671.

[32] E. Marin, M. Pressacco, S. Fusi, A. Lanzutti, S. Turchet, L. Fedrizzi, Characterization of grade 2 commercially pure trabecular titanium structures, Materials Science and Engineering: C 33 (5) (2013) 2648–2656.

[33] A. Barbas, A.-S. Bonnet, P. Lipinski, R. Pesci, G. Dubois, Development and mechanical characterization of porous titanium bone substitutes, Journal of the mechanical behavior of biomedical materials 9 (2012) 34–44.

[34] A. du Plessis, I. Yadroitsava, I. Yadroitsev, Ti6al4v lightweight lattice structures manufactured by laser powder bed fusion for load-bearing applications, Optics & Laser Technology 108 (2018) 521–528.

[35] A. Arjunan, M. Demetriou, A. Baroutaji, C. Wang, Mechanical performance of highly permeable laser melted ti6al4v bone scaffolds, journal of the mechanical behavior of biomedical materials 102 (2020) 103517.

[36] E. Alabort, D. Barba, R. C. Reed, Design of metallic bone by additive manufacturing, Scripta Materialia 164 (2019) 110–114.

[37] B. Zhang, X. Pei, C. Zhou, Y. Fan, Q. Jiang, A. Ronca, U. D'Amora, Y. Chen, H. Li, Y. Sun, et al., The biomimetic design and 3d printing of customized mechanical properties porous ti6al4v scaffold for load-bearing bone reconstruction, Materials & Design 152 (2018) 30–39.

140

[38] Y.-Z. Xiong, R.-N. Gao, H. Zhang, L.-L. Dong, J.-T. Li, X. Li, Rationally designed functionally graded porous ti6al4v scaffolds with high strength and toughness built via selective laser melting for load-bearing orthopedic applications, Journal of the mechanical behavior of biomedical materials 104 (2020) 103673.

[39] M. Dallago, S. Raghavendra, V. Luchin, G. Zappini, D. Pasini, M. Benedetti, The role of node fillet, unit-cell size and strut orientation on the fatigue strength of ti-6al-4v lattice materials additively manufactured via laser powder bed fusion, International Journal of Fatigue 142 (2021) 105946.

[40] P. Heinl, L. Müller, C. Körner, R. F. Singer, F. A. Müller, Cellular ti–6al–4v structures with interconnected macro porosity for bone implants fabricated by selective electron beam melting, Acta biomaterialia 4 (5) (2008) 1536–1544.

[41] F. Liu, D. Z. Zhang, P. Zhang, M. Zhao, S. Jafar, Mechanical properties of optimized diamond lattice structure for bone scaffolds fabricated via selective laser melting, Materials 11 (3) (2018) 374.

[42] C. Yan, L. Hao, A. Hussein, P. Young, Ti–6al–4v triply periodic minimal surface structures for bone implants fabricated via selective laser melting, Journal of the mechanical behavior of biomedical materials 51 (2015) 61–73.

[43] J. Ge, J. Huang, Y. Lei, P. O'Reilly, M. Ahmed, C. Zhang, X. Yan, S. Yin, Microstructural features and compressive properties of slm ti6al4v lattice structures, Surface and Coatings Technology 403 (2020) 126419.

[44] M. A. El-Sayed, K. Essa, M. Ghazy, H. Hassanin, Design optimization of additively manufactured titanium lattice structures for biomedical implants, The International Journal of Advanced Manufacturing Technology 110 (9) (2020) 2257–2268.

[45] P. Wang, X. Li, Y. Jiang, M. L. S. Nai, J. Ding, J. Wei, Electron beam melted heterogeneously porous microlattices for metallic bone applications: Design and investigations of boundary and edge effects, Additive Manufacturing 36 (2020) 101566.

[46] Y. Zhang, O. Andrukhov, S. Berner, M. Matejka, M. Wieland, X. Rausch-Fan, A. Schedle, Osteogenic properties of hydrophilic and hydrophobic titanium surfaces evaluated with osteoblast-like cells (mg63) in coculture with human umbilical vein endothelial cells (huvec), dental materials 26 (11) (2010) 1043–1051.

[47] L. Liu, P. Kamm, F. García-Moreno, J. Banhart, D. Pasini, Elastic and failure response of imperfect three-dimensional metallic lattices: the role of geometric defects

141

2845   induced by selective laser melting, Journal of the Mechanics and Physics of Solids 107 (2017) 160–184.

[48] G. H. van Lenthe, M. Stauber, R. Müller, Specimen-specific beam models for fast and accurate prediction of human trabecular bone mechanical properties, Bone 39 (6) (2006) 1182–1189.

2850 [49] G. Totten, D. MacKenzie, Introduction to titanium and its alloys, in: ASM Handbook Volume 4E - Heat Treating of Nonferrous Alloys, ASM International, 2016, pp. 481–497. doi:10.31399/asm.hb.v04e.a0006253.

[50] G. Welsch, R. Boyer, E. Collings, Materials properties handbook: titanium alloys, ASM international, 1993.

2855 [51] A. Kawakami, Study on segregation behavior of alloying elements in titanium alloys during solidification, Ph.D. thesis, University of British Columbia (2002).

[52] B. Vrancken, R. Wauthlé, J.-P. Kruth, J. Van Humbeeck, Study of the influence of material properties on residual stress in selective laser melting, in: Proceedings of the solid freeform fabrication symposium, 2013, pp. 393–407.

2860 [53] P. C. Priarone, V. Lunetto, E. Atzeni, A. Salmi, Laser powder bed fusion (l-pbf) additive manufacturing: On the correlation between design choices and process sustainability, Procedia CIRP 78 (2018) 85–90. doi:10.1016/j.procir.2018.09.058.

[54] B. Research, Powder metallurgy market size, share & industry analysis report, https://www.bccresearch.com/market-research/advanced-materials/
2865   powder-metallurgy-global-markets-to-markets-report.html, (Accessed on 06/13/2021) (11 2020).

[55] S. A. Tofail, E. P. Koumoulos, A. Bandyopadhyay, S. Bose, L. O'Donoghue, C. Charitidis, Additive manufacturing: scientific and technological challenges, market uptake and opportunities, Materials today 21 (1) (2018) 22–37.

2870 [56] T. DebRoy, T. Mukherjee, J. O. Milewski, J. W. Elmer, B. Ribic, J. J. Blecher, W. Zhang, Scientific, technological and economic issues in metal printing and their solutions, Nature Materials 18 (10) (2019) 1026–1032, number: 10 publisher: Nature Publishing Group. doi:10.1038/s41563-019-0408-2.

[57] ESA, 3d printed metal mutants arise from europe's amaze programme,
2875   http://www.esa.int/Enabling_Support/Space_Engineering_Technology/

3D_printed_metal_mutants_arise_from_Europe_s_AMAZE_programme, (Accessed on 06/13/2021) (11 2017).

[58] G. Electric, 3d printing in aerospace & aviation | ge additive, https://www.ge.com/additive/additive-manufacturing/industries/aviation-aerospace, (Accessed on 06/13/2021) (2021).

[59] 3ders, China shows off world largest 3d printed titanium fighter component | 3d printer & 3d printing news, https://www.3ders.org/articles/20130529-china-shows-off-world-largest-3d-printed-titanium-fighter-component.html, (Accessed on 06/13/2021) (5 2013).

[60] Metal-AM, Gkn & eos collaborate to focus on metal am for automotive market, https://www.metal-am.com/gkn-eos-collaborate-focus-metal-am-automotive-market/, (Accessed on 06/13/2021) (1 2017).

[61] P. Whittaker, Fraunhofer ilt and concept laser develop additive manufacturing for the automotive industry, https://www.pm-review.com/fraunhofer-ilt-and-concept-laser-develop-additive-manufacturing-for-the-automotiv (Accessed on 06/13/2021) (11 2012).

[62] CSIRO, World-first surgery saves cancer patient's leg, https://www.csiro.au/en/research/health-medical/biomedical/titanium-heel, (Accessed on 06/13/2021) (1 2021).

[63] ISO/ASTM52900-15, Standard terminology for additive manufacturing – general principles – terminology, Tech. rep., ASTM International, West Conshohocken, PA (2015). doi:10.1520/ISOASTM52900-15.

[64] D. Küpper, W. Heising, G. Corman, M. Wolfgang, C. Knizek, V. Lukic, Get ready for industrialized additive manufacturing, Tech. rep., Boston Consulting Group (April 2017).

[65] A. Salmi, F. Calignano, M. Galati, E. Atzeni, An integrated design methodology for components produced by laser powder bed fusion (l-pbf) process, Virtual and Physical Prototyping 13 (3) (2018) 191–202.

[66] C. Kamath, B. El-dasher, G. F. Gallegos, W. E. King, A. Sisto, Density of additively-manufactured, 316l ss parts using laser powder-bed fusion at powers up to 400 w,

143

The International Journal of Advanced Manufacturing Technology 74 (1-4) (2014) 65–78. doi:10.1007/s00170-014-5954-9.

[67] L. Ma, J. Fong, B. Lane, S. Moylan, J. Filliben, A. Heckert, L. Levine, Using design of experiments in finite element modeling to identify critical variables for laser powder bed fusion, in: International solid freeform fabrication symposium, Laboratory for Freeform Fabrication and the University of Texas Austin, TX, USA, 2015, pp. 219–228.

[68] F. Del Re, V. Contaldi, A. Astarita, B. Palumbo, A. Squillace, P. Corrado, P. Di Petta, Statistical approach for assessing the effect of powder reuse on the final quality of alsi10mg parts produced by laser powder bed fusion additive manufacturing, The International Journal of Advanced Manufacturing Technology 97 (5) (2018) 2231–2240.

[69] J. Gheysen, M. Marteleur, C. van der Rest, A. Simar, Efficient optimization methodology for laser powder bed fusion parameters to manufacture dense and mechanically sound parts validated on alsi12 alloy, Materials & Design 199 (2021) 109433.

[70] G. Tapia, S. Khairallah, M. Matthews, W. E. King, A. Elwany, Gaussian process-based surrogate modeling framework for process planning in laser powder-bed fusion additive manufacturing of 316l stainless steel, The International Journal of Advanced Manufacturing Technology 94 (9) (2018) 3591–3603.

[71] H. A. Kumar, S. Kumaraguru, C. Paul, K. Bindra, Faster temperature prediction in the powder bed fusion process through the development of a surrogate model, Optics & Laser Technology 141 (2021) 107122.

[72] T. Moges, Z. Yang, K. Jones, S. Feng, P. Witherell, Y. Lu, Hybrid modeling approach for melt-pool prediction in laser powder bed fusion additive manufacturing, Journal of Computing and Information Science in Engineering 21 (5) (2021) 050902.

[73] A. J. Wolfer, Physics-based surrogate modeling of laser powder bed fusion additive manufacturing, Ph.D. thesis, University of California, Davis (2020).

[74] W. E. King, A. T. Anderson, R. M. Ferencz, N. E. Hodge, C. Kamath, S. A. Khairallah, A. M. Rubenchik, Laser powder bed fusion additive manufacturing of metals; physics, computational, and materials challenges, Applied Physics Reviews 2 (4) (2015) 041304. doi:10.1063/1.4937809.

[75] E. R. Denlinger, M. Gouge, J. Irwin, P. Michaleris, Thermomechanical model development and in situ experimental validation of the laser powder-bed fusion process, Additive Manufacturing 16 (2017) 73–80.

[76] C. Tang, K. Le, C. Wong, Physics of humping formation in laser powder bed fusion, International Journal of Heat and Mass Transfer 149 (2020) 119172.

[77] S. A. Khairallah, A. Anderson, Mesoscopic simulation model of selective laser melting of stainless steel powder, Journal of Materials Processing Technology 214 (11) (2014) 2627–2636.

[78] C. Zhao, K. Fezzaa, R. W. Cunningham, H. Wen, F. De Carlo, L. Chen, A. D. Rollett, T. Sun, Real-time monitoring of laser powder bed fusion process using high-speed x-ray imaging and diffraction, Scientific reports 7 (1) (2017) 1–11.

[79] Q. Guo, C. Zhao, L. I. Escano, Z. Young, L. Xiong, K. Fezzaa, W. Everhart, B. Brown, T. Sun, L. Chen, Transient dynamics of powder spattering in laser powder bed fusion additive manufacturing process revealed by in-situ high-speed high-energy x-ray imaging, Acta Materialia 151 (2018) 169–180.

[80] X. Li, C. Zhao, T. Sun, W. Tan, Revealing transient powder-gas interaction in laser powder bed fusion process through multi-physics modeling and high-speed synchrotron x-ray imaging, Additive Manufacturing 35 (2020) 101362.

[81] A. A. Martin, N. P. Calta, S. A. Khairallah, J. Wang, P. J. Depond, A. Y. Fong, V. Thampy, G. M. Guss, A. M. Kiss, K. H. Stone, C. J. Tassone, J. N. Weker, M. F. Toney, v. T. Buuren, M. J. Matthews, Dynamics of pore formation during laser powder bed fusion additive manufacturing, Nature Communications 10 (1) (2019) 1987. doi:10.1038/s41467-019-10009-2.

[82] Z. Gan, O. L. Kafka, N. Parab, C. Zhao, L. Fang, O. Heinonen, T. Sun, W. K. Liu, Universal scaling laws of keyhole stability and porosity in 3d printing of metals, Nature communications 12 (1) (2021) 1–8.

[83] T.-N. Le, Y.-L. Lo, Effects of sulfur concentration and marangoni convection on melt-pool formation in transition mode of selective laser melting process, Materials & Design 179 (2019) 107866.

[84] Y. Chen, S. J. Clark, L. Sinclair, C. L. A. Leung, S. Marussi, T. Connolley, O. V. Magdysyuk, R. C. Atwood, G. J. Baxter, M. A. Jones, et al., In situ and operando

145

x-ray imaging of directed energy deposition additive manufacturing, arXiv preprint arXiv:2006.09087 (2020).

[85] S. A. Khairallah, A. T. Anderson, A. Rubenchik, W. E. King, Laser powder-bed fusion additive manufacturing: Physics of complex melt flow and formation mechanisms of pores, spatter, and denudation zones, Acta Materialia 108 (2016) 36–45. doi:10.1016/j.actamat.2016.02.014.

[86] W. E. King, H. D. Barth, V. M. Castillo, G. F. Gallegos, J. W. Gibbs, D. E. Hahn, C. Kamath, A. M. Rubenchik, Observation of keyhole-mode laser melting in laser powder-bed fusion additive manufacturing, Journal of Materials Processing Technology 214 (12) (2014) 2915–2925. doi:10.1016/j.jmatprotec.2014.06.005.

[87] M. Thomas, G. J. Baxter, I. Todd, Normalised model-based processing diagrams for additive layer manufacture of engineering alloys, Acta Materialia 108 (2016) 26–35.

[88] S. Shrestha, Y. Kevin Chou, A numerical study on the keyhole formation during laser powder bed fusion process, Journal of Manufacturing Science and Engineering 141 (10) (2019).

[89] M. Bayat, A. Thanki, S. Mohanty, A. Witvrouw, S. Yang, J. Thorborg, N. S. Tiedje, J. H. Hattel, Keyhole-induced porosities in laser-based powder bed fusion (l-pbf) of ti6al4v: High-fidelity modelling and experimental validation, Additive Manufacturing 30 (2019) 100835.

[90] A. M. Rubenchik, W. E. King, S. S. Wu, Scaling laws for the additive manufacturing, Journal of Materials Processing Technology 257 (2018) 234–243.

[91] W. Wang, J. Ning, S. Y. Liang, Prediction of lack-of-fusion porosity in laser powder-bed fusion considering boundary conditions and sensitivity to laser power absorption, The International Journal of Advanced Manufacturing Technology 112 (1) (2021) 61–70.

[92] S. J. Callens, D. C. T. né Betts, R. Müller, A. A. Zadpoor, The local and global geometry of trabecular bone, Acta Biomaterialia (2021).

[93] S. Kumar, S. Tan, L. Zheng, D. M. Kochmann, Inverse-designed spinodoid metamaterials, npj Computational Materials 6 (1) (2020) 1–10.

[94] A. Tonino, C. Davidson, P. Klopper, L. Linclau, Protection from stress in bone and its effects. experiments with stainless steel and plastic plates in dogs, The Journal of bone and joint surgery. British volume 58 (1) (1976) 107–113.

[95] J. H. Martin, B. D. Yahata, J. M. Hundley, J. A. Mayer, T. A. Schaedler, T. M. Pollock, 3d printing of high-strength aluminium alloys, Nature 549 (7672) (2017) 365–369.

[96] U. S. A. F. R. S. Office, Advanced manufacturing olympics event - technical challenges, https://www.afrso.com/advanced-manufacturing-olympics/technical-challenges/, (Accessed on 06/14/2021) (10 2020).

[97] B. Research, Lidar market size, share, trends & growth analysis report, https://www.bccresearch.com/market-research/photonics/light-detection-anging-lidar-technologies-global-markets-report.html, (Accessed on 06/14/2021) (3 2021).

[98] M. Vlasea, From failed builds to innovative and economical designs, https://www.sme.org/technologies/articles/2021/april/from-failed-builds-to-innovative-and-economical-designs/, (Accessed on 06/14/2021) (3 2021).

[99] H. Saito, Physics and applications of Invar alloys, Maruzen, 1978.

[100] I. Yadroitsev, Selective laser melting: Direct manufacturing of 3D-objects by selective laser melting of metal powders, LAP Lambert Academic Publishing, Saarbrücken, 2009.

[101] ISO 11146-1:2005, Lasers and laser-related equipment — test methods for laser beam widths, divergence angles and beam propagation ratios — part 1: Stigmatic and simple astigmatic beams, Tech. rep., International Organization for Standardization (ISO) (2005).

[102] ISO 11146-2:2005, Lasers and laser-related equipment — test methods for laser beam widths, divergence angles and beam propagation ratios — part 2: General astigmatic beams, Tech. rep., International Organization for Standardization (ISO) (2005).

[103] ISO 11146-3:2005, Lasers and laser-related equipment — test methods for laser beam widths, divergence angles and beam propagation ratios — part 3: Intrinsic and geometrical laser beam classification, propagation and details of test methods., Tech. rep., International Organization for Standardization (ISO) (2005).

[104] M. Tang, P. C. Pistorius, J. L. Beuth, Prediction of lack-of-fusion porosity for powder bed fusion, Additive Manufacturing 14 (Supplement C) (2017) 39–48. doi:10.1016/j.addma.2016.12.001.

147

[105] C. L. A. Leung, S. Marussi, R. C. Atwood, M. Towrie, P. J. Withers, P. D. Lee, In situ x-ray imaging of defect and molten pool dynamics in laser additive manufacturing, Nature Communications 9 (1) (2018) 1355. `doi:10.1038/s41467-018-03734-7`.

[106] V. Gunenthiram, P. Peyre, M. Schneider, M. Dal, F. Coste, I. Koutiri, R. Fabbro, Experimental analysis of spatter generation and melt-pool behavior during the powder bed laser beam melting process, Journal of Materials Processing Technology 251 (2018) 376–386.

[107] V. Gunenthiram, P. Peyre, M. Schneider, M. Dal, F. Coste, R. Fabbro, Analysis of laser–melt pool–powder bed interaction during the selective laser melting of a stainless steel, Journal of Laser Applications 29 (2) (2017) 022303.

[108] M. J. Matthews, G. Guss, S. A. Khairallah, A. M. Rubenchik, P. J. Depond, W. E. King, Denudation of metal powder layers in laser powder bed fusion processes, Acta Materialia 114 (2016) 33–42. `doi:10.1016/j.actamat.2016.05.017`.

[109] P. Mercelis, J.-P. Kruth, Residual stresses in selective laser sintering and selective laser melting, Rapid prototyping journal 12 (5) (2006) 254–265.

[110] M. Gouge, P. Michaleris, Thermo-Mechanical Modeling of Additive Manufacturing, Butterworth-Heinemann, 2017, google-Books-ID: MuxGDgAAQBAJ.

[111] M. Brandt, Laser Additive Manufacturing: Materials, Design, Technologies, and Applications, Woodhead Publishing, 2016.

[112] M. Mani, S. Feng, L. Brandon, A. Donmez, S. Moylan, R. Fesperman, Measurement science needs for real-time control of additive manufacturing powder-bed fusion processes, in: Additive Manufacturing Handbook, CRC Press, 2017, pp. 629–652.

[113] M. Mani, B. M. Lane, M. A. Donmez, S. C. Feng, S. P. Moylan, A review on measurement science needs for real-time control of additive manufacturing metal powder bed fusion processes, International Journal of Production Research 55 (5) (2017) 1400–1418. `doi:10.1080/00207543.2016.1223378`.

[114] S. Vock, B. Klöden, A. Kirchner, T. Weißgärber, B. Kieback, Powders for powder bed fusion: a review, Progress in Additive Manufacturing (2019) 1–15.

[115] W. J. Sames, F. A. List, S. Pannala, R. R. Dehoff, S. S. Babu, The metallurgy and processing science of metal additive manufacturing, International Materials Reviews 61 (5) (2016) 315–360. `doi:10.1080/09506608.2015.1116649`.

148

[116] I. Yadroitsau, Direct manufacturing of 3d objects by selective laser melting of metal powders, Ph.D. thesis, Saint-Etienne (2008).
URL http://www.theses.fr/2008STET4006

[117] J. A. Slotwinski, E. J. Garboczi, P. E. Stutzman, C. F. Ferraris, S. S. Watson, M. A. Peltz, Characterization of metal powders used for additive manufacturing, Journal of research of the National Institute of Standards and Technology 119 (2014) 460.

[118] H. Tang, M. Qian, N. Liu, X. Zhang, G. Yang, J. Wang, Effect of powder reuse times on additive manufacturing of ti-6al-4v by selective electron beam melting, Jom 67 (3) (2015) 555–563.

[119] H. Lee, C. H. J. Lim, M. J. Low, N. Tham, V. M. Murukeshan, Y.-J. Kim, Lasers in additive manufacturing: A review, International Journal of Precision Engineering and Manufacturing-Green Technology 4 (3) (2017) 307–322.

[120] C. Tenbrock, F. G. Fischer, K. Wissenbach, J. H. Schleifenbaum, P. Wagenblast, W. Meiners, J. Wagner, Influence of keyhole and conduction mode melting for top-hat shaped beam profiles in laser powder bed fusion, Journal of Materials Processing Technology 278 (2020) 116514. doi:10.1016/j.jmatprotec.2019.116514.

[121] P. Bidare, I. Bitharas, R. Ward, M. Attallah, A. J. Moore, Laser powder bed fusion at sub-atmospheric pressures, International Journal of Machine Tools and Manufacture 130 (2018) 65–72.

[122] S. Traore, M. Schneider, I. Koutiri, F. Coste, R. Fabbro, C. Charpentier, P. Lefebvre, P. Peyre, Influence of gas atmosphere (ar or he) on the laser powder bed fusion of a ni-based alloy, Journal of Materials Processing Technology 288 (2021) 116851.

[123] C. Pauzon, K. Dietrich, P. Forêt, S. Dubiez-Le Goff, E. Hryha, G. Witt, Control of residual oxygen of the process atmosphere during laser-powder bed fusion processing of ti-6al-4v, Additive Manufacturing 38 (2021) 101765.

[124] S. P. Moylan, J. A. Slotwinski, A. Cooke, K. Jurrens, M. A. Donmez, Lessons learned in establishing the nist metal additive manufacturing laboratory, NIST Technical Note (2013).

[125] B. Foster, E. Reutzel, A. Nassar, B. Hall, S. Brown, C. Dickman, Optical, layerwise monitoring of powder bed fusion, in: Solid Freeform Fabrication Symposium, Austin, TX, Aug, 2015, pp. 10–12.

149

[126] N. Peter, Z. Pitts, S. Thompson, A. Saharan, Benchmarking build simulation software for laser powder bed fusion of metals, Additive Manufacturing 36 (2020) 101531.

[127] J. P. Oliveira, A. LaLonde, J. Ma, Processing parameters in laser powder bed fusion metal additive manufacturing, Materials & Design 193 (2020) 108762.

[128] E. Malekipour, H. El-Mounayri, Common defects and contributing parameters in powder bed fusion am process and their classification for online monitoring and control: a review, The International Journal of Advanced Manufacturing Technology 95 (1) (2018) 527–550.

[129] C. Zitelli, P. Folgarait, A. Di Schino, Laser powder bed fusion of stainless steel grades: a review, Metals 9 (7) (2019) 731.

[130] K. V. Yang, P. Rometsch, T. Jarvis, J. Rao, S. Cao, C. Davies, X. Wu, Porosity formation mechanisms and fatigue response in al-si-mg alloys made by selective laser melting, Materials Science and Engineering: A 712 (2018) 166–174.

[131] M. Ghayoor, K. Lee, Y. He, C.-h. Chang, B. K. Paul, S. Pasebani, Selective laser melting of 304l stainless steel: Role of volumetric energy density on the microstructure, texture and mechanical properties, Additive Manufacturing 32 (2020) 101011.

[132] M. Guo, D. Gu, L. Xi, H. Zhang, J. Zhang, J. Yang, R. Wang, Selective laser melting additive manufacturing of pure tungsten: role of volumetric energy density on densification, microstructure and mechanical properties, International Journal of Refractory Metals and Hard Materials 84 (2019) 105025.

[133] U. S. Bertoli, A. J. Wolfer, M. J. Matthews, J.-P. R. Delplanque, J. M. Schoenung, On the limitations of volumetric energy density as a design parameter for selective laser melting, Materials & Design 113 (2017) 331–340.

[134] T. Eagar, N. Tsai, Temperature fields produced by traveling distributed heat sources, Welding journal 62 (12) (1983) 346–355.

[135] R. Rai, G. G. Roy, T. DebRoy, A computationally efficient model of convective heat transfer and solidification characteristics during keyhole mode laser welding, Journal of Applied Physics 101 (5) (2007) 054909. doi:10.1063/1.2537587.

[136] D. Hann, J. Iammi, J. Folkes, Keyholing or conduction–prediction of laser penetration depth, in: Proceedings of the 36th International MATADOR Conference, Springer, 2010, pp. 275–278.

150

[137] D. B. Hann, J. Iammi, J. Folkes, A simple methodology for predicting laser-weld properties from material and laser parameters, Journal of Physics D: Applied Physics 44 (44) (2011) 445401. doi:10.1088/0022-3727/44/44/445401.

[138] W. Ayoola, W. Suder, S. W. Williams, Parameters controlling weld bead profile in conduction laser welding, Journal of Materials Processing Technology 249 (2017) 522–530.

[139] J. C. Ion, H. R. Shercliff, M. F. Ashby, Diagrams for laser materials processing, Acta Metallurgica et Materialia 40 (7) (1992) 1539–1551.

[140] D. Westerbaan, Fiber laser welding of advanced high strength steels, Master's thesis, University of Waterloo (2013).

[141] A. Gusarov, I. Smurov, Modeling the interaction of laser radiation with powder bed at selective laser melting, Physics Procedia 5 (2010) 381–394.

[142] M. Russell, A. Souto-Iglesias, T. Zohdi, Numerical simulation of laser fusion additive manufacturing processes using the sph method, Computer Methods in Applied Mechanics and Engineering 341 (2018) 163–187.

[143] M. Afrasiabi, C. Lüthi, M. Bambach, K. Wegener, Multi-resolution sph simulation of a laser powder bed fusion additive manufacturing process, Applied Sciences 11 (7) (2021) 2962.

[144] M. H. Dao, J. Lou, Simulations of laser assisted additive manufacturing by smoothed particle hydrodynamics, Computer Methods in Applied Mechanics and Engineering 373 (2021) 113491.

[145] C. Meier, S. L. Fuchs, A. J. Hart, W. A. Wall, A novel smoothed particle hydrodynamics formulation for thermo-capillary phase change problems with focus on metal additive manufacturing melt pool modeling, Computer Methods in Applied Mechanics and Engineering 381 (2021) 113812.

[146] D. Liu, Y. Wang, Mesoscale multi-physics simulation of solidification in selective laser melting process using a phase field and thermal lattice boltzmann model, in: International Design Engineering Technical Conferences and Computers and Information in Engineering Conference, Vol. 58110, American Society of Mechanical Engineers, 2017, p. V001T02A027.

[147] M. Zheng, L. Wei, J. Chen, Q. Zhang, C. Zhong, X. Lin, W. Huang, A novel method for the molten pool and porosity formation modelling in selective laser melting, International Journal of Heat and Mass Transfer 140 (2019) 1091–1105.

[148] A. Cattenone, S. Morganti, F. Auricchio, Basis of the lattice boltzmann method for additive manufacturing, Archives of Computational Methods in Engineering (2019) 1–25.

[149] A. Zakirov, S. Belousov, M. Bogdanova, B. Korneev, A. Stepanov, A. Perepelkina, V. Levchenko, A. Meshkov, B. Potapkin, Predictive modeling of laser and electron beam powder bed fusion additive manufacturing of metals at the mesoscale, Additive Manufacturing 35 (2020) 101236.

[150] M. Krzyzanowski, D. Svyetlichnyy, A multiphysics simulation approach to selective laser melting modelling based on cellular automata and lattice boltzmann methods, Computational Particle Mechanics (2021) 1–17.

[151] T. Zhang, H. Li, S. Liu, S. Shen, H. Xie, W. Shi, G. Zhang, B. Shen, L. Chen, B. Xiao, et al., Evolution of molten pool during selective laser melting of ti–6al–4v, Journal of Physics D: Applied Physics 52 (5) (2018) 055302.

[152] Y. Mayi, M. Dal, P. Peyre, M. Bellet, C. Metton, C. Moriconi, R. Fabbro, Laser-induced plume investigated by finite element modelling and scaling of particle entrainment in laser powder bed fusion, Journal of Physics D: Applied Physics 53 (7) (2019) 075306.

[153] G. A. Gordeev, V. Ankudinov, E. V. Kharanzhevskiy, M. D. Krivilyov, Numerical simulation of selective laser melting with local powder shrinkage using fem with the refined mesh, The European Physical Journal Special Topics 229 (2-3) (2020) 205–216.

[154] U. Ali, R. Esmaeilizadeh, F. Ahmed, D. Sarker, W. Muhammad, A. Keshavarzkermani, Y. Mahmoodkhani, E. Marzbanrad, E. Toyserkani, Identification and characterization of spatter particles and their effect on surface roughness, density and mechanical response of 17-4 ph stainless steel laser powder-bed fusion parts, Materials Science and Engineering: A 756 (2019) 98–107.

[155] R. Esmaeilizadeh, U. Ali, A. Keshavarzkermani, Y. Mahmoodkhani, E. Marzbanrad, E. Toyserkani, On the effect of spatter particles distribution on the quality of hastelloy x parts made by laser powder-bed fusion additive manufacturing, Journal of Manufacturing Processes 37 (2019) 11–20.

152

[156] A. R. Nassar, M. A. Gundermann, E. W. Reutzel, P. Guerrier, M. H. Krane, M. J. Weldon, Formation processes for large ejecta and interactions with melt pool formation in powder bed fusion additive manufacturing, Scientific Reports 9 (1) (2019) 5038. doi:10.1038/s41598-019-41415-7.

[157] P. Bidare, I. Bitharas, R. M. Ward, M. M. Attallah, A. J. Moore, Fluid and particle dynamics in laser powder bed fusion, Acta Materialia 142 (2018) 107–120. doi:10.1016/j.actamat.2017.09.051.

[158] C. Weingarten, D. Buchbinder, N. Pirch, W. Meiners, K. Wissenbach, R. Poprawe, Formation and reduction of hydrogen porosity during selective laser melting of alsi10mg, Journal of Materials Processing Technology 221 (2015) 112–120. doi:10.1016/j.jmatprotec.2015.02.013.

[159] H. Choo, K.-L. Sham, J. Bohling, A. Ngo, X. Xiao, Y. Ren, P. J. Depond, M. J. Matthews, E. Garlea, Effect of laser power on defect, texture, and microstructure of a laser powder bed fusion processed 316l stainless steel, Materials & Design 164 (2019) 107534. doi:10.1016/j.matdes.2018.12.006.

[160] B. Fotovvati, S. F. Wayne, G. Lewis, E. Asadi, A review on melt-pool characteristics in laser welding of metals, Advances in Materials Science and Engineering 2018 (2018).

[161] B. Shanmugarajan, J. Chary, G. Padmanabham, B. Arivazhagan, S. K. Albert, A. Bhaduri, Studies on autogenous laser welding of type 304b4 borated stainless steel, Optics and Lasers in Engineering 51 (11) (2013) 1272–1277.

[162] W. Duley, Laser Welding, Wiley, 1998.

[163] P. Haglund, I. Eriksson, J. Powell, A. Kaplan, Surface tension stabilized laser welding (donut laser welding)—a new laser welding technique, Journal of laser applications 25 (3) (2013) 031501.

[164] I. Eriksson, J. Powell, A. F. Kaplan, Surface tension generated defects in full penetration laser keyhole welding, Journal of Laser Applications 26 (1) (2014) 012006.

[165] C. Panwisawas, C. Qiu, Y. Sovani, J. Brooks, M. Attallah, H. Basoalto, On the role of thermal fluid dynamics into the evolution of porosity during selective laser melting, Scripta Materialia 105 (2015) 14–17.

153

[166] G. G. Gladush, I. Smurov, Physics of laser materials processing: theory and experiment, Vol. 146, Springer Science & Business Media, 2011.

[167] T. Qi, H. Zhu, H. Zhang, J. Yin, L. Ke, X. Zeng, Selective laser melting of al7050 powder: Melting mode transition and comparison of the characteristics between the keyhole and conduction mode, Materials & Design[Online; accessed 2017-09-19] (2017). doi:10.1016/j.matdes.2017.09.014.
URL http://www.sciencedirect.com/science/article/pii/S0264127517308493

[168] S. Ly, A. M. Rubenchik, S. A. Khairallah, G. Guss, M. J. Matthews, Metal vapor micro-jet controls material redistribution in laser powder bed fusion additive manufacturing, Scientific Reports 7 (1) (2017) 4085. doi:10.1038/s41598-017-04237-z.

[169] S. A. Khairallah, A. A. Martin, J. R. Lee, G. Guss, N. P. Calta, J. A. Hammons, M. H. Nielsen, K. Chaput, E. Schwalbach, M. N. Shah, et al., Controlling interdependent meso-nanosecond dynamics and defect generation in metal 3d printing, Science 368 (6491) (2020) 660–665.

[170] T. DebRoy, H. Wei, J. Zuback, T. Mukherjee, J. Elmer, J. Milewski, A. M. Beese, A. d. Wilson-Heid, A. De, W. Zhang, Additive manufacturing of metallic components–process, structure and properties, Progress in Materials Science 92 (2018) 112–224.

[171] Y. Tian, D. Tomus, A. Huang, X. Wu, Experimental and statistical analysis on process parameters and surface roughness relationship for selective laser melting of hastelloy x, Rapid Prototyping Journal (2019).

[172] G. Strano, L. Hao, R. M. Everson, K. E. Evans, Surface roughness analysis, modelling and prediction in selective laser melting, Journal of Materials Processing Technology 213 (4) (2013) 589–597.

[173] E. Yasa, J.-P. Kruth, Application of laser re-melting on selective laser melting parts, Advances in Production engineering and Management 6 (4) (2011) 259–270.

[174] J.-P. Kruth, J. Deckers, E. Yasa, Experimental investigation of laser surface remelting for the improvement of selective laser melting process, in: Proceedings of the 19th Solid Freeform Fabrication Symposium, 2008, pp. 321–332.

154

[175] F. E. Pfefferkorn, N. A. Duffie, X. Li, M. Vadali, C. Ma, Improving surface finish in pulsed laser micro polishing using thermocapillary flow, CIRP Annals 62 (1) (2013) 203–206.

[176] M. Vadali, C. Ma, N. A. Duffie, X. Li, F. E. Pfefferkorn, Pulsed laser micro polishing: Surface prediction model, Journal of Manufacturing processes 14 (3) (2012) 307–315.

[177] C. Druzgalski, A. Ashby, G. Guss, W. King, T. Roehling, M. Matthews, Process optimization of complex geometries using feed forward control for laser powder bed fusion additive manufacturing, Additive Manufacturing 34 (2020) 101169.

[178] Y. Tian, D. Tomus, P. Rometsch, X. Wu, Influences of processing parameters on surface roughness of hastelloy x produced by selective laser melting, Additive Manufacturing 13 (2017) 103–112. `doi:10.1016/j.addma.2016.10.010`.

[179] J. C. Snyder, K. A. Thole, Understanding laser powder bed fusion surface roughness, Journal of Manufacturing Science and Engineering 142 (7) (2020).

[180] J. C. Fox, S. P. Moylan, B. M. Lane, Preliminary study toward surface texture as a process signature in laser powder bed fusion additive manufacturing, in: 2016 Summer Topical Meeting: Dimensional Accuracy and Surface Finish in Additive Manufacturing, 2016, pp. 321–332.

[181] J. C. Fox, S. P. Moylan, B. M. Lane, Effect of process parameters on the surface roughness of overhanging structures in laser powder bed fusion additive manufacturing, Procedia CIRP 45 (2016) 131–134. `doi:10.1016/j.procir.2016.02.347`.

[182] B.-Q. Li, Z. Li, P. Bai, B. Liu, Z. Kuai, Research on surface roughness of alsi10mg parts fabricated by laser powder bed fusion, Metals 8 (7) (2018) 524. `doi:10.3390/met8070524`.

[183] F. Calignano, Investigation of the accuracy and roughness in the laser powder bed fusion process, Virtual and Physical Prototyping 13 (2) (2018) 97–104. `doi:10.1080/17452759.2018.1426368`.

[184] E. Abele, M. Kniepkamp, Analysis and optimisation of vertical surface roughness in micro selective laser melting, Surface Topography: Metrology and Properties 3 (3) (2015) 034007.

[185] P. A. Hooper, Melt pool temperature and cooling rates in laser powder bed fusion, Additive Manufacturing 22 (2018) 548–559. `doi:10.1016/j.addma.2018.05.032`.

155

[186] T. Mukherjee, V. Manvatkar, A. De, T. DebRoy, Mitigation of thermal distortion during additive manufacturing, Scripta materialia 127 (2017) 79–83.

[187] L. Anderson, A. Venter, B. Vrancken, D. Marais, J. Van Humbeeck, T. Becker, Investigating the residual stress distribution in selective laser melting produced ti-6al-4v using neutron diffraction, in: Mater. Res. Proc, Vol. 4, 2018, pp. 73–78.

[188] B. Cheng, S. Shrestha, K. Chou, Stress and deformation evaluations of scanning strategy effect in selective laser melting, Additive Manufacturing 12 (2016) 240–251.

[189] A. Dunbar, E. Denlinger, J. Heigel, P. Michaleris, P. Guerrier, R. Martukanitz, T. Simpson, Development of experimental method for in situ distortion and temperature measurements during the laser powder bed fusion additive manufacturing process, Additive Manufacturing 12 (2016) 25–30.

[190] R. J. Williams, C. M. Davies, P. A. Hooper, A pragmatic part scale model for residual stress and distortion prediction in powder bed fusion, Additive Manufacturing 22 (2018) 416–425.

[191] Z.-C. Fang, Z.-L. Wu, C.-G. Huang, C.-W. Wu, Review on residual stress in selective laser melting additive manufacturing of alloy parts, Optics & Laser Technology 129 (2020) 106283.

[192] N. Levkulich, S. Semiatin, J. Gockel, J. Middendorf, A. DeWald, N. Klingbeil, The effect of process parameters on residual stress evolution and distortion in the laser powder bed fusion of ti-6al-4v, Additive Manufacturing 28 (2019) 475–484.

[193] F. Bosio, H. Shen, Y. Liu, M. Lombardi, P. Rometsch, X. Wu, Y. Zhu, A. Huang, Production strategy for manufacturing large-scale alsi10mg components by laser powder bed fusion, JOM 73 (3) (2021) 770–780.

[194] R. Rai, J. W. Elmer, T. A. Palmer, T. DebRoy, Heat transfer and fluid flow during keyhole mode laser welding of tantalum, ti–6al–4v, 304l stainless steel and vanadium, Journal of Physics D: Applied Physics 40 (18) (2007) 5753. doi:10.1088/0022-3727/40/18/037.

[195] J. Yang, J. Han, H. Yu, J. Yin, M. Gao, Z. Wang, X. Zeng, Role of molten pool mode on formability, microstructure and mechanical properties of selective laser melted ti-6al-4v alloy, Materials & Design 110 (Supplement C) (2016) 558–570. doi:10.1016/j.matdes.2016.08.036.

156

[196] A. Aggarwal, S. Patel, A. Kumar, Selective laser melting of 316l stainless steel: Physics of melting mode transition and its influence on microstructural and mechanical behavior, JOM[Online; accessed 2019-02-13] (12 2018). doi:10.1007/s11837-018-3271-8.
URL https://doi.org/10.1007/s11837-018-3271-8

[197] H. Wang, Y. Zou, Microscale interaction between laser and metal powder in powder-bed additive manufacturing: Conduction mode versus keyhole mode, International Journal of Heat and Mass Transfer 142 (2019) 118473. doi:10.1016/j.ijheatmasstransfer.2019.118473.

[198] J. Ye, A. M. Rubenchik, M. F. Crumb, G. Guss, M. J. Matthews, Laser absorption and scaling behavior in powder bed fusion additive manufacturing of metals, in: CLEO: Science and Innovations, Optical Society of America, 2018, pp. JW2A–117.

[199] C. Wuzhu, Z. Xudong, R. Jialie, W. Zhenjia, H. Guoqing, Z. Hongjnn, Study on welding mode transition and stability of welding process in laser welding [j], Chinese Journal of Lasers 7 (1996).

[200] X. Zhang, W. Chen, J. Ren, Y. Wang, G. Huang, H. Zhang, Effects of processing parameters on mode and stability of laser welding, in: Lasers as Tools for Manufacturing of Durable Goods and Microelectronics, Vol. 2703, International Society for Optics and Photonics, 1996, pp. 343–349.

[201] X. Zhang, W. Chen, J. Ren, G. Huang, H. Zhang, Laser welding mode transition and influence of thermal focusing on mode transition, in: Laser Processing of Materials and Industrial Applications, Vol. 2888, International Society for Optics and Photonics, 1996, pp. 306–315.

[202] T. Forsman, J. Powell, C. Lampa, A. Kaplan, C. Magnusson, Nd: Yag laser welding of aluminium: factors affecting absorptivity, Lasers in engineering (Print) 8 (4) (1999) 295–310.

[203] M. Matthews, J. Trapp, G. Guss, A. Rubenchik, Direct measurements of laser absorptivity during metal melt pool formation associated with powder bed fusion additive manufacturing processes, Journal of Laser Applications 30 (3) (2018) 032302. doi:10.2351/1.5040636.

[204] H. Zhao, D. White, T. DebRoy, Current issues and problems in laser welding of automotive aluminium alloys, International materials reviews 44 (6) (1999) 238–266.

157

[205] S. Nakamura, M. Sakurai, K. Kamimuki, T. Inoue, Y. Ito, Detection technique for transition between deep penetration mode and shallow penetration mode in co2laser welding of metals, Journal of Physics D: Applied Physics 33 (22) (2000) 2941–2948. doi:10.1088/0022-3727/33/22/311.

[206] S. Nakamura, M. Sakurai, Y. Ito, K. Kamimuki, T. Inoue, Detection of transition from keyhole-type to heat conduction-type welding in co2 laser welding of metals, in: International Congress on Applications of Lasers & Electro-Optics, Laser Institute of America, 1999, pp. E28–E33.

[207] E. Assuncao, S. Williams, D. Yapp, Interaction time and beam diameter effects on the conduction mode limit, Optics and Lasers in Engineering 50 (6) (2012) 823–828. doi:10.1016/j.optlaseng.2012.02.001.

[208] E. Goncalves Assuncao, Investigation of conduction to keyhole mode transition, Ph.D. thesis, Cranfield University (2012).

[209] S. Patel, H. Chen, M. Vlasea, Y. Zou, The influence of divergent laser beams on the laser powder bed fusion of a high reflectivity aluminium alloy (2021). arXiv:2105.07920.

[210] D. Rosenthal, The theory of moving sources of heat and its application of metal treatments, Transactions of ASME 68 (1946) 849–866.

[211] M. F. Ashby, K. E. Easterling, A first report on diagrams for grain growth in welds, Acta Metallurgica 30 (11) (1982) 1969–1978. doi:10.1016/0001-6160(82)90100-6.

[212] M. F. Ashby, K. E. Easterling, The transformation hardening of steel surfaces by laser beams—i. hypo-eutectoid steels, Acta Metallurgica 32 (11) (1984) 1935–1948. doi:10.1016/0001-6160(84)90175-5.

[213] J. C. Ion, K. E. Easterling, M. F. Ashby, A second report on diagrams of microstructure and hardness for heat-affected zones in welds, Acta Metallurgica 32 (11) (1984) 1949–1962. doi:10.1016/0001-6160(84)90176-7.

[214] N. N. Rykalin, A. A. Uglov, A. Kokora, Heat treatment and welding by laser radiation, in: Laser machining and welding, Pergamon, 1978, pp. 57–125.

[215] T. Mukherjee, H. L. Wei, A. De, T. DebRoy, Heat and fluid flow in additive manufacturing – part ii: Powder bed fusion of stainless steel, and titanium, nickel and aluminum base alloys, Computational Materials Science 150 (2018) 369–380. doi:10.1016/j.commatsci.2018.04.027.

158

[216] K. C. Mills, Recommended Values of Thermophysical Properties for Selected Commercial Alloys, Woodhead Publishing, 2002, google-Books-ID: eV0iTILEaxcC.

[217] Y. M. Wang, C. Kamath, T. Voisin, Z. Li, A processing diagram for high-density ti-6al-4v by selective laser melting, Rapid Prototyping Journal 24 (9) (2018) 1469–1478. doi:10.1108/RPJ-11-2017-0228.

[218] P. Bajaj, J. Wright, I. Todd, E. A. Jägle, Predictive process parameter selection for selective laser melting manufacturing: Applications to high thermal conductivity alloys, Additive Manufacturing 27 (2019) 246–258. doi:10.1016/j.addma.2018.12.003.

[219] G. E. Bean, D. B. Witkin, T. D. McLouth, D. N. Patel, R. J. Zaldivar, Effect of laser focus shift on surface quality and density of inconel 718 parts produced via selective laser melting, Additive Manufacturing 22 (2018) 207–215, publisher: Elsevier.

[220] H. Ki, J. Mazumder, P. S. Mohanty, Modeling of laser keyhole welding: Part i. mathematical modeling, numerical methodology, role of recoil pressure, multiple reflections, and free surface evolution, Metallurgical and Materials Transactions A 33 (6) (2002) 1817–1830. doi:10.1007/s11661-002-0190-6.

[221] H. Ki, J. Mazumder, P. S. Mohanty, Modeling of laser keyhole welding: Part ii. simulation of keyhole evolution, velocity, temperature profile, and experimental verification, Metallurgical and Materials Transactions A 33 (6) (2002) 1831–1842.

[222] C. J. Smithells, Metals reference book, Elsevier, 2013.

[223] R. Cunningham, S. P. Narra, C. Montgomery, J. Beuth, A. D. Rollett, Synchrotron-based x-ray microtomography characterization of the effect of processing variables on porosity formation in laser power-bed additive manufacturing of ti-6al-4v, JOM 69 (3) (2017) 479–484. doi:10.1007/s11837-016-2234-1.

[224] S. M. H. Hojjatzadeh, N. D. Parab, W. Yan, Q. Guo, L. Xiong, C. Zhao, M. Qu, L. I. Escano, X. Xiao, K. Fezzaa, W. Everhart, T. Sun, L. Chen, Pore elimination mechanisms during 3d printing of metals, Nature Communications 10 (1) (2019) 1–8. doi:10.1038/s41467-019-10973-9.

[225] H. Nakamura, Y. Kawahito, K. Nishimoto, S. Katayama, Elucidation of melt flows and spatter formation mechanisms during high power laser welding of pure titanium, Journal of Laser Applications 27 (3) (2015) 032012. doi:10.2351/1.4922383.

159

[226] J. Goldak, A. Chakravarti, M. Bibby, A new finite element model for welding heat sources, Metallurgical Transactions B 15 (2) (1984) 299–305. `doi:10.1007/BF02667333`.

[227] H. Ali, H. Ghadbeigi, K. Mumtaz, Residual stress development in selective laser-melted ti6al4v: a parametric thermal modelling approach, The International Journal of Advanced Manufacturing Technology 97 (5) (2018) 2621–2633. `doi:10.1007/s00170-018-2104-9`.

[228] P. Turchi, Viscosity and surface tension of metals, Tech. rep., Lawrence Livermore National Lab.(LLNL), Livermore, CA (2018).

[229] T. Graf, P. Berger, R. Weber, H. Hügel, A. Heider, P. Stritt, Analytical expressions for the threshold of deep-penetration laser welding, Laser Physics Letters 12 (5) (2015) 056002. `doi:10.1088/1612-2011/12/5/056002`.

[230] J. Bonnín Roca, P. Vaishnav, E. R. H. Fuchs, M. G. Morgan, Policy needed for additive manufacturing, Nature Materials 15 (8) (2016) 815–818, number: 8 publisher: Nature Publishing Group. `doi:10.1038/nmat4658`.

[231] A. Gisario, M. Kazarian, F. Martina, M. Mehrpouya, Metal additive manufacturing in the commercial aviation industry: A review, Journal of Manufacturing Systems 53 (2019) 124–149. `doi:10.1016/j.jmsy.2019.08.005`.

[232] S. M. Wagner, R. O. Walton, Additive manufacturing's impact and future in the aviation industry, Production Planning & Control 27 (13) (2016) 1124–1130. `doi:10.1080/09537287.2016.1199824`.

[233] M. Gorelik, Additive manufacturing in the context of structural integrity, International Journal of Fatigue 94 (2017) 168–177. `doi:10.1016/j.ijfatigue.2016.07.005`.

[234] J. C. Najmon, S. Raeisi, A. Tovar, 2 - review of additive manufacturing technologies and applications in the aerospace industry, in: F. Froes, R. Boyer (Eds.), Additive Manufacturing for the Aerospace Industry, Elsevier, 2019, pp. 7–31. `doi:10.1016/B978-0-12-814062-8.00002-9`.

[235] S. Singamneni, L. Yifan, A. Hewitt, R. Chalk, W. Thomas, D. Jordison, Additive manufacturing for the aircraft industry: A review, J. Aeronaut. Aerosp. Eng 8 (1) (2019). `doi:10.1016/B978-0-12-814062-8.00002-9Get`.

[236] M. Delic, D. R. Eyers, J. Mikulic, Additive manufacturing: empirical evidence for supply chain integration and performance from the automotive industry, Supply Chain Management: An International Journal 24 (5) (2019) 604–621, publisher: Emerald Publishing Limited. doi:10.1108/SCM-12-2017-0406.

[237] M. Richardson, B. Haylock, Designer/maker: the rise of additive manufacturing, domestic-scale production and the possible implications for the automotive industry, Computer-Aided Design & Applications PACE 2 (2012) 33–48. doi:10.3722/cadaps.2012.PACE.33-48.

[238] K.-M. Hong, Y. C. Shin, Prospects of laser welding technology in the automotive industry: A review, Journal of Materials Processing Technology 245 (2017) 46–69. doi:10.1016/j.jmatprotec.2017.02.008.

[239] M. Delic, D. R. Eyers, The effect of additive manufacturing adoption on supply chain flexibility and performance: An empirical analysis from the automotive industry, International Journal of Production Economics 228 (2020) 107689. doi:10.1016/j.ijpe.2020.107689.

[240] R. Leal, F. M. Barreiros, L. Alves, F. Romeiro, J. C. Vasco, M. Santos, C. Marto, Additive manufacturing tooling for the automotive industry, The International Journal of Advanced Manufacturing Technology 92 (5) (2017) 1671–1676. doi:10.1007/s00170-017-0239-8.

[241] I. Gibson, D. Rosen, B. Stucker, M. Khorasani, Additive manufacturing technologies, Vol. 17, Springer, 2014. doi:10.1007/978-3-030-56127-7.

[242] N. T. Aboulkhair, M. Simonelli, L. Parry, I. Ashcroft, C. Tuck, R. Hague, 3d printing of aluminium alloys: Additive manufacturing of aluminium alloys using selective laser melting, Progress in Materials Science 106 (2019) 100578. doi:10.1016/j.pmatsci.2019.100578.

[243] L. Brock, I. Ogunsanya, H. Asgari, S. Patel, M. Vlasea, Relative performance of additively manufactured and cast aluminum alloys, Journal of Materials Engineering and Performance 30 (1) (2021) 760–782. doi:10.1007/s11665-020-05403-7.

[244] F. Trevisan, F. Calignano, M. Lorusso, J. Pakkanen, A. Aversa, E. P. Ambrosio, M. Lombardi, P. Fino, D. Manfredi, On the selective laser melting (slm) of the alsi10mg alloy: Process, microstructure, and mechanical properties, Materials 10 (1), pMID: 28772436 PMCID: PMC5344617 (1 2017). doi:10.3390/ma10010076. URL https://www.ncbi.nlm.nih.gov/pmc/articles/PMC5344617/

161

[245] M. Pastor, H. Zhao, R. Martukanitz, T. Debroy, Porosity, underfill and magnesium loss during continuous wave nd: Yag laser welding of thin plates of aluminum alloys 5182 and 5754, Welding Journal 78 (6) (1999) 207s–216s.

[246] N. T. Aboulkhair, I. Maskery, C. Tuck, I. Ashcroft, N. M. Everitt, On the formation of alsi10mg single tracks and layers in selective laser melting: Microstructure and nano-mechanical properties, Journal of Materials Processing Technology 230 (2016) 88–98. doi:10.1016/j.jmatprotec.2015.11.016.

[247] L. Brock, Laser powder bed fusion of alsi10mg for fabrication of fluid power components, Master's thesis, University of Waterloo (2020).

[248] N. T. Aboulkhair, N. M. Everitt, I. Ashcroft, C. Tuck, Reducing porosity in alsi10mg parts processed by selective laser melting, Additive Manufacturing 1-4 (2014) 77–86. doi:10.1016/j.addma.2014.08.001.

[249] L. Thijs, K. Kempen, J.-P. Kruth, J. Van Humbeeck, Fine-structured aluminium products with controllable texture by selective laser melting of pre-alloyed alsi10mg powder, Acta Materialia 61 (5) (2013) 1809–1819. doi:10.1016/j.actamat.2012.11.052.

[250] J. Metelkova, Y. Kinds, K. Kempen, C. de Formanoir, A. Witvrouw, B. Van Hooreweder, On the influence of laser defocusing in selective laser melting of 316l, Additive Manufacturing 23 (2018) 161–169. doi:10.1016/j.addma.2018.08.006.

[251] S. Patel, A. Rogalsky, M. Vlasea, Towards understanding side-skin surface characteristics in laser powder bed fusion, Journal of Materials Research 35 (15) (2020) 2055–2064. doi:10.1557/jmr.2020.125.

[252] E. Brandl, U. Heckenberger, V. Holzinger, D. Buchbinder, Additive manufactured alsi10mg samples using selective laser melting (slm): Microstructure, high cycle fatigue, and fracture behavior, Materials & Design 34 (2012) 159–169. doi:10.1016/j.matdes.2011.07.067.

[253] M. Tang, P. C. Pistorius, Oxides, porosity and fatigue performance of alsi10mg parts produced by selective laser melting, International Journal of Fatigue 94 (2017) 192–201. doi:10.1016/j.ijfatigue.2016.06.002.

162

[254] A. D. Brandão, J. Gumpinger, M. Gschweitl, C. Seyfert, P. Hofbauer, T. Ghidini, Fatigue properties of additively manufactured alsi10mg – surface treatment effect, Procedia Structural Integrity 7 (2017) 58–66. doi:10.1016/j.prostr.2017.11.061.

[255] P. D. Enrique, A. Keshavarzkermani, R. Esmaeilizadeh, S. Peterkin, H. Jahed, E. Toyserkani, N. Y. Zhou, Enhancing fatigue life of additive manufactured parts with electrospark deposition post-processing, Additive Manufacturing 36 (2020) 101526. doi:10.1016/j.addma.2020.101526.

[256] S. Leuders, M. Thöne, A. Riemer, T. Niendorf, T. Tröster, H. A. Richard, H. J. Maier, On the mechanical behaviour of titanium alloy tial6v4 manufactured by selective laser melting: Fatigue resistance and crack growth performance, International Journal of Fatigue 48 (2013) 300–307. doi:10.1016/j.ijfatigue.2012.11.011.

[257] A. du Plessis, I. Yadroitsava, I. Yadroitsev, Effects of defects on mechanical properties in metal additive manufacturing: A review focusing on x-ray tomography insights, Materials & Design 187 (2020) 108385. doi:10.1016/j.matdes.2019.108385.

[258] Z. Chen, X. Wu, D. Tomus, C. H. J. Davies, Surface roughness of selective laser melted ti-6al-4v alloy components, Additive Manufacturing 21 (2018) 91–103. doi:10.1016/j.addma.2018.02.009.

[259] J. H. Robinson, I. R. T. Ashton, E. Jones, P. Fox, C. Sutcliffe, The effect of hatch angle rotation on parts manufactured using selective laser melting, Rapid Prototyping Journal 25 (2) (2019) 289–298, publisher: Emerald Publishing Limited. doi:10.1108/RPJ-06-2017-0111.

[260] Z. W. Chen, T. Guraya, S. Singamneni, M. A. L. Phan, Grain growth during keyhole mode pulsed laser powder bed fusion of in738lc, JOM 72 (3) (2020) 1074–1084. doi:10.1007/s11837-020-04012-y.

[261] M. Dimter, R. Mayer, L. Hummeler, R. Salzberger, J. Kotila, T. Syvanen, Method and device for manufacturing a three-dimensional object, source: Google Patents (10 2008).
URL https://patents.google.com/patent/US20080241392A1/en

[262] S. P. Narra, Melt pool geometry and microstructure control across alloys in metal based additive manufacturing processes, Ph.D. thesis, Carnegie Mellon University (5 2017). doi:10.1184/R1/6720569.v1.
URL   https://kilthub.cmu.edu/articles/Melt_Pool_Geometry_and_

163

Microstructure_Control_Across_Alloys_in_Metal_Based_Additive_
Manufacturing_Processes/6720569

[263] L. R. Scime, Methods for the expansion of additive manufacturing process space and the development of in-situ process monitoring methodologies, Ph.D. thesis, Carnegie Mellon University, dOI: 10.1184/R1/6720581.v1 (5 2018).
URL https://kilthub.cmu.edu/articles/Methods_for_the_Expansion_of_Additive_Manufacturing_Process_Space_and_the_Development_of_In-Situ_Process_Monitoring_Methodologies/6720581

[264] X. Nie, Z. Chen, Y. Qi, H. Zhang, C. Zhang, Z. Xiao, H. Zhu, Effect of defocusing distance on laser powder bed fusion of high strength al–cu–mg–mn alloy, Virtual and Physical Prototyping 15 (3) (2020) 325–339. doi:10.1080/17452759.2020.1760895.

[265] L. Gargalis, J. Ye, M. Strantza, A. Rubenchik, J. W. Murray, A. T. Clare, I. A. Ashcroft, R. Hague, M. J. Matthews, Determining processing behaviour of pure cu in laser powder bed fusion using direct micro-calorimetry, Journal of Materials Processing Technology 294 (2021) 117130.

[266] Y. Huang, M. B. Khamesee, E. Toyserkani, A comprehensive analytical model for laser powder-fed additive manufacturing, Additive Manufacturing 12 (2016) 90–99. doi:10.1016/j.addma.2016.07.001.

[267] Z. Zhang, Y. Huang, A. Rani Kasinathan, S. Imani Shahabad, U. Ali, Y. Mahmood-khani, E. Toyserkani, 3-dimensional heat transfer modeling for laser powder-bed fusion additive manufacturing with volumetric heat sources based on varied thermal conductivity and absorptivity, Optics & Laser Technology 109 (2019) 297–312. doi:10.1016/j.optlastec.2018.08.012.

[268] S. M. H. Hojjatzadeh, N. D. Parab, Q. Guo, M. Qu, L. Xiong, C. Zhao, L. I. Escano, K. Fezzaa, W. Everhart, T. Sun, L. Chen, Direct observation of pore formation mechanisms during lpbf additive manufacturing process and high energy density laser welding, International Journal of Machine Tools and Manufacture 153 (2020) 103555. doi:10.1016/j.ijmachtools.2020.103555.

[269] M. Salarian, H. Asgari, M. Vlasea, Pore space characteristics and corresponding effect on tensile properties of inconel 625 fabricated via laser powder bed fusion, Materials Science and Engineering: A 769 (2020) 138525. doi:10.1016/j.msea.2019.138525.

[270] H. Asgari, M. Salarian, H. Ma, A. Olubamiji, M. Vlasea, On thermal expansion behavior of invar alloy fabricated by modulated laser powder bed fusion, Materials & Design 160 (2018) 895–905. `doi:10.1016/j.matdes.2018.10.025`.

[271] X. Zhou, D. Wang, X. Liu, D. Zhang, S. Qu, J. Ma, G. London, Z. Shen, W. Liu, 3d-imaging of selective laser melting defects in a co–cr–mo alloy by synchrotron radiation micro-ct, Acta Materialia 98 (2015) 1–16. `doi:10.1016/j.actamat.2015.07.014`.

[272] S. Patel, M. Vlasea, Melting mode thresholds in laser powder bed fusion and their application towards process parameter development, in: Proceedings of the 20th Annual International Solid Freeform Fabrication Symposium, Austin, TX, 2019, pp. 1190–1199.

[273] L. Huang, X. Hua, D. Wu, F. Li, Numerical study of keyhole instability and porosity formation mechanism in laser welding of aluminum alloy and steel, Journal of Materials Processing Technology 252 (2018) 421–431. `doi:10.1016/j.jmatprotec.2017.10.011`.

[274] S. Milton, A. Morandeau, F. Chalon, R. Leroy, Influence of finish machining on the surface integrity of ti6al4v produced by selective laser melting, Procedia CIRP 45 (2016) 127–130.

[275] S. Marimuthu, A. Triantaphyllou, M. Antar, D. Wimpenny, H. Morton, M. Beard, Laser polishing of selective laser melted components, International Journal of Machine Tools and Manufacture 95 (2015) 97–104.

[276] S. Bose, S. F. Robertson, A. Bandyopadhyay, Surface modification of biomaterials and biomedical devices using additive manufacturing, Acta Biomaterialia 66 (2018) 6–22. `doi:10.1016/j.actbio.2017.11.003`.

[277] J. Tuomi, K.-S. Paloheimo, J. Vehviläinen, R. Björkstrand, M. Salmi, E. Huotilainen, R. Kontio, S. Rouse, I. Gibson, A. A. Mäkitie, A novel classification and online platform for planning and documentation of medical applications of additive manufacturing, Surgical Innovation 21 (6) (2014) 553–559. `doi:10.1177/1553350614524838`.

[278] T. D. Ngo, A. Kashani, G. Imbalzano, K. T. Q. Nguyen, D. Hui, Additive manufacturing (3d printing): A review of materials, methods, applications and challenges, Composites Part B: Engineering 143 (2018) 172–196. `doi:10.1016/j.compositesb.2018.02.012`.

165

[279] A. Koptioug, L. E. Rännar, M. Bäckström, M. Cronskär, Additive manufacturing for medical and biomedical applications: Advances and challenges, in: THERMEC 2013, Vol. 783 of Materials Science Forum, Trans Tech Publications Ltd, 2014, pp. 1286–1291. doi:10.4028/www.scientific.net/MSF.783-786.1286.

[280] S. Singh, S. Ramakrishna, R. Singh, Material issues in additive manufacturing: A review, Journal of Manufacturing Processes 25 (2017) 185–200. doi:10.1016/j.jmapro.2016.11.006.

[281] S. Stübinger, I. Mosch, P. Robotti, M. Sidler, K. Klein, S. J. Ferguson, B. von Rechenberg, Histological and biomechanical analysis of porous additive manufactured implants made by direct metal laser sintering: a pilot study in sheep, Journal of Biomedical Materials Research Part B: Applied Biomaterials 101 (7) (2013) 1154–1163.

[282] B. V. Krishna, W. Xue, S. Bose, A. Bandyopadhyay, Engineered porous metals for implants, Jom 60 (5) (2008) 45–48.

[283] F. Calignano, D. Manfredi, E. P. Ambrosio, L. Iuliano, P. Fino, Influence of process parameters on surface roughness of aluminum parts produced by dmls, The International Journal of Advanced Manufacturing Technology 67 (9-12) (2013) 2743–2751. doi:10.1007/s00170-012-4688-9.

[284] I. Yadroitsev, I. Smurov, Surface morphology in selective laser melting of metal powders, Physics Procedia 12 (2011) 264–270.

[285] C. Qiu, C. Panwisawas, M. Ward, H. C. Basoalto, J. W. Brooks, M. M. Attallah, On the role of melt flow into the surface structure and porosity development during selective laser melting, Acta Materialia 96 (2015) 72–79. doi:10.1016/j.actamat.2015.06.004.

[286] A. Gebhardt, J.-S. Hötter, D. Ziebura, Impact of slm build parameters on the surface quality, RTejournal - Forum für Rapid Technologie 2014 (1) (2014).

[287] L. Johnson, M. Mahmoudi, B. Zhang, R. Seede, X. Huang, J. T. Maier, H. J. Maier, I. Karaman, A. Elwany, R. Arróyave, Assessing printability maps in additive manufacturing of metal alloys, Acta Materialia 176 (2019) 199–210. doi:10.1016/j.actamat.2019.07.005.

166

[288] A. Rogalsky, I. Rishmawi, L. Brock, M. Vlasea, Low cost irregular feed stock for laser powder bed fusion, Journal of Manufacturing Processes 35 (2018) 446–456. doi:10.1016/j.jmapro.2018.08.032.

[289] V. Amrhein, S. Greenland, B. McShane, Scientists rise up against statistical significance, Nature 567 (7748) (2019) 305. doi:10.1038/d41586-019-00857-9.

[290] R. L. Wasserstein, A. L. Schirm, N. A. Lazar, Moving to a world beyond "p < 0.05", The American Statistician 73 (sup1) (2019) 1–19. doi:10.1080/00031305.2019.1583913.

[291] H. Pike, Statistical significance should be abandoned, say scientists, BMJ 364 (2019) l1374, pMID: 30910774. doi:10.1136/bmj.l1374.

[292] Y. Lee, W. Zhang, Mesoscopic simulation of heat transfer and fluid flow in laser powder bed additive manufacturing, in: Proceedings of International solid freeform fabrication symposium, Austin, TX, 2015, pp. 1154–1165.

[293] E. Yasa, J. Deckers, T. Craeghs, M. Badrossamay, J.-P. Kruth, Investigation on occurrence of elevated edges in selective laser melting, in: Proceedings of the 20th Annual International Solid Freeform Fabrication Symposium, Solid Freeform Fabrication Symposium, Austin, TX, 2009, pp. 673–685.

[294] I. Yadroitsev, P. Bertrand, I. Smurov, Parametric analysis of the selective laser melting process, Applied surface science 253 (19) (2007) 8064–8069.

[295] B. Dutta, F. Froes, Additive Manufacturing of Titanium Alloys: State of the Art, Challenges and Opportunities, Butterworth-Heinemann, 2016.

[296] C. Fleißner-Rieger, T. Pfeifer, T. Jörg, T. Kremmer, M. Brabetz, H. Clemens, S. Mayer, Selective laser melting of a near-α ti6242s alloy for high-performance automotive parts, Advanced Engineering Materials (2020) 2001194doi:10.1002/adem.202001194.

[297] Z. Liu, B. He, T. Lyu, Y. Zou, A review on additive manufacturing of titanium alloys for aerospace applications: directed energy deposition and beyond ti-6al-4v, JOM (2021) 1–15.

[298] B. Jackson, Norsk titanium to deliver the world's first faa-approved, 3d-printed, structural titanium components to boeing (4 2017).
URL https://www.norsktitanium.com/media/press/norsk-titanium-to-deliver-the-worlds-first-faa-approved-3d-printed-structural-tit

[299] M. Wang, X. Lin, W. Huang, Laser additive manufacture of titanium alloys, Materials Technology 31 (2) (2016) 90–97.

[300] J. Avila, S. Bose, A. Bandyopadhyay, Additive manufacturing of titanium and titanium alloys for biomedical applications, in: Titanium in Medical and Dental Applications, Elsevier, 2018, pp. 325–343.

[301] Y.-L. Hao, S.-J. Li, R. Yang, Biomedical titanium alloys and their additive manufacturing, Rare Metals 35 (9) (2016) 661–671.

[302] S. Singh, S. Ramakrishna, Biomedical applications of additive manufacturing: Present and future, Current Opinion in Biomedical Engineering 2 (2017) 105–115. doi:10.1016/j.cobme.2017.05.006.

[303] M. McGregor, S. Patel, S. McLachlin, M. Vlasea, Architectural bone parameters and the relationship to titanium lattice design for powder bed fusion additive manufacturing (2021). arXiv:2105.07945.

[304] K.-H. Richter, S. Orban, S. Nowotny, Laser cladding of the titanium alloy ti6242 to restore damaged blades, in: International Congress on Applications of Lasers & Electro-Optics, Vol. 2004, Laser Institute of America, 2004, p. 1506.

[305] V. M. Tabie, C. Li, W. Saifu, J. Li, X. Xu, Mechanical properties of near alpha titanium alloys for high-temperature applications-a review, Aircraft Engineering and Aerospace Technology (2020).

[306] A. Chamanfar, T. Pasang, A. Ventura, W. Z. Misiolek, Mechanical properties and microstructure of laser welded ti–6al–2sn–4zr–2mo (ti6242) titanium alloy, Materials Science and Engineering: A 663 (2016) 213–224. doi:10.1016/j.msea.2016.02.068.

[307] F. J. Ridgeon, M. J. Raine, D. Halliday, M. Lakrimi, A. Thomas, D. P. Hampshire, Superconducting properties of titanium alloys (ti-64 and ti-6242) for critical current barrels, IEEE Transactions on Applied Superconductivity 27 (4) (2016) 1–5.

[308] H. Fan, S. Yang, Effects of direct aging on near-alpha ti–6al–2sn–4zr–2mo (ti-6242) titanium alloy fabricated by selective laser melting (slm), Materials Science and Engineering: A 788 (2020) 139533.

[309] M. Lopez, C. Pickett, E. Arrieta, L. E. Murr, R. B. Wicker, M. Ahlfors, D. Godfrey, F. Medina, Effects of postprocess hot isostatic pressing treatments on the mechanical performance of ebm fabricated ti-6al-2sn-4zr-2mo, Materials 13 (11) (2020) 2604.

[310] T. Fujieda, Y. Cui, K. Aoyagi, Y. Koizumi, A. Chiba, Electron beam melting of boron-modified ti–6al–2sn–4zr–2mo–0.1 si alloy with superior tensile strength and oxidation resistance at elevated temperatures, Materialia 4 (2018) 367–372.

[311] Y. Cui, K. Aoyagi, Y. Koizumi, T. Fujieda, A. Chiba, Enhanced oxidation resistance of a titanium–based alloy by the addition of boron and the application of electron beam melting, Additive Manufacturing 31 (2020) 100971.

[312] Y. Chen, S. J. Clark, L. Sinclair, C. L. A. Leung, S. Marussi, T. Connolley, R. C. Atwood, G. J. Baxter, M. A. Jones, I. Todd, et al., Synchrotron x-ray imaging of directed energy deposition additive manufacturing of titanium alloy ti-6242, Additive Manufacturing 41 (2021) 101969.

[313] E8/E8M-21, Standard test methods for tension testing of metallic materials, Tech. rep., ASTM International, West Conshohocken, PA (2021). doi:10.1520/E0008_E0008M-21.

[314] A. Khorasani, I. Gibson, U. S. Awan, A. Ghaderi, The effect of slm process parameters on density, hardness, tensile strength and surface quality of ti-6al-4v, Additive Manufacturing 25 (2019) 176–186. doi:10.1016/j.addma.2018.09.002.

[315] T. Voisin, N. P. Calta, S. A. Khairallah, J. B. Forien, L. Balogh, R. W. Cunningham, A. D. Rollett, Y. M. Wang, Defects-dictated tensile properties of selective laser melted ti-6al-4v, Materials and Design 158 (2018) 113–126. doi:10.1016/j.matdes.2018.08.004.

[316] C. Kamath, Determination of process parameters for high-density, ti-6al-4v parts using additive manufacturing, Tech. rep., Lawrence Livermore National Lab.(LLNL), Livermore, CA (United States) (8 2017). doi:10.2172/1413166.
URL https://www.osti.gov/biblio/1413166

[317] H. Gong, H. Gu, K. Zeng, J. Dilip, D. Pal, B. Stucker, D. Christiansen, J. Beuth, J. J. Lewandowski, Melt pool characterization for selective laser melting of ti-6al-4v pre-alloyed powder, in: Proceedings of 15th Annual International Solid Freeform Fabrication Symposium, Austin, TX, 2014, pp. 256–267.

[318] G. Çam, J. F. Dos Santos, M. Koçak, Determination of process parameters for high-density, ti-6al-4v parts using additive manufacturing, Tech. rep., GKSS-Forschungszentrum Geesthacht GmbH, Germany (1997).
URL https://www.osti.gov/etdeweb/servlets/purl/595200

[319] B. Song, S. Dong, B. Zhang, H. Liao, C. Coddet, Effects of processing parameters on microstructure and mechanical property of selective laser melted ti6al4v, Materials & Design 35 (2012) 120–125. doi:10.1016/j.matdes.2011.09.051.

[320] M. F. Zaeh, G. Branner, Investigations on residual stresses and deformations in selective laser melting, Production Engineering 4 (1) (2010) 35–45.

[321] M. Narvan, A. Ghasemi, E. Fereiduni, S. Kendrish, M. Elbestawi, Part deflection and residual stresses in laser powder bed fusion of h13 tool steel, Materials & Design 204 (2021) 109659.

[322] J. J. Lewandowski, M. Seifi, Metal additive manufacturing: a review of mechanical properties, Annual review of materials research 46 (2016) 151–186.

[323] H. Rafi, N. Karthik, H. Gong, T. L. Starr, B. E. Stucker, Microstructures and mechanical properties of ti6al4v parts fabricated by selective laser melting and electron beam melting, Journal of materials engineering and performance 22 (12) (2013) 3872–3883.

[324] P. Karimi, E. Sadeghi, J. Ålgårdh, A. Keshavarzkermani, R. Esmaeilizadeh, E. Toyserkani, J. Andersson, Columnar-to-equiaxed grain transition in powder bed fusion via mimicking casting solidification and promoting in situ recrystallization, Additive Manufacturing (2021) 102086.

[325] L. Sochalski-Kolbus, E. Payzant, P. Cornwell, T. Watkins, S. Babu, R. Dehoff, M. Lorenz, O. Ovchinnikova, C. Duty, Comparison of residual stresses in inconel 718 simple parts made by electron beam melting and direct laser metal sintering, Metallurgical and Materials Transactions A 46 (3) (2015) 1419–1432.

[326] T. Simson, A. Emmel, A. Dwars, J. Böhm, Residual stress measurements on aisi 316l samples manufactured by selective laser melting, Additive Manufacturing 17 (2017) 183–189.

[327] Y. Liu, Y. Yang, D. Wang, A study on the residual stress during selective laser melting (slm) of metallic powder, The International Journal of Advanced Manufacturing Technology 87 (1) (2016) 647–656.

[328] G. Vastola, G. Zhang, Q. Pei, Y.-W. Zhang, Controlling of residual stress in additive manufacturing of ti6al4v by finite element modeling, Additive Manufacturing 12 (2016) 231–239.

[329] R. Silverstein, D. Eliezer, Hydrogen trapping in 3d-printed (additive manufactured) ti-6al-4v, Materials Characterization 144 (2018) 297–304. doi:10.1016/j.matchar.2018.07.029.

[330] B. Damkroger, G. Edwards, B. Rath, Investigation of subsolidus weld cracking in alpha-beta titanium alloys, Welding journal 68 (7) (1989) 290–302.

[331] D. M. Bowden, E. Starke, The effect of microstructure and deformation behavior on the hot ductility of ti-6al-2nb-1ta-0.8 mo, Metallurgical Transactions A 15 (9) (1984) 1687–1698.

[332] S. Tammas-Williams, I. Todd, Design for additive manufacturing with site-specific properties in metals and alloys, Scripta Materialia 135 (2017) 105–110.

[333] F. Geiger, K. Kunze, T. Etter, Tailoring the texture of in738lc processed by selective laser melting (slm) by specific scanning strategies, Materials Science and Engineering: A 661 (2016) 240–246.

[334] W. Xu, E. W. Lui, A. Pateras, M. Qian, M. Brandt, In situ tailoring microstructure in additively manufactured ti-6al-4v for superior mechanical performance, Acta Materialia 125 (2017) 390–400.

[335] V. Popovich, E. Borisov, A. Popovich, V. S. Sufiiarov, D. Masaylo, L. Alzina, Functionally graded inconel 718 processed by additive manufacturing: Crystallographic texture, anisotropy of microstructure and mechanical properties, Materials & Design 114 (2017) 441–449.

[336] M.-S. Pham, B. Dovgyy, P. A. Hooper, C. M. Gourlay, A. Piglione, The role of side-branching in microstructure development in laser powder-bed fusion, Nature communications 11 (1) (2020) 1–12.

[337] K. A. Sofinowski, S. Raman, X. Wang, B. Gaskey, M. Seita, Layer-wise engineering of grain orientation (lego) in laser powder bed fusion of stainless steel 316l, Additive Manufacturing 38 (2021) 101809.

[338] R. Acharya, J. A. Sharon, A. Staroselsky, Prediction of microstructure in laser powder bed fusion process, Acta Materialia 124 (2017) 360–371.

[339] Y. Zhang, J. Zhang, Modeling of solidification microstructure evolution in laser powder bed fusion fabricated 316l stainless steel using combined computational fluid dynamics and cellular automata, Additive Manufacturing 28 (2019) 750–765.

[340] T. M. Rodgers, D. Moser, F. Abdeljawad, O. D. U. Jackson, J. D. Carroll, B. H. Jared, D. S. Bolintineanu, J. A. Mitchell, J. D. Madison, Simulation of powder bed metal additive manufacturing microstructures with coupled finite difference-monte carlo method, Additive Manufacturing 41 (2021) 101953.

[341] S. Ghosh, M. Mahmoudi, L. Johnson, A. Elwany, R. Arroyave, D. Allaire, Uncertainty analysis of microsegregation during laser powder bed fusion, Modelling and Simulation in Materials Science and Engineering 27 (3) (2019) 034002.

[342] Y. Oshida, Bioscience and bioengineering of titanium materials, Elsevier, 2010.

[343] C. Song, A. Wang, Z. Wu, Z. Chen, Y. Yang, D. Wang, The design and manufacturing of a titanium alloy beak for grus japonensis using additive manufacturing, Materials & Design 117 (2017) 410–416.

[344] W.-S. Lin, T. L. Starr, B. T. Harris, A. Zandinejad, D. Morton, Additive manufacturing technology (direct metal laser sintering) as a novel approach to fabricate functionally graded titanium implants: preliminary investigation of fabrication parameters., The International journal of oral & maxillofacial implants 28 (6) (2013) 1490–1495.

[345] J. Ong, M. R. Appleford, G. Mani, Introduction to biomaterials: basic theory with engineering applications, Cambridge University Press, 2014.

[346] C. Emmelmann, P. Sander, J. Kranz, E. Wycisk, Laser additive manufacturing and bionics: redefining lightweight design, Physics Procedia 12 (2011) 364–368.

[347] A. du Plessis, C. Broeckhoven, I. Yadroitsava, I. Yadroitsev, C. H. Hands, R. Kunju, D. Bhate, Beautiful and functional: a review of biomimetic design in additive manufacturing, Additive Manufacturing 27 (2019) 408–427.

[348] L. Murr, K. Amato, S. Li, Y. Tian, X. Cheng, S. Gaytan, E. Martinez, P. Shindo, F. Medina, R. Wicker, Microstructure and mechanical properties of open-cellular biomaterials prototypes for total knee replacement implants fabricated by electron beam melting, Journal of the mechanical behavior of biomedical materials 4 (7) (2011) 1396–1411.

[349] X. Tan, Y. Tan, C. Chow, S. Tor, W. Yeong, Metallic powder-bed based 3d printing of cellular scaffolds for orthopaedic implants: A state-of-the-art review on manufacturing, topological design, mechanical properties and biocompatibility, Materials Science and Engineering: C 76 (2017) 1328–1343.

172

[350] S. Boonen, X. Cheng, J. Nijs, P. Nicholson, G. Verbeke, E. Lesaffre, J. Aerssens, J. Dequeker, Factors associated with cortical and trabecular bone loss as quantified by peripheral computed tomography (pqct) at the ultradistal radius in aging women, Calcified tissue international 60 (2) (1997) 164–170.

[351] J. Spadaro, F. Werner, R. Brenner, M. Fortino, L. Fay, W. Edwards, Cortical and trabecular bone contribute strength to the osteopenic distal radius, Journal of orthopaedic research 12 (2) (1994) 211–218.

[352] S. Majumdar, H. Genant, S. Grampp, D. Newitt, V.-H. Truong, J. Lin, A. Mathur, Correlation of trabecular bone structure with age, bone mineral density, and osteoporotic status: in vivo studies in the distal radius using high resolution magnetic resonance imaging, Journal of Bone and Mineral Research 12 (1) (1997) 111–118.

[353] H. Chen, X. Zhou, H. Fujita, M. Onozuka, K.-Y. Kubo, Age-related changes in trabecular and cortical bone microstructure, International journal of endocrinology 2013 (2013).

[354] B. L. Riggs, L. J. Melton III, R. A. Robb, J. J. Camp, E. J. Atkinson, J. M. Peterson, P. A. Rouleau, C. H. McCollough, M. L. Bouxsein, S. Khosla, Population-based study of age and sex differences in bone volumetric density, size, geometry, and structure at different skeletal sites, Journal of Bone and Mineral Research 19 (12) (2004) 1945–1954.

[355] S. Khosla, B. L. Riggs, E. J. Atkinson, A. L. Oberg, L. J. McDaniel, M. Holets, J. M. Peterson, L. J. Melton III, Effects of sex and age on bone microstructure at the ultradistal radius: a population-based noninvasive in vivo assessment, Journal of Bone and Mineral Research 21 (1) (2006) 124–131.

[356] K. M. Nicks, S. Amin, E. J. Atkinson, B. L. Riggs, L. J. Melton III, S. Khosla, Relationship of age to bone microstructure independent of areal bone mineral density, Journal of Bone and Mineral Research 27 (3) (2012) 637–644.

[357] H. M. Macdonald, K. K. Nishiyama, J. Kang, D. A. Hanley, S. K. Boyd, Age-related patterns of trabecular and cortical bone loss differ between sexes and skeletal sites: a population-based hr-pqct study, Journal of Bone and Mineral Research 26 (1) (2011) 50–62.

[358] J. Aaron, N. Makins, K. Sagreiya, The microanatomy of trabecular bone loss in normal aging men and women., Clinical orthopaedics and related research 215 (1987) 260–271.

173

[359] E. Seeman, Pathogenesis of bone fragility in women and men, The Lancet 359 (9320) (2002) 1841–1850.

[360] M. J. Munford, K. G. Ng, J. R. Jeffers, Mapping the multi-directional mechanical properties of bone in the proximal tibia, Advanced Functional Materials 30 (46) (2020) 2004323.

[361] E. F. Morgan, G. U. Unnikrisnan, A. I. Hussein, Bone mechanical properties in healthy and diseased states, Annual review of biomedical engineering 20 (2018) 119–143.

[362] M. A. Velasco, C. A. Narváez-Tovar, D. A. Garzón-Alvarado, Design, materials, and mechanobiology of biodegradable scaffolds for bone tissue engineering, BioMed research international 2015 (2015).

[363] R. W. McCalden, J. A. McGeough, M. B. Barker, et al., Age-related changes in the tensile properties of cortical bone. the relative importance of changes in porosity, mineralization, and microstructure., The Journal of bone and joint surgery. American volume 75 (8) (1993) 1193–1205.

[364] S. Peel, D. Eggbeer, Additively manufactured maxillofacial implants and guides–achieving routine use, Rapid Prototyping Journal (2016).

[365] H. E. Burton, S. Peel, D. Eggbeer, Reporting fidelity in the literature for computer aided design and additive manufacture of implants and guides, Additive Manufacturing 23 (2018) 362–373.

[366] S. L. Sing, J. An, W. Y. Yeong, F. E. Wiria, Laser and electron-beam powder-bed additive manufacturing of metallic implants: A review on processes, materials and designs, Journal of Orthopaedic Research 34 (3) (2016) 369–385.

[367] Y. M. Wang, T. Voisin, J. T. McKeown, J. Ye, N. P. Calta, Z. Li, Z. Zeng, Y. Zhang, W. Chen, T. T. Roehling, Additively manufactured hierarchical stainless steels with high strength and ductility, Nature materials 17 (1) (2018) 63–71.

[368] A. Broda, R. Casadei, Impact of vehicle weight reduction on fuel economy for various vehicle architectures, The Aluminum Association, Inc (2007).

[369] R. Mines, S. Tsopanos, Y. Shen, R. Hasan, S. McKown, Drop weight impact behaviour of sandwich panels with metallic micro lattice cores, International Journal of Impact Engineering 60 (2013) 120–132.

174

[370] G. Dong, Y. Tang, Y. F. Zhao, A survey of modeling of lattice structures fabricated by additive manufacturing, Journal of Mechanical Design 139 (10) (2017).

[371] G. Maliaris, E. Sarafis, Mechanical behavior of 3d printed stochastic lattice structures, in: Solid State Phenomena, Vol. 258, Trans Tech Publ, 2017, pp. 225–228.

[372] R. J. Mobbs, M. Coughlan, R. Thompson, C. E. Sutterlin, K. Phan, The utility of 3d printing for surgical planning and patient-specific implant design for complex spinal pathologies: case report, Journal of Neurosurgery: Spine 26 (4) (2017) 513–518.

[373] D. Kim, J.-Y. Lim, K.-W. Shim, J. W. Han, S. Yi, D. H. Yoon, K. N. Kim, Y. Ha, G. Y. Ji, D. A. Shin, Sacral reconstruction with a 3d-printed implant after hemisacrectomy in a patient with sacral osteosarcoma: 1-year follow-up result, Yonsei medical journal 58 (2) (2017) 453.

[374] W. J. Choy, R. J. Mobbs, B. Wilcox, S. Phan, K. Phan, C. E. Sutterlin III, Reconstruction of thoracic spine using a personalized 3d-printed vertebral body in adolescent with t9 primary bone tumor, World Neurosurgery 105 (2017) 1032–e13.

[375] N. Xu, F. Wei, X. Liu, L. Jiang, H. Cai, Z. Li, M. Yu, F. Wu, Z. Liu, Reconstruction of the upper cervical spine using a personalized 3d-printed vertebral body in an adolescent with ewing sarcoma, Spine 41 (1) (2016) E50–E54.

[376] T. Hilton, N. Campbell, K. Hosking, Additive manufacturing in orthopaedics: Clinical implications, SA Orthopaedic Journal 16 (2) (2017) 63–67.

[377] T. Schouman, M. Schmitt, C. Adam, G. Dubois, P. Rouch, Influence of the overall stiffness of a load-bearing porous titanium implant on bone ingrowth in critical-size mandibular bone defects in sheep, Journal of the mechanical behavior of biomedical materials 59 (2016) 484–496.

[378] S. Arabnejad, B. Johnston, M. Tanzer, D. Pasini, Fully porous 3d printed titanium femoral stem to reduce stress-shielding following total hip arthroplasty, Journal of Orthopaedic Research 35 (8) (2017) 1774–1783.

[379] J. Biemond, G. Hannink, N. Verdonschot, P. Buma, Bone ingrowth potential of electron beam and selective laser melting produced trabecular-like implant surfaces with and without a biomimetic coating, Journal of Materials Science: Materials in Medicine 24 (3) (2013) 745–753.

[380] S. Van Bael, Y. C. Chai, S. Truscello, M. Moesen, G. Kerckhofs, H. Van Oosterwyck, J.-P. Kruth, J. Schrooten, The effect of pore geometry on the in vitro biological behavior of human periosteum-derived cells seeded on selective laser-melted ti6al4v bone scaffolds, Acta biomaterialia 8 (7) (2012) 2824–2834.

[381] B. Otsuki, M. Takemoto, S. Fujibayashi, M. Neo, T. Kokubo, T. Nakamura, Pore throat size and connectivity determine bone and tissue ingrowth into porous implants: three-dimensional micro-ct based structural analyses of porous bioactive titanium implants, Biomaterials 27 (35) (2006) 5892–5900.

[382] O. L. Harrysson, O. Cansizoglu, D. J. Marcellin-Little, D. R. Cormier, H. A. West II, Direct metal fabrication of titanium implants with tailored materials and mechanical properties using electron beam melting technology, Materials Science and Engineering: C 28 (3) (2008) 366–373.

[383] K. Wong, S. Kumta, N. Geel, J. Demol, One-step reconstruction with a 3d-printed, biomechanically evaluated custom implant after complex pelvic tumor resection, Computer Aided Surgery 20 (1) (2015) 14–23.

[384] L. Wang, J. Kang, C. Sun, D. Li, Y. Cao, Z. Jin, Mapping porous microstructures to yield desired mechanical properties for application in 3d printed bone scaffolds and orthopaedic implants, Materials & Design 133 (2017) 62–68.

[385] J. Wieding, A. Wolf, R. Bader, Numerical optimization of open-porous bone scaffold structures to match the elastic properties of human cortical bone, Journal of the mechanical behavior of biomedical materials 37 (2014) 56–68.

[386] N. Soro, H. Attar, X. Wu, M. S. Dargusch, Investigation of the structure and mechanical properties of additively manufactured ti-6al-4v biomedical scaffolds designed with a schwartz primitive unit-cell, Materials Science and Engineering: A 745 (2019) 195–202.

[387] F. Bartolomeu, M. Costa, N. Alves, G. Miranda, F. Silva, Selective laser melting of ti6al4v sub-millimetric cellular structures: Prediction of dimensional deviations and mechanical performance, Journal of the Mechanical Behavior of Biomedical Materials 113 (2021) 104123.

[388] A. Balcı, F. Küçükaltun, M. F. Aycan, Y. Usta, T. Demir, Reproducibility of replicated trabecular bone structures from ti6al4v extralow interstitials powder by selective laser melting, Arabian Journal for Science and Engineering 46 (3) (2021) 2527–2541.

[389] K. Bari, A. Arjunan, Extra low interstitial titanium based fully porous morphological bone scaffolds manufactured using selective laser melting, Journal of the mechanical behavior of biomedical materials 95 (2019) 1–12.

[390] X.-Y. Zhang, X.-C. Yan, G. Fang, M. Liu, Biomechanical influence of structural variation strategies on functionally graded scaffolds constructed with triply periodic minimal surface, Additive Manufacturing 32 (2020) 101015.

[391] K. Phan, A. Sgro, M. M. Maharaj, P. D'Urso, R. J. Mobbs, Application of a 3d custom printed patient specific spinal implant for c1/2 arthrodesis, Journal of Spine Surgery 2 (4) (2016) 314.

[392] I. Yadroitsava, A. du Plessis, I. Yadroitsev, Bone regeneration on implants of titanium alloys produced by laser powder bed fusion: a review, Titanium for Consumer Applications (2019) 197–233.

[393] A. Charles, A. Elkaseer, L. Thijs, S. G. Scholz, Dimensional errors due to overhanging features in laser powder bed fusion parts made of ti-6al-4v, Applied Sciences 10 (7) (2020) 2416.

[394] X. Wang, K. Chou, Effect of support structures on ti-6al-4v overhang parts fabricated by powder bed fusion electron beam additive manufacturing, Journal of Materials Processing Technology 257 (2018) 65–78.

[395] L. Newton, N. Senin, E. Chatzivagiannis, B. Smith, R. Leach, Feature-based characterisation of ti6al4v electron beam powder bed fusion surfaces fabricated at different surface orientations, Additive Manufacturing 35 (2020) 101273.

[396] K. Cooper, P. Steele, B. Cheng, K. Chou, Contact-free support structures for part overhangs in powder-bed metal additive manufacturing, Inventions 3 (1) (2018) 2.

[397] N. Soro, N. Saintier, J. Merzeau, M. Veidt, M. S. Dargusch, Quasi-static and fatigue properties of graded ti–6al–4v lattices produced by laser powder bed fusion (lpbf), Additive Manufacturing 37 (2021) 101653.

[398] A. Du Plessis, S. M. J. Razavi, F. Berto, The effects of microporosity in struts of gyroid lattice structures produced by laser powder bed fusion, Materials & Design 194 (2020) 108899.

[399] I. Echeta, X. Feng, B. Dutton, R. Leach, S. Piano, Review of defects in lattice structures manufactured by powder bed fusion, The International Journal of Advanced Manufacturing Technology 106 (5) (2020) 2649–2668.

[400] T. J. Webster, J. U. Ejiofor, Increased osteoblast adhesion on nanophase metals: Ti, ti6al4v, and cocrmo, Biomaterials 25 (19) (2004) 4731–4739.

[401] N. Gui, W. Xu, D. Myers, R. Shukla, H. Tang, M. Qian, The effect of ordered and partially ordered surface topography on bone cell responses: a review, Biomaterials science 6 (2) (2018) 250–264.

[402] L. Chougrani, J.-P. Pernot, P. Véron, S. Abed, Lattice structure lightweight triangulation for additive manufacturing, Computer-Aided Design 90 (2017) 95–104.

[403] G. Shanbhag, M. Vlasea, The effect of reuse cycles on ti-6al-4v powder properties processed by electron beam powder bed fusion, Manufacturing Letters 25 (2020) 60–63.

[404] X. Gong, T. Anderson, K. Chou, Review on powder-based electron beam additive manufacturing technology, in: International Symposium on Flexible Automation, Vol. 45110, American Society of Mechanical Engineers, 2012, pp. 507–515.

[405] D. Melancon, Z. Bagheri, R. Johnston, L. Liu, M. Tanzer, D. Pasini, Mechanical characterization of structurally porous biomaterials built via additive manufacturing: experiments, predictive models, and design maps for load-bearing bone replacement implants, Acta biomaterialia 63 (2017) 350–368.

[406] A. Cuadrado, A. Yánez, O. Martel, S. Deviaene, D. Monopoli, Influence of load orientation and of types of loads on the mechanical properties of porous ti6al4v biomaterials, Materials & Design 135 (2017) 309–318.

[407] A. Townsend, N. Senin, L. Blunt, R. Leach, J. Taylor, Surface texture metrology for metal additive manufacturing: a review, Precision Engineering 46 (2016) 34–47.

[408] O. Al-Ketan, R. Rowshan, R. K. A. Al-Rub, Topology-mechanical property relationship of 3d printed strut, skeletal, and sheet based periodic metallic cellular materials, Additive Manufacturing 19 (2018) 167–183.

[409] S. Li, H. Hassanin, M. M. Attallah, N. J. Adkins, K. Essa, The development of tini-based negative poisson's ratio structure using selective laser melting, Acta Materialia 105 (2016) 75–83.

[410] A. Du Plessis, I. Yadroitsev, I. Yadroitsava, S. G. Le Roux, X-ray microcomputed tomography in additive manufacturing: a review of the current technology and applications, 3D Printing and Additive Manufacturing 5 (3) (2018) 227–247.

[411] A. M. Vilardell, A. Takezawa, A. Du Plessis, N. Takata, P. Krakhmalev, M. Kobashi, I. Yadroitsava, I. Yadroitsev, Topology optimization and characterization of ti6al4v eli cellular lattice structures by laser powder bed fusion for biomedical applications, Materials Science and Engineering: A 766 (2019) 138330.

[412] E. Eschner, T. Staudt, M. Schmidt, Correlation of spatter behavior and process zone formation in powder bed fusion of metals, CIRP Annals 69 (1) (2020) 209–212.

APPENDICES

Appendix A

Architectural bone parameters and the relationship to titanium lattice design for powder bed fusion additive manufacturing

A.1 Preface

Additive manufacturing (AM) of titanium (Ti) and Ti-6Al-4V lattices has been proposed for bone implants and augmentation devices. Ti and Ti-6Al-4V have favourable biocompatibility, corrosion resistance and fatigue strength for bone applications; yet, the optimal parameters for Ti-6Al-4V lattice designs corresponding to the natural micro- and meso-scale architecture of human trabecular and cortical bone are not well understood. A comprehensive review was completed to compare the natural lattice architecture properties in human bone to Ti and Ti-6Al-4V lattice structures for bone repair and augmentation. Ti and Ti-6Al-4V lattice porosity has varied from 15% to 97% with most studies reporting a porosity between 50-70%. Cortical bone is roughly 5-15% porous and lattices with 50-70% porosity are able to achieve comparable stiffness, compressive strength, and yield strength. Trabecular bone has a reported porosity range from 70-90%, with trabecular thickness varying from 120-200 µm. Existing powder bed fusion technologies have produced strut and wall thicknesses ranging from 200-1669 µm. This suggests limited overlap between current AM of Ti and Ti-6Al-4V lattice structures and trabecular bone architecture, indicating that replicating natural trabecular bone parameters with latticing is prohibitively

challenging. This review contributes to the body of knowledge by identifying the correspondence of Ti and Ti-6Al-4V lattices to the natural parameters of bone microarchitectures, and provides further guidance on the design and AM recommendations towards addressing recognized performance gaps with powder bed fusion technologies. For this work, my major contributions included: designing the LPBF lattice structure, conducting the LPBF manufacturing, X-ray computed tomography analysis, and writing the section on additive manufactured lattices for bone repair and augmentation and the discussion on manufacturability considerations [303].

A.2 Introduction

The use of Ti-6Al-4V is well established in the medical device industry [342]. Titanium and titanium alloys are ideal for replacing hard tissues, such as bone, due to their biocompatibility and excellent strength-to-weight ratio [343, 344]. Ti-6Al-4V also exhibits excellent fatigue strength and corrosion resistance allowing implants to withstand the cyclic loading in high ion environments present in vivo during activities of daily living [345]. These properties of titanium and Ti-6Al-4V have led such alloys to become some of the most widely used metal materials for joint replacement and fracture fixation procedures in the orthopaedic industry.

Despite their widespread use in the medical device industry for the augmentation and repair of bone, pure titanium and Ti-6Al-4V do not have material properties similar to those of bone. Ti-6Al-4V is roughly twice as stiff as human cortical bone with up to seven times the compressive strength [346, 347, 348]. Bone is mechanoresponsive and requires regular loading in order to proliferate new bone. Implanting a stiffer material like titanium adjacent to bone can cause stress shielding of bone, resorption of the surrounding bone tissue which can lead to implant loosening and failure [94]. Therefore, it is imperative that designs of titanium and titanium alloy implants are tailored to more closely match the natural mechanical response of bone tissue. One approach to reducing stress shielding near the bone-implant interface is by light-weighting implants through latticing in an effort to reduce mechanical properties from those of the stiffness of the material. Additive manufacturing allows for unique design approaches thereby allowing for control of mechanical properties, while minimizing weight through unique geometries and graded material properties. Additive manufacturing technologies are of particular use in the medical device industry where implants are made for specific applications in which weight and mechanical properties are integral to implant function. Production of Ti-6Al-4V lattice structures through additive manufacturing for biomedical applications was thoroughly reviewed by

Tan et al. in 2017. They concluded that optimal guidelines for lattice design in biological environments has not yet been established and that the field is rapidly and continually evolving [349]. Since the review by Tan et al. in 2017 was completed, many additional studies have successfully progressed toward this goal by manipulating lattice parameters such as porosity, pore size, and strut thickness in order to produce unit cells that more closely exhibit stiffness, compressive strength and fatigue strength of human bone. Lattice parameters vary widely across the literature and while general recommendations have been made, there remain questions as to which lattice design produces the optimal structure for implant fixation and reduction of stress shielding through mechanical property optimization.

A consideration that is notably overlooked in developing lattice structures for bone repair and augmentation is how to best model the architectural parameters of human bone. Therefore, a comprehensive literature review is needed to examine the parameters of bone micro-architecture in correspondence with lattice design parameters used in additive manufacturing. A review of existing additive manufacturing literature was completed to determine which titanium lattice parameters have been examined for implants used to replace or augment human bone. Lastly, recommendations are made on how to best use this information towards the design and additive manufacturing of improved titanium and Ti-6Al-4V lattice structures for bone repair and augmentation.

A.3 Review of human bone properties relevant to lattice design

A.3.1 Review of human bone function

Bone is a tough, elastic tissue that gives structural support to the human body. As a living tissue, bone adapts to its environment and loading conditions through the breakdown of existing bone by osteoclasts and the proliferation of new bone by osteoblasts. This process leads bone to exhibit mechanoresponsive behaviour, wherein the more it is loaded, the thicker and denser it becomes. Bone can be categorized into two main types: cortical bone and trabecular bone, see Figure A.1. Different bones in the human body consist of different amounts and configurations of cortical and trabecular bone. Long bones, such as the femur, tibia, radius, and humerus, have a long shaft made up of primarily cortical bone. The articulating ends of long bones are made of primarily trabecular bone contained by a thin shell of cortical bone. Short bones, such as vertebrae, carpals, and tarsals,

are made primarily of trabecular bone with a thin cortical shell making them strong and compact. Cortical bone density and trabecular bone density are important indicators of bone strength, and decrease with age, for instance by approximately 0.41% and 0.65% per year, respectively, for women ages 70 to 87 years old [350]. However, studies have demonstrated that trabecular bone has a higher correlation to bone strength than cortical bone [351].

A.3.2   Trabecular bone

Trabecular bone, or cancellous bone, is a lattice-like structure that allows bone to maintain its strength, while being relatively lightweight. Trabecular bone is primarily located at the articulating ends of long bones and in the body of short bones, which allows for improved load transfer through these structures. The exact configuration of trabecular bone microstructure is still being discovered. The most established theory characterizes the trabeculae, or struts, by their thickness, spacing, number and spatial configuration. Measurement techniques for these parameters are well established and widely published to comparatively describe trabecular bone quality, with more and thicker trabeculae suggesting better bone health [352]. However, emerging and more advanced geometric models consider the shape of trabecular surface and the rod vs plate-like structures of trabecular architecture in greater detail [92, 48].

The integrity of trabecular bone microstructure is often used as an indicator for overall bone health. At any given age, men have a higher trabecular bone mass than women, however decreases in trabecular bone density due to aging are similar in women and men [353, 354, 355, 356, 357]. Age-related changes cause buckling of trabeculae due to a decrease in the number and thickness of trabeculae, and an increase in trabecular length [352]. Collectively, these changes result in a decreased trabecular density; however, the pathology of this reduction differs in men and women [352]. In women, the decrease in bone volume occurs primarily due to a decrease in the number of trabeculae, whereas in men, it may be predominantly attributed to the thinning of trabeculae [353, 358]. The decrease in trabeculae in women is related to menopause, where less estrogen is produced, which increases bone reabsorption [359]. Therefore, in making design considerations for orthopaedic medical devices, the patient population, age and sex should be carefully considered. Changes may be made to lattices designs to model the reduction in bone density with age. Lattice structures with fewer shorter features may better represent aging female bone and lengthening features may better model aging male bone. Lower density lattice designs should also be considered for older adults and post-menopausal women.

184
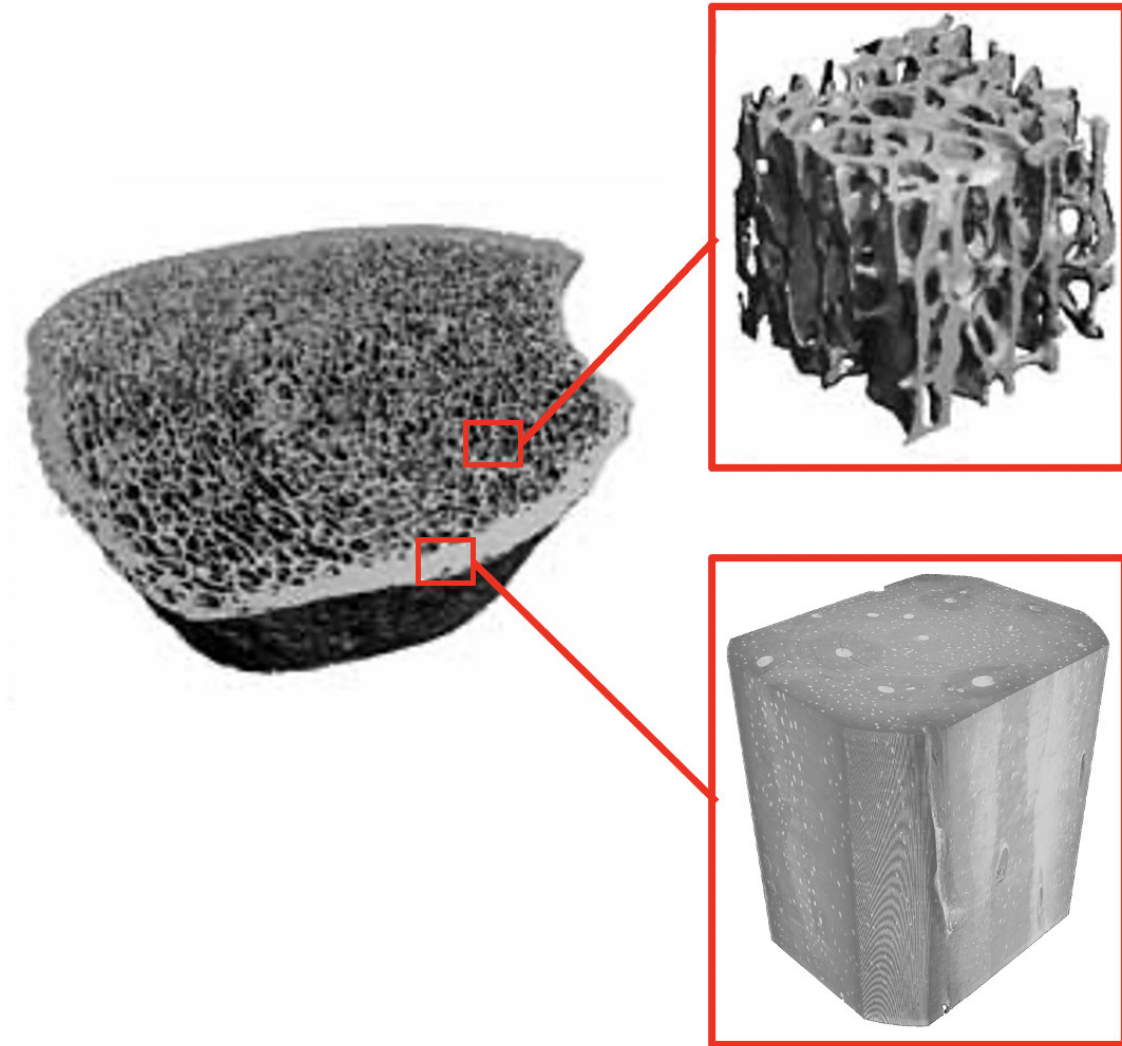
Figure A.1: Human bone can be categorized into two main types: cortical and trabecular. Cortical bone is the stiffer, more dense bone which encapsulates short bones, the ends of long bones and comprises the shaft of long bones. Trabecular bone is the lattice like structure which makes up the majority of short bone structure as well as the ends of long bones. This figure was adapted from the μCT work of Lui et al. and Gauthier et al. [12, 13]

Micro-architecture of trabecular bone

The micro-structure of trabecular bone can be characterized by the individual trabeculae and the spaces between them. To determine bone porosity, the volume of bone (BV) is divided by the total volume (TV) for a given sample (BV/TV). Other groups have also compared total bone surface area (BS) with respect to bone volume (BS/BV) or total specimen volume (BS/TV) as another form of trabecular quality indicator. Trabeculae are further characterized by thickness of individual vertical trabeculae (TbTh), the distance between trabeculae (TbSp), and the number of trabeculae that intersect with a given two-dimensional distance metric (TbN), typically 1 cm, as shown in Figure A.2.
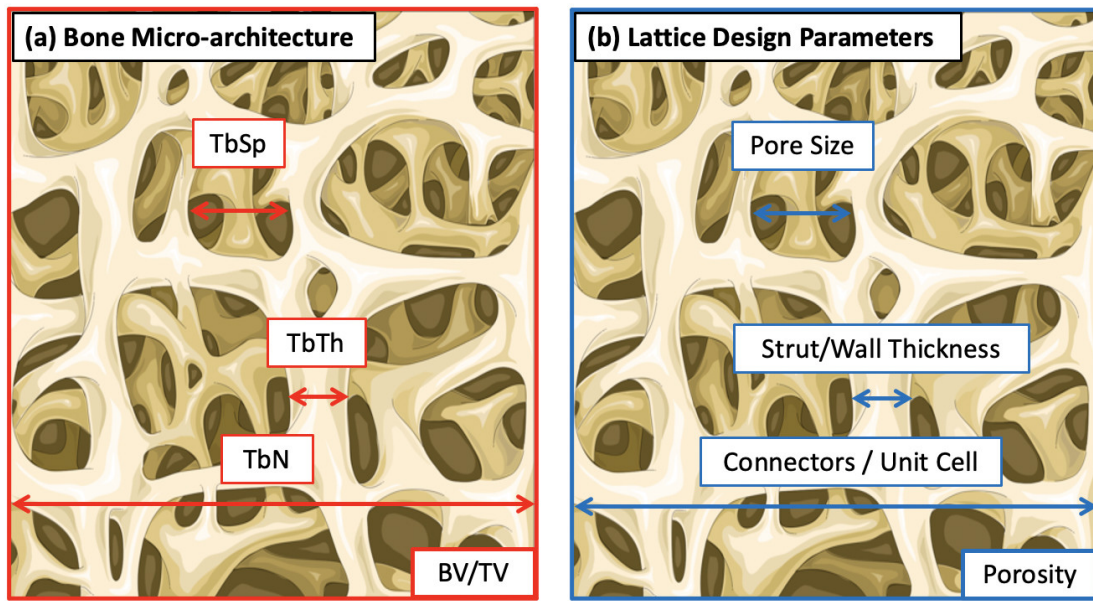
Figure A.2: Commonly reported measurements of trabecular bone microstructure (red) may be used to describe lattice parameters commonly used in additive manufacturing (blue).

Methods of calculating bone architectural parameters may vary between studies; however, the technique proposed by Hildebrand et al. is the most widely accepted in general literature, as shown in Table A.1. Hildebrand et al. proposed a two-dimensional (2D) plate model that allows for calculation of 2D parameters such as TbTh, TbSp and TbN [14].

Trabecular bone density and parameters vary greatly with anatomical location, as shown in Figure A.3. When determining design considerations for bone replacing im-

Trabecular Bone Parameter	Measurement/Calculation
Apparent bone density	BV/TV
Porosity	1 - BV/TV
Bone surface fraction	BS/BV or BS/TV
Trabecular thickness	TbTh = 2 BV/BSs
Trabecular spacing	TbSp = 2 (TV-BV)/BS
Trabecular number	TbN = 0.5 BS/TV

Table A.1: The Hildebrand et al. method for calculating two dimensional trabecular measurements from known bone volume fractions.

plants, anatomical location and device function should be considered. Hildebrand et al. undertook an in-depth in vitro study comparing the micro-architecture of trabecular bone at different sites across the skeleton [14].

Mechanical properties of trabecular bone

The mechanical properties of trabecular bone vary significantly with respect to bone density. For instance, trabecular bone density predicts 81% of axial strength variation in the human tibia [360]. The porosity of human trabecular bone ranges from 40-95%, dependent on skeletal location, bone region, and population parameters [361]. Stiffness and strength of trabecular bone is significantly greater in the direction of loading, z-axis, and lower, but similar, however still anisotropic, in the x- and y-axis respectively. Young's modulus of trabecular bone can range from 1-5 GPa along the axis of loading and 50-700 MPa off-axis. As such, the compressive and tensile strength of trabecular bone ranges from 0.1-30 MPa and 6-8 MPa, respectively [16, 17, 362].

A.3.3   Cortical bone

Cortical bone, or compact bone, is much more dense than trabecular bone and acts as a stiff outer layer for short bones, joints in long bones and the sole composition of the hollow shafts of long bones. Cortical shells allow for a continuous surface at the joints for ligamentous and tendonous attachment. Cortical bone improves the overall fracture toughness and provides structural integrity to limbs allowing for gross movement.

Iliac Crest

Porosity = 84%
Feature Thickness = 0.15 (mm)
Pore Size = 0.75 (mm)
Features/mm = 1.40 (mm^{-1})

BV/TV = 0.16
TbTh = 0.15 (mm)
TbSp = 0.75 (mm)
TbN = 1.40 (mm^{-1})

L2 Vertebra

BV/TV = 0.08
TbTh = 0.12 (mm)
TbSp = 0.79 (mm)
TbN = 1.28 (mm^{-1})

Porosity = 92%
Feature Thickness = 0.12 (mm)
Pore Size = 0.79 (mm)
Features/mm = 1.28 (mm^{-1})

Femoral Head

Porosity = 74%
Feature Thickness = 0.19 (mm)
Pore Size = 0.64 (mm)
Features/mm = 1.60 (mm^{-1})

BV/TV = 0.26
TbTh = 0.19 (mm)
TbSp = 0.65 (mm)
TbN = 1.60 (mm^{-1})

L4 Vertebra

BV/TV = 0.09
TbTh = 0.14 (mm)
TbSp = 0.85 (mm)
TbN = 1.16 (mm^{-1})

Porosity = 91%
Feature Thickness = 0.14 (mm)
Pore Size = 0.85 (mm)
Features/mm = 1.16 (mm^{-1})

Calcaneal Core

Porosity = 88%
Feature Thickness = 0.13 (mm)
Pore Size = 0.68 (mm)
Features/mm = 1.46 (mm^{-1})

BV/TV = 0.12
TbTh = 0.13 (mm)
TbSp = 0.68 (mm)
TbN = 1.46 (mm^{-1})

Proximal Tibia*

BV/TV = 0.15
TbTh = 0.11 (mm)
TbSp = 0.67 (mm)
TbN = 1.32 (mm^{-1})

Porosity = 85%
Feature Thickness = 0.11 (mm)
Pore Size = 0.67 (mm)
Features/mm = 1.32 (mm^{-1})

Figure A.3: A comprehensive summary of two- and three-dimensional measurements of trabecular bone at the femoral head, illiac crest, calcaneal core, L2 vertebra and L4 vertebra as described by Hildebrand et al. [14]. The mean data reported by Hildebrand et al. was supplemented with Thomsen et al.'s report [15] of trabecular bone parameters at the proximal tibia to form an original visual representation*. Bone microstructure data is outlined in red and suggested translation to lattice design parameters is outlined in blue. The values listed represent the mean value of the each measurement.

Micro-architecture of cortical bone

Cortical bone is much more dense than trabecular and exhibits only 5-15% porosity [361]. It is well documented that cortical bone porosity and thickness decrease with age [353]. Interestingly, micro-structural analysis has shown that the cortical bone stiffness, fatigue strength and fracture toughness decrease with age [363]. It should also be noted that studies have indicated that the decrease in cortical bone density is significant in women, but insignificant in men [353].

Mechanical properties of cortical bone

Cortical bone is widely considered to be transversely isotropic, with mechanical properties along the axis of loading, or the z-axis, being significantly greater than those in the x- and y- axis. The transversely isotropic mechanical properties of human cortical bone have been collated from literature to provide a holistic visual representation, see Figure A.4 [16, 17, 18].

E_z = 15-20 GPa
$\sigma c_{,z}$ = 170-190 MPa
$\sigma t_{,z}$ = 120-130 MPa

z

x

y

G = 3-3.5 GPa
σ_s = 68 MPa

$E_{x,y}$ = 5-11.5 GPa
$\sigma_{c,xy}$ = 133 MPa
$\sigma_{t,xy}$ = 51 MPa
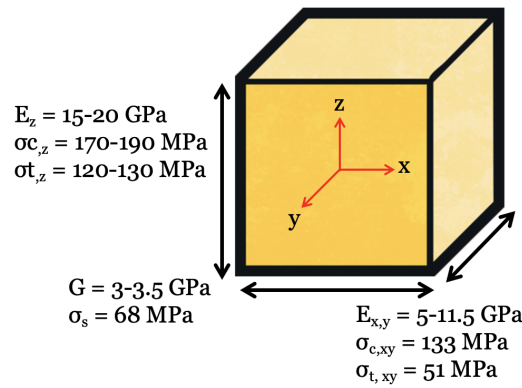
Figure A.4: Cortical bone exhibits transversely isotropic mechanical properties with nearly double the stiffness occurring along the axis of loading. [16, 17, 18] Young's modulus, ultimate compressive strength, and ultimate tensile strength in the longitudinal direction are denoted E_z, $\sigma_{c,z}$, and $\sigma_{t,z}$ respectively. The subscript "x,y" is given to denote mechanical properties in the transverse axes.

A.4 Additively manufactured lattices for bone repair and augmentation

Computer aided design (CAD) and additive manufacturing (AM) have advanced technological readiness, enabling the regulatory pathways and component mechanical performance to be ready for wide-scale application in the medical device industry [364, 365]. Existing literature on additively manufactured medical devices for bone repair and augmentation is widely spread based on target audience, research background, and study type. Research on additively manufactured medical devices can be found in surgical, tissue, biomedical engineering, additive manufacturing and/or material science journals. Collating the existing body of research into a cohesive overview proves challenging, as the focus of research covers a wide array of topics from AM process parameters, material properties, and biocompatibility, all the way to medical function and clinical outcomes. In order to review metal additive manufacturing as a technology for bone repair and augmentation an overview of metal AM and lattice design approaches has been included below.

A.4.1 Review of additive manufacturing for metals: powder bed fusion

Laser powder bed fusion (LPBF) and electron beam powder bed fusion (EB-PBF) are AM processes in which a heat source is directed towards a powdered material to micro-weld the material together, layer-by-layer. During the LPBF process, a fine laser beam (with beam spot sizes (σ) generally between 50 to 100 µm) is generally directed through a series of lenses towards an X-Y plane via scanning mirrors which direct the beam towards the build platform. In EB-PBF (beam spot sizes (σ) generally greater than 200 µm) the same phenomenon is achieved through a directed high energy electron beam rather than a laser. In both cases, the build platform contains a bed of powdered material. As each layer is micro-welded together, the build platform lowers and a new layer of powder is deposited over the build platform with a blade or rake. This process is repeated layer-by-layer until the part is complete. Post-processing may be required to ensure certain material properties, part geometry and/or surface finish.

Some of the major advantages of LPBF when compared to other metal AM processes are its fine resolution [115], wide range of materials available for the technology [366], and the potential to obtain performance superior to conventional manufacturing processes [367]. The superior resolution of LPBF when compared to direct energy deposition (DED)

and EB-PBF makes it an ideal candidate for manufacturing intricate lattices used in light-weighting parts, as well as for manufacturing complex lattice structures with fine feature sizes. LPBF also has the largest range of metal material options of any metal AM technologies. One such material is Ti-6Al-4V, a widely used biomaterial in the medical device industry. There are some benefits to considering EB-PBF for the fabrication of biomedical devices: the reduction in residual stresses resulting in reduced part distortion due to the elevated environment temperature during production, the powder layer is pre-heated into a powder cake which serves as a thermal dissipation pathway, reducing the need for extensive support structures except for part substrate anchoring requirements. As such, both LPBF and EB-PBF will be considered in this work, with a focus on lattice structure design, performance, and manufacturability for orthopaedic bone repair and augmentation devices.

A.4.2   Review of lattice designs

Lattice structures are a form of hierarchical design structures used to minimize unnecessary material with respect to design function. Lattices are typically designed for a specific application or function such as reducing weight while maintaining mechanical strength, or improving energy absorption characteristics of a design component [368, 369]. Lattice structures can be categorized into two main structure types: designed cellular lattices and stochastic (random) lattices [241].

Designed cellular structures

The majority of lattice structures can be categorized as cellular structures that are made up of unit cells with distinct, repeatable features. Cellular lattice structures are made up of struts and/or walls that are repeatedly interconnected in 3D-space by nodes. Designed cellular lattices can then be further categorized into periodic and pseudo-periodic lattices that are of homogeneous or heterogeneous organizations [370]. The periodicity of a lattice refers to the size of the unit-cells throughout the structure and homogeneity refers to the thickness of the unit-cell elements such as struts and walls. Therefore, a periodic lattice would have a uniform unit-cell size throughout its structure and a pseudo-periodic structure would have variable unit cell size. Both periodic and pseudo-periodic lattices can be further categorized into homogeneous or heterogeneous wherein they have either uniform or gradient-based strut and/or wall thickness, respectively [370].

Stochastic lattices

Stochastic, or random, lattice structures consist of irregular and non-periodic cells resulting in a network of interconnected struts and/or surfaces. Unlike other lattice structures there are no distinct cellular features that are repeated in 3D space and each cell contains a unique configuration of struts and nodes. Stochastic lattices have superior performance under both compressive and shear loading when compared to regular lattice structures [371]. However, due to their complex design, there are not as many readily available tools for the design and implementation and therefore they are not as commonly examined in literature. The final lattice type to be examined are spinodoid lattices [93], which are a subset of stochastic lattices and surface lattices. The major differentiating characteristic of spinodal lattices is that they are non-periodic. This allows for a larger design space and more achievable control of the directional mechanical properties. The benefit of spinodal surfaces is that they are immune to the symmetry-breaking defects present in cellular lattices, thus improving their mechanical properties [93].

Strut- vs surface-based lattices

Another form of categorization for lattice structures is by the cellular organization of structure. The two cellular organizations of lattice structures are strut-based lattices and surface-based lattices. Strut-based lattices are generated by determining unit cell size, the number nodes located throughout the unit cell, and the number and configuration of connectors linking nodes to each other. Porosity of the lattice may be controlled directly, or strut thickness may be selected as the control variable for lattice density. Surface-based lattices consist of a locus of points defined by a function. The most commonly used and discussed surface lattice family are triply period minimal surface (TPMS) lattices. TPMS lattices are defined by implicit functions for which the function has a constant value. TPMS structures may be periodic or pseudo-periodic and heterogeneous or homogeneous.

A.5   Review methodology

A comprehensive literature review was completed to better understand how lattice parameters are controlled in additively manufactured titanium and titanium alloy parts aimed at repairing or augmenting bone. In order to collect the most relevant data, all powder bed additive manufacturing processes were considered, pure titanium and titanium alloys were considered, and all study types were considered; however, studies were only included

when bone was the target tissue for replacement, repair and/or augmentation, to enhance the relevant scope of the designed architectures. A total of 50 journal articles fit the above criteria and the effect of lattice design parameters on mechanical properties was extracted and examined [372, 373, 374, 375, 19, 20, 376, 377, 378, 21, 379, 22, 23, 24, 25, 380, 381, 26, 28, 29, 30, 382, 383, 384, 344, 33, 385, 34, 35, 386, 36, 37, 387, 388, 38, 39, 389, 40, 41, 42, 44, 45, 390, 391, 31, 348, 43].

Existing literature describing additive manufactured titanium implants for bone repair and augmentation fits into two main categories of critical design focus: studies focused on improving osseointegration and studies focused on targeted mechanical properties. Osseointegration refers to bone's ability to grow on the surface of the implants and infiltrate the porous implant to improve implant fixation or joint fusion. In general, literature focused on osseointegration was found to have fewer reported AM and lattice parameters provided and often focused on *in vivo* results in animals or human case studies. The primary target audience for this category seems to be medical and academic researchers interested in bone tissue mechanics, growth and healing and secondarily, the additive manufacturing community. The other category of literature aims at matching the mechanical properties of bone by controlling the lattice design parameters and by controlling the printing process parameters of the respective technologies. Literature focused on matching mechanical properties of lattice structures to bone, primarily targets the additive manufacturing community with implications for bone tissue and device design being secondary suggestions. It is noteworthy to highlight this lack of apparent synergy between the two categories; such synergy is required to ensure advancements in this field.

A wide cross-section of lattice design information was collected from the bone and AM focused journals and was collated. Key parameters collected include: Young's modulus, compressive strength, lattice porosity, pore size, feature thickness, lattice type and material used. When studies compared more than one lattice design parameter, all relevant data points were collected in order to make the most robust comparison possible. Data points were then plotted on alongside Ashby plots for trabecular and cortical bone to assist in making recommendations for future lattice designs focused on titanium implant designs for bone repair and replacement (CES EduPack software, Granta Design Limited, Cambridge, UK, 2009).

A.6 Results and discussion

A.6.1 Lattice considerations

Porosity

The exercise of understanding trabecular and cortical bone porosity provides insight into the porosity required to match the structural properties of bone through titanium and Ti-6Al-4V latticing [19, 20, 21, 22, 23, 24, 25, 26, 27, 28, 29, 30, 31, 32, 33, 34, 35, 36, 37, 38, 39, 40, 41, 42, 43, 44, 45]. The most common lattice parameter reported in literature focused on additively manufactured titanium and titanium-alloy lattice structures was macro-scale porosity or void fraction. Designed lattice porosity varied from 15% to 97% with the majority of studies reporting a designed porosity between 50-70%. Titanium and titanium alloy lattices within this designed porosity range were successful in matching the stiffness of cortical bone which is known to be 5-15% porous. However, few were successful in matching mechanical properties of trabecular bone, as depicted in Figure A.5. Trabecular bone is 70-90% porous, and through this review, it was determined that titanium and Ti-6Al-4V lattices must have a designed porosity of >80% to replicate mechanical properties of trabecular bone. These findings indicate that matching material properties of titanium and Ti-6Al-4V via latticing may be challenging with existing AM technologies.

Pore size

Two-dimensional micro-architecture measurements of bone can also be described in terms of lattice parameters. When considering TbSp as a surrogate bone pore size, Hildebrand et al. reported a range from 638 μm in the femoral head to 854 μm in the lumbar spine [14]. In the literature focused on osseointegration for additively manufactured titanium lattice designs, the lattice parameter most commonly reported was pore size. The pore sizes reported ranged from 100-1500 μm. Recommendations for tailoring pore size to optimize bone in-growth or osseointegration were consistent and conclusions were drawn surrounding an acceptable range for optimal boney ingrowth. A minimum pore size of 200 μm should be considered to allow for initial cell adhesion [22]. However, to maximize cell proliferation and limit cell occlusion, large pore sizes >1000 μm are recommended [27]. Therefore, a functionally graded lattice which combines small pores for initial cell attachment and large pores to avoid cell occlusion would account for both recommendations [380, 392]. Pore size did not exhibit a trend with respect to compressive strength and Young's modulus as seen in Figure A.6 [19, 20, 21, 22, 24, 25, 26, 27, 29, 30, 32, 33, 36, 46, 38, 40, 42, 43].

194
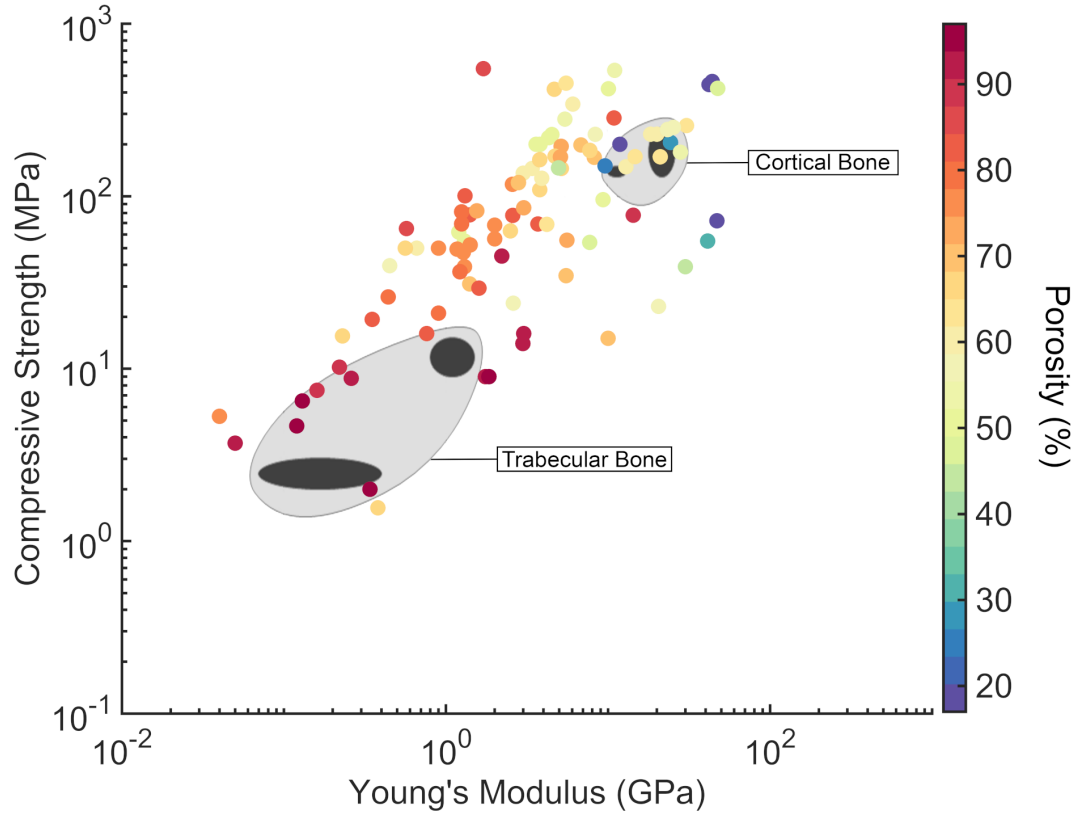
Figure A.5: Porosity is the most common lattice parameter reported in literature. Compressive strength and Young's modulus of additively manufactured lattice structures were plotted over the Ashby plots of human trabecular and cortical bone. Lattice porosity ranged from 15-97% and was plotted in a gradient to depict how best to design for material property matching [19, 20, 21, 22, 23, 24, 25, 26, 27, 28, 29, 30, 31, 32, 33, 34, 35, 36, 37, 38, 39, 40, 41, 42, 43, 44, 45].

Therefore, pore size should be viewed as a design parameter for biological reaction rather than mechanical function.
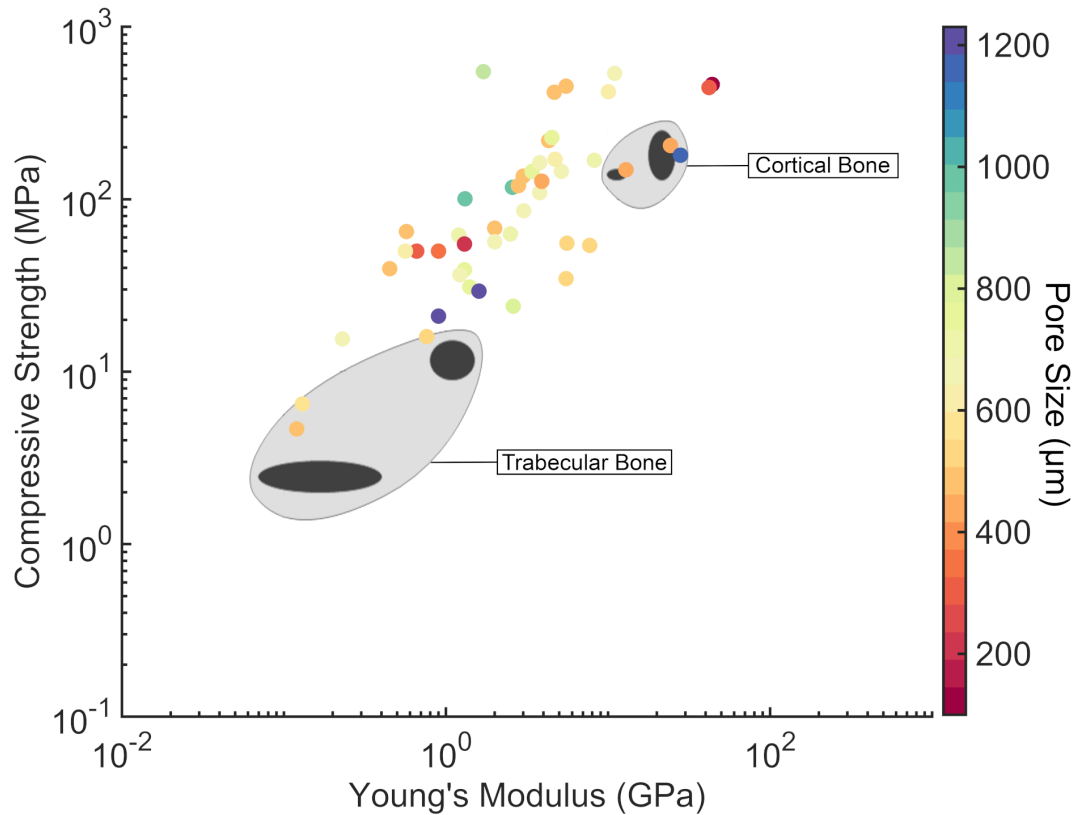
Figure A.6: Designed pore size of additively manufactured Ti and Ti-6Al-4V lattice structures was plotted in a gradient over a compressive strength versus Young's modulus Ashby plot for human trabecular and cortical bone tissues to depict how best to design for material property matching
[19, 20, 21, 22, 24, 25, 26, 27, 29, 30, 32, 33, 36, 46, 38, 40, 42, 43].

Feature Thickness

4340   Trabecular thickness can be related to feature, strut or wall thickness. Across the human skeleton, trabecular thickness varies from roughly 120-200 µm [14]. This is lower than 400 µm, or the minimum feature thicknesses typically recommended for powder bed fusion.

This is most likely due to the part resolution that can be obtained through current additive manufacturing technologies. While there were no strong trends in the effect of feature thickness on compressive strength and Young's modulus for the feature size range captured in these studies, decreasing feature thickness is one way to control lattice porosity, which is critical to manipulating mechanical properties, as seen in Figure A.7 [19, 20, 23, 24, 25, 26, 28, 29, 30, 31, 34, 37, 38, 39, 44, 45].

Figure A.7: Feature thickness was plotted in a gradient over a compressive strength versus Young's modulus Ashby plot for human trabecular and cortical bone tissues to depict how best to design for material property matching [19, 20, 23, 24, 25, 26, 28, 29, 30, 31, 34, 37, 38, 39, 44, 45].

Lattice type

When compared to strut-based lattices, surface-based lattices, such as TPMS structures, allow for better osseointegration [392]. This is thought to be due to the increased surface area available in surface-based lattices for cellular adhesion. However, the designed lattice porosity needed to match the mechanical properties of trabecular bone requires very thin wall thickness. Surface lattices also have lower stress concentrations under angular load simulation, which may make them further suitable for bone implants [392]. A recent study from Alabort et al. showed promising results for reaching the mechanical properties of trabecular bone through the use of TPMS surface lattices, specifically Schwartz's diamond surface structures [36]. In this review, lattice type had no noticeable influence on compressive strength nor Young's modulus of titanium and Ti-6Al-4V lattice structures aimed at human bone repair and augmentation, see Figure A.8 [19, 20, 23, 26, 27, 28, 29, 30, 33, 34, 36, 37, 38, 39, 40, 47, 42, 43, 44].

Material selection

Finally, material choice was examined and Ti and Ti-6Al-4V lattices were compared for their ability to achieve comparable Young's Modulus and compressive strength to human bone tissues [19, 20, 21, 22, 24, 25, 26, 27, 28, 29, 30, 32, 33, 34, 35, 36, 37, 38, 39, 40, 41, 42, 43, 44, 45]. Despite having slightly different stiffness, Ti and Ti-6Al-4V lattices did not differ in ability to reach bone properties, see Figure A.9. This may be due to other lattice design decisions, such as porosity, pore size and feature thickness, that were made to tailor overall mechanical properties.

A.6.2 Manufacturability Considerations

The potential of powder bed fusion AM technologies such as LPBF and EB-PBF to manufacture parts with higher geometric complexity compared to traditional manufacturing, makes them well suited for fabricating lattice structures mimicking bone properties. The complex features involved in the design of most lattice structures tests the manufacturability limits of LPBF and EB-PBF. This is mainly because most lattice structures used for bone repair and augmentations require fine feature sizes, particularly to replace trabecular bone. The minimum feature size strongly depends upon the beam spot size used which is generally between 50-100 µm for LPBF and >200 µm for EB-PBF. Additionally, lattice structure designs generally incorporate numerous overhanging features within a unit cell, which are challenging to produce by both LPBF [393, 177] and EB-PBF [394, 395, 396].
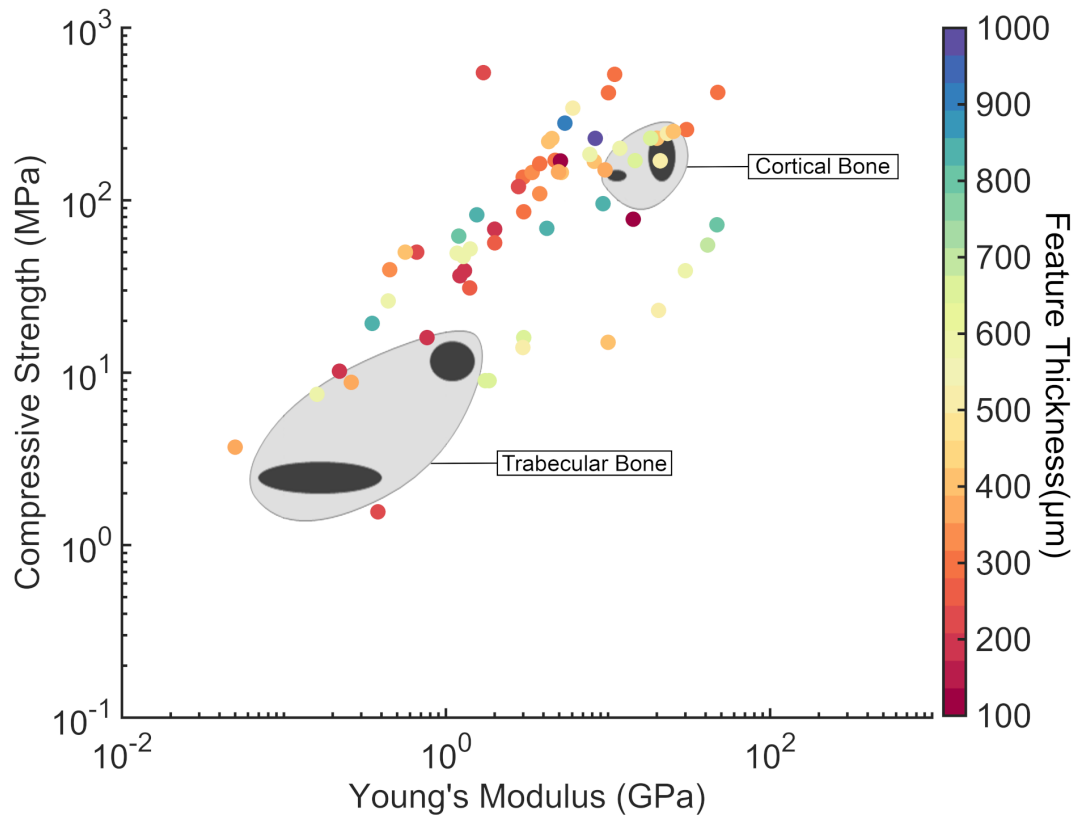
Figure A.8: Lattice type, strut- vs surface-based, was plotted in a gradient over a compressive strength versus Young's modulus Ashby plot for human trabecular and cortical bone tissues to depict how best to design for material property matching [19, 20, 23, 26, 27, 28, 29, 30, 33, 34, 36, 37, 38, 39, 40, 47, 42, 43, 44].
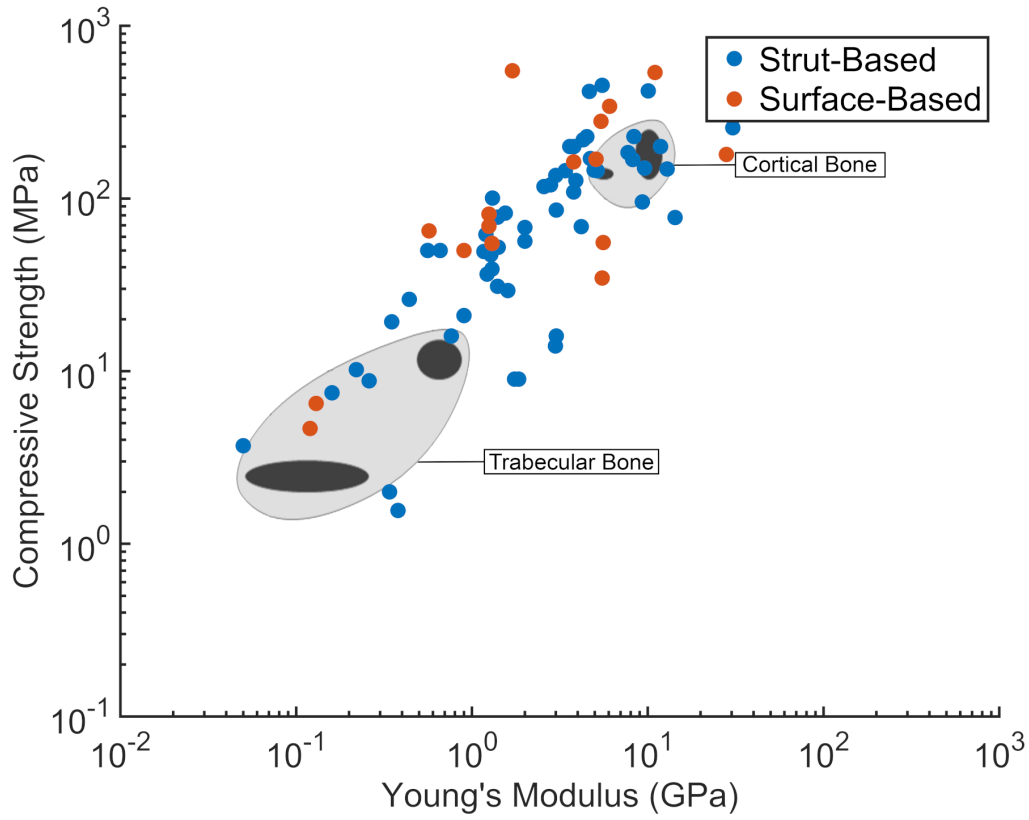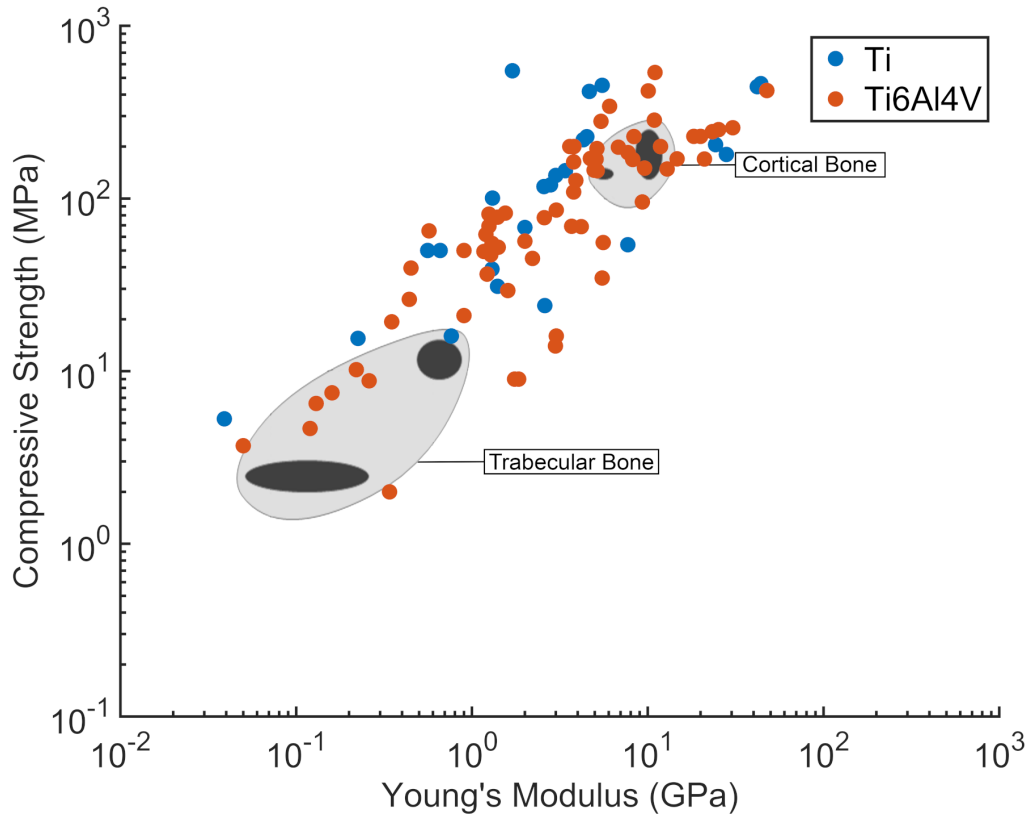
Figure A.9: Material type, Ti vs Ti-6Al-4V, was plotted in a gradient over a compressive strength versus Young's modulus Ashby plot for human trabecular and cortical bone tissues to depict how best to design for material property matching [19, 20, 21, 22, 24, 25, 26, 27, 28, 29, 30, 32, 33, 34, 35, 36, 37, 38, 39, 40, 41, 42, 43, 44, 45].

Pushing the design boundaries in LPBF and EB-PBF to achieve lattice architectures tailored for bone repair and augmentation necessitates an understanding of the three main categories of manufacturability challenges which arise in these AM technologies - defects (micro-porosity within the manufactured lattice structure), surface roughness, and geometric fidelity.

Porous defects

Due to the fatigue strength and stiffness requirements associated with manufacturing titanium-based bone repair and augmentations, understanding defects is important, as they directly impact both stiffness and fatigue life of a given AM part. It is well documented in AM literature that defects are particularly deleterious for fatigue properties [397, 398, 399]. In most of the articles reviewed in this work, stiffness values and lattice design details were commonly reported for titanium alloy lattice structures used for bone repair and augmentations, but studies into the defects within the lattice structures and their effects on fatigue life were less frequently reported.

The amount of defects and their typical morphology observed in powder bed fusion (PBF) AM depends on the process parameters used for manufacturing a given lattice structure. A low energy input is typically associated with the formation of irregularly shaped lack-of-fusion defects [10], with a high aspect ratio (width/depth) which are are known to be more detrimental to the fatigue strength of lattice structures [398], when compared to rounded keyhole defects typically associated with high energy inputs [10]. It is important to note that the presence of rounded or irregularly-shaped defects is not only dependent upon the energy input, but rather requires an understanding of PBF process parameters, particularly power, beam velocity, beam spot size, powder layer thickness, and hatching distance. It is quite possible to obtain irregularly shaped, lack-of-fusion defects within a lattice structure that uses high energy keyhole mode parameters, as shown by an X-ray computed tomography visualization of the defect space within a Ti-6Al-4V Voronoi lattice structure manufactured by LPBF in Figure A.10. A summary of the LPBF processing details and XCT measurements of the lattice structure are provided in Appendix E.

Surface roughness

Surfaces in PBF parts are generally identified with their orientation with respect to the build plate used for manufacturing as shown by the left image in Figure A.10. The four type of surfaces shown in Figure A.10 include - horizontal up-facing surfaces that are
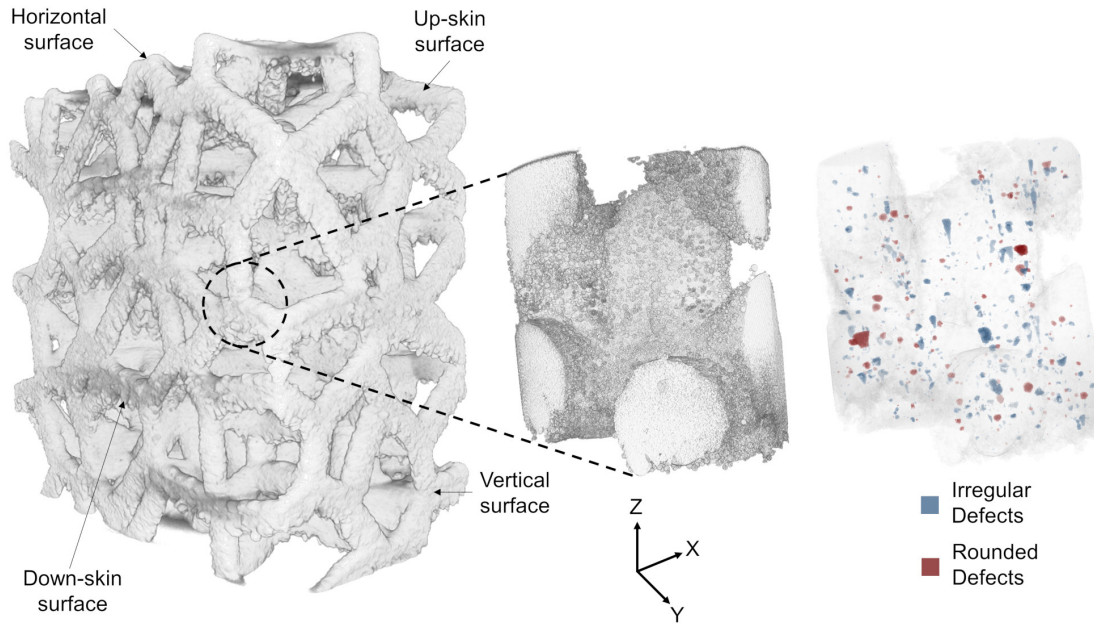
201

Figure A.10: A three-dimensional XCT visualization of the different types of surfaces observed in a laser powder bed fusion Ti-6Al-4V Voronoi lattice structure with respect to the build orientation along the Z-axis (left), a high resolution XCT image of a portion of the Voronoi lattice structure (center), visualization of the defects inside the printed lattice structure (right).

parallel to the build plate (along the XY plane), vertical surfaces that are perpendicular to build plate (along the Z axis and also known as side-skin surfaces), upward facing surfaces (known as up-skin surfaces) which are typically on an incline, but facing upwards, and downward facing surfaces (known as downskin surfaces) [251]. Since most lattices used for bone repair and augmentation are comprised of a combination of all four surface types, these surfaces are distinctly different contributors towards the final surface roughness in the printed lattice structures. Side-skin (vertical) surfaces [251, 184] and down-skin surfaces [258, 178, 399] are associated with a higher number of challenges when trying to obtain lower surface roughness values in as-printed PBF lattices, when compared to horizontal up-facing and up-skin surfaces.

In PBF AM processes, an interplay between process parameters, build file characteristics, machine characteristics, and powder characteristics drive the final surface topography of a given lattice structure. More precisely, processing parameters such as power, scan speed and layer thickness, build file characteristics such as feature geometry, feature orientation, feature location on the build plate, and beam path strategy, machine and energy source characteristics such as beam spot size, laser beam quality, and gas flow (for LPBF), and powder morphology and size distribution are some of the primary drivers for roughness of a given lattice structure.

Out of the four influencing factors, PBF process parameters are known to have the greatest effect on roughness and are also the most readily controllable for a given lattice. Horizontal and up-skin surface roughness possibly depend upon the overall size of the melt pools [179, 171], where the roughness on these surface features generally includes visibility of the melt pool tracks alongside partially fused adhered powder, particularly for the up-skin surfaces. Down-skin surface features include partially fused adhered powder as sources of coarse roughness and dross (at higher energy inputs); overall, the down-skin roughness strongly depends on the melt pool depth [178, 179]. A melt pool depth close to the powder layer thickness is generally considered to be useful for lowering down-skin surface roughness values [178]. Remelting scans of horizontal, up-skin, and down-skin surfaces are known to improve the roughness values of these surfaces [179]. Side-skin (vertical) surfaces are an exception, wherein remelting would generally not help further improve surface roughness, when compared to a well-executed first side-skin scan [183]. Side-skin surfaces are generally dominated by partially fused adhered powder in PBF, but the effects of powder can be reduced by an appropriate energy input selection which enables a dominance of melt pool track features on the side-skin that are associated with lower surface roughness values [10, 184].

Surface roughness of AM titanium lattices for bone repair and augmentation applications has been previously examined in literature. Webster and Ejiofor examined osteoblast

proliferation on 90-95% dense Ti and Ti-6Al-4V structures. They reported that osteoblasts prefer titanium surfaces with nanometer topology features [400]. Conversely, Zhang et al. reported that a surface roughness of 1-2 μm improved osteogenic properties of titanium bone implants [46]. There is still no consensus on optimal surface topology and roughness for osseointegration and adhesion, as changes in the microstructure and nanostructure of lattice surfaces both influence the cell response in bone tissues [401].

Geometric fidelity of lattice features

The fine and complex features involved in the CAD of most lattices used for bone repair and augmentations test the manufacturability limits of both LPBF and EB-PBF. This implies that a lattice structure with a fine feature size might print successfully, but not conform to the original CAD, leading to dimensional inaccuracies. Inaccuracies in additively manufactured lattices would directly impact their performance as bone repair and augmentations, since the reality of the AM structure would differ from the modelling efforts and design decisions used to determine the feature size and morphology of the lattice. Attempts at reporting the geometric fidelity of AM lattices, however, have been scarce.

In literature where dimensional inaccuracies have been reported, significant under-sizing and over-sizing of additively manufactured lattices compared to the original CAD are observed, sometimes over 100%, as reviewed by Echeta et al [399]. Dimensional inaccuracies in AM lattices depend on numerous factors, including build file setup (location, orientation, recoater offset angle, etc.) [124], PBF process parameters [293, 251], CAD file resolution [402], powder size and morphology [115, 403], and beam properties such as wavelength, operating mode, shape and quality [119, 404].

When it comes to strut-based lattices, higher dimensional inaccuracies are reported for diagonal and horizontal struts, when compared to vertically printed struts [47, 405, 406]. This is because horizontal and diagonal struts contain the highest proportion of overhanging features which are known to have the highest surface roughness-related concerns, as noted in section A.6.2. Additionally, for inclined up-skin surfaces in diagonal struts, a 'stair step' effect is commonly observed, wherein the edges of individual layers during PBF manufacturing are visible alongside effects of partially fused adhered powder [172, 407]. This is caused primarily due to the stepped approximation of curves in inclined surfaces by layers for PBF, which further adds to dimensional inaccuracies of a manufactured lattice structure. In 2D and 3D comparison of a Voronoi lattice structure manufactured using LPBF shown in Figure A.11, numerous dimensional anomalies of the printed lattice structure (compared to original CAD) can be observed, especially for the horizontal and diagonal struts which consist of down-skin surface areas. Additionally, nodes within strut
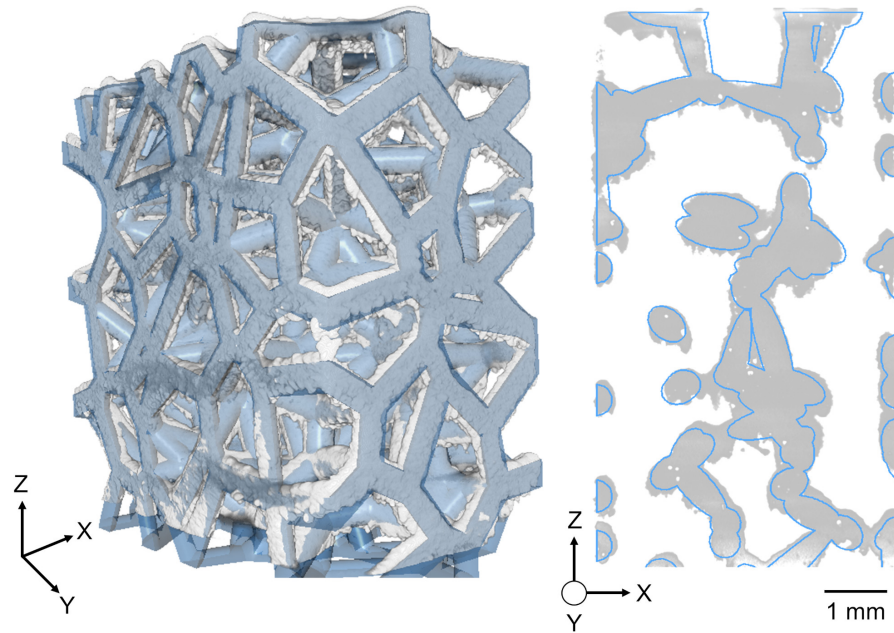
Figure A.11: A 3D comparison of the XCT visual (shown in grey) and the original CAD (shown in blue) of a Ti-6Al-4V Voronoi lattice structure manufactured by laser powder bed fusion (left) and a 2D comparison of a slice along the XZ plane of the XCT visual (shown in grey) and the original CAD (shown in blue) of the lattice structure (right)

based lattices are known to be regions with highest dimensional inaccuracies and defects [399], especially when compared to surface based lattices [408]. Nodes in strut based lattices are complex surfaces which involve a combination of up-skin, down-skin, and vertical surfaces. This complexity adds to the 'stair step' effect [408] alongside effects of partially fused adhered powder [409]. Additionally, there could a compounded effect of joining multiple struts together in the subsequent layers, wherein due to residual stresses caused by large areas, the struts may not converge to a single point in space as observed in the CAD. These issues of geometric fidelity in AM lattices would be deleterious for bone repair and augmentation applications, and hence must be evaluated well before use.

X-ray computer tomography (XCT) of AM lattices is the most common method currently used to evaluate the geometric fidelity of printed lattices by comparison of the XCT scanned model with the original CAD model [410, 411, 399], as also demonstrated in Figure A.11. Other methods include scanning electron microscopy (SEM), optical microscopy, and Vernier calliper based comparisons of the AM lattice with the original CAD dimensions [399].

Advanced considerations for trabecular geometry

This review compared trabecular bone micro-architecture to lattice parameters that can be deployed in additive manufacturing. A simplistic model of trabeculae thickness and spacing was used to relate to the lattice parameters of strut thickness and pore size, respectively. However, trabecular bone has a more complex micro-architecture than traditional strut-based lattices and therefore surface-based lattices should be considered more closely in this application. Furthermore, van Lenthe et al recognized that trabecular bone exhibits both rod and plate-like behaviour and suggested that a combined strut- and surface-based lattice configuration may best represent the trabecular bone micro-structure, see Figure A.12 [48]; such structures can now be closer to attainable from a manufacturability stand point.

Callens et al. proposed a mathematical model for describing local and global trabecular micro-architecture which suggested that bone does not exhibit mean zero curvature, like those exhibited in TMPS structures [92]. Therefore, a stochastic surface-based lattice may be the best selection for modelling trabecular bone. This has been successfully attempted by Kumar et al. [93] and their work should be considered an emerging opportunity for the design of titanium lattice architectures for bone repair and augmentation. Overall, surface lattices have shown success in replicating the mechanical properties of trabecular bone for titanium and titanium alloys and it is recommended that this avenue be pursued further [392].

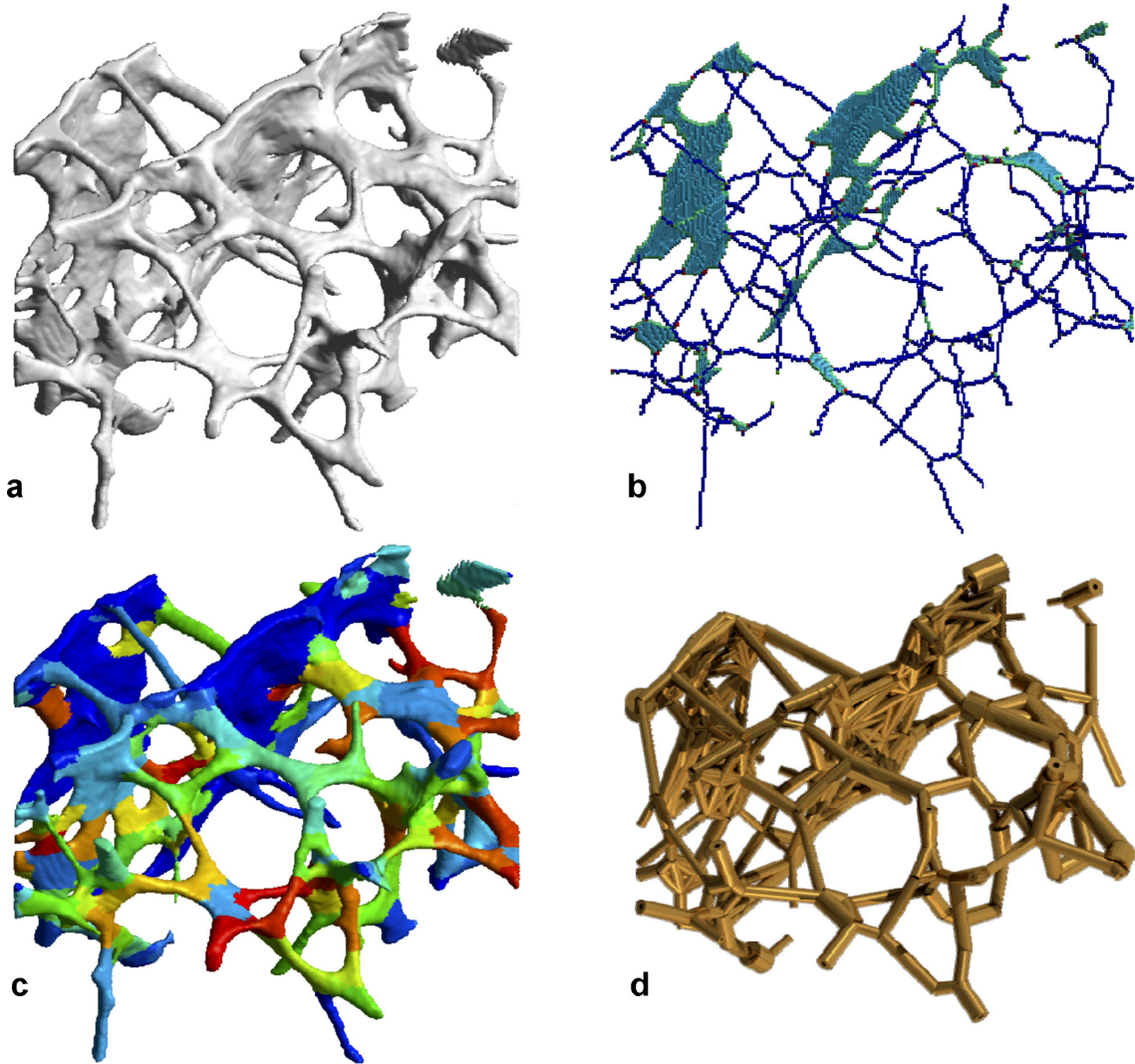Figure A.12: van Lenthe et al., used a micro computed tomographical (micro-CT) image of a human trabecular bone to develop a specimen-specific beam finite-element model. The process is shown above: (a) micro-CT reconstruction, (b) point cloud generation, (c) multi-colour dilation, and (d) assignment of element thickness and volume to finite element beams. Figure reprinted with permission from [48].

A.7 Conclusions

This review covers the breath of human bone geometry, mechanical properties of cortical and trabecular bone and the attempts made at replacing these tissues with additively manufactured titanium lattice structures. Human bone, particularly trabecular bone varies significantly with age, sex, disease state, skeletal location and region of the individual bones. Therefore, a site and function specific design approach should be considered when designing for human bone repair and augmentation. Titanium lattice structures generated through additive manufacturing have shown success in replicating cortical bone mechanical properties, promoting osseointegration for improved implant fixation and reduction of stress shielding at the bone-implant interface.

Overall, many studies were able to tune lattice parameters to obtain a Young's modulus and compression stiffness within the range of human cortical bone, with challenges in addressing the porous network architecture concomitantly. Cortical bone is roughly 5-15% porosity and titanium lattices with roughly 50-70% porosity were most successful in achieving comparable stiffness and compressive strength. Matching mechanical properties of trabecular bone was less achievable in the current literature. Trabecular thickness, or feature thickness, of human trabecular bone is on the cusp of what is attainable with existing metal additive manufacturing powder bed fusion technologies. Additionally, matching trabecular thickness to feature thickness in titanium-based lattices does not account for the difference in stiffness. Therefore, matching feature thickness to trabecular bone thickness is not a recommended technique for matching the mechanical properties of titanium lattice structures to those of human trabecular bone. Control of pore size, porosity and lattice type may yield better results when attempting to replace trabecular bone with additively manufactured titanium lattices.

Future work should include a transfer function that better relates the stiffness of titanium and Ti-6Al-4V to the lattice parameters required to generate structures that more seamlessly match the mechanical properties of human cortical and trabecular bone. Due to the large variations in bone porosity and microstructure throughout the human skeleton and the increase of bone porosity with age and in women, patient specific design may yield the best outcome with respect matching mechanical properties of bone with additively manufactured lattices. Improved lattice design for bone repair and augmentation will allow for improved orthopaedic implant design and may ultimately reduce the risk of stress shielding at the bone implant interface.

Appendix B

Scalmalloy manufacturing summary

Laser powder bed fusion (LPBF) was chosen for as the metal AM technology for the work, as it is already being implemented for part production in numerous industrial sectors, including aerospace. LPBF is often deployed as it enables the ability to manufacture components with high geometric complexity and has the potential to reduce cost and lead times. Ultimately, there is a potential to locally tailor material properties from the microscale to the macroscale using this additive manufacturing approach.

Scalmalloy was the material of choice for this work as it is one of the most mature high strength aluminum alloys available that is not susceptible to cracks during manufacturing. Toyal America supplied the sample of the Scalmalloy powders for the Advanced Manufacturing Olympics, as the quality of their powder sample was stated to be "ultraspherical with low oxygen content", rendering this to be a good option for the target of accelerated process parameter optimization in LPBF. Depending on the industry, the TRL of Scalmalloy varies from 6 to 9, with multiple suppliers and production in tons per year; examples of such sectors are aerospace, automotive, and high-performance recreational industries. In addition, process parameters for LPBF are scarce in literature, with a good opportunity to deploy innovative strategies to improve performance. Post build thermal processing consists of a stress-relief/aging cycle with an optional HIP, which removes concerns with quench-induced distortion and residual stresses in typical precipitation-hardened alloys. The manufactured Scalmalloy coupons were subjected to an aging heat treatment at 325 °C for 4 hours.

The approach to optimizing the properties of Scalmalloy involved the use of physics-driven processing diagrams, temperature prediction models, and beam path planning. First, normalized processing diagrams and the temperature prediction model developed by

in Chapter 3 of this thesis were used to quickly identify conduction mode LPBF processing parameters for Scalmalloy which help offset the probability of obtaining keyhole defects

₄₅₈₀ and alloying element vaporization, which are common issues while working with aluminum alloys [10, 209]. Using conduction mode processing parameters for the core of the parts also enables reduction in spatter formation, which has been shown to cause irregularities in microstructure and surface roughness [169, 79, 412, 2], while also affecting the quality of nearby parts [155] thereby leading to lesser repeatability in mechanical performance

₄₅₈₅ of laser powder bed fusion parts. To achieve this conduction mode approach, a dynamic laser beam de-focusing strategy was deployed in the core region, with the added benefit of increased productivity rates. The current process parameter development strategies have been implemented successfully in numerous alloy classes including titanium, aluminum, nickel, and ferrous alloys. Secondly, keyhole mode LPBF processing parameters with a

₄₅₉₀ focused laser beam approach were used to improve the surface finish over the typical build parameters [251]. Lastly, during the LPBF process, a lower heat input was used in the overhanging surfaces to reduce the dross formation commonly observed in laser powder bed fusion components [177]. To achieve the goals and complete the manufacturing of all necessary coupons, a commercial modulated laser system with focusing/de-focusing capabilities

₄₅₉₅ (Renishaw AM 400) was deployed.

Military application will benefit from having a high-strength aluminum alloy for laser powder bed fusion in several ways:

- Firstly, the higher forecasted mechanical properties will benefit sustainment by providing an AM alternative for the replacement of more highly loaded parts originally
₄₆₀₀ made from 2xx, 3xx, 2xxx, 6xxx, and 7xxx alloys.

- Secondly, a high-strength alloy with simple post-processing will enable more optimized future designs without the complications of solution annealing and quenching that can result in residual stresses and distortion.

- Finally, a high-strength alloy with broad industrial use and multiple powder suppliers
₄₆₀₅ will ensure both availability of powder and a competitive pricing environment, especially as demand for Scalmalloy grows and additional sources of alloying elements become available.

All the coupons were manufactured on the reduced build volume (RBV) of a modulated beam LPBF system. The entire process parameter optimization and manufacturing cycle,

₄₆₁₀ from receiving the powder to printing the products, spanned 4 business days. Due to an extremely tight timeline for obtaining approvals for the new alloy for use in the full

build volume and timelines for material changeover, the RBV was deployed. This led to a maximum length (height) of 55 mm possible for the tensile blanks, built across 4 build cycles. The tensile blanks had to be manufactured in the Z-axis (build direction) orientation due to recoating issues arising in the reduced build volume when working other orientations for the tensile blanks. The build orientations of all coupons are illustrated in Figure B.1. Electro-discharge machining (EDM) was used to cut-out the samples from their respective build plates.
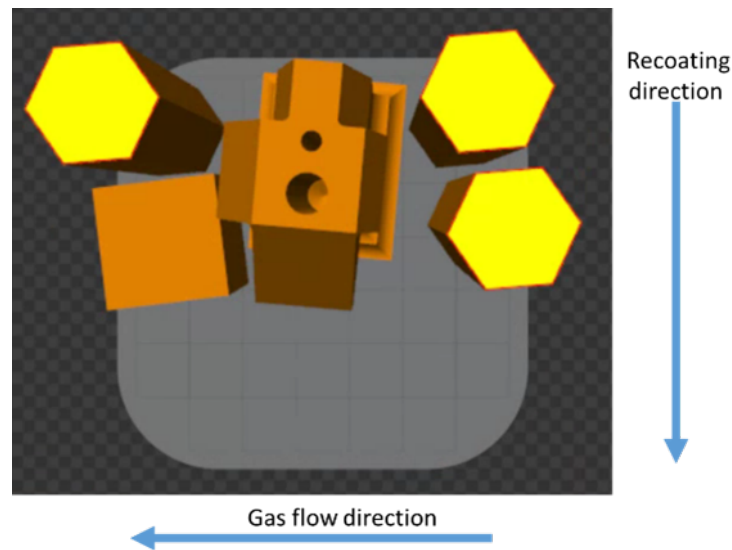

Figure B.1: Illustration of the powder flow (recoating) and gas flow directions with respect to part orientations on the reduced build plate of the Renishaw AM 400.

Appendix C

Monolithic interferometer - manufacturing summary

The LPBF system for this work was a modulated LPBF system (a Renishaw AM 400), in which, the beam velocity variable is split up in two: point distance and exposure time. This modulation of the laser beam gives provides an additional degree of control which is not possible in continuous LPBF systems. Additionally, the Renishaw AM 400 system allows for changes to the beam spot diameter which make it easier for develop process parameters for a new and challenging material system such as Invar36 using a combination of processing diagrams, micro-scale simulations, beam path planning, advanced microstructure characterization and part performance characterization methods from this thesis.

Due to the locally concentrated energy input in LPBF, localized thermal loads are generated, leading to numerous challenges while adopting this technology for new materials, including the material selected for this work – Invar36. At a composition of approximately 36 wt.% Ni, the Invar36 alloy takes a characteristically low coefficient of thermal expansion (CTE) compared to most known Invar alloys [99]. Due to this characteristic, Invar36 alloy is widely used in many applications requiring high dimensional stability such as precision instruments and tooling, metrology, cryogenic liquid storage and transport, and optical mounting in the space industry [270]. The low CTE of Invar36 hence also makes it suitable for this work.

A graphical summary of the ground-up manufacturing steps used to obtain the final monolithic quantum sensing interferometer is shown in Figure C.1. The initial goal shown in the bottom left side of Figure C.1 was to identify the best set of laser powder bed fusion (LPBF) process parameters to print complex and large structures as shown in the

212

top right side of Figure C.1. To this purpose, the first objective was to maximize density (core and sub-surface) and minimize surface roughness (side skin, down skin, up skin). Of note, the Invar36 material is not a common LPBF material system, with scarcity in literature to inform the process parameters to achieve desired density and surface topography performance.
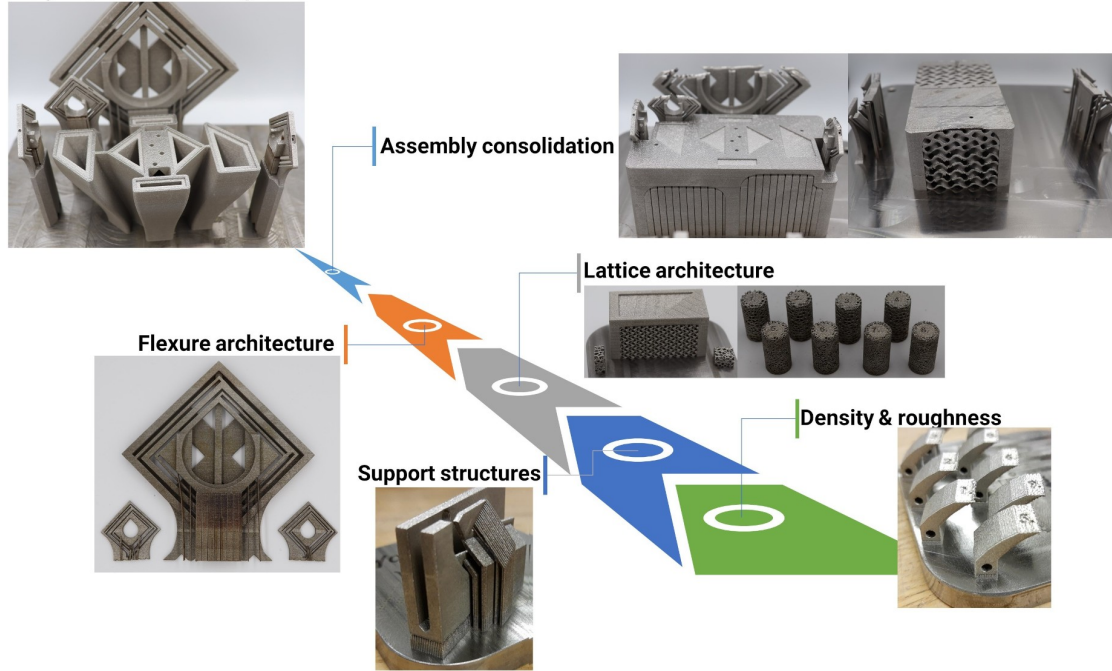
Figure C.1: Graphical abstract of the manufacturing steps used to obtain the monolithic quantum sensing interferometer. The ground-up manufacturing steps are shown from bottom right to the final assembly on the top left.

The initial print consisted of 8 coupons designed in a way such that density could be tested using an X-ray computed tomography (XCT) setup and surface roughness could be tested using a laser profilometer, as shown in Figure C.2. In addition, the quality of through-holes was also assessed using this type of geometric coupon. Each of the coupon explored a different combination of process parameters spanning the three melting modes in LPBF predicted by the processing diagrams develop in Chapter 3 of this thesis. From this initial print, an ideal set of LPBF process parameter was identified which was used in the subsequent prints as illustrated in Figure C.1. The manufactured coupons were built on support structures on the substrate, with the resulting manufactured samples shown on the far left of Figure C.2. The roughness of best LPBF coupon is showcased in the

center of Figure C.2. The sample with the best performance for both surface topography and density was assessed by using XCT overlayed with original CAD outline of the part, as illustrated in the right side of Figure C.2. The XCT data of the LPBF coupon is shown in grey, while the CAD is shown in yellow in Figure C.2.
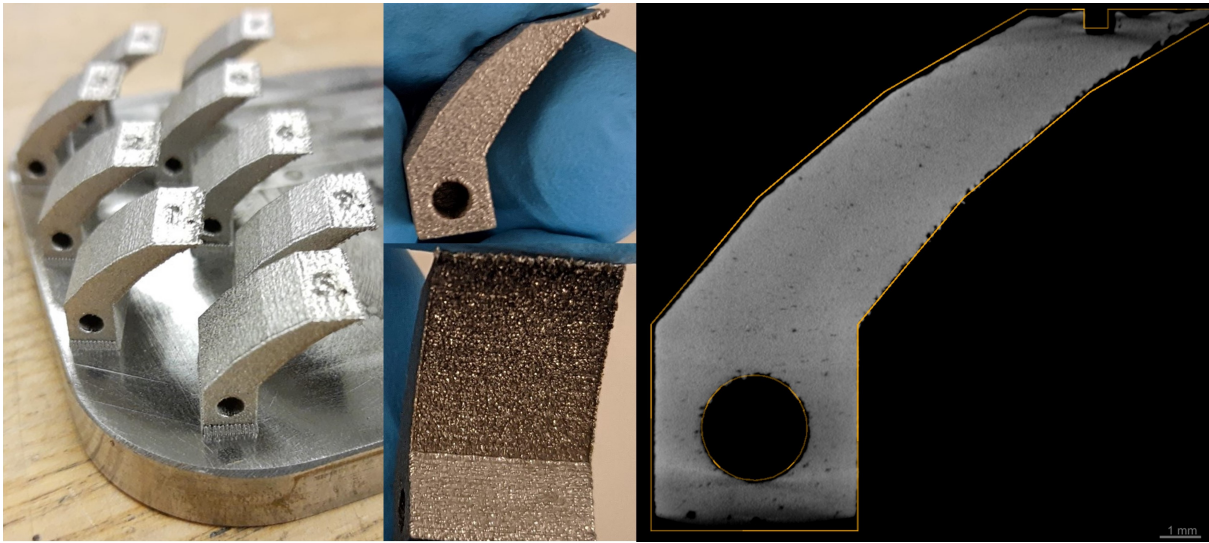
Figure C.2: Image of coupons from initial print on a the RBV build plate of Renishaw AM 400 (left), images showcasing the roughness of the best coupon (center), comparison of the best LPBF coupon with the CAD using XCT (right).

The remaining steps in manufacturing the monolithic interferometer, as noted by the milestones from Figure C.1 involved:

- Identifying the best set of LPBF process parameters to print support structures needed for complex and large structures in the final monolithic structure

- Designing and building a lattice architecture best suited for providing mechanical and thermal stability to position the optical mirrors (required for the interferometer to function) along with light-weighting the structure.

- Designing and building flexures that are capable of being manufactured using LPBF in a monolithic design.

- Designing and building a monolithic setup that includes all the required flexures and the plinth setup for the optical mirrors using LPBF additive manufacturing.

214

This work was completed from concept to print in less than 6 months, without any of the collaborators ever being in the same room.

Appendix D

Experimental results from Ti-6Al-4V and AlSi10Mg weld line datasets

D.1   Ti-6Al-4V datasets

Methods

The total number of weld lines analyzed was 16 and the locations of the weld lines on the build plate is shown in Figure D.1. The depth, width, and height of the weld lines were analyzed using a laser confocal microscope (Keyence VK-X250). The results from the weld lines printed on the substrate artifacts and the base plate are summarized in the following section.

Figure D.1: Layout of the 16 sets of weld lines on the build plate of Renishaw AM 400. Each set involves 5 weld lines where each weld lines is separated by a hatching distance of 100 μm.

Results

An image of the melt pool morphology measurements for one of the 16 set of weld lines is given in Figure D.2. The melt pool depth, height, and width measurements are reported in Table D.1. The beam spot diameter for all the weld lines in Table 1 was 70 µm which is the value for the Renishaw AM 400 laser at the focal point.
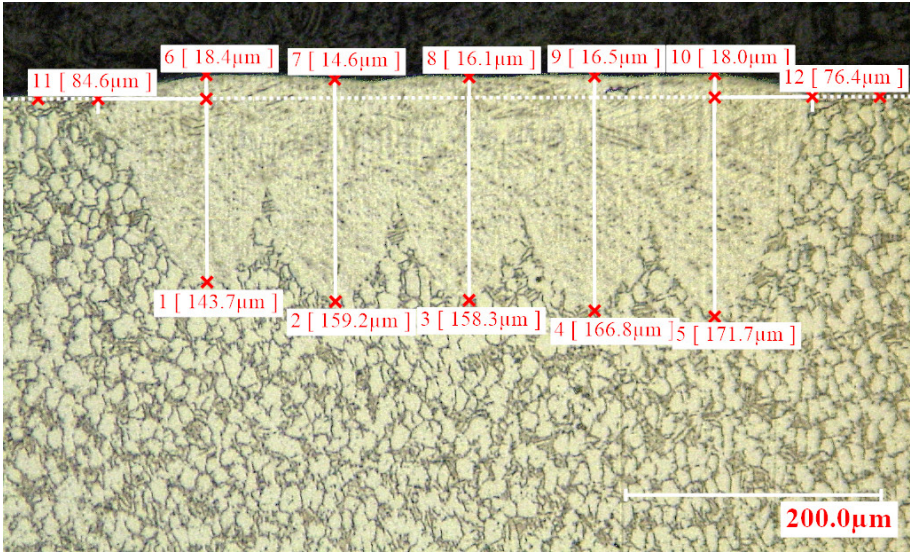
Figure D.2: The melt pool depths (lines 1-5), melt pool heights (lines 6-10), and melt pool width (line 11 + line 12) at laser power of 300 W, point distance of 55 µm, and exposure time of 45 µs on Renishaw AM 400.

D.2   AlSi10Mg datasets

Methods

The total experimental combinations for weld lines analyzed was 55 and the locations of the weld lines on substrate artifacts on the build plate is shown in Figure D.3. Substrate artifacts are 10 mm cubes which were build on top of the LPBF system build plate. The last layer on top of the substrate artifacts were the weld lines as shown in Figure D.3. Conduction mode melt pools on the Renishaw AM 400 were obtained by defocusing the focal point of the laser beam to a point above the build of the system. The transition mode

Table D.1: The melt pool depth, height, and width for the 16 sets of weld lines, along with the laser power, point distance, and exposure time settings.

Power [W]	p_d [µm]	t_e [µs]	Depth [µm] Avg.	Depth [µm] Std. dev.	Height [µm] Avg.	Height [µm] Std. dev.	Width [µm]
150	75	45	51.96	1.84	19.98	3.08	105.80
150	55	55	80.50	5.76	19.80	4.56	126.60
150	55	65	76.30	10.57	19.02	13.35	134.50
200	75	55	91.36	9.01	30.60	5.11	129.70
200	55	45	97.50	3.70	16.54	5.63	139.40
200	55	55	106.74	7.93	22.98	11.47	134.50
200	55	65	93.04	11.51	30.44	8.90	123.50
250	75	55	137.62	10.81	38.58	6.49	154.00
250	55	45	137.42	9.58	19.88	10.55	146.9
250	55	55	137.70	4.69	28.26	18.21	140.80
250	55	65	124.16	7.66	28.04	11.85	126.20
300	75	45	180.78	19.06	43.12	11.28	169.20
300	75	55	207.48	20.07	31.94	8.06	154.70
300	55	45	159.94	10.63	16.72	1.53	161.00
300	65	65	120.90	11.26	21.28	8.81	127.00
300	55	65	233.56	21.24	39.32	6.85	144.30

melt pools were obtained from a similar build plate layout with the only change being an increased layer thickness of 35-50 µm instead of the 30 µm used for the conduction mode melt pools. The depth, width, and height of the weld lines were analyzed using a laser confocal microscope (Keyence VK-X250). The results from the weld lines printed on the substrate artifacts are summarized in the following section.
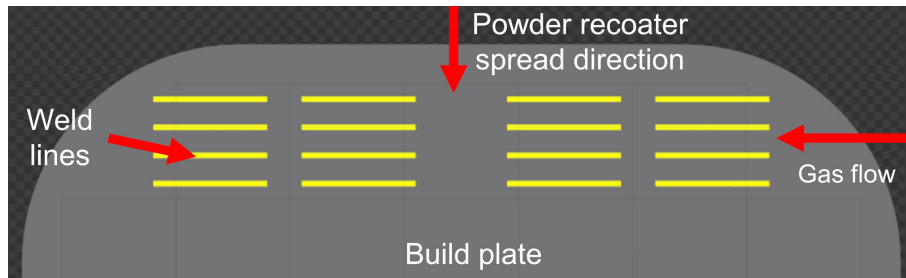
Results

An image of the melt pool morphology measurements for one set of weld lines is given in Figure D.4. The melt pool depth and width measurements are reported in Table D.2. Melt pool morphology images for individual melt pools can be provided upon reasonable request.
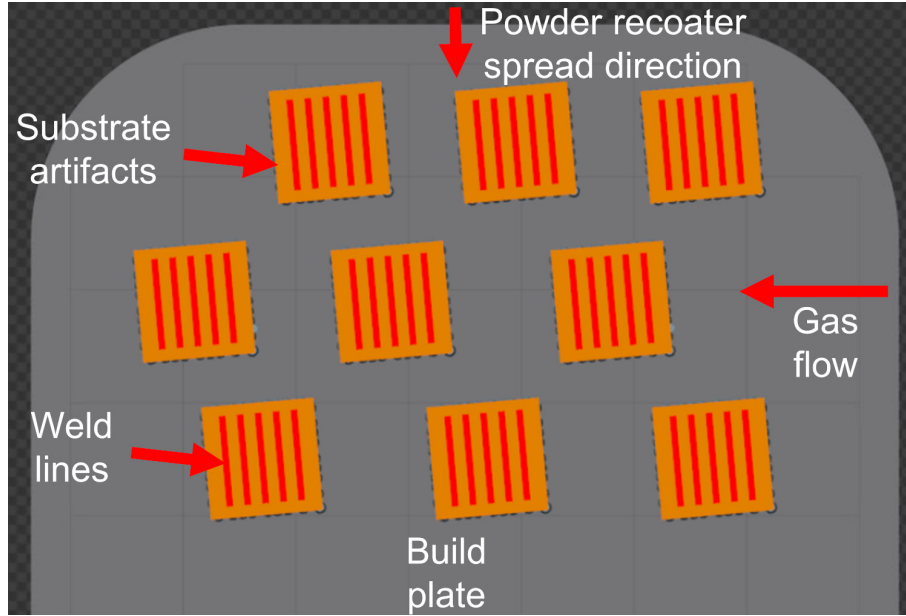
Figure D.3: Layout of the weld lines on substrate artifacts manufactured on the build plate of Renishaw AM 400. Each set involves 5 weld lines where each weld line is separated by a hatching distance of 100 µm.
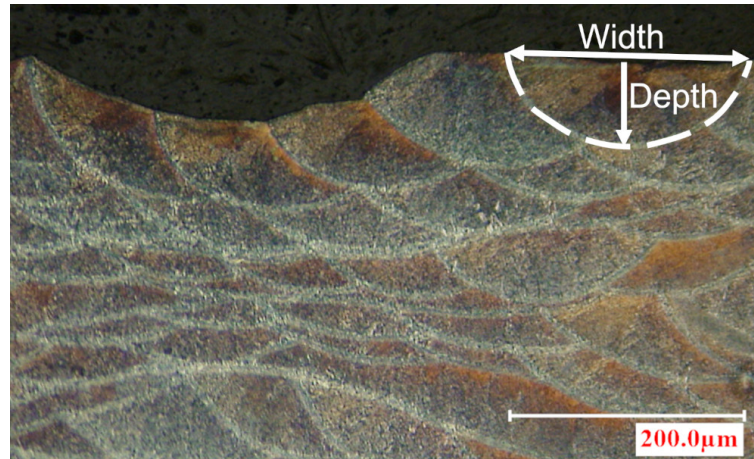

Figure D.4: The melt pool depth and melt pool width measurement illustration of a solidified melt pool at laser power of 200 W, point distance of 55 µm, and exposure time of 60 µs, and beam spot diameter of 128 µm on Renishaw AM 400.

Table D.2: The melt pool depth and width for the weld lines, along with the laser power, point distance, exposure time, and beam spot diameter settings.

Power [W]	p_d [µm]	t_e [µs]	l_t [µm]	σ [µm]	Depth [µm] Avg.	Depth [µm] Std. Dev.	Width [µm]
150	55	80	30	108	63.76	9.22	207.50
200	55	100	30	108	79.50	4.64	220.50
200	55	60	30	108	67.20	0.99	185.10
250	55	80	30	108	72.66	4.81	205.00
250	55	60	30	108	66.18	13.27	195.60
300	55	100	30	108	87.68	2.57	231.00
300	55	80	30	108	78.22	3.29	223.10
300	55	60	30	108	69.96	7.51	202.40
350	55	80	30	108	78.33	12.25	234.70
350	55	60	30	108	77.70	5.04	239.40
400	55	100	30	108	100.70	7.34	256.00
400	55	80	30	108	94.43	9.41	268.00
400	55	60	30	108	84.90	5.93	227.60
200	55	60	30	128	63.10	6.58	187.80
250	55	60	30	128	68.14	6.09	206.80
300	55	60	30	128	74.56	3.18	223.10
350	55	60	30	128	80.54	5.77	223.80
400	55	60	30	128	87.85	4.88	249.40
200	55	60	30	146	66.92	6.98	196.90
250	55	60	30	146	69.93	4.11	206.40
300	55	60	30	146	74.38	3.15	245.80
350	55	60	30	146	87.14	9.24	244.60
400	55	60	30	146	105.88	15.97	264.20
200	55	60	30	167	63.90	6.72	230.40
250	55	60	30	167	78.57	1.84	271.20
300	55	60	30	167	82.38	7.03	271.60
350	55	60	30	167	84.86	5.78	270.90
400	55	60	30	167	90.90	9.83	277.60
200	55	80	30	183	74.34	9.72	240.10
250	55	80	30	183	86.96	12.02	252.90

Power [W]	p_d [µm]	t_e [µs]	l_t [µm]	σ [µm]	Depth [µm]		Width [µm]
					Avg.	Std. Dev.	
300	55	80	30	183	98.10	8.46	288.30
350	55	80	30	183	103.76	9.41	321.90
400	55	80	30	183	112.24	7.06	317.90
300	55	100	30	203	97.56	9.39	340.10
350	55	100	30	203	110.06	6.30	349.10
400	55	100	30	203	117.40	9.73	364.10
123	60	230	35	70	64.06	44.39	126.97
156	60	110	35	70	87.29	34.57	157.65
193	60	70	35	70	103.26	15.26	198.22
234	60	50	35	70	90.48	24.90	187.29
390	60	24	35	70	106.15	26.16	149.02
161	60	230	35	70	101.95	33.25	197.17
212	60	110	35	70	160.79	30.58	273.12
270	60	70	35	70	177.04	39.41	254.05
334	60	50	35	70	170.36	23.03	260.50
177	60	110	35	70	106.29	27.96	203.77
193	60	70	35	70	96.51	16.93	177.18
255	60	50	35	70	138.52	14.62	196.49
287	60	38	35	70	111.54	23.07	175.82
240	45	60	50	70	130.43	28.51	188.75
240	60	60	50	70	139.27	26.44	204.08
240	75	75	50	70	112.96	21.82	178.50
200	60	170	50	70	168.23	44.49	254.46
200	60	119	50	70	85.70	26.03	180.79
200	60	60	50	70	94.87	21.98	156.78

Appendix E

Voronoi lattice structure manufacturing and analysis

Manufacturing details

The Voronoi lattice structure was designed using nTopology and manufactured using Ti-6Al-4V powder on the reduced build volume (RBV) of a modulated laser powder bed fusion (LPBF) system (AM 400, Renishaw, UK). The powders used were plasma atomized (grade 23) with a size distribution of 15-45 µm (d10 of 20 µm, d50 of 34 µm, and d90 of 44 µm), provided by AP&C (Quebec, Canada). A powder layer thickness value of 30 µm and a hatching distance of 100 µm was used. The laser power and velocity settings were selected as per the LPBF system manufacturer's recommendation for Ti-6Al-4V which are predicted to lie in the transition melting mode from previous work [10]. For the AM 400 system, the beam spot radius at the focal point is given by $r_b = 35$ µm, which was kept constant for this study. The scan strategy followed this order: scanning of the core using the meander scanning strategy, followed by a border scan that involves melting of the edge of each contour within a layer specified by the CAD of the lattice structure.

X-ray computed tomography details

The Ti-6Al-4V Voronoi lattice structure was analyzed in a 3D X-ray computed tomography (XCT) scanner (ZEISS Xradia 520 Versa). The important processing parameters used to obtain the XCT results for the entire lattice structure (left of Figure A.10 in Chapter A)

are shown in Table 1, and the parameters used for the high resolution scan (centre and right of Figure A.10 in Chapter A) are shown in Table 2. To visualize the defect space within the sample, the XCT scanned file was then analyzed using an image processing software (Dragonfly 3.0, Object Research Systems Inc., Montreal, QC). The brightness, contrast, and opacity of the data volume was adjusted to highlight the features of interest within the XCT data volume.

Table E.1: X-ray computed tomography parameters used for scanning the entire Ti-6Al-4V Voronoi lattice structure.

Parameter	Unit	Value
Voxel size	[µm]	12.5401
Source power	[W]	7
X-ray energy	[kV]	80
Filter	-	LE6
X-ray optic	-	0.4x lens
Source position	[mm]	23.019
Detector position	[mm]	130.0033
Exposure time	[s]	1.5
Number of projections	-	2401
Binning level	-	2

Table E.2: X-ray computed tomography parameters used for scanning the high-resolution scan of a portion of the Ti-6Al-4V Voronoi lattice structure.

Parameter	Unit	Value
Voxel size	[µm]	2.0029
Source power	[W]	7
X-ray energy	[kV]	80
Filter	-	LE6
X-ray optic	-	4x lens
Source position	[mm]	14.0390156
Detector position	[mm]	103.0033
Exposure time	[s]	4
Number of projections	-	3001
Binning level	-	2